Andrew Fwu Tay Leong

Phase Contrast X-ray Imaging for Quantifying Pulmonary Form and Function

Submitted in total fulfillment of the requirements

of the degree of Doctor of Philosophy.

School of Physics and Astronomy

Monash University

March 2015

Copyright Notices

Notice 1

Contents

Abstract

This thesis presents newly developed propagation-based phase contrast x-ray (PB-PCX) imaging-based methods for studying lung form and function. The structure of the lungs is highly complex and arguably even more so its respiratory behavior. Whilst many imaging-based advances have been made to provide insight into the structure and mechanics of the lung, none have yet possessed the capabilities to render highly detailed images of the lungs and provide real-time tracking of its behavior. Achieving greater insight into the structure-function relationship of the lungs can potentially lead to more accurate and sensitive diagnostic tools for respiratory diseases. Moreover, it can help design safer and more effective ventilation strategies for patients in respiratory distress.

PB-PCX imaging provides strong soft tissue contrast to enable the fine features of the lungs visible, including the intricate network of the airways, and provide real-time imaging. The radiation dose per image is no more and potentially less than conventional x-ray imaging. These properties motivate the work presented here in utilizing PB-PCX imaging for developing methods to study the lungs. In many other lung imaging techniques, a contrast agent or a large radiation dose are often required to visualize lung tissue.

Chapter 3 presents a method that involves aligning two PB-PCX chest images to segment the bony anatomy and isolate the lungs before applying the single image phase retrieval algorithm (SIPRA) to regionally measure the relative change in lung air volume. This expands on a previous method that utilizes only SIPRA, which was found to be accurate only for measuring regional lung air volume across large areas of the lungs. From PB-PCX chest images of rabbit kittens being ventilated while immersed in a water-filled tube (this is required to implement SIPRA), regional lung air volume is found to be less accurately measured using the previous method (SIPRA only) than the improved method (bone segmentation and SIPRA). This justifies the importance of segmenting the bones to perform local measures of lung air volume and validates the bone segmentation algorithm developed here. Applying the improved method to a mechanically ventilating rabbit, volumetric maps show lung aeration can be highly heterogeneous.

The drawback of the new method described above is that as the lung air volume increases, the bones are less accurately aligned and segmented, resulting in errors in regional lung volume measures. A different approach is taken by representing the PB-PCX chest image in Fourier space.

Since the bones and airways of the lungs are of different length scales, the latter being much smaller in dimensions than the former, they occupy different bands of spatial frequencies. The signal corresponding to the airways is known as lung speckle since they appear as a spatially random distribution of bright and dark intensity spots in PB-PCX chest images. Focusing only on the spatial frequencies belonging to the lung, chapter 4 presents a theoretical model of the lung speckle power spectrum based on the solution to Helmholtz equation while treating the lung as a random distribution of spherical voids embedded in soft tissue. This model is validated in simulated PB-PCX lung images using the angular spectrum formulation of scalar diffraction integrals. It shows that the integral over the domain of spatial frequencies occupied by the lung is dependent on lung air volume. This fact has enabled a relationship to be determined between these two parameters by calibrating them using PB-PCX images of mechanically ventilated rabbit kittens in water-filled tubes. The calibration curve is used to measure lung air volumes from PB-PCX chest images of rabbit kittens *without* having to immerse the animals in water-filled tubes, and shows strong agreement with that measured from a gold standard technique (flowmeter). Besides avoiding needing to align the bones to segment them from the lungs, a higher signal-to-noise ratio is achieved due to removing x-ray attenuation from water in the tube.

In a final study, this thesis shows that the integral of the lung speckle power spectrum encodes information about the number and size of alveoli in the lung. Chapter 5 presents a method that extracts this information based on the theoretical model developed in chapter 4. That model assumes the alveoli are uniformly randomly distributed, but at increasing lung air volume the alveoli become closely packed and give rise to short-range ordering; hence the underlying theory is generalized to account for short-range-ordering. However, additional information on the radial distribution of the alveoli is required to adopt this more general theoretical model into this method. To determine whether it was necessary to account for short-range-ordering, PB-PCX imaging experiments were performed on samples of glass microspheres of known size. It is shown that the method using the original model is robust against the effects of short-range-ordering, thereby it can be used to accurately measure the number and dimensions of alveoli in the lungs over a large range of lung air volumes. The reason is found to be that short-range-order affects the shape of the lung speckle power spectrum but not its integral, thus avoiding needing to use the theoretical model that accounts for short-range-order. This method is applied to rabbit kittens and shows the presence of alveolar recruitment/de-recruitment, highlighting that alveoli may open/collapse instead of just varying in size to accommodate the flow of air. Findings such as this will help shape how diagnosis respiratory diseases and ventilation strategies are improved.

General Declaration

Monash University

Declaration for thesis based or partially based on conjointly published or unpublished work

General Declaration

In accordance with Monash University Doctorate Regulation 17.2 Doctor of Philosophy and Research Master's regulations the following declarations are made:

I hereby declare that this thesis contains no material which has been accepted for the award of any other degree or diploma at any university or equivalent institution and that, to the best of my knowledge and belief, this thesis contains no material previously published or written by another person, except where due reference is made in the text of the thesis.

This thesis includes 3 original papers published in peer reviewed journals. The core theme of the thesis is developing phase contrast x-ray imaging-based quantitative techniques for studying the lungs. The ideas, development and writing up of all the papers in body of the thesis were the principal responsibility of myself, the candidate, working within the School of Physics and Astronomy under the supervision of Marcus J. Kitchen and David M. Paganin.

The inclusion of co-authors reflects the fact that the work came from active collaboration between researchers and acknowledges input into team-based research.

Signed:

Andrew Fwu Tay Leong

Acknowledgments

This study was undertaken with the mantra that seclusion was the key to maintaining one's focus in order to achieve one's goals. Initially this seemed to bode well with the work achieved. However, over time a realization was dawned upon that something was amiss, the mind–no matter how brilliant it is–cannot accomplish without regardless of how hard one tries. The strange and mysterious inhabitants that occupy the same micro-ecosystem as this author, who viewed them at first as aloof and irrelevant, eventually learned to appreciate and were needed to complete this work. Hence, the author wishes to give its most sincere thanks since giving it in person will be both unpleasant and inelegant for both parties.

To my supervisors, Dr. Marcus J. Kitchen and Prof. David M. Paganin, your support and occasional tough love has positively shaped how I will approach and tackle new obstacles for the remainder of my career and life in general. I love physics even more now not because of what I have learned from you, but the excitement in knowing there is so much more to learn.

To the beamline scientist and collaborators whom I met at the SPring-8 synchrotron facility, I am grateful for your assistance in our work and readiness to share your exciting work with us. It has been insightful to witness the world of physics so often confined in theory applied to the real-world.

I would like to thank the School of Physics for its financial support through a Faculty of Science Dean's Postgraduate Research Scholarship in 2011 then an Australian Postgraduate Award in 2012-2014. Also, to the Monash University Institute of Graduate Research for offering a travel grant to attend an overseas conference and to perform experiments at SPring-8.

To the staff of School of Physics, your assistance and ability to tolerate my lack of organizational skill is much appreciated-particularly Jean Pettigrew. To the people running the 2nd year teaching labs, thank you for giving me the opportunity to teach, it has helped strengthen my own understanding in the fundamentals of physics and made me realize the hardship of teaching-something I did not readily appreciate as an undergraduate student.

My past and present fellow colleagues, you have made the days slightly more tolerable (sometimes too 'tolerable'!). Particularly to Wan, you've inspired me in so many ways that it made the short time we hanged out bittersweet. I stand here with the utmost respect to cricket, you have been

a huge part of my life and given me something to look forward to every week. I am glad to have shared this passion with so many great people. Jerry and Gayan, you guys have been my escape from the stresses of research, distracting me with your shenanigans and quirky humor.

To my family–Dad, Mum and brother–zhòng guā dé guā, zhòng dòu dé dòu. Thank you for all the advice, support and guidance. It has been an amazing journey and I am glad to have shared it with you.

Abbreviations

1D one-dimensional.

2D two-dimensional.

3D three-dimensional.

AB area-based.

AB-PCX analyzer-based phase contrast x-ray.

AP airway pressure.

CC cross correlation.

CLSM confocal laser scanning microscopy.

CNR contrast-to-noise ratio.

CT computed tomography.

DES dual-energy subtraction.

EM electromagnetic.

ESF edge spread function.

FAH feature and area-based hybrid.

FFT fast Fourier transform.

FOP fiber optic.

FOV field-of-view.

FRC functional residual capacity.

FWHM full width half max.

IB-PCX interferometric-based phase contrast x-ray.

V_L lung air volume.

LDIPR Laue dual-image phase retrieval.

MI mutual information.

MIR multiple image radiography.

MPS maximal planar subdivision.

MRI magnetic resonance imaging.

MTF modulation transfer function.

NFIE near-field intensity equation.

NIST National Institute of Standards and Technology.

OCT optical coherence tomography.

ODD object-to-detector propagation distance.

PS_{Area} area under the power spectrum.

PS_{Peak} position of the first order peak in the power spectrum.

PB-PCX propagation-based phase contrast x-ray.

PCX phase contrast x-ray.

PET positron emission tomography.

PMMA polymethyl methacrylate.

PSF point spread function.

PV pressure-volume.

PVII Pearson type VII distribution function.

$\mathbf{R^2}$ Pearson product-moment correlation coefficient.

RDTI relative difference in total intensity.

ROI region-of-interest.

SAAM speckle-based alveolar analysis method.

SAD sum of absolute differences.

SIPRA single image phase retrieval algorithm.

SLG soda lime glass.

SNR signal-to-noise ratio.

SOD source-to-object distance.

SPECT single photon emission computed tomography.

SRO short-range-order.

SSD sum of squared differences.

USAXS ultra small angle x-ray scattering.

VILI ventilation-induced lung injury.

VR vertebra-rib.

List of Tables

List of Figures

Introduction 1

1.1 Motivation

The principal function of the lung is to supply the human cells with oxygen and remove byproducts of cellular activity, such as carbon dioxide[1]. The lung is often described as a balloon that expands to draw air in, where gases such as oxygen and carbon dioxide are exchanged between the lung and cardiovascular system, then deflates to push air back out (Fig. 1.1(a)). More realistically, however, the lung is much more complex as it is made up of many tiny "balloons" (instead of one big balloon), known as alveoli, which are connected by small airways, in order to increase the total surface area over which gas exchange can take place (Fig. 1.1(b)). It is at the alveolar level that the behavior of the lung is poorly understood. Specifically, it is not well known how air distributes itself to each alveolus, how each of the alveoli behaves, and how they affect each other during respiration. This lack of understanding is due to the complexity of the alveolar structure and mechanics together with limited imaging capabilities.

The highly complex structure and behavior of the lung have attracted interest from biomedical engineers, physicists and mathematicians (Bates, 2009). Their common interest is fundamentally to understand how the mechanical processes of the lung make breathing almost effortless. Studying alveolar behavior and air ventilation (flow rate of air) during breathing would help towards understanding the mechanics of the lungs. Considering that the alveolar size is on the order of tens of microns and is rapidly changing in time with breathing, an imaging system with both high spatial and temporal resolution is required to study the lung at the alveolar level *in vivo* (Daly et al., 1975; Ochs et al., 2004). Tomographic modalities, namely, computed tomography (CT), positron emission tomography (PET) and magnetic resonance imaging (MRI), are able to provide lung ventilation mappings but require contrast agents and/or high radiation doses (Simon,

[1]The lungs also play an important role in maintaining the blood pH, participating in heat exchange and fluid balance in the body (Serikov et al., 1992).

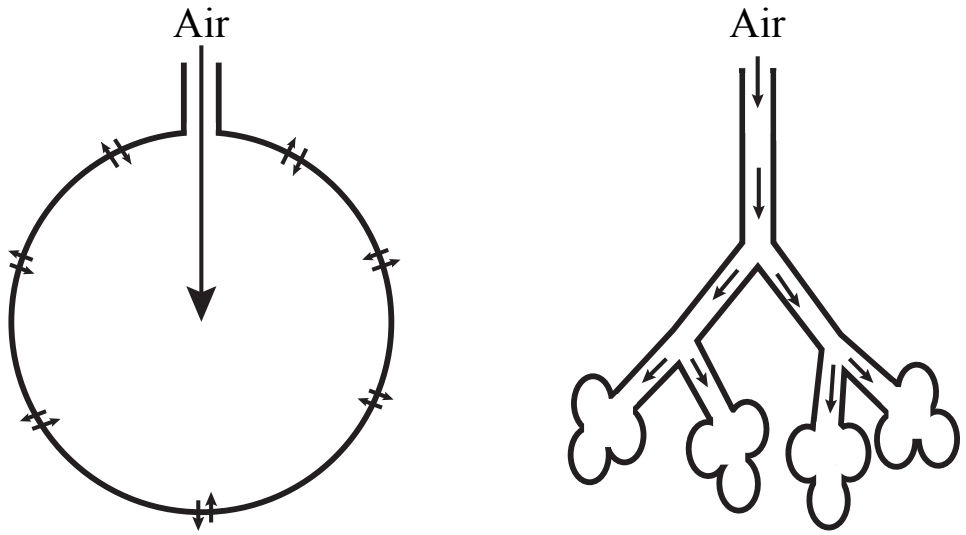

Figure 1.1: In its most simplistic form, the lung can be considered as a balloon as shown in (a), but a more realistic depiction is given in (b) as a network of small airways and small balloons (alveoli); each of which behave slightly differently in response to changing air pressure and volume.

2000; Wellman et al., 2010; Kyriazis et al., 2012). Contrast agents are expensive and carry with it potential health risks associated with the inhalation of them (Segen and Wade, 2002; Buch, 2010). These tomographic modalities for measuring ventilation will be described in chapter 2. In studying alveolar mechanics, tomographic imaging systems generally have insufficient spatial resolution to differentiate individual alveoli. Not to mention it would be even more difficult to detect differential changes in size since these changes are generally smaller than the alveolar size. In comparison to tomography, optical imaging techniques such as optical coherence tomography and confocal laser scanning microscopy have superior spatial and temporal resolution that enables the alveolar behavior to be tracked (Gaertner et al., 2012). However, the lack of penetrative depth and field-of-view limits to only a few hundred alveoli being analyzed at any one time. Ultrasound is also a viable option to imaging the lungs but it lacks the required spatial resolution to resolve alveoli and is contaminated by artefacts (Lichtenstein, 2014). However, the backscattered sound waves encode information on alveolar shape and size (Insana et al., 1990). Ultrasound and optical microscopes are discussed in greater detail in section 5.2.

Phase contrast x-ray (PCX) imaging is an emerging medical tool for studying biological objects with high spatial and contrast resolution (Momose et al., 1996; Briedis et al., 2005; Liu et al., 2006; Shinohara et al., 2008; Coan et al., 2010; Ismail et al., 2010; Zhang et al., 2011). It can produce highly detailed images by exploiting both the differential attenuation and deviation (phase

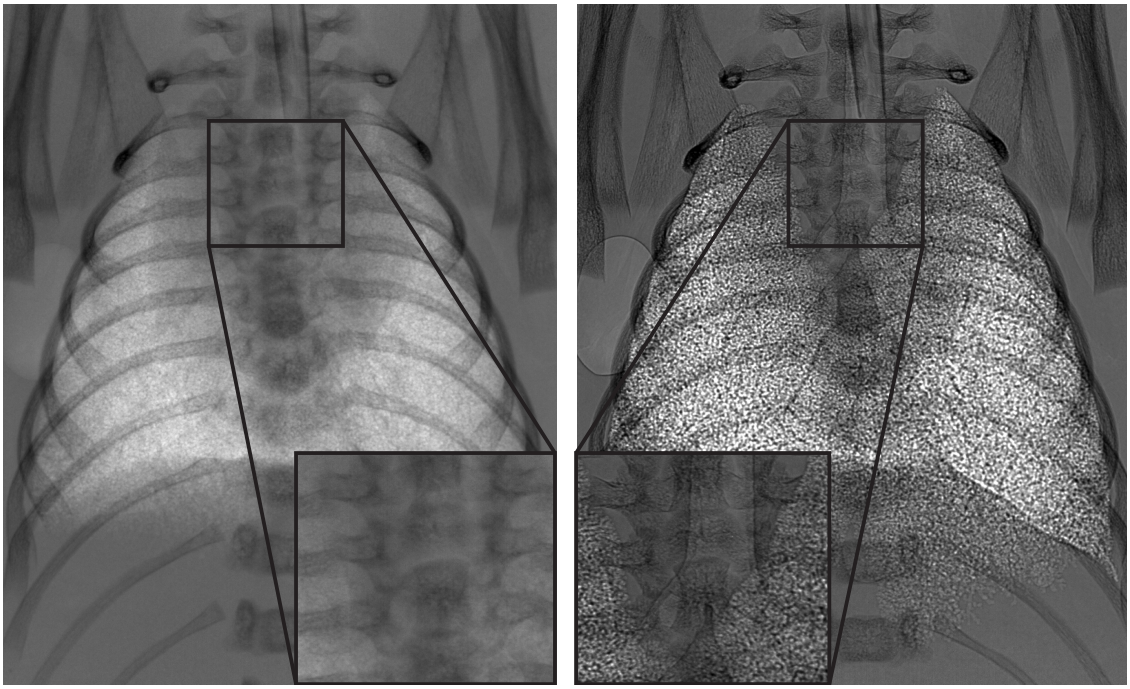

(a)

Figure 1.2: A conventional x-ray image (left) and PB-PCX chest image at 3 m ODD (right) of a rabbit kitten. These 19.8×24.4 mm^2 (inset: 6.1×5.8 mm^2) images were recorded at 24 keV.

shift) of x-rays upon transmission through an object (Zhou and Brahme, 2008). In comparison, conventional x-ray imaging is based only on the former property, making imaging of the bone ideal as it is highly attenuating relative to soft tissues at diagnostic x-ray energies. While this is similarly true for soft tissue against air, the majority of the airway are of the order of tens of microns in size. Consequently, the attenuation contrast of the airways are often masked by image noise. PCX imaging is able to render differential phase shifts into intensity modulations (phase contrast), which add to the attenuation contrast. These intensity modulations are prevalent along air-tissue interfaces and are much stronger than its counterpart attenuation contrast (Zhou and Brahme, 2008). Consequently, it is often able to overcome image noise and reveal the entire lung's highly intricate network of airways and alveoli. To demonstrate this, Fig. 1.2 compares a conventional x-ray image and a particular type of PCX image (namely propagation-based phase contrast x-ray (PB-PCX) imaging; see section 1.7.1) of a rabbit kitten's chest. The PCX image of the chest shows finer details of the bone and enhanced edge contrast of the airways compared to that seen in the conventional x-ray image. Furthermore, PCX lung imaging can be done in real-time as only single projections are required. It does not require any contrast agents or large radiation doses, at least no more than conventional x-ray imaging, which makes it a viable option for imaging humans.

Better understanding of the intricacy of lung mechanics using PCX imaging can lead to deeper insight into lung development, mechanical ventilation and respiratory diseases. During early infancy, the mechanical stress imparted along the airway walls during respiration have been found to play an important role in lung development through signaling of cellular function (Chess et al., 2000; Garcia et al., 2006; Trepat et al., 2007). Understanding the types of mechanical stress that is important in the maturation of the lung will have important ramifications on how mechanical ventilators are used to resuscitate or maintain respiratory function in newborn infants. Improper ventilation can hamper lung development and risk causing ventilation-induced lung injury (VILI). Studies have shown that it takes only a few damaging breaths to cause VILI through over-distension of the alveolar walls (Jackson et al., 1991; Hillman et al., 2007).

Respiratory diseases such as lung cancer and emphysema are some of the most common causes of death globally (Wolrld Health Organization, 2008; Cancer Research UK, 2014). Early diagnosis of these diseases underpins more successful and less aggressive treatments. The onset of respiratory diseases begins on a cellular level by altering cell behavior that is not apparent using current diagnostic tools, namely static medical images and global pulmonary tests. However, these alterations may be evident through changes in lung mechanics at the alveolar level (Kauczor and Bankier, 2004).

While PCX imaging of the lung is highly detailed, the images formed are only two-dimensional (2D) projections of the tissues. Consequently, the small airways overlap and cannot easily be visualized individually, making it difficult to study lung ventilation and alveolar behavior. Regardless, there have been many studies that have proven the usefulness of PCX imaging for studying lung function[2] and lung development (Lewis et al., 2005; Hooper et al., 2009; Fouras et al., 2012). Kitchen et al. (2008, 2011) demonstrated that PCX images can be used to accurately measure regional lung aeration to assess regional lung function, which has assisted in developing safer methods of resuscitating infants at birth (Hooper et al., 2009, 2011). However, extracting quantitative lung information at the alveolar scale from PCX images is still only in its infancy, leaving many novel developments and improvements yet to be discovered. This thesis focuses on what and how other quantitative information of the lungs can be extracted from PCX images. In the remainder of this chapter, the relevant theoretical background of PCX imaging is laid. In particular, the classical electrodynamic description of how x-rays are generated and interact with matter that lead to the formation of phase contrast is outlined. Understanding the link between phase contrast and the structural properties of matter is important towards the work presented herein.

[2]In this thesis, lung function refers to the dynamic changes in lung volume and structure.

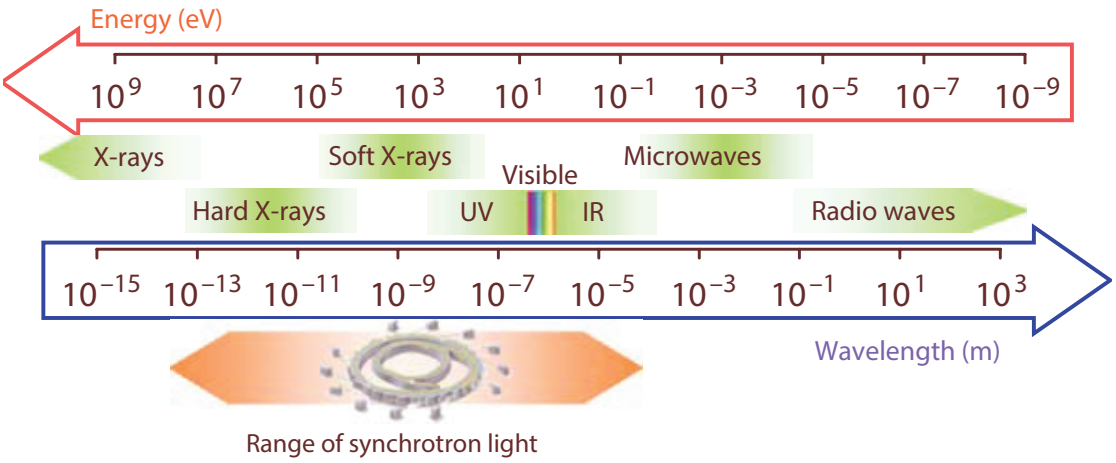

Figure 1.3: Electromagnetic spectrum for a range of wavelengths (bottom) and energies (top) (Gomez et al., 2009).

1.2 Classical Electrodynamic Description of X-rays

X-rays are a form of electromagnetic (EM) radiation that cover a large part of the energy spectrum from kilo-electron volt (eV) to mega-electron volt (MeV) energies (as shown in Fig. 1.3). The ability to generate x-rays of a range of wavelengths enable materials of different length scales to be studied, from microscopic objects like viruses to macroscopic objects like volcanic rock (Polacci et al., 2010; Shtykova et al., 2013). Also, x-rays can penetrate deep within objects, enabling their internal structures to be imaged. This is particularly beneficial in studying encapsulated objects such as the bones and organs.

Broadly speaking, x-rays are made of electric (**E**) and magnetic (**B**) vector fields. These fields can be explained within the framework of classical electrodynamics, which is governed by the four Maxwell equations in free space (Maxwell, 1865)[3]:

$$\nabla \cdot \mathbf{E}(\mathbf{r}, t) = 0, \tag{1.1}$$

$$\nabla \cdot \mathbf{B}(\mathbf{r}, t) = 0, \tag{1.2}$$

$$\nabla \times \mathbf{E}(\mathbf{r}, t) + \frac{\partial}{\partial t}\mathbf{B}(\mathbf{r}, t) = \mathbf{0}, \tag{1.3}$$

$$\nabla \times \mathbf{B}(\mathbf{r}, t) - \epsilon_o \mu_o \frac{\partial}{\partial t}\mathbf{E}(\mathbf{r}, t) = \mathbf{0}. \tag{1.4}$$

[3]Maxwell's equations were formulated by James Clark Maxwell, but the formulation was built on previous works, which is delved into thoroughly by Sengupta and Sarkar (2003).

Here, ∇,$\nabla\cdot$ and $\nabla\times$ are the three-dimensional gradient, divergence and curl operators, respectively. $\mathbf{r} = (x, y, z)$ are Cartesian coordinates, t is time and $\mathbf{0}$ is the zero length vector. ϵ_o and μ_o denote the electrical permittivity and magnetic permeability of free space, respectively. Maxwell's equations can be manipulated into second order differential wave equations known as the d'Alembert wave equations for the $\mathbf{E}$ and $\mathbf{B}$ fields:

$$\left(\frac{\partial^2}{\partial t^2} - \frac{1}{\epsilon_o\mu_o}\nabla^2\right)\mathbf{E}(\mathbf{r}, t) = \mathbf{0}, \tag{1.5}$$

$$\left(\frac{\partial^2}{\partial t^2} - \frac{1}{\epsilon_o\mu_o}\nabla^2\right)\mathbf{B}(\mathbf{r}, t) = \mathbf{0}. \tag{1.6}$$

Equation 1.5 is derived by first taking the curl of Eq. 1.3 and using the vector identity $\nabla \times [\nabla \times \mathbf{A}(\mathbf{r})] = \nabla[\nabla \cdot \mathbf{A}(\mathbf{r})] - \nabla^2\mathbf{A}(\mathbf{r})$ for a well-behaved vector field $\mathbf{A}(\mathbf{r})$. Combining this with Eqs. 1.1 and 1.4 gives Eq. 1.5. Similar steps are taken to derive Eq. 1.6.

The simplest non-trivial solution to Eqs. 1.5 and 1.6 is the monochromatic plane wave, defined as $\mathbf{A}\exp[i(\mathbf{k}\cdot\mathbf{r} - \omega t)]$, where $\mathbf{A}$ is a real non-zero constant polarization vector. The plane wave describes a sinusoidally varying function with amplitude $|\mathbf{A}|$ and wavelength, $\lambda = \frac{2\pi}{|\mathbf{k}|}$, defined as the number of unit lengths per wave, and angular frequency, ω, with units of radians per second (see Fig. 1.4)[4]. The parallel planes, or wavefronts, extending out to infinity in Fig. 1.4 represent surfaces of constant phase defined at $constant = \mathbf{k}\cdot\mathbf{r} - \omega t$. These wavefronts propagate with velocity $v_p = \left|\frac{dr}{dt}\right|_\varphi = \omega/|\mathbf{k}| = 1/\sqrt{\epsilon_o\mu_o}$ in the direction $\mathbf{k}$, where v_p is known as the phase velocity. The subscript φ means it is treated as a constant when taking the absolute derivative. Comparing the expression for v_p, it can be seen that v_p is the square root of the negative value of the coefficient in front of the Laplacian operator ∇^2 in Eqs. 1.5 and 1.6.

Without any loss of generality, consider an $\mathbf{E}$-field plane wave traveling along the positive z-direction in free space and rewrite Eqs. 1.3 and 1.4 into its scalar components:

$$\frac{\partial E_y}{\partial z} = -\frac{\partial B_x}{\partial t}, \tag{1.7a}$$

$$\frac{\partial E_x}{\partial z} = -\frac{\partial B_y}{\partial t}, \tag{1.7b}$$

$$\frac{\partial B_y}{\partial z} = -\epsilon_o\mu_o\frac{\partial E_x}{\partial t}, \tag{1.7c}$$

[4]While $\mathbf{A}\cos(\mathbf{k}\cdot\mathbf{r} - \omega t)$ or $\mathbf{A}\sin(\mathbf{k}\cdot\mathbf{r} - \omega t)$ are the real solutions to the wave equation, the complex notation is conventionally used to simplify mathematical manipulations. The real part of the final solution is then taken to extract the real-valued solution.

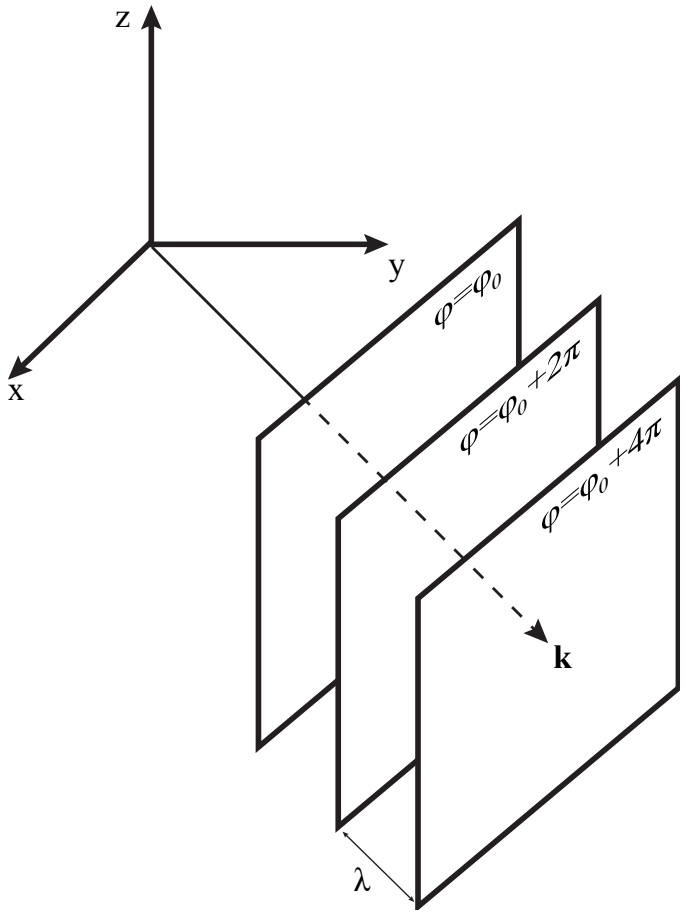

Figure 1.4: A schematic depiction of a plane wave at an instant of time with wavelength λ traveling in the direction $\mathbf{k}$. A corresponding one-dimensional diagram can be drawn of a sinusoidal wave at an instant in space over time with λ replaced by $f = \frac{\omega}{2\pi}$, defined in units of cycles per unit of time.

$$\frac{\partial B_x}{\partial z} = -\epsilon_o \mu_o \frac{\partial E_y}{\partial t}. \tag{1.7d}$$

In arriving at these equations, note for a **E**-field plane wave traveling in the z-direction, $E_z = 0$ and that E_x and E_y are only functions of z. According to Eqs. 1.7c and 1.7d, each **E**-field vector component in (x,y) will induce a **B**-field vector component in the perpendicular direction propagating also along z with a sinusoidally varying amplitude that is in phase with **E**. This culminates into a **B**-field plane wave. Similarly, Eqs. 1.7a and 1.7b shows that a **B**-field plane wave will induce an **E**-field plane wave traveling along z. **E** and **B** can therefore coexist indefinitely in vacuum as an EM plane wave field through self-perpetuation. X-rays, and all forms of light, can also travel indefinitely in vacuum. The decisive proof that EM-fields are light and therefore x-rays came when the values of ϵ_o and μ_o, first measured by Weber and Kohlrausch (1856), was substituted into $v_p = 1/\sqrt{\epsilon_o \mu_o}$ to find that the propagation speed of EM-fields is almost equal to that of light measured separately by Fizeau (1849) in free space.

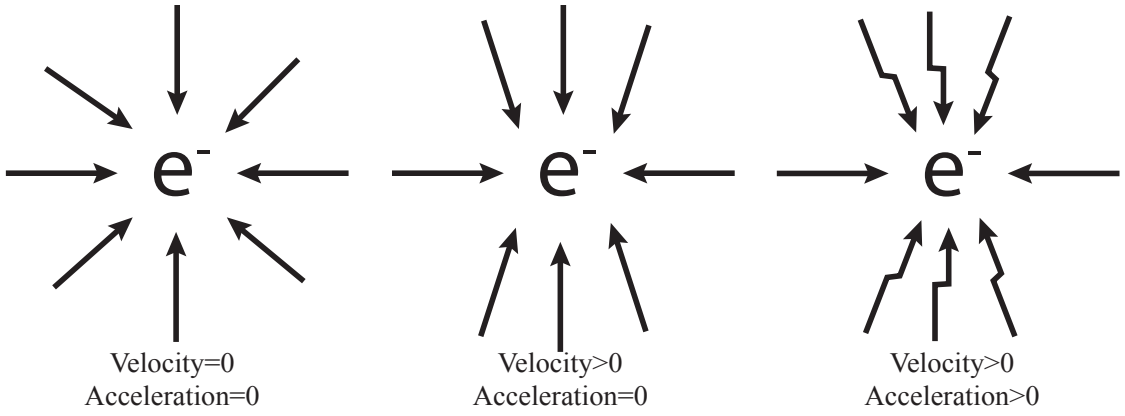

Figure 1.5: Electric field lines terminating on a charge that is stationary (left), uniformly moving (middle), and accelerating (right) to the right.

Having established the classical description of how either **E**- and **B**-field plane waves manifest into EM-fields (that is x-rays), it has not yet been made clear where the **E**-field or **B**-field plane waves originated. The answer is from the acceleration of charged particles. Electrons are predominantly used in the medical field as more radiation power can be generated because of its low mass compared to other charges (Paganin, 2006, p. 140). An electron at rest emanates a uniform radially distributed **E**-field, but in motion the field lines become concentrated perpendicular to the velocity vector (see Fig. 1.5). Since only a constant **B**-field is induced, it does not lead to a self-perpetuating EM-field. But an accelerating electron does emit x-rays. The **E**-field continuously realigns with the electron as it accelerates; however, **E**-fields have a finite propagation speed of c in vacuum. Thus, the **E**-field closest to the electron is aligned to its current position but those on the outer are still aligned to where it was sometime before (see Fig. 1.5). According to Gauss' law, these two fields must be connected. If they were not, a closed surface enclosing the ends of one of the field lines would result in a non-zero net electric flux through the closed surface. This violates Gauss' law, which states that any closed surface enclosing no charge must have a net electric flux of zero. Consequently, the electric field connecting the two fields forms a kink (see Fig. 1.5). It can be viewed as an **E**-field pulse, which is shown in section 1.7.1 to be re-expressible as a sum of **E**-field plane waves with a range of $\mathbf{k}$ and ω values. Since the d'Alembert wave equations are linear, the **E**-field pulse is a solution and each **E**-field plane wave leads to an EM-field.

Quantum electrodynamics represents a more powerful formalism for describing x-rays, where it treats x-rays as photons rather than EM-fields and their behavior is probabilistic rather than deterministic. Classical electrodynamics is an adequate formalism for dealing with problems such as elastic scattering (see section 1.4) and the refractive index of materials (see section 1.5).

Conversely, it cannot describe all processes such as those that occur over short time scales in the order of the atomic electron orbital period or inelastic scattering (Compton, 1923; Slowik and Santra, 2013)[5]. These require the formalism of quantum electrodynamics to accurately account for these events. The work done herein focuses on recovering the refractive index of materials from images recorded using information only from elastic scattering. Classical electrodynamics is then an adequate formalism to describe this work.

1.3 Production and Properties of X-rays for Phase Contrast X-ray Imaging

The classical understanding of the origin of x-rays has led to the development of two types of x-ray generator: x-ray tubes and synchrotrons. Both have completely different designs but their mechanism is fundamentally identical in generating x-rays by accelerating electrons.

In x-ray tubes, electrons ionized from heating metal are accelerated by a potential difference that are then rapidly decelerated when they collide with a metallic material (anode) to induce x-ray emission (Bushberg et al., 2012). The emission spectrum from a typical x-ray tube is shown in Fig. 1.6. The broad 'Bremsstrahlung' spectrum corresponds to x-rays emitted from electrons decelerated by the deflective force of the anode. The sharp peaks are known as characteristic x-rays that exist at certain energies corresponding to the differences between electron shell energy levels of the anode. The energy quantization of characteristic x-rays falls under the formalism of quantum electrodynamics but the mechanism can still be partially described by classical mechanics. Electrons with energy $\mathbf{E} = \hbar c|\mathbf{k}|$, where $\hbar$ is the reduced Planck constant, can cause bound electrons to oscillate (i.e. accelerate) between electron shell energy levels whose energy difference equals that of the electrons, and which emit an EM-field of the same energy. The origin of the discrete energy levels, however, falls outside the domain of classical electrodynamics.

Unlike x-ray tubes, synchrotrons accelerate electrons to relativistic speeds and instead of using a metal anode, electrons are de-accelerated by magnetic dipoles to induce x-ray emission. There are three types of magnetic dipoles that produce different x-ray spectra: bending magnets, wigglers and undulators. A bending magnet comprises a single magnetic dipole where electrons are deviated once to produce a large frequency bandwidth of x-rays. Wigglers are made up of n magnetic dipoles, each producing a pulse of light that add up incoherently to be n times brighter than that

[5] Studies have shown the scattering pattern of orbiting electrons over a few femtoseconds by a pulse of light is inadequately described using classical electrodynamic theory and instead requires a quantum electrodynamic treatment (Dixit et al., 2013; Slowik and Santra, 2013)

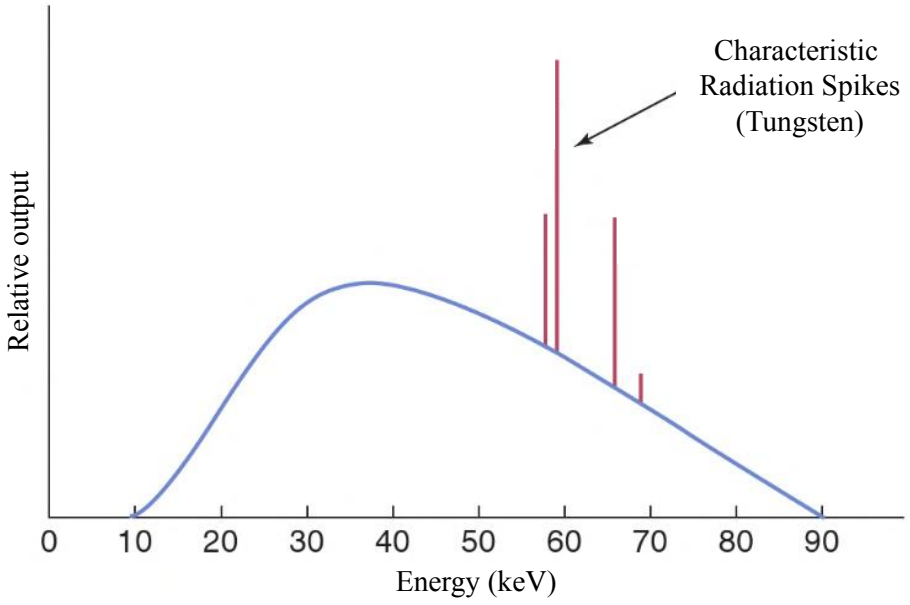

Figure 1.6: A typical spectrum of characteristic (red) and Bremsstrahlung (blue) x-rays. Adapted from Bushberg et al. (2012, p.176).

from a bending magnet. Undulators are also made up of multiple dipole magnets but the magnetic field is sufficiently weak for all the pulses of light to be emitted in the same direction and interfere coherently. The light emitted is many orders brighter with a narrow frequency bandwidth.

To compare the properties of x-rays emitted from synchrotrons and x-ray tubes, wavefield coherence is first introduced. It is introduced also because it is an important requirement for PCX imaging. Here, x-rays will be treated as a complex scalar wavefield $\Psi(\mathbf{r}, t)$ that satisfies the wave equation given in Eq. 1.5, rather than vectors $\mathbf{E} = (E_x, E_y, E_z)$ and $\mathbf{B} = (B_x, B_y, B_z)$. This is a valid transition when working in free space as there is no coupling between vector components (Green and Wolf, 1953; Paganin, 2006). It is also valid in matter if the charge and current density is slowly varying over length scales comparable to the x-ray wavelength, which is certainly true for the vast majority of biological tissues studied in this thesis. The coherence of a scalar wavefield is a measure of the correlation of the wavefield over space-time. A common parameter that represents the wavefield coherence is the mutual coherence function, Γ, of the scalar wavefield at two space points, $\mathbf{r}_1$ and $\mathbf{r}_2$ (Paganin, 2006):

$$\Gamma(\mathbf{r_1}, \mathbf{r_2}, \tau) = \left\langle \Psi(\mathbf{r}_1, t) \Psi^*(\mathbf{r}_2, t + \tau) \right\rangle, \tag{1.8}$$

where τ is the time delay between $\Psi(\mathbf{r}_1, t)$ and $\Psi(\mathbf{r}_1, t + \tau)$ and the angular brackets $\langle\rangle$ denotes the time average. A physical interpretation of Eq. 1.8 will be given by deriving it in the context of Young's interference pattern. Consider a completely absorbing screen with two pierced small

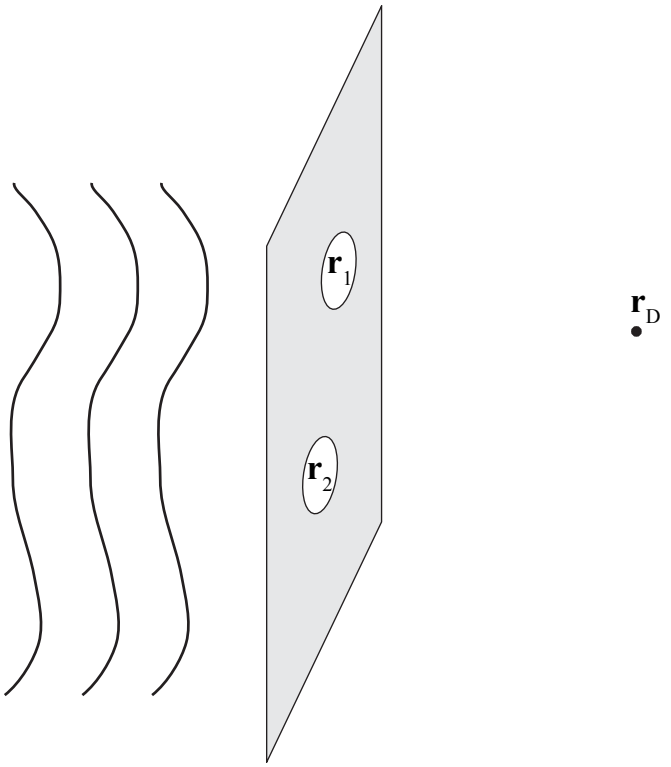

Figure 1.7: A two-dimensional black screen with two pinholes at $\mathbf{r}_1$ and $\mathbf{r}_2$ illuminated by an arbitrary scalar wavefield. The visibility of the interference pattern produced by the two pinholes is determined at $\mathbf{r}_D$.

pinholes located at $\mathbf{r}_1$ and $\mathbf{r}_2$ (Fig. 1.7). The wavefield at some point $\mathbf{r}_D$ downstream of the absorbing screen is given by:

$$\Psi(\mathbf{r}_D, t) = K_1\Psi(\mathbf{r}_1, t+\tau) + K_2\Psi(\mathbf{r}_2, t), \tag{1.9}$$

where τ is the time difference (or delay) between the wavefields in reaching $\mathbf{r}_D$. The transfer function that propagates the wavefields, $\Psi(\mathbf{r}_1, t+\tau)$ and $\Psi(\mathbf{r}_2, t)$, from the pinhole to the observation point $\mathbf{r}_D$ is denoted by K_1 and K_2, respectively. The observed intensity is given by the magnitude squared time averaged value of Eq. 1.9:

$$\begin{aligned}\bar{I}(\mathbf{r}_D) &= \left\langle |K_1\Psi(\mathbf{r}_1, t+\tau) + K_2\Psi(\mathbf{r}_2, t)|^2 \right\rangle \\ &= \left\langle |K_1\Psi(\mathbf{r}_1, t+\tau)|^2 \right\rangle + \left\langle |K_2\Psi(\mathbf{r}_2, t)|^2 \right\rangle + 2\,|K_1K_2|\,Re\left\{\left\langle \Psi(\mathbf{r}_1, t+\tau)\Psi^*(\mathbf{r}_2, t)\right\rangle\right\}.\end{aligned} \tag{1.10}$$

Note that $K_1K_2^*$ is positive and real, which allowed it to be brought outside the brackets.

The first two terms on the second line of Eq. 1.10 represent the intensity contribution from each pinhole individually, which are denoted as $\bar{I}_1(\mathbf{r}_D) =< |K_1\Psi(\mathbf{r}_1, t+\tau)|^2 >$ and $\bar{I}_2(\mathbf{r}_D) =< |K_2\Psi(\mathbf{r}_2, t)|^2 >$. These terms represent the intensity which would have been observed at $\mathbf{r}_D$ if the

other pinhole was blocked. The third term represents the correlation between the wavefields from each pinhole at the plane of the pinholes and can be seen to be equal to the real part of the mutual coherence function. Equation 1.10 therefore becomes:

$$\overline{I}(\mathbf{r}_\mathrm{D}) = \overline{I}_1(\mathbf{r}_\mathrm{D}) + \overline{I}_2(\mathbf{r}_\mathrm{D}) + 2\,|K_1K_2|\,\mathrm{Re}\left\{\Gamma(\mathbf{r}_1, \mathbf{r}_2, \tau)\right\}. \tag{1.11}$$

To study the dependency between the mutual coherence function and the intensity downstream, consider $\Psi(\mathbf{r}, t)$ to be a monochromatic wavefield $\exp(i[\phi(\mathbf{r}) - \omega t])$, where $\varphi(\mathbf{r})$ is a real-valued arbitrary function describing the wavefront over space. Substituting this wavefield into Eq. 1.11 gives:

$$\overline{I}(\mathbf{r}_\mathrm{D}) = 2\{1 + \cos[\phi(\mathbf{r}_1) - \phi(\mathbf{r}_2) - \omega\tau]\}. \tag{1.12}$$

Equation 1.12 shows that the mutual coherence function (cosine) term is responsible for oscillating the intensity between 0 and 4. These oscillating intensities are known as interference fringes. The visibility of these fringes is defined by:

$$V = \frac{I_{max} - I_{min}}{I_{max} + I_{min}}. \tag{1.13}$$

Substituting the expressions for the maximum (I_{max}) and minimum (I_{min}) intensity of Eq. 1.12 into Eq. 1.13, the fringe visibility for a monochromatic wavefield is $V = 1$. These fringes represent the phase contrast seen in PCX imaging and are responsible for increasing image contrast. To generalize V for any wavefield, Eq. 1.11 is substituted into Eq. 1.13 and assuming equal intensity from both pinholes (that is, $\overline{I}_1(\mathbf{r}_\mathrm{D}) = \overline{I}_2(\mathbf{r}_\mathrm{D})$):

$$V = |\gamma(\mathbf{r}_1, \mathbf{r}_2, \tau)|. \tag{1.14}$$

where

$$\gamma(\mathbf{r}_1, \mathbf{r}_2, \tau) = \frac{\Gamma(\mathbf{r}_1, \mathbf{r}_2, \tau)}{\sqrt{\Gamma(\mathbf{r}_1, \mathbf{r}_1, 0)\Gamma(\mathbf{r}_2, \mathbf{r}_2, 0)}}, \tag{1.15}$$

is known as the complex degree of coherence representing the normalized mutual coherence function.

Equation 1.14 shows that fringe visibility is directly proportional to the magnitude of the complex degree of coherence. Using the Schwarz inequality, it can be shown that $|\gamma(\mathbf{r}_1, \mathbf{r}_2, \tau)| \leq 1$ and therefore $V \leq 1$ (Paganin, 2006, p. 43). This shows fringe visibility is maximal when the complex degree of coherence is maximal, which only occurs when the wavefield is fully coherent.

While as the wavefield coherence decreases so too does the fringe visibility. Hence why PCX imaging requires a sufficiently coherent wavefield to produce phase contrast (fringes). Even though Eq 1.14 was derived by considering a two-pinhole screen, the screen need not be there, Eq 1.14 can be generalized to describing the fringe visibility at $\mathbf{r}_\mathrm{D}$ resulting from a wavefield at a point in space-time interfering with another at some other point in space-time.

Realistically, x-ray tubes and synchrotrons do not emit perfectly coherent wavefields because of the stochastic process of x-ray emission. Electrons are accelerated at random intervals and emit plane waves of finite length (wavetrains). The overall wavefield is then partially coherent.

For a quantifiable analysis of the effects of partially coherent wavefields on fringe visibility, coherence is divided into two classes: temporal and spatial coherence. The degree of temporal coherence is defined as $\gamma(\mathbf{r}_1, \mathbf{r}_1, \tau)$, that is, the correlation of a wavefield at fixed position $\mathbf{r}_1$ delayed by τ. The degree of spatial coherence is defined as $\gamma(\mathbf{r}_1, \mathbf{r}_2, 0)$, which is the correlation between two points of a wavefield with zero time lag. Each electron accelerated from a synchrotron or x-ray tube emits a wavetrain described by the plane wave $e^{-i[\mathbf{k}\cdot\mathbf{r}-\omega t]}$ modulated by the amplitude function $\sqrt{I(\mathbf{r}, t)}$ and a phase factor $e^{-i\varphi}$:

$$\Psi(\mathbf{r}, t) = \sqrt{I(\mathbf{r}, t)} e^{-i(\mathbf{k}\cdot\mathbf{r}-\omega t)} e^{-i\varphi}. \tag{1.16}$$

The phase φ remains constant over the time period $T_c = \frac{L_c}{c}$, where L_c is the length of the wavetrain, and randomly changes for x-rays emitted from another accelerated electron. With this setup, temporal coherence can be expressed as (Loudon, 2000):

$$\gamma(\mathbf{r}_1, \mathbf{r}_1, \tau) = \frac{\left\langle \left\{ \sum_{\mathrm{i}=1}^{v} \sqrt{I_\mathrm{i}(\mathbf{r}_1, t)} e^{-i(\mathbf{k}\cdot\mathbf{r}_1-\omega_\mathrm{i} t)} e^{i\varphi_\mathrm{i}} \right\} \left\{ \sum_{\mathrm{i}=1}^{v} \sqrt{I_\mathrm{i}(\mathbf{r}_1, t+\tau)} e^{-i[\mathbf{k}\cdot\mathbf{r}_1-\omega_\mathrm{i}(t+\tau)]} e^{-i\varphi_\mathrm{i}} \right\} \right\rangle}{\left\langle \left\{ \sum_{\mathrm{i}=1}^{v} \sqrt{I_\mathrm{i}(\mathbf{r}_1, t)} e^{-i(\mathbf{k}\cdot\mathbf{r}_1-\omega_\mathrm{i} t)} e^{i\varphi_\mathrm{i}} \right\} \left\{ \sum_{\mathrm{i}=1}^{v} \sqrt{I_\mathrm{i}(\mathbf{r}_1, t)} e^{-i[\mathbf{k}\cdot\mathbf{r}_1-\omega_\mathrm{i}(t)]} e^{-i\varphi_\mathrm{i}} \right\} \right\rangle}, \tag{1.17}$$

where $i = 1...v$ represents the different wavetrains.

Expanding the brackets in Eq. 1.17, the phase values of the wavetrains emitted from different electrons are statistically independent with random phase values and amplitudes, consequently, their cross terms sum to cancel out. The remaining terms are:

$$\begin{aligned} \gamma(\mathbf{r}_1, \mathbf{r}_1, \tau) &= \frac{\sum_{\mathrm{i}=1}^{v} \left\langle \sqrt{I_\mathrm{i}(\mathbf{r}_1, t) I_\mathrm{i}(\mathbf{r}_1, t+\tau)} e^{-i\omega_\mathrm{i}\tau} \right\rangle}{\sum_{\mathrm{i}=1}^{v} \langle I_\mathrm{i}(\mathbf{r}_1, t) \rangle} \\ &= \frac{\sum_{\mathrm{i}=1}^{v} \Gamma_\mathrm{i}(\mathbf{r}_1, \mathbf{r}_1, \tau)}{\sum_{\mathrm{i}=1}^{v} \Gamma_\mathrm{i}(\mathbf{r}_1, \mathbf{r}_1, 0)}. \end{aligned} \tag{1.18}$$

The temporal coherence of the beam is thus the sum of that of the individual wavetrains normalized against the total time averaged intensities of the individual wavetrains. It can be seen

that the temporal coherence of the beam correspond to that of the average wavetrain. Hence, it would remain appreciably above zero over the average time delay $\langle\tau\rangle = \langle T_c\rangle$. Thus, having longer wavetrains on average (that is, larger $\langle L_c\rangle$) increases $\langle\tau\rangle$ over which temporal coherence and therefore fringe visibility remains high. Consider the double pinhole setup again in Fig. 1.7 with a light source emitting a wavetrain with average length $\langle L_c\rangle$ illuminating the two pinholes. At increasing distance, in the direction parallel to the screen, away from the pinholes, the fringe visibility gradually decreases as the average time delay of the wavefields emanating from the two pinholes increases beyond T_c. Alternatively, the average $\langle L_c\rangle$ can be expressed as:

$$\langle L_c\rangle = \left\langle \frac{\lambda^2}{\Delta\lambda} \right\rangle. \tag{1.19}$$

To derive Eq. 1.19, the following two pieces of information were used: (1) the equation $v_p = c = f\lambda$, where the x-ray frequency $f = \frac{\omega}{2\pi}$ is differentiated with respect to λ to give $\frac{\Delta f}{\Delta\lambda} = -\frac{c}{\lambda^2}$ (the negative sign is dropped when arriving at Eq. 1.19), and (2) the optical uncertainty principle $\Delta f \Delta t \approx 1$, where $\Delta t = \tau$. The optical uncertainty principle can be interpreted as stating that the longer the wavetrain the more certainty there is in the frequency. From hereon, the ensemble average operation will be dropped for notational simplicity but implicitly assumed.

Equation 1.19 shows that L_c, and therefore temporal coherence, is inversely proportional to the wavelength bandwidth $\Delta\lambda$.[6] A wavetrain can therefore be viewed instead as a band of monochromatic wavefields, which enables temporal coherence to be more easily quantified. To understand how an increase in $\Delta\lambda$ leads to a decrease in fringe visibility, consider the two-pinhole screen (Fig. 1.7) again illuminated by a partially temporally coherent wavefield having a broad band of wavelengths. Each wavelength produces its own fringe pattern downstream of the screen. Summing the individual fringe patterns gives the overall fringe pattern of the partially coherent wavefield source. Since the fringe patterns from each wavelength are slightly different in fringe period, the overall fringe pattern has a reduced visibility.

In keeping with the model of an x-ray source having source size S comprised of electrons emitting wavetrains, spatial coherence at the source plane would be close to zero as there is little correlation between wavetrains at any given time. However, spatial coherence improves at increasing distance away from the extended incoherent source, as proven from the formula given by the van Cittert Zernike theorem (Zernike, 1938; Sharma, 2006):

[6] As mentioned in the main text, the x-rays emitted from each magnetic dipole in a undulator add coherently. This means the wavetrains superimpose to form a longer wavetrain. This leads to an increase in L_c and from Eq. 1.19 a narrower bandwidth. This is why their energy spectrum of an undulator exhibits a sharp peak (Margaritondo, 2002, p. 37).

$$|\gamma(\mathbf{r}_1, \mathbf{r}_2, 0)| = \left| \frac{\int I(\mathbf{r}) \exp[i\mathbf{k} \cdot (\mathbf{r}_1 - \mathbf{r}_2)] \mathrm{d}\mathbf{r}}{\int I(\mathbf{r}) \mathrm{d}\mathbf{r}} \right|. \tag{1.20}$$

This expression represents the spatial coherence of an incoherent source, which depends only on the intensity distribution of the incoherent source. It is derived by propagating the spatial coherence of the incoherent source away from the source plane at a distance much larger than the source size. This is well satisfied in synchrotrons and x-ray tubes. There are a number of ways in which spatial coherence can be propagated, one of which is the angular spectrum formulation of scalar diffraction integrals described in section 1.7.1. For a complete derivation of Eq. 1.20, see Paganin (2006, sec. 1.9).

To examine Eq. 1.20 explicitly, consider a planar incoherent circular source $I(\mathbf{r})$ of size S and uniform intensity I_o. At a sufficiently large distance away from the source, Eq. 1.20 and therefore the spatial coherence can be expressed as (Agarwal et al., 2004):

$$|\gamma(\mathbf{r}_1, \mathbf{r}_2, 0)| = \left| \frac{J_1(Sq/2D\lambda)}{(Sq/2D\lambda)} \right|, \tag{1.21}$$

where D is the source-to-object distance (SOD) and q is the transverse distance from the center of the observation plane. J_1 denotes the Bessel function of the first kind of order 1.

With the aim of interpreting Eq. 1.21, it is plotted in Fig. 1.8 with the parameters $D = 210$ m, $S = 150$ μm and $\lambda = 5.167 \times 10^{-11}$ m, which were the same parameters set for recording the phase contrast images presented in Fig. 1.2 and similarly for all other such images presented in this thesis. It shows that fringe visibility reduces to zero at $q \approx 0.55$ mm. Hence, within the area of $\pi(0.55)^2 = 0.95$ mm^2 centered at the center of the observation plane, known as the coherence area, spatial coherence is high. Beyond the coherence area spatial coherence oscillates with a damped amplitude. The coherence area can be increased by decreasing the source size or increasing the SOD[7]. However, the PCX images presented throughout this thesis such as that in Fig. 1.2 show the calculated coherence area of 0.95 mm^2 is adequate to achieve strong fringes.

To achieve both highly spatially and temporally coherent x-rays for PCX imaging, both a small source size/large SOD and monochomator are required. Monochromators are detailed in section 1.7.2. In x-ray tubes, electrons convert most of their kinetic energy into heat as they collide

[7]To understand how fringe visibility is affected by source size, consider again the double pinhole setup illustrated in Fig. 1.7. Assuming that the wavefield emitted from an electron behind the screen is coherent, the wavefield illuminates both pinholes to produce a fringe pattern downfield of the screen. Increasing the source size by including more independent electron emitters and spacing them further apart reduces the fringe visibility since each emitter produces their own fringe pattern downfield of the screen that are slightly displaced from one another. Hence they add to form a resultant fringe pattern with reduced visibility.

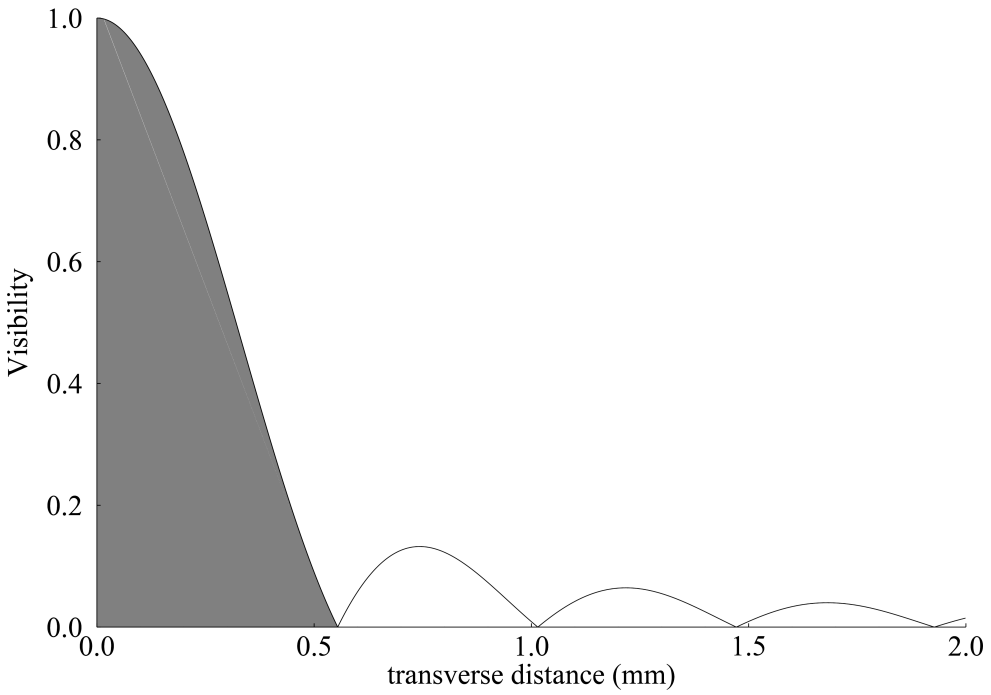

Figure 1.8: Visibility plotted against the transverse distance from the center of the observation plane. The shaded region up to the first minimum represents a quarter slice through the coherence area.

with the anode. While a small source size can be set to achieve high spatial coherence, x-ray flux is severely limited to avoid overheating of the anode. Several designs have been introduced to improve the efficiency in dissipating the heat, such as: immersing the anode in a heat sink, and rotating the anode to spread the heat over a larger surface area (Bushberg et al., 2012, p.180-182,189). However, the brightness of x-ray beams achievable from x-ray tubes is still insufficient for real-time or even static PCX lung imaging as impractically long exposure times are required (Gundogdu et al., 2007; Vine et al., 2007; Marenzana et al., 2014). Furthermore, as shown in Fig. 1.6, x-rays emitted by x-ray tubes are broadband polychromatic; in order to achieve a higher degree of temporal coherence, a monochromator is required. This further reduces the x-ray source brightness. However, not all PCX imaging modalities require high temporal coherence. For example, PB-PCX imaging is much more sensitive to spatial rather than temporal coherence, as described in section 1.7.1.

Synchrotrons are able to produce extremely bright x-rays. Bending magnets produce the least bright x-ray sources compared to wigglers and undulators. However, they are capable of producing x-rays with at least 4 orders-of-magnitude more brightness than that from x-ray tubes with a non-rotating anode even after being filtered by a monochromator (Goto et al., 2001; Bushberg et al., 2012). The main reason is that in synchrotrons, electrons are accelerated to relativistic speeds. This results in more photons emitted per electron over a narrow angular range. This can be understood

by referring back to Fig. 1.5 and comparing the spread of electric field lines between the stationary and moving charge. The electric lines bunch closer in the direction perpendicular to its direction of motion and continue to do so at increasing speeds. Synchrotron source sizes are actually similar to that of x-ray tubes but are able to achieve high spatial coherence because of large SODs. There are ongoing improvements in the manufacturing of x-ray tubes to achieve smaller spot sizes with high brightness. The most promising work has been the introduction of liquid-metal-jet anodes, which increases both the conversion efficiency of electrons to x-rays and the heat capacity (Hemberg et al., 2003; Tuohimaa et al., 2007; Garson et al., 2013). Together with the development of detectors with better signal-to-noise ratio (SNR) characteristics, these advancements are helping bring PCX imaging outside the synchrotron and closer to clinical application.

1.4 X-ray Interactions with Matter

Bulk matter comprises many x-ray scatterers and absorbers, which include atomic electrons, nucleons, photons and mesons (Muecke et al., 1999; Macovei, 2010; Bushberg et al., 2012). In the medical diagnostic x-ray range (10-150 keV), x-ray interaction with the latter three are negligible and thus will not be discussed herein (Hubbell, 1969). Limiting discussion to x-ray interactions with free and bounded electrons, these interactions can be broadly categorized as scattering and absorbing. While x-rays were described as waves in the previous section, x-ray-electron interactions are generally a quantum effect, as such they are treated as particles known as photons with a well-defined indivisible quantum of energy that is proportional to its wavelength[8].

In photon absorption, a photon is absorbed by a bound electron if the photon's energy is greater than the binding energy of that electron. The bound electron is ejected with kinetic energy equal to the difference between the incident photon energy and the binding energy, leaving behind a vacant electron shell. Photon absorption can also occur when the photon has energy equal to the difference in binding energy between electron shells, causing an electron from the lower energy shell to excite to the higher energy shell if there is vacancy. In both cases, the vacant electron shell will be filled by an outer electron and emit a photon in a random direction with energy equal to the difference in binding energy between electron shells involved in the transition (Fig. 1.9(a)).

In the event of scattering, an incoming x-ray photon collides with an electron that is assumed

[8]Treating photons as particles implies that they are spatially localized, yet they have a well-defined wavelength, which requires complete spatial de-localization. This ambiguous pictorial of a photon is due to its wave-particle duality. For the curious reader, treatments in the field of quantum electrodynamics investigating the properties of photons can be found in Weinberg (1996).

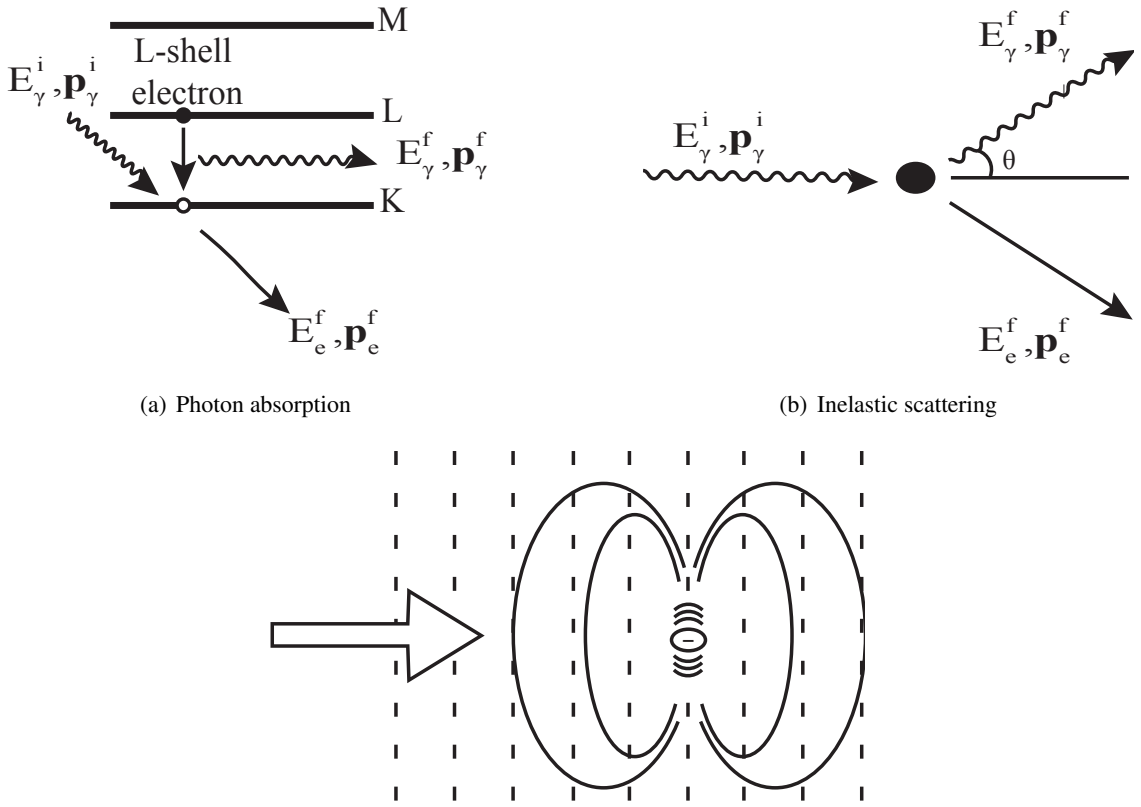

(a) Photon absorption

(b) Inelastic scattering

(c) Elastic scattering

Figure 1.9: Interaction of x-rays with matter. (a) Photon absorption involves a bound electron absorbing an x-ray with sufficient energy to eject from the shell, with the vacancy left behind being filled by an electron from a higher energy shell and a lower energy photon being emitted. X-rays may undergo (b) inelastic scattering where energy (E) and momentum ($\mathbf{p}$) is lost to the electron, or (c) elastic scattering where no energy is lost. Elastic scattering can be described by (b) for the special case of $E_\gamma^i = E_\gamma^f$ and $\left|\mathbf{p}_\gamma^i\right| = \left|\mathbf{p}_\gamma^f\right|$ but instead the corresponding classical description is given in (c) of an oscillating dipole to aid in explaining subsequent sections.

to be stationary[9]. The photon imparts a proportion of its momentum and kinetic energy to the electron. This is known as Compton scattering, also referred to as inelastic scattering (Fig. 1.9(b)) (Compton, 1923). The total momentum and energy of this closed system is conserved, which leads to a relation between the ratio of the photon energy after (E_γ^f) and before (E_γ^i) the collision took place to the scattering angle (θ) (Paganin, 2006):

$$\frac{E_\gamma^f}{E_\gamma^i} = \left[1 + \frac{2E_\gamma^i sin^2(\theta/2)}{m_e c^2}\right]^{-1}, \tag{1.22}$$

where m_e is the mass of the electron.

Equation 1.22 shows that the ratio of the final and initial energy of the scattered photon is a

[9]Collision of a photon with a non-stationary electron can result in inverse Compton scattering, where energy is transferred from the electron to the photon.

function of its initial energy. When $E_\gamma^i << m_e c^2$, the second term in the square brackets of Eq. 1.22 becomes negligible, resulting in $\frac{E_\gamma^f}{E_\gamma^i} \approx 1$. That is, if the initial photon energy is significantly less than the rest mass energy of the electron, the energy of the scattered photon remains unchanged and the scattering is considered to be elastic (Jauch and Rohrlich, 1955, sec. 11.1). Elastic scattering was observed in plasmas[10] by British physicist J. J. Thomson before Compton scattering was formalized (Thomson, 1906). Thus, elastic scattering of x-rays from free electrons was known as Thomson scattering. A classical description provided by Thomson, before quantum mechanics was well established, could adequately describe the mechanism of elastic scattering. There the electric field component of an EM-field plane wave imparts a Lorentz force with alternating direction to cause the electron to oscillate. The electron becomes an accelerating charge and re-radiates an outgoing x-ray wavefield with the same frequency in all directions but with zero amplitude along the direction of oscillation (Fig. 1.9(c))[11]. For electrons that are not free or loosely bound, but instead have high binding energy, m_e in Eq. 1.22 is re-defined as the atomic mass (or molecular mass) as the entire atom takes part in the collision (Khare, 2006, sec. 2.5). For this case, scattering is again considered elastic when $E_\gamma^i << m_e c^2$, and is then classified as Rayleigh scattering[12]. Elastic scattering (Rayleigh and Thomson) is coherent as the scattered and unscattered wavefields are of the same frequency and maintain a fixed phase relationship between one another. Conversely, inelastic (Compton) scattering is incoherent as the scattered wavefields are of different wavelength and therefore have no fixed phase relationship between them (Cremer, 2012).

Thus far in this section, the mechanism for scattering and absorption have been described, but the probability of these processes occurring has yet to be quantified. The likelihood of a photon interaction depends on many parameters such as its energy and the scatterer type, and to accurately quantify the interaction likelihood a quantum treatment must continue to be adopted. A full derivation of such a treatment will not be presented here. Instead, their relative contribution to the total number of interactions will be numerically compared for the object of interest in our study, namely lung tissue. The parameter that represents the probability of a type of photon-electron interaction event occurring is the total cross-section given in any direction in 4π steradians. Strictly speaking, if there are N scatterers in a given sample per unit area illuminated by I_o photons per

[10] Plasmas are one of the four states of matter (the others being gas, liquid and solid) that comprise of ionized particles and free electrons. This state arises when sufficient energy is imparted from, for example, high temperature or a high external electric field, which separates matter into ionized particles and free electrons.

[11] The outgoing wavefield is approximately spherical when far from the oscillating electron (Hecht, 2002, sec. 3.4.3).

[12] In this thesis, Rayleigh scattering is defined as elastic scattering between a photon and an atomic bound electron. In many studies, its definition is slightly more restrictive in that it includes the above definition but the wavelength of photon must be much larger than the atomic size of the atom that the electron the photon scatters off is bound to (Young, 1982).

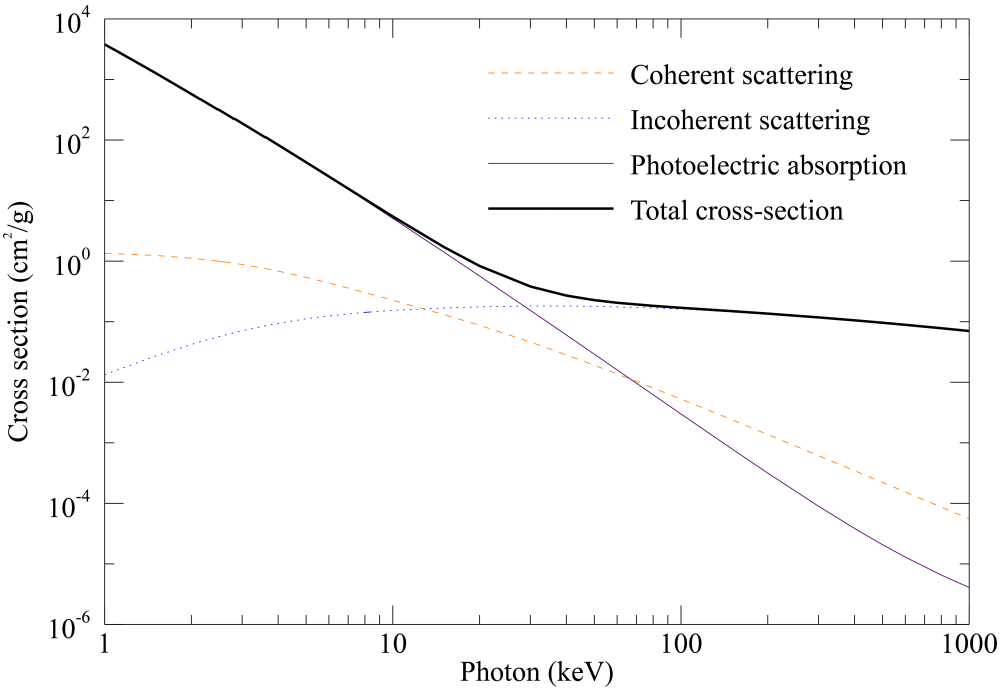

Figure 1.10: Cross-sections of lung tissue for photoelectric absorption, coherent scattering (Rayleigh scattering) and incoherent scattering (Compton Scattering), normalized against mass. The total cross-section (attenuation) is the sum of the aforementioned cross-sections (NIST, 2014).

second, the total cross-section, σ, is defined as:

$$\sigma = \frac{\text{Number of scatter/absorption events per second}}{I_o N}. \tag{1.23}$$

Figure 1.10 shows cross-sections in the photon energy range of 10-1000 keV for the different types of photon-electron interactions in lung tissue (NIST, 2014). The cross-section for Compton (incoherent) scattering was computed using the Klein-Nishina formula (Klein and Nishina, 1929) and the impulse approximation to account for atomic binding effects. The coherent scattering cross-section was computed using the Thomson cross-section formula, together with the atomic form factor (explained in detail in section 1.5), to account for interference between photons scattered by bound electrons (Storm and Israel, 1970). The photoelectric cross-section was semi-empirically determined by subtracting the total cross-section obtained experimentally using a narrow beam source from the total (coherent and incoherent) scattering cross-sections computed as outlined earlier in this paragraph. The sum of the absorption and scattering cross-section gives the total cross-section (attenuation). Hubbell (1969) explains these methods for calculating the cross-sections in more detail.

Coherent scattering is the underlying mechanism in the enhancement of soft tissue contrast

in PCX imaging, as will be elaborated upon in the next section. However, Fig. 1.10 shows that a significant proportion of scattering events are due to incoherent scattering. Fortunately, incoherently scattered x-rays distribute spatially evenly in the recorded intensity image and have random phases. Such scattered x-rays essentially act as noise and reduce the SNR with increasing energy from 10-100 keV (Paganin, 2006). Despite this, PCX imaging at higher energies is more beneficial to the patient; as Fig. 1.10 shows at increasing energy the absorption cross-section decreases. This reduces the radiation dose and while the coherent scattering cross-section also decreases at increasing energy, it is at a slower rate than that of absorption, hence phase contrast effects can potentially be still quite strong even at high energies.

1.5 Macroscopic Manifestation of X-ray Interactions with Matter

In the previous section, the different types of x-ray interaction with scatterers were explored individually. In matter, x-rays encounter and interact with many scattering bodies, from free electrons and atoms to long-chained molecules. The wavefields produced from each interaction superimpose to form an overall wavefield. Accounting for the individual x-ray interactions with matter is inherently complex, but it can be simplified by macroscopically averaging over a number of interactions in space. Incoherent scattering will be ignored and considered as a source of image noise, as justified at the end of the previous section. Thus, macroscopically, these interactions can be described by the complex refractive index, n:

$$n = 1 - \delta + i\beta, \tag{1.24}$$

where δ and β are the refractive index decrement and the attenuation index, respectively.

The derivation and physical interpretation of n will be presented soon, but first the real part of the complex refractive index is defined as $\mathrm{Re}\{n\} = c/v_p$, where v_p is the phase velocity of light traveling through some medium and c is the speed of light in free space[13]. In free space, the wavefield travels at $v_p = c$ (i.e. $n = 1$). But in other media that contain scatterers, v_p can be greater or less than c (i.e. $n \neq 1$). A classical derivation of n, from the perspective of wave optics, will now be presented, which follows from that given by Cremer Jnr (2013). However, the derivation will be heuristic, highlighting the salient steps, in order to provide a physical interpretation of the complex refractive index. See Cremer Jnr (2013) for the complete derivation.

[13] In this thesis, the real part of the complex refractive index will be referred to simply as the refractive index.

To begin deriving the complex refractive index, the wave equation for an electric wavefield in a scattering medium is introduced[14]:

$$\left(\frac{\partial^2}{\partial t^2} - c^2\nabla^2\right)\mathbf{E}(\mathbf{r},t) = -\frac{1}{\epsilon_o}\frac{\partial \mathbf{J}(\mathbf{r},t)}{\partial t} - \frac{c^2}{\epsilon_0}\nabla\rho(\mathbf{r},t). \tag{1.25}$$

This is the form Eq. 1.5 takes in the presence of scatterers, where $\mathbf{E}(\mathbf{r},t)$ is the sum of the incident and scattered wavefields. Two source terms appear in the form of the current density $\mathbf{J}(\mathbf{r},t)$ and charge density $\rho(\mathbf{r},t)$. The magnitude of the current density $\mathbf{J}(\mathbf{r},t)$ is proportional to the number of electric charges passing through any given point per unit time and unit area. The charge density $\rho(\mathbf{r},t)$ is the number of scatterers per unit volume in space and is here assumed to be slowly varying over length scales of the order of the wavelength of $\mathbf{E}(\mathbf{r},t)$ such that $\nabla\rho(\mathbf{r},t)$ is negligible. This is true for x-rays as they have very short wavelengths over which $\rho(\mathbf{r},t)$ does not vary appreciably. Consequently, the second term on the right hand side of Eq. 1.25 can be ignored. The current density

$$\mathbf{J}(\mathbf{r},t) = -e\sum_{q=1}^{Q} n_q \sum_{h=1}^{Z} \mathbf{v}_{h,q}(\mathbf{r},t), \tag{1.26}$$

where e is the elementary electric charge, n_q is the number of atoms of type q per unit area, and $\mathbf{v}_{h,q}(\mathbf{r},t)$ is the velocity of an electron occupying shell h of atom type q.

While electrons are constantly in motion orbiting the central nucleus, their velocity vectors point in random directions and therefore the net electron velocity is zero. However, x-rays drive electrons to oscillate around their equilibrium position in the direction of the electric field. Electrons will oscillate less randomly and produce a net electron velocity, $\mathbf{v}_{h,q}(\mathbf{r},t) = \frac{\partial \mathbf{x}_{h,q}(\mathbf{r},t)}{\partial t}$, where the displacement of each electron from its resting equilibrium position is denoted by $\mathbf{x}_{h,q}(\mathbf{r},t)$. To determine an explicit form for $\mathbf{v}_{h,q}(\mathbf{r},t)$ in Eq. 1.26, the following second-order non-homogeneous differential equation defining the net force acting on the bounded electrons is written as:

$$-e\mathbf{E}(\mathbf{r},t) - m_e\omega_{h,q}^2\mathbf{x}_{h,q}(\mathbf{r},t) - m_e\gamma_q\frac{\mathrm{d}\mathbf{x}_{h,q}(\mathbf{r},t)}{\mathrm{d}t} = m_e\frac{\mathrm{d}^2\mathbf{x}_{h,q}(\mathbf{r},t)}{\mathrm{d}t^2}, \tag{1.27}$$

where m_e is the electron mass. The explicit dependency of $\mathbf{x}_{h,q}(\mathbf{r},t)$ and $\mathbf{v}_{h,q}(\mathbf{r},t)$ on $\mathbf{r}$ and t will now be dropped for notational simplicity.

On the left hand side of Eq. 1.27, the first term represents the driving force induced by the electric field $\mathbf{E}(\mathbf{r},t)$, which is opposed respectively by the restoring and dissipative forces denoted

[14]The magnetic field component of x-rays also interacts with atomic electrons but is negligible compared to that by $\mathbf{E}$. Although textbooks often depict EM-fields comprising of $\mathbf{E}$ and $\mathbf{B}$ components being of equal amplitudes, the amplitude of $\mathbf{B}$ is actually $|\mathbf{E}|/c$ (Hecht, 2002, ch. 3).

by the second and third terms. The former is proportional to the imaginary spring constant $k_{h,q}$, which is redefined as the resonant frequency $\omega_{h,q} = \sqrt{\frac{k_{h,q}}{m_e}}$.[15] The latter assumes the dissipation force is sufficiently small that it can be linearized with respect to the electron velocity $\mathbf{v}_{h,q}$ and has an amplitude proportional to the damping factor γ[16]. The term on the right hand side is from Newton's second law of motion, which expresses the applied net force on an electron as a product of its mass and acceleration.

Assuming that the electrons oscillate in the same direction as $\mathbf{E}(\mathbf{r}, t)$, this enables $\mathbf{x}_{h,q}$ to be analytically solved from Eq. 1.27. Differentiating $\mathbf{x}_{h,q}$ with respect to time t then gives:

$$\mathbf{v}_{h,q} = \frac{\mathrm{d}\mathbf{x}_e}{\mathrm{d}t} = \frac{-e}{m_e}\left\{\frac{g_{h,q}}{\omega^2 - \omega_{h,q}^2 - i\gamma_q\omega}\right\}\frac{\mathrm{d}\mathbf{E}(\mathbf{r}, t)}{\mathrm{d}t}. \tag{1.28}$$

Here, $g_{h,q}$ are known as oscillator strengths, which can be viewed as weighting factors for each electron shell. Atomic electrons that respond more strongly to an external field are given more weighting[17].

By substituting Eqs. 1.28 and 1.26 into 1.25, and performing some rudimentary manipulations, the following equation is obtained:

$$\left[\frac{\partial^2}{\partial t^2} - c^2\left(1 - \frac{e^2}{\epsilon_o m_e}\sum_{q=1}^{Q} n_q \sum_{h=1}^{Z}\left\{\frac{g_{h,q}}{\omega^2 - \omega_{h,q}^2 - i\gamma_q\omega}\right\}\right)^{-1}\nabla^2\right]\mathbf{E}(\mathbf{r}, t) = \mathbf{0}. \tag{1.29}$$

As mentioned in section 1.2, the coefficient in front of ∇^2 of a wave equation is equal to v_p^2. Therefore, from Eq. 1.29, v_p of $\mathbf{E}(\mathbf{r}, t)$ is known and, since $\mathrm{Re}\{n\} = c/v_p$, the complex refractive index is given by:

$$n = \sqrt{1 - \frac{e^2}{\epsilon_o m_e \omega^2} f^0(\omega)}, \tag{1.30}$$

where $f^0(\omega)$ is the atomic scattering in the forward direction defined as:

$$f^0(\omega) = \omega^2 \sum_{q=1}^{Q} n_q \sum_{h=1}^{Z}\left\{\frac{g_{h,q}}{\omega^2 - \omega_{s,q}^2 - i\gamma_q\omega}\right\}. \tag{1.31}$$

[15] From the quantum electrodynamics viewpoint, the resonant frequency corresponds to the difference in frequency of the electron shells between which the electron is oscillating.

[16] If there was no dissipative force, the electron would continue to oscillate even after the x-ray has passed through and continuously generated an EM-field. However, the energy is carried away in the form of photons and phonons.

[17] As mentioned in the main text, from the viewpoint of quantum electrodynamics, electrons oscillate between electron shells in the presence of an external EM-field. Low oscillator strength values are assigned to electrons most tightly bound as they respond more weakly to an external EM-field than those weakly bounded. This is due to the density of electron energy states increasing with decreasing binding energy. Also, very low oscillator strength values are given to forbidden atomic transitions.

The phrase 'forward direction' means only those photons scattered at $\theta \ll 1$ radian with respect to the direction of the incident field contribute to n and therefore the phase velocity. This is true at x-ray energies as they deviate away from their original direction at very small angles. For x-rays, the second term in Eq 1.30 is many orders-of-magnitude smaller than unity, thus n can be binomially expanded to first order, and separated into real and imaginary terms:

$$n = 1 - \frac{e^2}{2\epsilon_o m_e \omega^2}\left\{\mathrm{Re}[f^0(\omega)] + \mathrm{Im}[f^0(\omega)]\right\}. \tag{1.32}$$

Referring back to the original definition of n in Eq. 1.24, the refractive index decrement (δ) and absorptive index (β) can be equated to Eq. 1.32 to give:

$$\delta = \frac{e^2}{2\epsilon_o m_e \omega^2}\sum_{q=1}^{Q} n_q \sum_{h=1}^{Z} \frac{g_{h,q}\omega^2(\omega^2 - \omega_{h,q}^2)}{(\omega^2 - \omega_{h,q}^2)^2 + \omega^2\gamma_q^2}, \tag{1.33a}$$

$$\beta = -\frac{e^2}{2\epsilon_o m_e \omega^2}\sum_{q=1}^{Q} n_q \sum_{h=1}^{Z} \frac{g_{h,q}\omega^3}{(\omega^2 - \omega_{h,q}^2)^2 + \omega^2\gamma_q^2}. \tag{1.33b}$$

Equations 1.33a and 1.33b were computed from the National Institute of Standards and Technology (NIST) to calculate n in this thesis[18]. For a physical interpretation of these terms, Eq. 1.29 is solved for a homogeneous material, for which the simplest non-trivial solution is the plane wave. Consider the plane wave to be traveling along z and only its x-component amplitude is non-zero, the solution is then:

$$E_x(z,t) = A\exp(-k\beta z)\exp\left[-i\left(kz - \omega t - k\delta z\right)\right]. \tag{1.34}$$

Compared to the plane wave in free space, $A\exp[-i(kz - \omega t)]$, the plane wave in the homogeneous material has its amplitude decreased by $\exp(-k\beta z)$ and its phase shifted by $\Delta\varphi = -k\delta z$ (see Fig. 1.11). The latter of these is equivalent to a change in the phase velocity[19]. These expressions show the attenuation index (β) and refractive index decrement (δ) are responsible for attenuating the amplitude and shifting the phase of the wavefield, respectively. It is the latter which PCX imaging takes advantage of to enhance the contrast along the boundaries of materials. These enhancements

[18]Equations 1.33a and 1.33b were derived assuming that the electrons were bounded. However, the corresponding equations for free electrons can easily be determined. At increasing x-ray energy, the bound electrons essentially become free. Consequently, the driving force ω is much larger than the resonant frequency $\omega_{h,q}$ and damping factor γ_q. Equations. 1.33a and 1.33b reduce to $\delta = \frac{e^2QZ}{2\epsilon_o m_e\omega^2} \propto \frac{1}{\omega^2}$ and $\beta = -\frac{e^2QZ}{2\epsilon_o m_e\omega^3} \propto \frac{1}{\omega^3}$ [sec. 2.2](Spiller, 1994).

[19]The phase velocity of Eq. 1.34 can be determined from the equation $v_p = \left|\frac{dr}{dt}\right|_\varphi$ that was introduced in section 1.2. This gives $v_p = c/(1-\delta)$. For x-rays, since $\omega \ll \omega_s$, then $(1-\delta) < 1$, which means x-rays have a phase velocity faster than c. While it seems to violate Einstein's law of special relativity that information cannot travel faster than c, the phase velocity does not carry any information (Einstein, 1920).

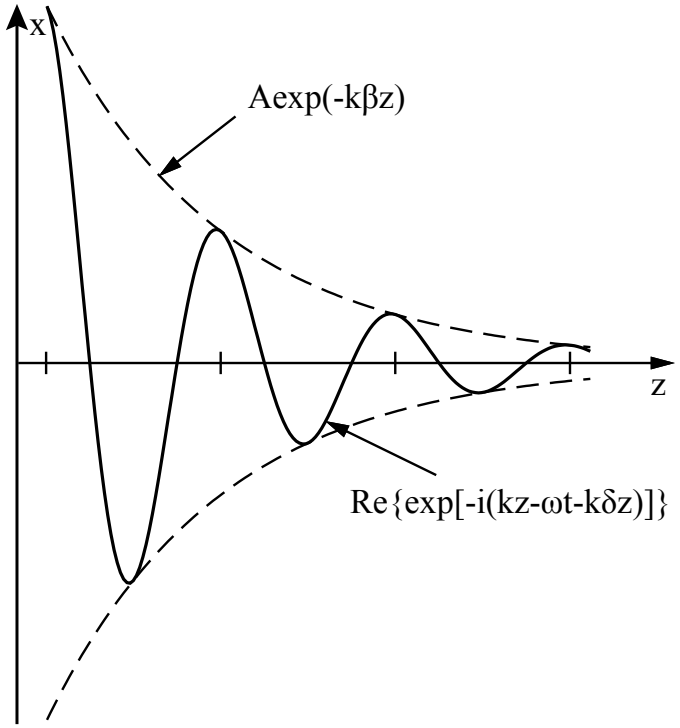

Figure 1.11: The x-component of an electric field propagating along z in some scattering material with complex refractive index $n = 1 - \delta + i\beta$. This shows β is responsible for attenuation and δ alters the phase velocity. Modified from Feynman et al. (2013, sec. 32-4).

arise from the different δ's across the boundaries, which produce non-zero phase shift gradients that lead to refraction and diffraction.

Refraction is commonly observed in our daily lives, such as the illusion of distorting objects at the bottom of a pond. These distortions arise from alterations in the direction of the rays or, from a wave optics perspective, phase gradients in the wavefield due to variations in the surface height of the pond. To explain this effect, refer back to Thomson's description of elastic scattering (see section 1.4). An incident plane wave propagating in material n_1 drives the scatterers to oscillate and emit approximately outgoing spherical waves. These spherical waves add to form the next wavefront of the plane wave. The vector normal to the wavefront represents the direction of the rays. When the wavefield encounters a surface of material n_2 ($n_1 < n_2$) at angle θ_1 from the plane normal to the surface (see Fig. 1.12(a)), it also cause scatterers within that material to emit outgoing spherical waves. However, these waves travel at phase velocity $v_2 = c/n_2$ whereas in material n_1, the waves travel at $v_1 = c/n_1$. This causes the wavefront to change direction, that is, refract, to now travel at angle θ_2 from the plane normal to the surface. These parameters are governed by Snell's law: $n_1 \sin\theta_1 = n_2 \sin\theta_2$ (Hecht, 2002, sec. 4.4.1). For light scattered back out to material

n_1, their wavefronts add constructively at angle $-\theta_1 + \pi$ from its incident direction. This is known as reflection and is mentioned for completeness but is not relevant to PCX imaging.

Consider a more complex surface between materials n_1 and n_2. An incoming wavefield refracts, causing distortion of its wavefront or change in direction of the rays as shown in Fig. 1.12(b). These distortions give rise to non-zero phase shift gradients along the x-direction. At regions where rays converge, there is an associated increase in intensity downfield, while the converse occurs for those that diverge, as illustrated in Fig. 1.12(b).

Diffraction arises from scattering at edges. A simple example of diffraction is depicted in Fig. 1.12(c). An incoming plane wave incident on a half-plane opaque screen results in an outgoing spherical wave originating from the edge. Beyond the edge and towards the half-plane, the wavefield is completely absorbed and is therefore zero. There the phase is undefined. The outgoing spherical wave interferes with the unscattered incident plane wave and constructively interferes at certain directions and destructively interferes in other directions. The resultant intensity is a series of bright and dark fringes. To explain this from a ray optics perspective, consider again the half-plane opaque screen redrawn in Fig. 1.12(d), where it shows the discontinuity in the exit surface phase at the edge. The rays at the edge diffract in all directions and those diffracted forward interfere with the unscattered rays downfield to form bright and dark fringes[20].

1.6 The Projection Approximation

For an arbitrarily shaped multi-material object, an incident wavefield undergoes absorption, refraction and diffraction many times, resulting in the wavefield evolving in a highly complex fashion as it traverses the object. For this study, biological objects are considered to be weakly interacting in the diagnostic x-ray regime. That is, from the perspective of geometrical optics, the rays do not deviate from their unscattered path in the presence of scatterers. While in the previous section, rays alter their trajectory when undergoing refraction or diffraction, biological objects do not possess hard edges for diffraction to occur and given that the refractive index of biological materials in the diagnostic x-ray regime are extremely close to unity, the refraction angle according to Snell's law is extremely small. Consequently, the phase shift and attenuated intensity of the wavefield become greatly simplified as they can be approximated to be the integral of the complex refractive index along the unscattered path of the x-ray. This simplification is known as the

[20]The use of rays to explain diffraction comes from the geometrical theory of diffraction. It was developed by Keller (1962) as an extension to geometrical optics to account for diffraction. The diffracted rays are assigned phase, computed from their optical path length, and amplitude to ensure the total energy is conserved before and after diffraction.

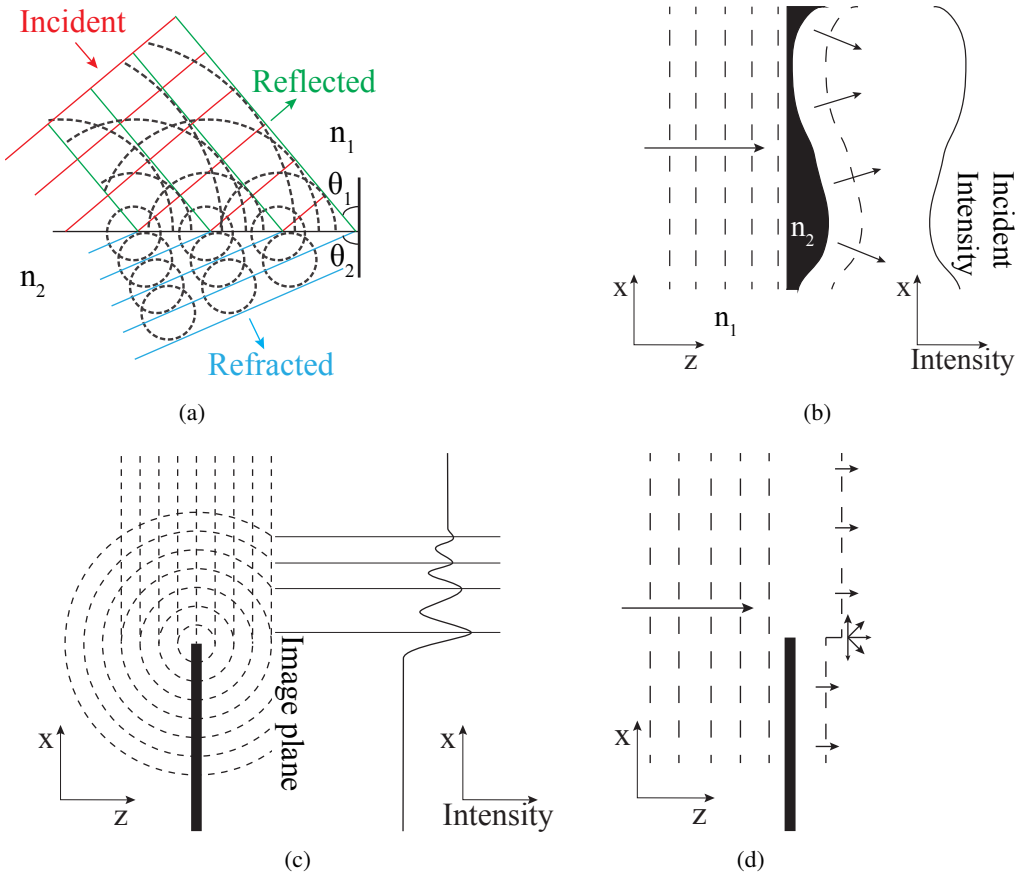

Figure 1.12: Special cases of elastic x-ray scattering. (a) In refraction, an incident plane wave (red) propagating in material n_1 encounters the surface of material n_2. Outgoing spherical waves, produced by oscillating scatterers, manifests into refracted (blue) and reflected (green) waves. In (b), a more complex object than the simple straight interface in (a) shows that refraction causes distortions in the resultant wavefield that lead to intensity modulations because of rays converging and diverging. (c) In diffraction, an opaque material illuminated by an incident plane wave produces scattered outgoing spherical waves that interfere with the incident plane wave to produce bright and dark fringes during constructive and destructive interference, respectively. In (d), the same edge as in (c) showing diffraction produces a discontinuity in the resultant wavefield at the edge. Under the geometrical theory of diffraction, the rays at that discontinuity diffract in all directions. Only those that will interfere with the unscattered rays downfield are shown.

projection approximation, which is an increasingly better approximation at higher x-ray energies since refractive index approaches unity as energy increases (see Eq. 1.33a). If the initial x-ray wavefield is monochromatic, paraxial (i.e., the beam divergence is small) and is traveling along the z-axis from the entrance surface $z = -T$ to the exit surface $z = 0$ of an object, then under the projection approximation the expressions for the phase shift $\Delta\varphi(\mathbf{r}_\perp, z = 0)$ and attenuated intensity $I(\mathbf{r}_\perp, z = 0) = |\Psi(\mathbf{r}_\perp, t)|^2$ of the wavefield at the exit surface $z = 0$ are[21]:

$$\Delta\varphi(\mathbf{r}_\perp, z = 0) = -k \int_{-T}^{0} \delta(\mathbf{r}) dz \tag{1.35a}$$

and

$$I(\mathbf{r}_\perp, z = 0) = I(\mathbf{r}_\perp, z = -T) \exp\left[-2k \int_{-T}^{0} \beta(\mathbf{r}) dz\right], \tag{1.35b}$$

where $\mathbf{r}_\perp = (x, y)$. Equation 1.35b is the well known Beer-Lambert law. A more rigorous derivation of the projection approximation can be found in Paganin (2006, p. 71-76). The projection approximation is assumed for all the objects in the work presented in this thesis. The Δ symbol from $\Delta\varphi(\mathbf{r}_\perp, z = 0)$ that indicates the phase relative to the free space phase will be dropped from here on for notational simplicity.

To justify the projection approximation, a generalized expression for its domain of validity is presented. Consider a plane wave encountering an arbitrarily shaped pure phase object (negligible attenuation), causing its wavefront to distort like that in Fig. 1.12(b). The angle θ between the wavevector $\mathbf{k}$ (represented by the rays) and the optic axis z at the object exit surface $z = 0$ can be expressed for small angles ($\theta \ll 1$ radian) as:

$$\theta(\mathbf{r}_\perp, z = 0) \approx \frac{|\nabla_\perp \varphi(\mathbf{r}_\perp, z = 0)|}{|\mathbf{k}|}, \tag{1.36}$$

where $|\nabla_\perp \varphi(\mathbf{r}_\perp, z = 0)|$ is the transverse magnitude of the phase gradient, and $\nabla_\perp = (\frac{\partial}{\partial x}, \frac{\partial}{\partial y})$.[22]

Omitting the explicit dependency of φ on $\mathbf{r}_\perp$ and $z = 0$ for the sake of notational simplicity, the projection approximation is valid when the maximum transverse deviation, $T\theta$ (where T is the object thickness) of the rays is less than some value Δx at the exit surface plane $z = 0$, that is:

[21] The intensity, I, is related to $\mathbf{E}$ and $\mathbf{B}$ via the following expression: $I = c^2\epsilon_0 < \mathbf{E} \times \mathbf{B} >_t$. This expression draws on the concept of EM-field as energy propagating through space, described by the Poynting vector, $c^2\epsilon_0 \mathbf{E} \times \mathbf{B}$. Intensity is the time averaged energy per unit time and space, and is why the Poynting vector is time averaged, as represented by $<>_t$. A great introduction on treating vector electromagnetic wavefields in terms of energy flow can be found in Born and Wolf (1999, sec. 1.1.4).

[22] To derive the expression $\theta(\mathbf{r}_\perp, z = 0) \approx \frac{|\nabla_\perp \varphi(\mathbf{r}_\perp, z=0)|}{|\mathbf{k}|}$, consider an arbitrary time-independent wavefield whose phase value at any localized point can be approximated by a plane wave: $\varphi(\mathbf{r}) = \mathbf{k} \cdot \mathbf{r}$. The wavevector $\mathbf{k}$ points in the direction normal to the tangent plane of the wavefront at that localized phase value. An expression relating $\mathbf{k}$ to its transverse component, $\mathbf{k}_\perp$, is $\sin(\theta) = \frac{|\mathbf{k}_\perp|}{|\mathbf{k}|}$. Under the small angle approximation, $\theta \approx \frac{|\mathbf{k}_\perp|}{|\mathbf{k}|}$. Since $|\mathbf{k}_\perp| = |\nabla_\perp \varphi(\mathbf{r})|$, then $\theta \approx \frac{|\nabla_\perp \varphi(\mathbf{r})|}{|\mathbf{k}|}$. Hence for any point $\mathbf{r}_\perp$ along the plane $z = T$, $\theta(\mathbf{r}_\perp, z = 0) \approx \frac{|\nabla_\perp \varphi(\mathbf{r}_\perp, z=0)|}{|\mathbf{k}|}$ as required.

$$\frac{|\nabla_{\perp}\varphi|_{\max} T\lambda}{2\pi} < \Delta x. \tag{1.37}$$

The value set for Δx is equal to the detector pixel size. Having larger pixel sizes requires lesser stringency imposed on the projection approximation as rays scattered by less than a pixel will not be observed to deflect from the direct beam. Morgan et al. (2010b) compared the PCX image simulated at diagnostic energies using the projection approximation and the exact solution for a polymethyl methacrylate object, which have similar complex refractive index to biological materials. They showed the former was a valid approximation except at extremely small ODDs.

1.7 Phase Contrast X-ray Imaging

In the previous section it was described how an object both attenuates the intensity and shifts the phase of an incident wavefield. These are exploited to form an image of an object. In conventional x-ray imaging, objects are rendered visible based on variability in attenuation only. This provides excellent contrast of bone with soft tissue due to the large difference in their β values. In imaging the airways of the lungs, the attenuation contrast of air with soft tissue is poor. This can be seen in Fig. 1.2(a) by the lack of visible airways due to its attenuation contrast being typically comparable to and/or less than image noise. Conversely, the bones can be clearly seen owing to the combined effects of the β values between bone and soft tissue being much larger than that between air and soft tissue in the diagnostic x-ray regime, and the dimensions of bone being many orders-of-magnitude greater than that of the smaller airways.

Alternatively, objects can be resolved based on object-induced phase gradients rather than variability in attenuation. However, due to the limited temporal resolution of detectors, phase gradients cannot be directly measured. PCX imaging represents a class of techniques to render phase gradients visible as intensity variations. This section describes three of the most commonly used PCX imaging techniques: PB-PCX imaging, analyzer-based phase contrast x-ray (AB-PCX) imaging and interferometric-based phase contrast x-ray (IB-PCX) imaging. This thesis focuses primarily on PB-PCX imaging, since it is utilized for all the work as presented in chapters 3-5. Hence a detailed mathematical description is provided of the image formation process for this technique only.

As mentioned in section 1.3, all forms of PCX imaging require that the wavefield illuminating the object is at least partially coherent. That is, there is some form of a fixed or predictable phase relationship. The type of coherence (i.e. spatial or temporal) and the level required is technique

dependent. Conversely, there are no coherence requirements for conventional x-ray imaging, which exploits only amplitude and not phase gradients to the wavefield imparted by the sample. A fixed or predictable phase relationship allows PCX imaging to render phase gradients into phase-induced intensity variations. These phase gradients are prominent along object boundaries, resulting in an edge-enhancing effect. The wavefront profile of an incoherent wavefield varies randomly, producing no fixed object-induced transverse phase gradients. Consequently, no discernible phase contrast appears (i.e. fringe visibility is close to zero). Coherence is one of the limiting factors preventing the use of a standard lab-based x-ray source to perform PCX imaging. However, the proceeding subsections will show methods recently developed that allow the use of an incoherent source without applying excessive filtration to the x-ray beam.

1.7.1 Propagation-based Phase Contrast X-ray Imaging

PB-PCX imaging, also known as propagation-based imaging (PBI), has a very similar experimental setup to that of conventional x-ray imaging. In both setups x-rays transmitted through an object are recorded using some type of spatially resolved area detector (see Fig. 1.13). Whereas the detector is placed at or very close to the object exit surface plane in conventional x-ray imaging, the ODD is extended in PB-PCX imaging. PB-PCX imaging also requires a moderate degree of spatial coherence, but not temporal coherence. Wilkins et al. (1996) first derived theoretically and proved experimentally that strong phase contrast is maintained even when temporal coherence is relaxed.

Under the projection approximation, the monochromatic paraxial exit surface scalar wavefield $\Psi(\mathbf{r}_\perp, z = 0, t) = \Psi(\mathbf{r}_\perp, z = -T, t) \exp\left\{-k \int_{-T}^{0} [\beta(\mathbf{r}) + i\delta(\mathbf{r})] dz\right\} \exp\{-i\omega t\}$. At the exit surface plane ($z = 0$), where attenuation-based x-ray imaging is usually performed, the intensity is $I(\mathbf{r}_\perp, z = 0) = |\psi(\mathbf{r}_\perp, z = T)|^2 = \exp\left[-2k \int \beta(\mathbf{r}) dz\right]$. Since this equation is independent of δ it can be seen that there is no phase contrast at that plane. However, at increasing ODD phase-induced

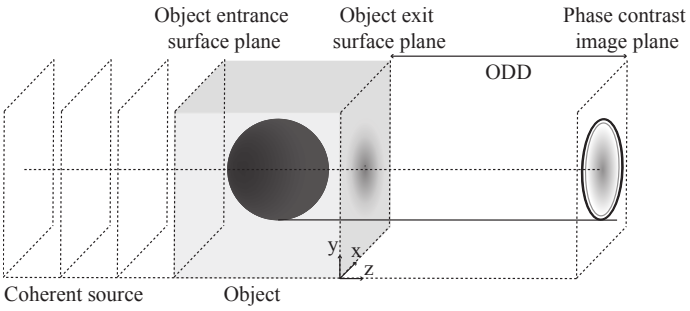

Figure 1.13: Schematic of a PB-PCX imaging setup.

intensity changes arise from refraction and diffraction as shown in Fig. 1.12. This is the basis of how PB-PCX imaging renders similarly absorbing objects visible, such as the boundaries between soft tissue and air. The remainder of this section is used to derive an expression for the image intensity downstream of the object in terms of its exit surface wavefield by making use of the angular spectrum formulation of scalar diffraction integrals. The following derivation follows from that given by Paganin (2006, sec. 1.2).

To begin, the reader is reminded of the wave equation given in Eq. 1.5 for the complex scalar wavefield traveling in free space:

$$\left(\frac{\partial^2}{\partial t^2} - \frac{1}{\epsilon_o \mu_o}\nabla^2\right)\Psi(\mathbf{r}, t) = 0, \tag{1.38}$$

for which the simplest solution is the plane wave. Since Eq. 1.38 is a linear partial differential equation, any linear combination of plane waves are also solutions. Consequently, any arbitrary three-dimensional (3D) wavefield can be described by a linear combination of 3D planes waves, hence a generalized solution to Eq. 1.38, assuming a monochromatic wavefield, can be expressed as:

$$\begin{aligned}\Psi(\mathbf{r}, t) &= \int_{\mathbf{k}} \widetilde{\Psi}(\mathbf{k}) \exp(i\mathbf{k}\cdot\mathbf{r})\mathrm{d}\mathbf{k} e^{-i\omega t} \\ &= \psi_\omega(\mathbf{r}) e^{-i\omega t},\end{aligned} \tag{1.39}$$

where $\widetilde{\Psi}(\mathbf{k})$ is a weighting factor for each wavevector $\mathbf{k}$ and is assumed to be non-zero only when $k = |\mathbf{k}| = \frac{\omega}{c}$. The ω subscript is a reminder that the time-independent scalar wavefield $\psi_\omega(\mathbf{r})$ has functional dependance on this quantity.

Substituting Eq. 1.39 into Eq. 1.38 gives:

$$\left[\nabla^2 + \frac{\omega^2}{c^2}\right] e^{-i\omega t} = 0, \tag{1.40}$$

remembering that $c = \frac{1}{\sqrt{\epsilon_o \mu_o}}$. Since the harmonic time factor $e^{-i\omega t}$ is non-zero, the quantity in square brackets must equal zero. This gives the well known Helmholtz equation governing the spatial evolution of the time-independent scalar monochromatic wavefield:

$$\left[\nabla^2 + k^2\right]\psi_\omega(\mathbf{r}) = 0. \tag{1.41}$$

Next a solution is sought for $\psi_\omega(\mathbf{r}_\perp)$ at the phase contrast plane $z = L$ in terms of the exit surface plane of the object at $z = 0$, after which the intensity distribution at the phase contrast plane can be determined directly from the relation: $I(\mathbf{r}_\perp) = |\psi(\mathbf{r}_\perp)|^2$.

Consider first the simplest non-trivial solution to the Helmholtz equation given in Eq. 1.41 to be one of the elementary time-independent plane waves:

$$\psi_\omega(\mathbf{r}) = \exp(2\pi i \mathbf{k} \cdot \mathbf{r}). \tag{1.42}$$

This plane wave equation at $z = 0$ is:

$$\psi_\omega(\mathbf{r}_\perp, z = 0) = \exp(2\pi i \mathbf{k}_\perp \cdot \mathbf{r}_\perp) \tag{1.43}$$

and given that $k^2 = k_x^2 + k_y^2 + k_z^2 \Rightarrow k_z = \sqrt{k^2 - k_\perp^2}$ where $k_\perp^2 = k_x^2 + k_y^2$, the plane wave equation at $z = L \geq 0$ is:

$$\psi_\omega(\mathbf{r}_\perp, z = L) = \exp(2\pi i \mathbf{k}_\perp \cdot \mathbf{r}_\perp) \exp\left(2\pi i L \sqrt{k^2 - k_\perp^2}\right). \tag{1.44}$$

Equations 1.43 and 1.44 can be equated to give:

$$\psi_\omega(\mathbf{r}_\perp, z = L) = \psi_\omega(\mathbf{r}_\perp, z = 0) \exp\left(2\pi i L \sqrt{k^2 - k_\perp^2}\right), \tag{1.45}$$

which is still a solution to the Helmholtz equation.

Equation 1.45 shows that if the plane wave at $z = 0$ is known, then multiplying it by $\exp\left(2\pi i L \sqrt{k^2 - k_\perp^2}\right)$ (angular spectrum propagation term) gives the wavefield at $z = L$. This approach can be generalized to determining the 2D wavefield at $z = L$ from any arbitrary time-independent monochromatic 2D wavefield at $z = 0$. To show how, remember that any 3D wavefield can be written as a weighted sum of 3D plane waves. Similarly, 2D wavefields can be written as a weighted sum of 2D plane waves. Therefore, any 2D wavefield can be decompose into its constituent 2D plane waves, where each plane wave is propagated using the angular spectrum propagation term then summed to form the wavefield at $z = L$. This can be expressed as:

$$\psi_\omega(\mathbf{r}_\perp, z = L) = \int_{\mathbf{k}_\perp} \widetilde{\psi}_\omega(\mathbf{k}_\perp, z = 0) \exp(2\pi i \mathbf{k}_\perp \cdot \mathbf{r}_\perp) \exp\left(2\pi i L \sqrt{k^2 - k_\perp^2}\right) \mathrm{d}\mathbf{k}_\perp. \tag{1.46}$$

Equation 1.46 is known as the angular spectrum representation of the propagated wavefield. It can be expressed in operator form by introducing the operator forms of the 2D Fourier transform pairs, $\mathcal{F}^{-1}$ and $\mathcal{F}$, denoted as the inverse Fourier and Fourier transforms, respectively. The following Fourier transform convention is adopted throughout this thesis, where for a function $f(\mathbf{r}_\perp)$, its Fourier transform is:

$$\widetilde{f}(\mathbf{k}_\perp) = \int f(\mathbf{r}_\perp) \exp(-i2\pi\mathbf{k}_\perp \cdot \mathbf{r}_\perp) \mathrm{d}\mathbf{r}_\perp = \mathcal{F}\{f(\mathbf{r}_\perp)\}, \tag{1.47}$$

and its inverse Fourier transform is:

$$f(\mathbf{r}_\perp) = \int \widetilde{f}(\mathbf{k}_\perp) \exp(i2\pi\mathbf{k}_\perp \cdot \mathbf{r}_\perp) \mathrm{d}\mathbf{k}_\perp = \mathcal{F}^{-1}\left\{\widetilde{f}(\mathbf{k}_\perp)\right\}. \tag{1.48}$$

The 2D Fourier transform decomposes any 2D function into 2D plane waves of amplitude $\widetilde{f}(\mathbf{k}_\perp)$. The 2D inverse Fourier transform recovers any function from its Fourier transform by summing over their weighted 2D plane waves. These Fourier transform pairs can easily be numerically computed with minimal computation time by using the fast Fourier transform (FFT) (Rao et al., 2011). Therefore, Eq. 1.46 in operator form is:

$$\psi_\omega(\mathbf{r}_\perp, z = L) = \mathcal{F}^{-1} \exp\left(2\pi i L \sqrt{k^2 - k_\perp^2}\right) \mathcal{F}\psi_\omega(\mathbf{r}_\perp, z = 0). \tag{1.49}$$

Given that synchrotron radiation is exclusively used for the work presented in this thesis, the wavefield is inherently collimated (Margaritondo, 2002) and continues to be so after traversing the object whence the projection approximation is valid. Consequently, the paraxial approximation can be made, which is equivalent to approximating $k_\perp \ll k$. This allows the terms inside the exponential of the angular spectrum propagation term to undergo Taylor expansion truncated up to first order. Then, Eq. 1.49 reduces to what is known as the Fresnel propagator equation:

$$\psi_\omega(\mathbf{r}_\perp, z = L) = e^{ikz} \mathcal{F}^{-1} \exp\left[\frac{-iLk_\perp^2}{2k}\right] \mathcal{F}\psi_\omega(\mathbf{r}_\perp, z = 0) \tag{1.50}$$

If:

$$\left|\frac{Lk_\perp^2}{2k}\right| \ll 1, \tag{1.51}$$

then Eq. 1.50 can be further simplified by having its exponential term Taylor expanded up to first order:

$$\exp\left[\frac{-iLk_\perp^2}{2k}\right] \approx 1 - \frac{iLk_\perp^2}{2k}. \tag{1.52}$$

The propagated wavefield now simplifies to:

$$\psi_\omega(\mathbf{r}_\perp, z = L) = e^{ikz} \mathcal{F}^{-1}\left[1 - \frac{iLk_\perp^2}{2k}\right] \mathcal{F}\psi_\omega(\mathbf{r}_\perp, z = 0). \tag{1.53}$$

By bringing the propagation term inside $\mathcal{F}$ and using the Fourier derivative theorem (Paganin, 2006, sec. A.4), the Fourier transform pair cancels to give:

$$\psi_\omega(\mathbf{r}_\perp, z = L) = e^{ikz}\left[1 + \frac{iL\nabla_\perp^2}{2k}\right]\psi_\omega(\mathbf{r}_\perp, z = 0). \tag{1.54}$$

To reiterate, the propagated intensity is the center of interest of this study, thus:

$$\begin{aligned} I_\omega(\mathbf{r}_\perp, z = L) &= |\psi_\omega(\mathbf{r}_\perp, z = L)|^2 \\ &= \psi_\omega(\mathbf{r}_\perp, z = L)\psi_\omega^*(\mathbf{r}_\perp, z = L) \\ &= I_\omega(\mathbf{r}_\perp, z = 0) - \frac{L}{k}\nabla_\perp \cdot [I_\omega(\mathbf{r}_\perp, z = 0)\nabla_\perp\varphi_\omega(\mathbf{r}_\perp, z = 0)], \end{aligned} \tag{1.55}$$

where * represents the complex conjugate[23]. Equation 1.55 is hereafter termed the near-field intensity equation (NFIE). Also, ω will be dropped from Eq. 1.55 for notational simplicity.

In going from line 2 to 3 of Eq. 1.55 the complex wavefield $\psi(\mathbf{r}_\perp, z = 0)$ was replaced by its polar form $\sqrt{I(\mathbf{r}_\perp, z = 0)}\exp[i\varphi(\mathbf{r}_\perp, z = 0)]$ and terms quadratic with L were discarded as they are at least $\frac{L}{k}$ multiplicative factor smaller than the other terms, which for x-rays typically imaged at $L \backsim 1$ m is $\backsim 10^{-11}$. At the attenuation plane $z = 0$, Eq. 1.55 reduces to only the first term that if the projection approximation is satisfied, becomes the Beer-Lambert law. At increasing L, the second term of Eq. 1.55 introduces intensity variations proportional to the Laplacian of $\varphi(\mathbf{r}_\perp, z = 0)$. This equation provides the underlying mathematical description to how phase gradients give rise to propagation-induced intensity variations shown in Fig. 1.12. For instance, consider $\varphi(\mathbf{r}_\perp, z = 0)$ to be a step function created from illuminating a half-plane edge. The Laplacian of the step function is a pair of bright and dark intensity fringes. From Fig. 1.12(c) this is as expected; however, it shows there should be more than one pair of bright/dark intensity fringes. Equation 1.55 fails to account for these due to the inequality requirement in Eq. 1.51 being made.

The inequality in Eq. 1.51 can be manipulated into a more useful form by approximating $k_\perp = \frac{2\pi}{a}$, where a is the characteristic length scale of the object, and substituting $k = \frac{2\pi}{\lambda}$, to arrive at:

$$\frac{a^2}{L\lambda} \gg \pi. \tag{1.56}$$

The left hand side of Eq. 1.56 is the well known Fresnel number N_F, where for NFIE (Eq. 1.55) to hold N_F must be much greater than π. This is known as the near-field condition and the ODD (L) over which this condition is valid is known as the near-field regime. However, since this near-field

[23]Equation 1.55 can also be derived by making the finite difference approximation to the transport-of-intensity equation (TIE): $-k\frac{\partial I(\mathbf{r})}{\partial z} = \nabla_\perp \cdot [I(\mathbf{r})\nabla_\perp\phi(\mathbf{r})]$ (Reed Teague, 1983). The finite difference approximation is made on the LHS of the TIE to arrive at Eq. 1.55. This approximation is valid when the second order derivative or higher of $I(\mathbf{r})$ is less than unity. However, this is not easily quantifiable and therefore difficult to determine when the approximation is valid. Conversely, the derivation presented in the main text gives a more quantifiable condition in the form of Eq. 1.51.

condition is an approximation of Eq. 1.51 it does not guarantee that NFIE will hold. To understand why, refer back to Eq. 1.51. That equation states that the propagation term given in Eq. 1.52 can only accurately propagate plane waves with transverse wavevectors $k_\perp^2 \ll \frac{2k}{L}$ (cf. Eq. 1.51) over a propagation distance of L. Therefore, only for wavefields whose spectral power presides predominantly within the disc of spatial frequencies $k_\perp^2 \ll \frac{2k}{L}$ can Eq. 1.56 accurately describe their intensity field at L. Determining the maximum value $k_\perp$ of the unpropagated wavefield to check if it is less than $\frac{2k}{L}$ for NFIE to be valid is difficult without knowing the unpropagated wavefield. Often, the maximum value of $k_\perp$ is approximated to be equal to $\frac{2\pi}{a}$, where the characteristic length a of the object can be measured. This approximation makes sense, since a large object (i.e. large a) would have most of its power concentrated in the lower transverse wavevectors, and vice versa. However, the complex refractive index also affects the distribution of the power in the unpropagated wavefield. Increasing values of β or δ produce larger phase and intensity gradients in the wavefield, respectively, resulting in the plane waves scattering at larger angles, and therefore redistributes more of the power to larger $k_\perp$. Gureyev et al. (2008) incorporated δ into the N_F to generalize the near-field condition to be $N_F \gg \max\{\pi, |\varphi(\mathbf{r}_\perp, z=0)|_{max}\}$ where $|\varphi(\mathbf{r}_\perp, z=0)|_{max}$ is the maximum transverse phase shift over some length σ at the plane $z = 0$ of the initial wavefield. However, this near-field condition is considered too stringent and is relaxed to $N_F \geq \max\{\pi, |\varphi|_{max}\}$.[24] The explicit dependance of φ on $\mathbf{r}_\perp$ and z was omitted for the sake of notational simplicity and will continue to be from hereon.

NFIE is central to achieving the main objective of this thesis: to study the form and function of the lungs. If the PB-PCX image $I(\mathbf{r}_\perp, z = L)$ of the lungs is recorded, then this equation enables the exit surface phase $\varphi(\mathbf{r}_\perp, z = 0)$ and amplitude $\sqrt{I(\mathbf{r}_\perp, z = 0)}$ to be recovered, from which important information about the lungs can be extracted. The recovery of both of these is known as phase-amplitude retrieval (or simply phase retrieval), where many such techniques have been developed. The technique adopted for this thesis is called the single image phase retrieval algorithm (SIPRA) that involves solving NFIE. Section 1.8 details how SIPRA is derived along

[24] In other works (Mayo et al., 2002, 2003), the near-field condition was relaxed in this way, yet no justification was provided there or in other published work. However, after correspondence with Prof. David Paganin, the following qualitative argument was made on why $N_F \gg \max\{\pi, |\varphi|_{max}\}$ is too conservative. The near-field condition originates from the first order Taylor approximation of the exponential term in the Fresnel propagator equation (Eq. 1.50). Generally, the first order approximation of a function is valid only when the total sum of the higher order terms is $\ll 1$. This is approximately equivalent to stating that the magnitude of the second order term is $\ll 1$, this being the leading order of the higher order terms, which is the basis on how the near-field approximation was derived. However, the exponential term is a complex function. In the complex plane, each higher order term represents a vector with a given direction and magnitude. Even if the magnitude of the second order term is close to or ≥ 1, that of the vector sum of the higher order terms may be $\ll 1$, causing the first order Taylor approximation to be still valid. Consequently, the near-field condition $N_F \gg \max\{\pi, |\varphi|_{max}\}$ can underestimate the validity range. Based on these arguments, this justifies why it is possible the near-field condition can be relaxed to $N_F \geq \max\{\pi, |\varphi|_{max}\}$.

with a broad literature review of some of the other alternative phase retrieval techniques. In the following chapters, various PB-PCX imaging-based techniques developed for extracting structural information of the lung is based around using SIPRA. While phase retrieval can be done to extract lung information with other PCX imaging modalities, PB-PCX imaging requires no post-object optics and the requirement for high temporal coherence can be significantly relaxed (Wilkins et al., 1996). Consequently, compared to other PCX modalities, PB-PCX imaging has the simplest setup, and makes fuller use of the x-ray source brightness as a monochromator is not required. This is a favorable trait for dynamic imaging utilizing standard laboratory-based x-ray sources as it can be performed with relatively short exposure times with relatively comparable SNRs.

1.7.2 Analyzer-based Phase Contrast X-ray Imaging

AB-PCX imaging utilizes a crystal analyzer placed between the object and detector in the setup shown in Fig. 1.13 (Davis et al., 1995; Ingal and Beliaevskaya, 1995; Rigon et al., 2003, 2008; Zhou and Brahme, 2008). The intensity of x-rays diffracted off a crystal analyzer is dependent on changes in the x-ray direction that arise from phase shifts imparted by the object.

The periodic arrangement of atomic scatterers in a crystal analyzer causes x-rays undergoing elastic scattering to constructively interfere and form strong peaks in reflectivity at certain angles with the atomic planes of the crystal. These are known as Bragg peaks, named after son and father William Lawrence Bragg and William Henry Bragg, respectively, who developed the geometrical interpretation of x-ray diffraction from crystals (Bragg, 1913). Under this interpretation, the Bragg peaks are infinitely thin, but this is only true for infinitely large and perfect crystals in the presence of monochromatic plane wave illumination. Realistic crystals are of finite size and contain structural imperfections, resulting in an increase in the Bragg peak width to the order of microradians (Ewald, 1969)[25]. This angularly dependent reflectivity function is known as a Darwin reflectivity curve or more commonly a rocking curve as one must rotate (rock) the crystal to measure this effect. In the diagnostic energy range, biological tissues typically refract/diffract x-rays on the order of microradians. So by placing an analyzer crystal in the beam downstream of the sample, and aligning the crystal at an angle close to or exactly at a Bragg peak, phase-shift-sensitive intensity images can be recorded. The sensitivity (width) of the rocking curve is dependent on many parameters including: crystal type/size/orientation/thickness and x-ray beam divergence and

[25]The relationship between the Bragg peak shape and the aforementioned parameters in the main text are accounted for in the Dynamical theory of diffraction as first developed by Darwin (1914) and further developed by others such as Friedrich (1922) and Ewald (1969). It accounts for the imperfectness of a crystal and the effects of multiple scattering between the incident and diffracted wavefield to provide a more complete description of the Bragg peaks compared that to given by Bragg (1913) using geometrical optics.

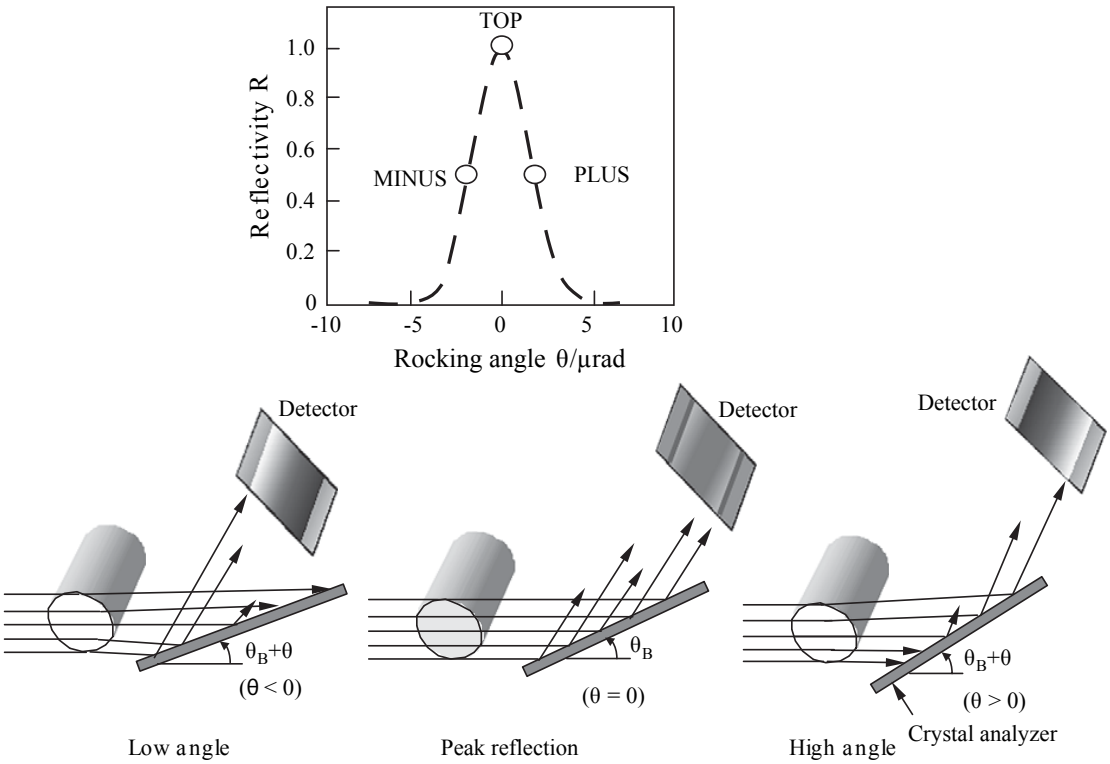

Figure 1.14: The rocking curve of an analyzer crystal is shown with reflectivity of $R = 1$ at the Bragg angle (θ_B) situated at the rocking angle θ=0 μrad. The analyzer crystal can be orientated at different angles to alter the image phase contrast. In the middle panel (peak reflection), the analyzer is orientated for unscattered rays to undergo 100% reflectivity. The image produced is dominated by attenuation contrast with dark bands appearing along the edge of the cylinder due to large diffraction/refraction. Alternatively, the crystal may be rotated below (low angle) or above (high angle) the Bragg peak such that rays refracted can have increased and decreased reflectivity. Note that areas receiving more photons appear brighter than those that receive less photons (Zhou and Brahme, 2008).

energy (Mittemeijer, 2010, ch. 5). These parameters can be adjusted to cater for specific AB-PCX imaging experiments.

As an illustrative example of the working principle of AB-PCX imaging, consider Fig. 1.14, which shows a plane wave represented by rays illuminating a cylinder and undergoing refraction. An analyzer crystal can be orientated at different angles to achieve different contrast images. Three such orientations are shown in Fig. 1.14. Aligning the rocking curve half way up on either side of the peak with the direction of the incident wavefield creates an intensity gradient across the width of the cylinder due to refraction. Rays illuminating one side of the cylinder along its width refract higher up on the rocking curve and therefore scatter off the analyzer with greater intensity than those illuminating on the other side of the cylinder. Aligning the top of the rocking curve with the direction of the unscattered ray causes all refracted rays to scatter off the crystal with reduced intensity. Thus, the image contrast is dominated by that of attenuation.

AB-PCX imaging possesses many advantages over PB-PCX imaging. Crystal analyzers are able to reject inelastically scattered light because they scatter at angles greater than the width of the rocking curve. As mentioned in section 1.4, inelastic scattering contributes to the overall noise of the image, hence, AB-PCX imaging can produce images with better SNR than PB-PCX imaging. Furthermore, attenuation, refraction and ultra small angle x-ray scattering (USAXS) can be extracted from AB-PCX images as three separate images (this will be discussed in more detail in section 2.2.2). In a refraction image, each pixel represents a small part of the object where the x-rays have refracted at a well-defined angle. That is, the x-rays have sampled only one part of the rocking curve at each pixel. USAXS data are recordings of x-rays having sampled multiple parts of the rocking curve per pixel (Rigon et al., 2003). For example, at the edge of the cylinder in Fig. 1.14 the x-rays would scatter at high angles and converge with x-rays scattered at different angles from other parts of the cylinder towards the same pixel. Consequently each pixel contains x-rays refracted at different angles. Each has shown to provide useful diagnostic information, for example, an image only of USAXS gives details about small sized structures (Arfelli et al., 2013).

Despite the benefits of AB-PCX imaging, there are several drawbacks. The inclusion of a highly sensitive analyzer crystal makes it experimentally more challenging to align and maintain its position over time (Connor et al., 2012). Unlike PB-PCX imaging, AB-PCX imaging requires a high temporally, but not spatially, coherent collimated x-ray beam. Also, since the analyzer can only be rotated in one direction, phase contrast is only present parallel to that direction. The acquisition time can be as long or even longer than PB-PCX imaging to record a single image depending on the mode of recording. The two modes are the full x-ray beam and slot scanning approach (Nesch et al., 2009; Parham et al., 2009). The slot scanning approach utilizes only a thin slice of the x-ray beam and scans across the sample. The individual images are then stitched together during post-processing. The advantages of this approach is it reduces beam divergence and maintains a narrow frequency bandwidth at high energies when passing through a monochromator. However, scanning time significantly increases the total acquisition time, making dynamic imaging currently unfeasible. Using the full x-ray beam instead reduces the total acquisition time but requires a large beam of low divergence, which is difficult to achieve with high flux for dynamic imaging.

1.7.3 Interferometry-based Phase Contrast X-ray Imaging

IB-PCX imaging defines a class of techniques that renders phase-induced intensity modulations by superimposing two or more coherent or partially coherent wavefields. The first x-ray interferometer was the Bonse-Hart interferometer (Bonse and Hart, 1965), as depicted in Fig. 1.15. There are

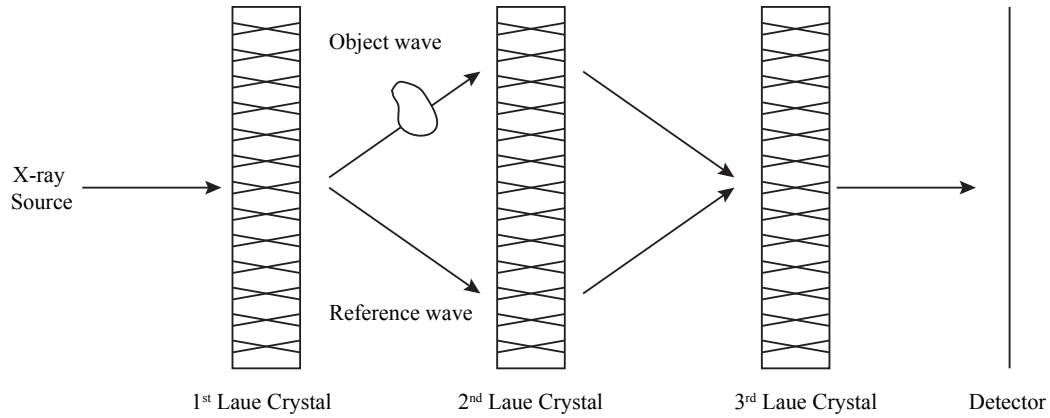

Figure 1.15: A schematic diagram of a Bonse-Hart interferometer with the beam propagating towards the detector. The x-ray beam is split in two by diffracting off two different atomic planes, which are sketched within the three crystals.

three identical Laue crystals[26], the first crystal splits the beam into a transmitted and diffracted beam[27], where a sample is placed in front of and distorts the phase of one of the beams. The second crystal redirects the beams towards the third crystal to recombine the beams. The output image shows phase-sensitive intensity variation, from which the exit surface phase can be retrieved using the method developed by Takeda et al. (1982). Theirs was a Fourier-based method that recovers phase constrained to the interval $[0, 2\pi)$, consequently it returns accurate phase maps only of wavefields with slowly-varying phase. For objects that induce large phase shifts in the wavefield, phase unwrapping can be performed during post processing to recover the correct exit surface phase map (Momose, 2002). Alternatively, multiple output images can be recorded, where for each image the reference beam is phase retarded to a different degree by a phase shifter (for example, a kapton wedge) to solve for the exit surface phase map (Paganin, 2006, pp. 312).

One major setback to the Bonse-Hart interferometer is it requires both a highly spatially and temporally coherent x-ray source. These stringent requirements are relaxed in grating-based interferometry (David et al., 2002; Momose et al., 2003; Bech et al., 2013; Wen et al., 2013), where Laue crystals are replaced with gratings, as shown in Fig. 1.16. The gratings are made up of regularly spaced elongated elements. The elements for the first grating (source grating) are

[26] X-ray scattering from crystals may occur either in reflection (Bragg crystal) or transmission (Laue crystal). The analyzer crystals depicted in Fig. 1.14 are examples of a Bragg crystal.

[27] X-rays transmitted and diffracted through a Laue crystal do not suffer much significant loss in intensity. There is an increase in the transparency of crystals at Bragg angles even if they are sufficiently thick to absorb all radiation. This is known as the Borrmann effect. For further reading, refer to Saccocio and Zajac (1965); Cowley (1995).

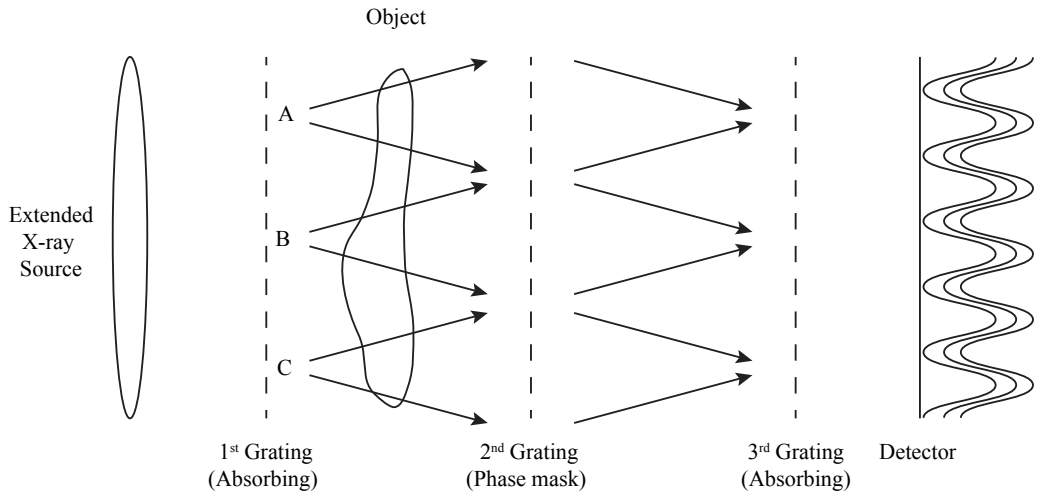

Figure 1.16: A schematic diagram of a Grating interferometer with the beam propagating towards the detector. The three fringe patterns that are in phase at the detector plane correspond to the three line sources labeled as A, B and C.

absorbing, and it converts an incoherent x-ray source into a periodic line of mutually independent spatially coherent sources. The second grating acts as a phase mask, where each element imparts only a phase shift. This imprints a periodic phase modulation on the beam. In the region satisfied by the Fresnel diffraction integral given by the Fresnel propagator equation (Eq. 1.50) the periodic phase modulations reappear as fringes, of the same period as the second grating, at periodic propagation distance intervals. This is known as the Talbot effect. Each line source (labeled as A, B and C in Fig. 1.16) from the first grating produces its own set of fringes. By carefully designing the periodicity of the first grating, these fringes coherently interfere at the detector (phase lock). The fringe spacings are however too small to be resolved by most detectors, thus a third grating with identical periodicity to the second grating, but which is absorbing, is positioned at one of the Talbot distances. The intensity at each pixel is recorded as the third grating is translated along the direction of the fringes (phase stepping). This traces out a peak as the third grating will go from completely blocking the fringes to allowing them all through. The shift in the peak with and without the object represents the refraction angle, from which the phase can be determined via spatial integration (see Eq. 1.36). Similar to AB-PCX imaging, phase contrast could initially only be achieved along one direction – perpendicular to the elements of the gratings. But one of the many advancements in IB-PCX imaging listed in the next paragraph shows 2D phase contrast is now possible.

IB-PCX imaging is considered the most sensitive out of the three discussed PCX imaging

techniques as the fringe spacings is inversely proportional to the refraction angle (Zhou and Brahme, 2008). Many extensions have been made to the grating interferometry such as, conducting phase measurements in two directions (Kottler et al., 2007), performing tomography (Wang et al., 2013), and using a multi-line x-ray source instead of a source grating (Du et al., 2012). However, recording multiple images is needed to retrieve the phase through phase stepping, which for live dynamic lung imaging, is disadvantageous. Ge et al. (2014) developed a step-like grating for the third grating to avoid the need to perform phase stepping but this is traded-off with spatial resolution.

1.8 Phase Retrieval from PB-PCX images

It was shown in section 1.7.1 how the wavefield at the exit surface plane evolves with propagation and forms PB-PCX images downfield of the sample. This will help recover the exit surface wavefield from PB-PCX images in order to extract information about the sample.

Phase retrieval has provided a rich field of study that extends from electron microscopy to x-ray crystallography (Millane, 1990; Hüe et al., 2010). Many methods for recovering the exit surface phase have been developed such as the multiple isomorphous replacement method (Taylor, 2010), the multi-wavelength anomalous diffraction (Son et al., 2011), the Gerchberg-Saxton algorithm (Gerchberg and Saxton, 1971, 1972), and a neural network-based method (Burian et al., 2000). These methods are designed to recover the exit surface wavefield from far-field images rather than from near-field images (PB-PCX image) and therefore are not directly applicable for the work done here.

Several methods exist for recovering the exit surface wavefield from the near-field intensity (PB-PCX) images through solving NFIE. These include methods based on the full multigrid algorithm (Gureyev et al., 1999; Allen and Oxley, 2001), the orthogonal-series-expansion based method (Gureyev and Nugent, 1996), the Green-function method (Reed Teague, 1983), and the fast-Fourier-transform-based method (Paganin and Nugent, 1998; Schmalz et al., 2011). The main drawback to these methods is that they require at least two PB-PCX images at different ODDs. For a moving object such as the chest, these images must be recorded almost simultaneously to accurately recover the exit surface wavefield. However, a successful method of achieving this has yet to be developed as issues such as image alignment and low frequency noise amplification are difficult to overcome.

Paganin et al. (2002) developed a SIPRA that requires only a single PB-PCX image to recover the exit surface wavefield, but assumes the object is made of a single material. Despite the object studied in this thesis being the chest, which is a multi-material object, SIPRA is still applicable for

the work done here as will be made apparent in later chapters. The derivation of SIPRA will now be presented by first rewriting the NFIE (Eq. 1.55) with all terms as originally defined:

$$I(\mathbf{r}_\perp, z = L) = I(\mathbf{r}_\perp, z = 0) - \frac{L}{k}\nabla_\perp \cdot [I(\mathbf{r}_\perp, z = 0)\nabla_\perp \varphi(\mathbf{r}_\perp, z = 0)]. \tag{1.57}$$

Here, the wavefield is still assumed monochromatic but the ω subscript has been dropped for notational simplicity.

Under the projection approximation (section 1.6) for a homogeneous material with complex refractive index $n = 1 - \delta + i\beta$ and projected thickness $T(\mathbf{r}_\perp)$, the phase shift and attenuated intensity of a wavefield traveling along axis z can be written as:

$$\Delta\varphi(\mathbf{r}_\perp, z = 0) = -k\delta T(\mathbf{r}_\perp) \tag{1.58a}$$

and

$$I(\mathbf{r}_\perp, z = 0) = I(\mathbf{r}_\perp, z = -T)\exp\left[-2k\beta T(\mathbf{r}_\perp)\right], \tag{1.58b}$$

respectively, and substituted into Eq. 1.57 to give:

$$I(\mathbf{r}_\perp, z = L) = I_o e^{-\mu T(\mathbf{r}_\perp)} + L\delta\nabla_\perp \cdot \left[I_o e^{-\mu T(\mathbf{r}_\perp)}\nabla_\perp T(\mathbf{r}_\perp)\right]. \tag{1.59}$$

Here, $I_o = I(\mathbf{r}_\perp, z = 0)$ denotes the incident intensity and the substitution $\mu = 2k\beta$ was made, where μ is known as the linear attenuation coefficient.

By recognizing that $\nabla_\perp e^{-\mu T} = -\mu e^{-\mu T}\nabla_\perp T$, and making use of the Fourier derivative theorem, $T(\mathbf{r}_\perp)$ is made the subject:

$$T(\mathbf{r}_\perp) = -\frac{1}{\mu}\ln\left[\mathcal{F}^{-1}\left\{\frac{\mathcal{F}\{I(\mathbf{r}_\perp, z = L)/I_o\}}{1 + (L\delta/\mu)k_\perp^2}\right\}\right]. \tag{1.60}$$

Finally, by substituting Eq. 1.60 into Eqs. 1.58a and 1.58b, an expression respectively for the exit surface phase and intensity of a homogeneous material are respectively derived:

$$\Delta\varphi(\mathbf{r}_\perp, z = 0) = \frac{k\delta}{\mu}\ln\left[\mathcal{F}^{-1}\left\{\frac{\mathcal{F}\{I(\mathbf{r}_\perp, z = L)/I_o\}}{1 + (L\delta/\mu)k_\perp^2}\right\}\right] \tag{1.61a}$$

and

$$I(\mathbf{r}_\perp, z = 0) = I_o\mathcal{F}^{-1}\left\{\frac{\mathcal{F}\{I(\mathbf{r}_\perp, z = L)/I_o\}}{1 + (L\delta/\mu)k_\perp^2}\right\}. \tag{1.61b}$$

Equation 1.60 shows that SIPRA multiplies the PB-PCX image in Fourier space by a low pass filter to remove the high frequency phase-induced fringes and recover the exit surface wavefield.

There are other phase retrieval algorithms, which require only a single PB-PCX image, that also utilize a low pass filter (Burvall et al., 2011). However, the denominator of their low pass filters contain zeroes whereas that of SIPRA never does. This makes SIPRA far more stable since there is no division by zero.

1.9 Numerical Simulations using the Angular Spectrum Formalism

Many of the advances in PB-PCX imaging of the lungs made in this thesis are aided by numerical simulation. Therefore, a brief detour is now taken to describe the mathematical framework upon which these simulations are formed. The method adopted employs the angular spectrum representation of propagated wavefields introduced in section 1.7.1. Specifically, Eq. 1.49 is used to propagate a scalar wavefield at one plane to yield its propagated wavefield in another plane.

To correctly simulate PB-PCX images utilizing Eq. 1.49, it is important that both the initial wavefield ($\psi(\mathbf{r}_\perp, z = 0)$) and the angular spectrum propagation term $\left(\exp\left(2\pi i L\sqrt{k^2 - k_\perp^2}\right)\right)$ are sufficiently finely sampled. In addressing the former, consider that it is sampled over an $N \times N$ Cartesian grid with pixel size Δx and that it is frequency bandlimited. That is, its Fourier transform is non-zero up to a certain spatial frequency[28] defined as the Nyquist frequency f_N. According to the Shannon-Nyquist sampling theorem, a bandlimited signal is adequately sampled when the pixel size $\Delta x \leq \frac{1}{2f_N}$.

Herein this thesis, the projection approximation is used to calculate the intensity $I(\mathbf{r}_\perp, z = 0)$ and phase $\phi(\mathbf{r}_\perp, z = 0)$ to determine the initial wavefield $\psi(\mathbf{r}_\perp, z = 0) = \sqrt{I(\mathbf{r}_\perp, z = 0)}\exp[i\phi(\mathbf{r}_\perp, z = 0)]$. To determine how finely sampled the intensity and phase must be so that the initial wavefield is sufficiently finely sampled at $\Delta x \leq \frac{1}{2f_N}$, notice that the product of the two functions, $\sqrt{I(\mathbf{r}_\perp, z = 0)}$ and $\exp[i\phi(\mathbf{r}_\perp, z = 0)]$, to form $\psi(\mathbf{r}_\perp, z = 0)$ is equivalent to their convolution in Fourier space. Verbeek (1985) showed that the convolution of two bandlimited function limits the resultant product to the sum of their bandwidths. Hence, considering that $\psi(\mathbf{r}_\perp, z = 0)$ is bandlimited at f_N, the two functions are also bandlimited at $2f_N$, this is assuming that both have equal bandwidths (Verbeek, 1985). They must then be sampled with pixel size $\Delta x \leq \frac{1}{4f_N}$. Since $\sqrt{I(\mathbf{r}_\perp, z = 0)}$ must be sampled at $\Delta x \leq \frac{1}{4f_N}$, then $I(\mathbf{r}_\perp, z = 0)$ must also be approximately sampled at $\Delta x \leq \frac{1}{4f_N}$ (Marks II, 2008, pp. 239-241). For $\exp[i\phi(\mathbf{r}_\perp, z = 0)]$ to be adequately sampled at $\Delta x = \frac{1}{4f_N}$, the pixel size chosen for $\phi(\mathbf{r}_\perp, z = 0)$ must be such that the magnitude of its gradient is less than $\frac{\pi}{2}$ per pixel across every

[28] The terms spatial frequency and transverse wavevector will be utilized interchangeably throughout this thesis.

pixel[29].

Turning now to the issue of adequately sampling the angular spectrum propagation term in Eq. 1.49, its discrete form can be written as:

$$\exp(i\phi) = \exp\left[2\pi i L\left(\frac{1}{\lambda^2} - \frac{i^2 + j^2}{N^2(\Delta x)^2}\right)^{\frac{1}{2}}\right]. \tag{1.62}$$

For it to be adequately sampled, the magnitude of the phase gradient must also be less than $\frac{\pi}{2}$ per pixel[30]. Since the phase is proportional to $i^2 + j^2$, the maximum phase gradient occurs at $r = \sqrt{i^2 + j^2} = N/\sqrt{2}$ where $i = j = N/2$. Hence,

$$\left|\frac{\mathrm{d}\phi}{\mathrm{d}r}\right|_{r=N/\sqrt{2}} = \left|\frac{d}{dr} 2\pi L\left[\frac{1}{\lambda^2} - \frac{r^2}{N^2(\Delta x)^2}\right]^{\frac{1}{2}}\right|_{r=N/\sqrt{2}} < \frac{\pi}{2}. \tag{1.63}$$

Evaluating Eq. 1.63 and rearranging to make Δx the subject gives (Barty, 2000, ch. 9):

$$\Delta x > \left[\frac{\lambda^2}{4}\left(1 + \sqrt{1 - \frac{128L^2}{N^2\lambda^2}}\right)\right]^{\frac{1}{2}}. \tag{1.64}$$

In summary, there is both a lower and an upper limit on the pixel size in order for the initial wavefield and angular spectrum propagator term to be adequately sampled, respectively. Interestingly, the upper limit of the pixel size corresponds to an upper limit to the propagation distance L through rearrangement of Eq. 1.64. Hence, it is seen that the discretisation effectively places a lower bound on the Fresnel number N_F (see Eq. 1.56) that can be achieved via numerical simulation. These conditions were met for all numerical simulations presented in this thesis, to ensure the simulated PB-PCX images were accurately simulated.

1.10 Concluding Remarks and Thesis Overview

This chapter focused on how the different types of x-ray interactions with matter, namely absorption and elastic/inelastic scattering, manifested into the measurable observables of interest: attenuation and phase gradients of the x-ray wavefield. In the x-ray regime, different biological materials have similar attenuation strength but can impart large phase gradients between different materials. This led to major developments in PCX imaging for biomedical imaging applications, which represents

[29] To understand why the phase gradient must be less than $\frac{\pi}{2}$ per pixel, remember that the complex exponential term is, according to Euler's formula, $\exp(i\phi) = \cos(\phi) + i\sin(\phi)$. Usually to adequately sample the sine and cosine function their phase must be sufficiently sampled such that the phase gradient is less than π per pixel. However, since $\exp(i\phi)$ is part of a product to form the initial wavefield, the phase gradient must instead be less than $\frac{\pi}{2}$ per pixel.

[30] Since the angular spectrum propagator term is multiplied by the Fourier transform of the initial wavefield, the magnitude of the phase gradient must be less than $\frac{\pi}{2}$ per pixel, and not π per pixel, for adequate sampling of the propagated wavefield.

a broad class of techniques that renders object-induced phase gradients as visible intensity changes. Three PCX imaging techniques were covered in this chapter: PB-PCX imaging, AB-PCX imaging and IB-PCX imaging. Each of these imaging modalities have demonstrated significant increase in soft tissue contrast. However, beyond the aesthetic improvements that PCX imaging brings, they can also provide greater quantitative information about biological objects than is possible with attenuation contrast alone. The aim of this thesis is to develop PB-PCX imaging-based techniques for extracting dynamic quantitative information of the lung. PB-PCX imaging represents the most suitable imaging modality because of its simple optics setup and the fact that quantitative information about an object can be robustly recovered from a single image.

Chapter 2 provides an overview of some of the common clinically available imaging-based techniques for measuring lung air volume (V_L) regionally. V_L is one of the most important parameters for assessing lung functionality. However, these methods generally have poor spatial resolution and require a high dose of x-ray radiation or contrast agents. Furthermore, many of them have inadequate temporal resolution to measure V_L in real-time on a breath-by-breath basis to determine lung ventilation, which is another important parameter of lung function. To that end, chapters 3 and 4 present two PB-PCX imaging-based techniques that provide highly localized measures of V_L in real-time.

Chapter 3 introduces a PB-PCX imaging-based technique for measuring regional ventilation that is now published by the author and co-workers in *Medical Physics* (see Leong et al. (2013a)). This is an extension to the PB-PCX volumetric imaging method developed by Kitchen et al. (2008). They developed a phase retrieval-based method to recover the change in V_L between two PB-PCX chest images, but their method was restricted to large areas of the lung due to the differential movement of the bone. This chapter provides a method to remove the bone through aligning two PB-PCX images using a cross-correlation-based approach before applying the phase retrieval-based method. Success of this approach enables the projected V_L to be measured in real-time on a pixel-by-pixel basis.

The difficulty associated with the techniques described in chapter 3 is that they require the subject to be immersed in water. This would be prohibitive if the techniques were to be used for human imaging. A further limitation to these techniques is that they largely utilize attenuation contrast to measure V_L. As such, they require the beam intensity to be highly stable during image acquisition. This susceptibility is exposed in synchrotrons and lab x-ray sources that do fluctuate in intensity due to movement of the beam and heating/cooling of various optics and metals that encounter the beam. Moreover, only changes in relative V_L can be calculated unless an image

of the fluid-filled lung is available. Chapter 4 proposes a new method of measuring absolute V_L from PB-PCX images. This new method performs such measurements by calibrating the speckled intensity pattern (lung speckle) contrast in PB-PCX chest images that arise from the many alveoli to known lung volumes. On live animals the lung speckle-volume calibration curve is found to be accurate in measuring absolute volumes of air in the lungs by comparing it to that measured using a gold standard technique. The bulk of this work has been published by the author and co-workers in *Optics Express* (see Leong et al. (2013b)).

From the investigation in chapter 4, it is shown that lung speckle encodes more than just V_L information. Alveolar size and population can also be measured from lung speckle. One of the important reasons for measuring alveolar size and population was highlighted in section 1.1, in that it can improve the limited understanding of alveolar mechanics. Chapter 5 introduces a method that combines the volumetric technique developed by Kitchen et al. (2008) and the derivation presented in chapter 4 to measure alveolar size and population. This is tested on glass particles of similar size to alveoli and is shown to be in excellent agreement. In animals, the calculated alveolar sizes and populations over a single breath is measured and is shown to compare well with that measured from CT images. This work has been publish by the author and co-workers in *Biomedical Optics Express* (see Leong et al. (2014)).

Chapter 6 discusses possible future directions for research arising as a result of these studies and provides a conclusion embodying the bulk of this thesis.

2 Localized Measures of Lung Ventilation

In this chapter, clinically available imaging-based techniques for measuring regional lung ventilation are compared. As will be shown, each have limitations that serve as a prelude to two new propagation-based phase contrast x-ray (PB-PCX) imaging-based methods that remove some of these restrictions. These new methods form the basis of chapters 3 and 4.

2.1 Current Clinical Lung Ventilation Imaging Techniques

One of the first tools for measuring lung ventilation were spirometers (Khandpur, 2003, ch. 13). These exist in many different forms that include measuring the flow of air (ventilation) through: (1) the pressure it exerts on a fixed laminar flow element (pneumotachometers); (2) the drop in temperature of a wire heated by an electric current (hot wire anemometers); and (3), the change in resistance of an electrical current applied to the chest (impedance pneumography). While spirometers have unquestionable benefits in clinical settings, they only provide a global lung function test. Local measures of air distribution can increase sensitivity and localization to early onset acute respiratory diseases and lung injuries. This section covers some of the standard imaging-based approaches for measuring the distribution and local flow of air in the lungs.

2.1.1 Computed Tomography

Analyzing lung air volume (V_L) from two-dimensional (2D) x-ray images is complicated by the superposition of the heart, diaphragm and bones (see for example Fig. 1.2 in section 1.1). Computed tomography (CT) is the reconstruction of three-dimensional (3D) linear attenuation coefficient maps ($\mu(x, y, z)$) from multiple projected 2D x-ray images of objects recorded at different angles. It separates these components spatially to isolate the lungs. Since the concept of CT was first introduced during the 1940's, the procedure for 3D image reconstruction has evolved dramatically

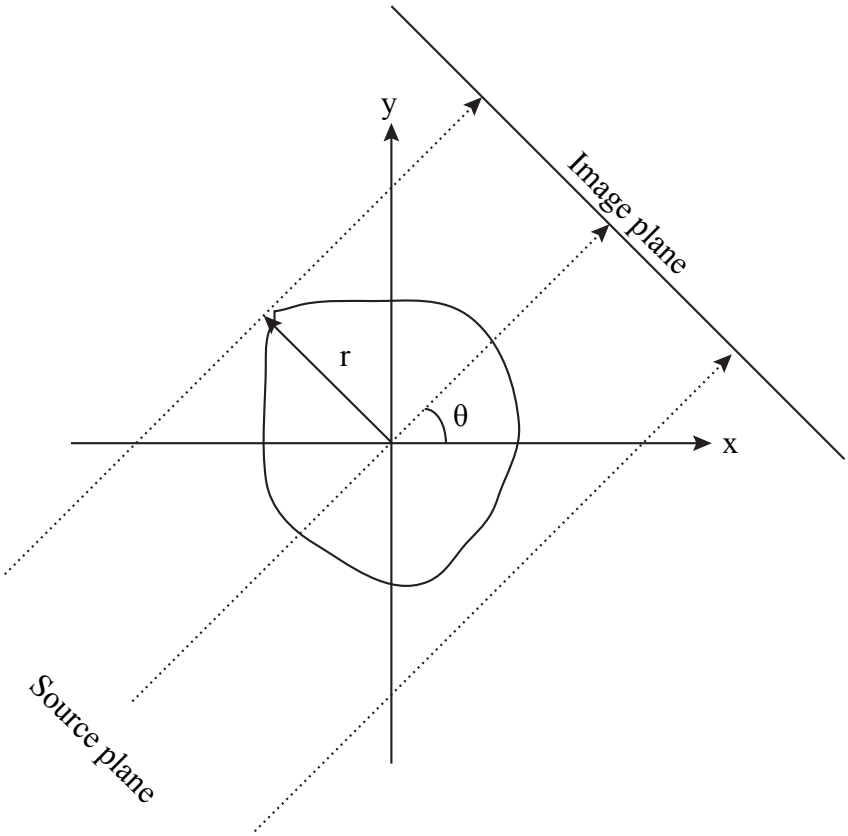

Figure 2.1: A schematic diagram of x-ray CT.

to encompass different classes of both iterative and non-iterative reconstruction techniques (Liu and Huang, 2008). Here, a non-iterative reconstruction technique referred to as filtered backprojection is described Jähne (2005, sec. 8.6.3). This was used to reconstruct experimental tomograms shown in this thesis.

Consider a sample uniformly illuminated by a parallel x-ray beam of intensity (I_o) subtending an angle (θ) with the x-axis (see Fig. 2.1). The logarithm of the projected x-ray image ($I(x, y)$) at the image plane is the line integral of the linear attenuation coefficient map along the direction of the beam. This is equivalent to Beer-Lambert's law given in Eq. 1.35b, which was integrated along the z-direction. Eq. 1.35b can be generalized to be along any direction:

$$\log_e \left\{ \frac{I(x, y, z)}{I_o} \right\} = \int \int \int \mu(x, y, z) \delta(r - x\cos(\theta) - y\sin(\theta)) \delta(z - z_0) \mathrm{d}x\mathrm{d}y\mathrm{d}z, \qquad (2.1)$$

where r is the distance normal to the direction of the ray from the origin. δ is the Dirac delta function that is zero everywhere except at its origin and its integral over $\mathbf{R}^3$ is unity. $\delta(z - z_0)$ represents a slice through the object along the xy-plane at $z = z_0$. By inversion of the Radon transform it is possible to reconstruct the 3D map of $\mu(x, y, z)$. To begin solving for $\mu(x, y, z)$,

Eq. 2.1 is Fourier transformed with respect to r. Then, using the Fourier sifting property (Paganin, 2006, sec. A.5), Eq. 2.1 becomes:

$$\mathcal{F}_r\left\{\log_e\left\{\frac{I(x,y,z)}{I_o}\right\}\right\} = \int\int\int \mu(x,y,z)\exp\left[-i2\pi k_\perp(x\cos(\theta)+y\sin(\theta))\right]\delta(z-z_0)\mathrm{d}x\mathrm{d}y\mathrm{d}z, \tag{2.2}$$

where $k_\perp$ is the transverse spatial frequency corresponding to r in Fourier space. By making the following changes of variable, $u = k_\perp\cos(\theta)$ and $v = k_\perp\sin(\theta)$, an important theorem, namely the Fourier slice theorem, for reconstructing tomograms is derived:

$$\mathcal{F}_r\left\{\log_e\left\{\frac{I(x,y,z)}{I_o}\right\}\right\} = \int\int\int \mu(x,y,z)\mathrm{d}z\exp\left[-i2\pi(ux+vy)\right]\delta(z-z_0)\mathrm{d}x\mathrm{d}y\mathrm{d}z. \tag{2.3}$$

Equation 2.3 shows that the Fourier transform of a logarithmic projection image at angle θ is equivalent to that of a slice through $\mu(x,y,z)$ at angle θ crossing $u = v = 0$. Thus, a complete Fourier transform of $\mu(x,y,z)$, denoted as $\widetilde{\mu}(u,v,z)$, can be constructed from 2D projection images at a range of θ. While the inverse Fourier transform can then be performed to recover $\mu(x,y,z)$ using Eq. 1.48, it is natural to perform the transform in polar $(k_\perp,\theta)$ coordinates. This is because each point on the projection image falls on a polar grid as shown in Fig. 2.1. First, the inverse Fourier transform given in Eq. 1.48 is rewritten with $f(\mathbf{r}_\perp) = \mu(x,y,z=z_0)$ and $\widetilde{f}(\mathbf{k}_\perp) = \widetilde{u}(u,v,z=z_0)$ for a slice along the xy-plane at $z = z_0$:

$$\mu(x,y,z=z_0) = \int_u\int_v \widetilde{\mu}(u,v,z=z_0)\exp(i2\pi\mathbf{k}_\perp\cdot\mathbf{r}_\perp)\mathrm{d}u\mathrm{d}v, \tag{2.4}$$

then the Cartesian coordinates in Fourier space are converted into polar coordinates using the relations $u = k_\perp\cos(\theta)$ and $v = k_\perp\sin(\theta)$ to give:

$$\begin{aligned}\mu(x,y,z=z_0) &= \int_{k_\perp}\int_\theta \widetilde{P}(k_\perp,\theta)\exp(i2\pi k_\perp[x\cos(\theta)+y\sin\theta])|k_\perp|\mathrm{d}k_\perp\mathrm{d}\theta \\ &= \int_\theta\int_{k_\perp}\left[\widetilde{P}(k_\perp,\theta)|k_\perp|\right]\exp(i2\pi k_\perp r'_\perp)\mathrm{d}k_\perp\mathrm{d}\theta,\end{aligned} \tag{2.5}$$

where $r'_\perp = x\cos(\theta)+y\sin(\theta)$, $\mathrm{d}u\mathrm{d}v = \begin{vmatrix} \frac{\partial u}{\partial k_\perp} & \frac{\partial u}{\partial\theta} \\ \frac{\partial v}{\partial k_\perp} & \frac{\partial v}{\partial\theta}\end{vmatrix}\mathrm{d}k_\perp\mathrm{d}\theta = |k_\perp|\mathrm{d}k_\perp\mathrm{d}\theta$ and $\widetilde{\mu}(k_\perp,\theta) = \widetilde{P}(k_\perp,\theta)|k_\perp|$ (cf. Eq. 2.4).

Finally, by making use of the convolution theorem, $\mathcal{F}^{-1}\{AB\} = \mathcal{F}^{-1}\{A\} * \mathcal{F}^{-1}\{B\}$, applied to two well-behaved functions A and B, where $*$ is the symbol for the convolution operator, Eq. 2.5 can be written as:

$$\mu(x, y, z = z_0) = \int_\theta [P(r'_\perp, \theta) * K(r'_\perp)]\mathrm{d}\theta, \tag{2.6}$$

where $P(r'_\perp, \theta) = \mathcal{F}^{-1}\left\{\widetilde{P}(k_\perp, \theta)\right\}$ is known as the sinogram and $K(r'_\perp) = \mathcal{F}^{-1}\{|k_\perp|\}$ is referred to as a ramp filter. This shows that $\mu(x, y, z = z_0)$ can be reconstructed by collating the projection images to construct a sinogram, convolved with a ramp filter, then integrated over θ.[1] The ramp filter can be seen as assigning greater weighting to high frequencies as they are more sparsely sampled. Without the filter, the image would appear blurred. However, this has an undesirable effect of enhancing image noise. There are modified filters that correctly reconstruct the image while reducing image noise (Lyra and Ploussi, 2011).

Regional V_L can be quantified at each voxel in a CT image based on the values of $\mu(x, y, z)$ since air will have a distinctly different range of values compared to surrounding tissues (Simon, 2000; Yamamoto et al., 2011). To study ventilation, multiple CT images in a single breath are required. This has been achieved through a number of means: recording a small number of projections using a multi-row detector (Law et al., 2001; van Daatselaar et al., 2004; Moser et al., 2014), gating the projection images to the phase of the respiratory cycle (Suga et al., 2004; Callahan et al., 2014), and injecting the contrast gas agent xenon into the lungs and measuring its volume at the end of each breath (Porra et al., 2004; Chae et al., 2008; Kim et al., 2012). However, these approaches share a number of drawbacks in that they impart large radiation doses, can only reconstruct a small number of CT images per breath, and can only achieve volumetric resolutions of the order of sub-millimeters. Minimizing radiation dose is particularly critical when imaging infants as they are more susceptible to radiation-induced illness (Thome et al., 1998; Arad et al., 2009). Studying ventilation from a small number of time points over a single breath does not entirely capture its highly dynamical process. Recent developments of iterative reconstruction techniques have the capacity to achieve relatively high spatial and/or contrast resolution from limited projections but require *a priori* knowledge of object geometry and x-ray beam characteristics such as its energy spectrum (Beister et al., 2012).

2.1.2 Nuclear Lung Imaging

Three nuclear lung imaging modalities currently utilized in clinics are: scintigraphy, single photon emission computed tomography (SPECT) and positron emission tomography (PET).

[1] Integrating over θ means the relative intensity at any point (x, y) on the tomogram is calculated by summing over every point $(r'_\perp, \theta)$ in the sinogram, whose projection line it represents intercept the point in (x, y) of the tomogram.

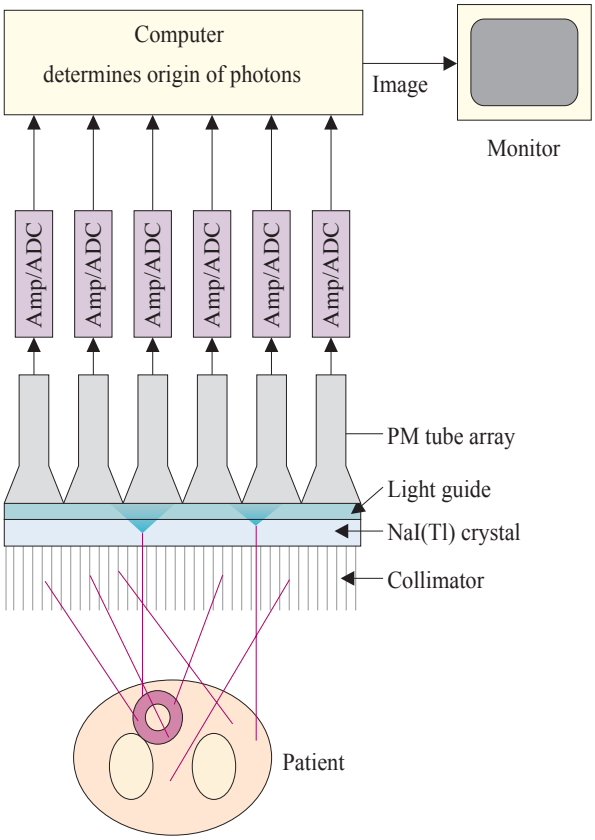

Figure 2.2: Schematic of 2D scintigraphy. A transverse section of a patient injected with a radioactive tracer that emits photons in all directions. Photons not traveling parallel to the direction of the detector are absorbed by the collimator. NaI(Tl) crystal, an example of a scintillator, converts those that travel parallel the collimator into lower energy visible light. These are amplified and digitized using an analog-to-digital convertor (ADC) (Cherry et al., 2012, p. 195).

A schematic example of scintigraphy is shown in Fig. 2.2. Photons are emitted in all directions from a gamma emitting radioactive tracer placed in the patient. γ-ray detectors positioned at an image plane collect the emitted photons to record a 2D image. These detectors are comprised of: (1) absorptive collimators that allow through only photons whose direction is perpendicular to the projected plane (otherwise the angle of incidence will not be known), and (2) a material that can convert photons directly/indirectly into an electrical signal; such examples include certain gases, semiconductors and scintillators (Cherry et al., 2012). The material is part of the photomultiplier (PM) tube that amplifies the photon number before the photons are converted into an electrical signal.

In SPECT, a 3D image of the tracer density is reconstructed from multiple projections of 2D scintigraphy images utilizing algorithms such as the filtered backprojection described in section 2.1.1. PET can also produce 3D tracer density maps but is achieved using a different approach. The tracers utilized for PET undergo β^+ decay and emit positrons (first postulated by

Dirac (1928)). The positrons travel 1-2 mm in the patient, scattering and losing kinetic energy until they collide with an electron; a process known as positron-electron annihilation (Blokland et al., 2002). This causes the emission of two photons and, because the electron and positron collide with almost zero kinetic energy, both of the emitted γ-rays have energy close to 511 keV, which is the rest mass energy of an electron/positron. They also collide with almost zero net momentum, hence the γ-rays travel in opposite directions to conserve the total momentum. A pair of detectors positioned at opposite sides of the object detects these two photons. The location of the annihilation event can be pinpointed somewhere along the 'coincidence' line connecting the detected pair. Time and energy are gated to only register photons that enter the detectors almost simultaneously and having energies close to 511 keV. This filters out scattered and random coincidence photons. A sinogram representing the total density of tracers along the coincidence line at different angles can be constructed and converted to a 3D image using filtered backprojection (described in the previous section).

Similar to CT, lung volumes can be measured based on the tracer density value of the reconstructed 3D image, however, there are several major drawbacks. γ-rays emitted from the center of the patient attenuate more than those emitted at the periphery. Consequently, images require attenuation correction before quantifying V_L. This correction procedure requires additional doses of radiation (Zwijnenburg et al., 1988). The intensity signal from tracers is significantly weaker than that of x-ray sources, thus nuclear lung imaging require longer exposures and consequently has poorer temporal resolution than CT (Rahmim and Zaidi, 2008; Bushberg et al., 2012). Moreover, the images will suffer from greater motion blur. Alternatively, inhalation and exhalation of the tracer ^{13}N-nitrogen while taking breath holds at the end of each breath to record an image reduces motion blur and enables ventilation analysis (Rhodes et al., 1989a,b; Richard et al., 2005). This is similar to the method developed by Porra et al. (2004) that was described in the previous section using CT. The spatial resolution of nuclear lung imaging is limited by many factors such as the dimensions of the detector collimator and scintillator thicknesses (Cherry et al., 2012). The latest spatial resolution achievable is of the order of millimeters (Beltrame et al., 2011; Bushberg et al., 2012). This makes it inferior to CT as images are recorded directly on the detector without requiring a collimator (Rahmim and Zaidi, 2008; Moses, 2011; Xie et al., 2013). Tracers are expensive to produce and store, but an upside is that they can be bonded to compounds of biological importance such as therapeutic drugs to monitor their uptake in the lungs (Conway, 2012).

2.1.3 Magnetic Resonance Imaging

Unlike CT and nuclear imaging, magnetic resonance imaging (MRI) does not require any ionizing radiation to reconstruct 3D images. It operates on the principle of nuclear magnetic resonance (NMR). A brief description of NMR will be provided and how this is utilized in MRI to provide structural information about the lungs.

Neutrons and protons exist in pairs in the atomic nucleus. In each pair the net magnetic moment is zero. For atoms made up of an odd number of neutrons or protons, for example ^{1}H and ^{3}Li, the net magnetic moment is non-zero. In the presence of an external magnetic field (B_o), the magnetic moment of the atom aligns either parallel or anti-parallel to B_o (Kuperman, 2000, ch. 1). However, they do not align exactly, but precess around B_o with a frequency, known as the Larmor frequency, that is dependent on the strength of the magnetic moment and B_o. This is a consequence of the Heisenberg uncertainty principle, which allows only one component of the orbital angular momentum to be known exactly; in this case, the component in the direction of B_o (Edmonds, 1996, sec. 2.4).

Consider a homogeneous material made of identical atoms with non-zero magnetic moments. A uniform external magnetic field will induce the atoms to align either parallel or anti-parallel to it, precessing all at the same Larmor frequency. This causes a split in the energy levels, with atoms aligned parallel to B_o being the lower energy state than those anti-parallel. An incoming photon source with frequency equal to the Larmor frequency is absorbed by atoms occupying the lower energy state, elevating them to that of the higher energy state. The photons will be re-emitted as the atoms revert back to the lower energy state. This process of absorption and re-emission of photons of the same energy (resonance) from the nucleus is where the term NMR originated. The Larmor frequency, and hence the energy of the photon emitted, will depend on the type of atom and its surrounding molecular bonds, but is often in the radio wave range (see Fig. 1.3). Therefore, materials can be characterized by the energy and intensity of emitted photons. This led to the development of MRI to differentiate materials made of different atoms and molecular structure with non-zero spin states. Soft tissues have similar x-ray attenuation properties, which provides only weak contrast in CT, but they have an abundance of ^{1}H, whose density is dependent on the type of soft tissue, making MRI ideal for providing strong contrast of soft tissue (Bushberg et al., 2012, sec. 1.2).

A 3D MRI image is constructed by applying external magnetic field gradients in three dimensions to determine the origins of the emitted photons. Ventilation measurements have been performed by calibrating the MRI signal to the volume of air in the lungs (Mahieu-Caputo et al.,

2001; Bauman et al., 2009; Wild, 2009; Kyriazis et al., 2012). However, MRI of the lungs is highly challenging. H^1 density in the lung airspaces is low and when imaging at high spatial resolution, each voxel has very few H^1 to emit a signal. Hyperpolarized ^{3}He is often inhaled to increase the MRI signal, which can reduce the acquisition time to 80 ms (Kyriazis et al., 2012). The quality of the reconstructed image suffers from inhomogeneity of the externally applied magnetic field gradients and magnetic moment-induced internal magnetic field gradients (Hashemi et al., 2012; Poustchi-Amin et al., 2013). The former limits the spatial resolution achievable to ~1 mm (Mahieu-Caputo et al., 2001; Uecker et al., 2010; Kyriazis et al., 2012). The latter is a major problem for lung imaging as there are many air-tissue interfaces. Air and tissue have different magnetic moments, consequently the internal magnetic field induced between them is different. This creates a local magnetic field gradient across their interface that distorts the externally applied magnetic field gradients. This results in artefacts in the MRI due to a loss of signal and image distortion. Injection of a superparamagnetic contrast agent intravenously, which perfuses into lung tissue, can alter its magnetic moment to match that of air. This removes the local magnetic field gradients (Vignaud et al., 2005). However, MRI contrast agents in general are expensive and, moreover, MRI itself is expensive to operate. Consequently, it is not readily availability everywhere in clinics (Ginde et al., 2008; Biederer, 2009). Furthermore, patients with metallic implants such as hip replacement joints and pacemakers cannot have an MRI scan.

2.2 Volumetric Phase Contrast Lung X-ray Imaging Techniques

The latest forefront for image-based lung volumetric analysis is phase contrast x-ray (PCX) imaging. Two such techniques, that use PB-PCX and analyzer-based phase contrast x-ray (AB-PCX) imaging, are described in this section. The ability to extract V_L from PCX images, combined with the associated enhancement of tissue contrast, simultaneously provides both anatomical and physiological information of the lung at high spatial resolution. PCX imaging can also be done in real-time, which allows subtle changes in lung function to be studied. While PCX imaging only provides volumetric information in 2D, whereas some of the other volumetric techniques that were described in the previous section achieve this in 3D, it has superior spatial and temporal resolution over those techniques. Moreover, lung volumetric information in 2D can still help towards understanding lung behavior and possibly serve as a complementary diagnostic tool for lung diseases.

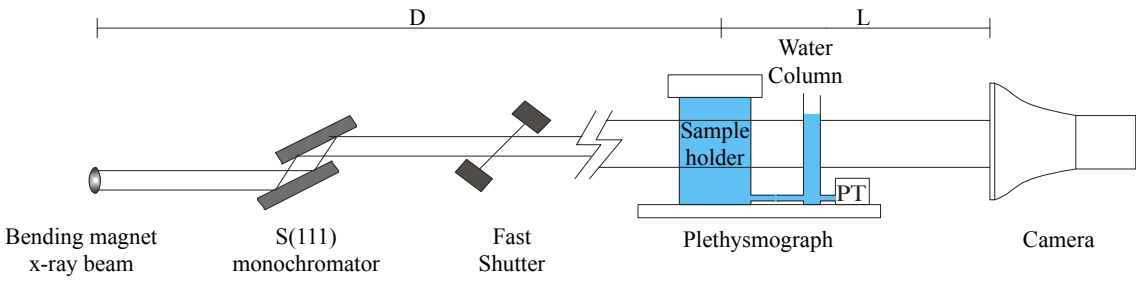

Figure 2.3: The PB-PCX imaging setup for acquiring chest images at L m from the object. The distance from the x-ray source to the sample is denoted by D. Note that the water column is not within the path of the x-ray beam and PT=pressure transducer (Leong et al., 2013a).

2.2.1 PB-PCX imaging-based Volumetric Technique

A technique for measuring changes in V_L using PB-PCX chest images was developed by Kitchen et al. (2008). By adapting the PB-PCX imaging setup, the subject is placed in a tightly sealed water-filled polymethyl methacrylate (PMMA) sample holder as shown in Fig. 2.3. Since soft tissue shares approximately the same complex refractive index as water in the diagnostic x-ray range (10-150 keV), there are effectively three types of materials present within the sample holder: water, bone and PMMA. Air is not counted as a material since x-rays in that energy range only interact weakly with air. During breathing the lungs inflate with air, pushing water out of the sample holder and into the water column, and vice versa upon deflation. By restricting the imaging region-of-interest (ROI) to the sample holder containing the chest, the total change in volume enclosed within the sample holder over time (ΔV_{AB}) can be calculated from between two $N \times M$ pixel sized PB-PCX images of that ROI, in image A and image B:

$$\Delta V_{AB} = \sum_{i}^{N} \sum_{j}^{M} (\Delta x)^2 [T_A(i\Delta x, j\Delta x) - T_B(i\Delta x, j\Delta x)], \tag{2.7}$$

where Δx is the pixel size and T is the total projected thickness of all three materials within the sample holder at each pixel location $(i\Delta x, j\Delta x)$. If the ROI enclosed is sufficiently large to include the entire chest in both images, ΔV_{AB} would equal the volume of water displaced as the volume of bone and PMMA remain constant between images and consequently cancel out. Since the volume of water displaced is equal to the volume of air entering the lungs, $-\Delta V_{AB}$ is equal to the change in V_L.

To calculate ΔV_{AB}, T can be determined using the single image phase retrieval algorithm (SIPRA) given in Eq. 1.60. However, it assumes a single material, which is not the case for the chest that is comprised of water and bone. Kitchen et al. (2008) assumed that the chest was made

of water only and therefore the input parameters for SIPRA, δ and μ, were substituted in for water. Beltran et al. (2010) showed that for such a case the projected thickness image of water is correctly reconstructed while that of bone is not, particularly along the interface where the phase-induced fringes are not properly smoothed out. Despite this, Kitchen et al. (2008) demonstrated that the degree of error in the reconstructed projected thickness image of the bone is approximately constant between recorded chest images of an aerating lung. Therefore, by having a sufficiently large detector ROI such that ROI A and B enclose the same volume of bone, ΔV_{AB} is largely that of water. By ensuring this condition is satisfied, Kitchen et al. (2008) showed V_L as small as 25 μL could be accurately measured by comparing it to a plethysmograph[2] attached to the sample holder (see Fig. 2.3). Herein lies the major limitation to this technique, namely that the minimum area of the detector ROI from which the change in V_L can be accurately calculated is limited by the degree of bone motion. Whilst breathing, the bony rib cage can move out of and into the detector ROI. Thus, only from relatively large areas of the lungs does the bone volume remain constant within the ROI. The work presented in chapter 3 addresses this issue.

2.2.2 AB-PCX imaging-based Volumetric Technique

From AB-PCX imaging, three separate images containing attenuation, refraction angle (defined in Eq. 1.36), and ultra small angle x-ray scattering (USAXS) information of the object can be recovered (Hu et al., 2009; Yang et al., 2014). USAXS will dominate in small structured objects that have many large phase gradients within the object. Larger structured objects produce slowly varying phase gradients, for which these are encoded in the refraction angle map. The exit surface phase can be retrieved from the refraction angle map of the object using Eq. 1.36. Together with the attenuation map, Eqs. 1.35a and 1.35b can be used to solve for T of an object made of up to two different materials, provided the projection approximation is valid. For the chest, this means T can be calculated for bone and water/soft tissue (remember that water and soft tissue have similar complex refractive indices). By immersing the chest in a water bath, the projected thickness of water/soft tissue can be calculated for two images, from which the change in V_L between them can be calculated using Eq. 2.7. The advantage of this technique over the PB-PCX imaging-based volumetric technique, described in section 2.2.1, is that the separation of bone and water allows the minimum region of interest, over which the change in V_L can be accurately measured, to be equal

[2]The plethysmograph utilized for that study was water-based. During respiration, the flow of air forces water in and out of the water column, which are proportional to the pressure changes in the water column. These pressure changes, measured using a pressure transducer, can be calibrated to measure V_L by injecting known volumes of water into the water column.

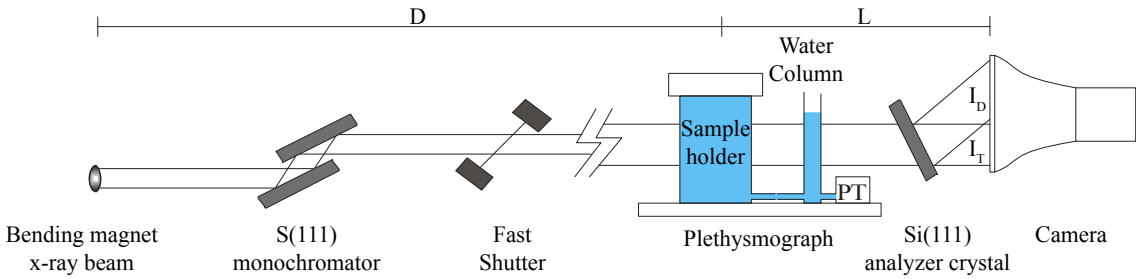

Figure 2.4: The AB-PCX imaging setup is almost identical to that of the PB-PCX setup displayed in Fig. 2.3 but an analyzer (Laue) crystal is placed between the sample and camera to split the x-ray beam and acquire diffraction (I_D) and transmitted (I_T) images.

to the detector spatial resolution.

Two common methods of simultaneously recovering the attenuation, refraction angle and USAXS information are: multiple image radiography (MIR) (Wernick et al., 2003) and Laue dual-image phase retrieval (LDIPR) (Kitchen et al., 2011). MIR records the rocking curve at each pixel of the detector with and without the sample present by rotating the analyzer over several micron-radians about the Bragg peak. The attenuation and refraction angle can be extracted from the decrease in area and shift in the position of the rocking curve, respectively, while deconvolving the object rocking curve with the intrinsic rocking curve (without object) recovers the USAXS information. The lengthy time required to record the object rocking curve makes it unsuitable for dynamic imaging. Conversely, LDIPR requires multiple exposures to record the intrinsic rocking curve but only a single exposure of the object to extract all three images (i.e. attenuation, refraction and USAXS). From this single exposure, the x-ray beam traverses the object and is split in two by a Laue crystal to form a diffracted and transmitted beam. The diffracted and transmitted beam arise from the x-ray beam that reflected from one of the Bragg planes and propagated straight through the Laue crystal, respectively (Fig. 2.4).

While image acquisition time is significantly lessened in LDIPR in comparison to MIR, post-image processing is more arduous as LDIPR is a semi-iterative process. By having only two images, that of the diffracted and transmitted intensity, to recover three lots of information (attenuation, refraction angle and USAXS), the USAXS information is first iteratively determined to allow the other two be analytically solved. *A priori* knowledge of the USAXS strength as a function of the projected scatterer thickness (scatterer refers to the small structured objects with large phase gradients) is required to initiate the iterative algorithm. Thereafter, the iterative process may take on the order of hours to converge to within a set limit of a cost function. LDIPR is also prone to

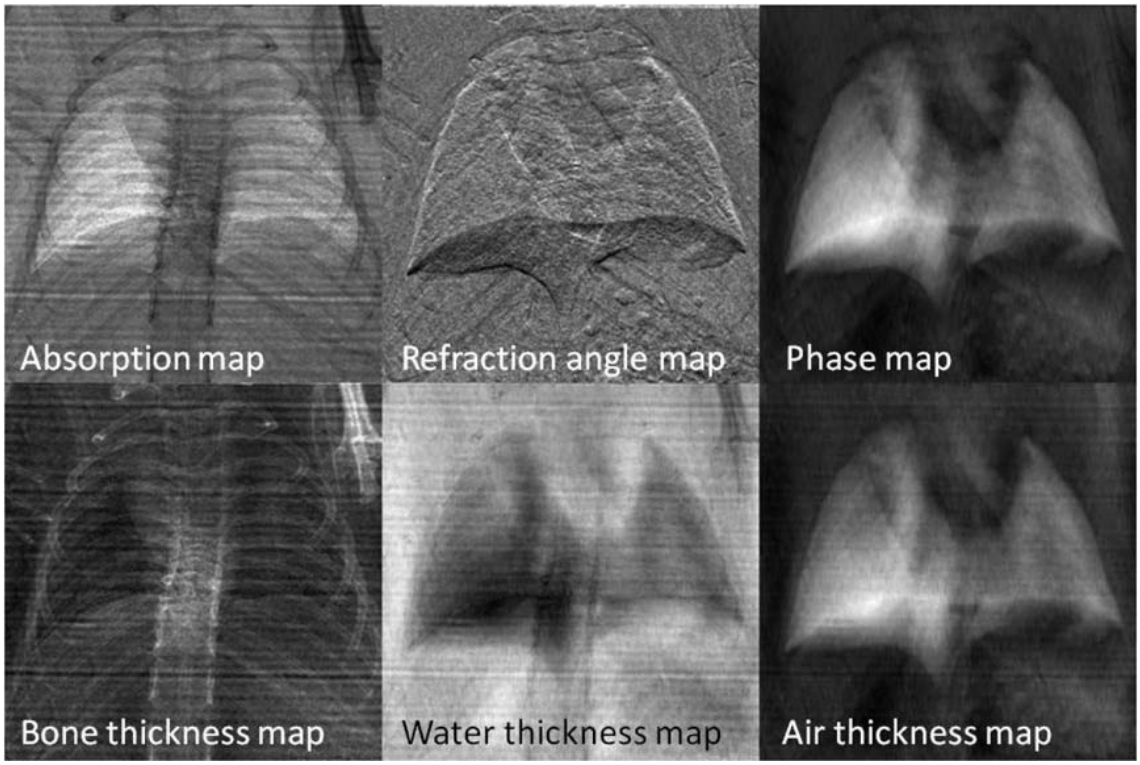

Figure 2.5: Montage of 16.2×14.4 mm^2 chest images consisting of the recovered information possible using LDIPR (Kitchen et al., 2011).

low frequency noise because of integrating the refraction angle map to recover the phase map[3]. Calculated projected thickness maps may then contain low frequency artefacts and consequently erroneous V_L values. Figure 2.5 shows a montage of images recorded and determined using LDIPR. The low frequency trends from integrating the refraction angle map have been removed by applying a high pass filter[4].

2.3 Concluding Remarks

In this chapter, clinically available imaging-based methods for measuring lung air volumes were surveyed, namely scintigraphy, CT, SPECT, PET and MRI. The latter four can measure ventilation by recording multiple sets of projection images to reconstruct multiple tomographs in a single breath. This is challenging to achieve with high spatial resolution. One way of overcoming this challenge is by inhaling a contrast agent and reconstruct only one tomograph per breath. The

[3]Integration in real space is equivalent in Fourier space to dividing the function by the spatial frequency. That is, for a 1D function $G(x)$, $\mathcal{F}\left\{\int G(x)\mathrm{d}x\right\} = \frac{\mathcal{F}\{G(x)\}}{i2\pi k_x}$ (Kumar, 2013). It can be seen then that any low frequency noise present in $G(x)\}$ will be significantly increased.

[4]A high pass filter is a function multiplied in Fourier space by a function designed to attenuate amplitudes at lower frequencies and to leave untouched those at higher frequencies.

change in concentration of the contrast agent over multiple breaths can be related to ventilation. However, this represents the average ventilation over an entire breathing cycle. Much information is left unknown about the high temporal variation in ventilation during a single breath. Scintigraphy records only single projections and therefore offers better temporal resolution than SPECT at the cost of only providing regional ventilation maps in 2D. Regardless, nuclear lung imaging techniques in general have inferior spatial and temporal resolution compared to CT and are more suited to studying uptake of pharmaceutical drugs. All of these imaging-based methods, except MRI, require the use of contrast agents and radioactive tracers but are expensive and hazardous to human health. While MRI does not involve any radioactive contrast agents, it does suffer from image artifacts.

PCX imaging-based volumetric techniques have the potential to offer a safer and/or more effective alternative than the clinically available imaging-based techniques. They do not require any contrast agents, making them cheap, and impart low radiation dose by utilizing relatively higher energy x-rays since strong phase contrast can still be maintained (Zhou and Brahme, 2008). Two PCX imaging-based techniques were described that measure lung volumes directly from x-ray phase contrast signals. With the phase contrast signal being much stronger than that given by other imaging modalities, it enables shorter exposures times while still being sensitive to small volumetric changes. However, in the PB-PCX imaging-based volumetric technique, the size of the region over which V_L can be accurately measured is limited by the movement of bone. While the AB-PCX imaging-based volumetric technique can measure V_L over a single pixel, the post-processing time is long and prone to artefacts. The original research presented in chapters 3 and 4 shows two new techniques that were developed specifically to overcome these limitations.

3 High Spatiotemporal Resolution Measurement of Regional Lung Air Volumes from PB-PCX Images

In the previous chapter a technique developed by Kitchen et al. (2008) was introduced for performing regional volumetric measurements of lung aeration. This was a huge improvement from current clinical lung imaging-based volumetric techniques with respect to the high temporal resolution and low radiation dose, allowing ventilation to be studied in real-time while simultaneously rendering a highly detailed image of the chest. However, the differential movement of the bones making up the thoracic cage with respect to the lung tissue limited the minimum region-of-interest (ROI) size from which lung air volume (V_L) could be accurately measured. This problem is elaborated upon in section 3.1.

In this chapter, a method is presented to counteract the movement of the thoracic cage through segmentation of the image of the lungs from that of the bony structures. This is achieved by capturing an image of the thorax with fluid-filled (non-aerated) lungs, then aligning and subtracting the bony structures from images of the subsequently air-filled thorax. Section 3.2 defines and explains image alignment and surveys common methods applied on medical images. Section 3.2.4 presents the testing of different image alignment methods to determine which is most suitable for aligning the bony anatomy of the thoracic cage between propagation-based phase contrast x-ray (PB-PCX) chest images. Based on the findings, two approaches to aligning the thoracic cage were developed and tested on images of newborn rabbit kittens, the outcomes of which are presented in sections 3.3 and 3.4. This chapter expands on the work published in *Medical Physics* (Leong et al., 2013a).

3.1 Importance of Bone Segmentation

When measuring changes in V_L utilizing the technique developed by Kitchen et al. (2008), segmentation of bone is important for accurate measures of regional V_L. Consider the panel of

images in Fig. 3.1. The spherical object can be considered a pocket of air within lung tissue and the rectangular object as a piece of bone. The PB-PCX images were produced by generating a 1000×1000 pixel projected thickness map of the objects, from which their exit surface wavefields were computed using the projection approximation (section 1.6). Then, their wavefields were numerically propagated (described in section 1.9) forward by 3 m with the pixel size set to 4.05 μm. The μ and δ values assigned for bone were $\mu_b = 461.1\ \mathrm{m}^{-1}$ and $\delta_b = 7.145 \times 10^{-7}$. For lung tissue, $\mu_w = 13.983\ \mathrm{m}^{-1}$ and $\delta_w = 3.99 \times 10^{-7}$. These values were calculated from the National Institute of Standards and Technology (NIST) database corresponding to a 24 keV source (NIST, 2014).

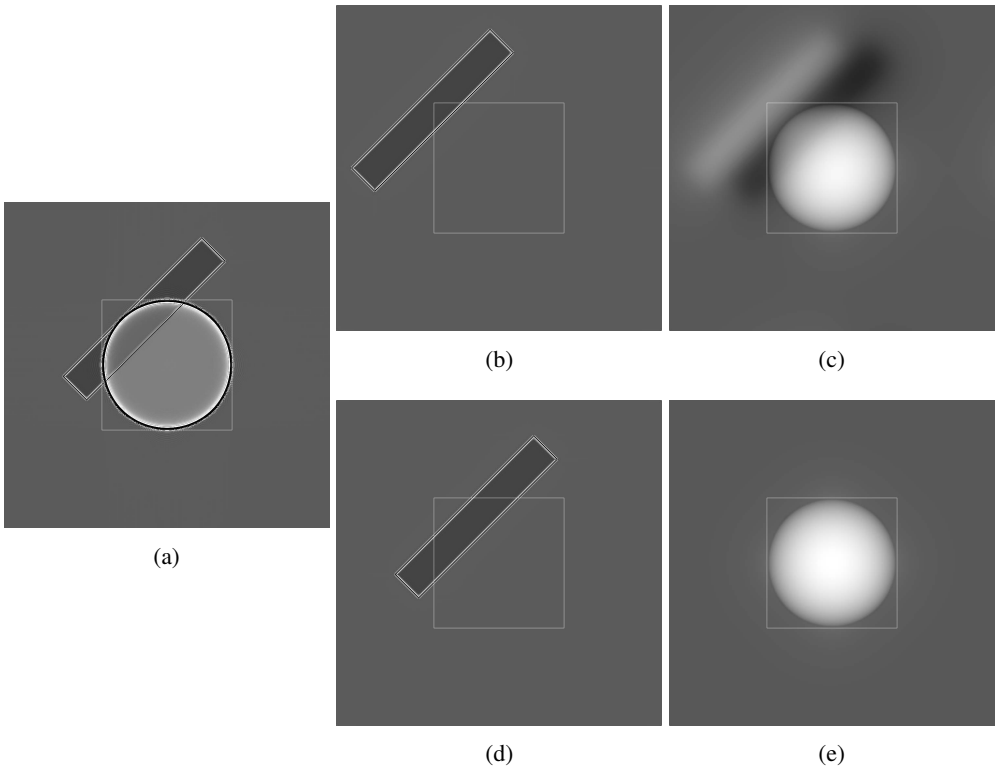

Figure 3.1: Simulated images to demonstrate the necessity of segmenting bone for measuring regional lung air volumes. (a) A PB-PCX image enclosing two objects, namely a hollow sphere (simulating an air bubble) and a cuboid (simulating bone tissue), projected onto one another and immersed in water. In (b) and (d) the PB-PCX image of only the bone (i.e. with no air bubble) is respectively misaligned and aligned with that in (a). Each image underwent phase retrieval using SIPRA and subtraction was performed of their projected thickness between (a) and (b) and (a) and (d) to yield the change in projected thickness at each pixel. These results are shown in (c) and (e), respectively. The change in air volume due to the sphere was calculated from these subtracted images using the entire field-of-view and using just the small ROI within the white border to demonstrate the need for image alignment for regional volume measurements.

To measure the change in V_L, the total projected thickness (T_{tot}) of the sample, which is assumed to comprise of water only, is calculated at each pixel denoted by the indices i, j over the $N \times M$ pixel size image using the single image phase retrieval algorithm (SIPRA). Since the chest

is a two-material sample, bone (T_b) and water (T_w), SIPRA returns:

$$T^*_{tot} = \sum_i^N \sum_j^M T_w + \frac{\mu_b}{\mu_w} \sum_i^N \sum_j^M T^*_b. \tag{3.1}$$

The symbol * indicates that the projected thickness returned by SIPRA is blurred due to assuming a water only object (Beltran et al., 2010).

Consider an image, as shown in Fig. 3.1(b), containing only the bone displaced relative to that in Fig. 3.1(a) towards the top right corner of the image. This is to mimic what occurs during respiration. Directly subtracting Fig. 3.1(a) from Fig. 3.1(b) after performing SIPRA (again assuming the sample is comprised of water only) shows the bones do not perfectly align as shown in Fig. 3.1(c). If the field-of-view (FOV) is sufficiently large, for example the FOV being the entire image, to encompass both the bone and alveoli, then the total change in the projected thickness (ΔT_{tot}) is:

$$\Delta T_{tot} = \Delta T_w = -\Delta T_{air}, \tag{3.2}$$

since the total thickness of bone and their degree of blurring remains approximately constant between images. The volume of the sphere was calculated, using Eq. 2.7, as 2.218 µl in comparison to the known volume of 2.226 µl. This demonstrates that the technique developed by Kitchen et al. (2008) is accurate in measuring the total change in V_L without needing to align the bones when the FOV is sufficiently large. The slight discrepancy of just < 1% (8 nL) is likely attributed to the slight difference in the degree of smoothing of the bone between the images. That is, $\Delta T^*_{air} \simeq \Delta T_{air}$. When the FOV was restricted to a smaller region, as shown by the white border in Fig. 3.1, the volume of bone within the smaller region in Figs. 3.1(a) and 3.1(b) is different. ΔT_{tot} then becomes:

$$\Delta T^*_{tot} = \Delta T_w + \tau \left[\frac{\mu_b}{\mu_w} \Delta T^*_b \right] \neq -\Delta T_{air}, \tag{3.3}$$

where $0 \leq \tau \leq 1$ is the fraction of bone not removed after subtraction. The change in regional water volume calculated between Figs. 3.1(a) and 3.1(b) gave an air volume of just 1.688 µl; approximately a 32% error. If the bones were aligned prior to subtraction (Fig. 3.1(d)), their contribution can be canceled out when the projected thickness maps are subtracted, as shown in Fig. 3.1(e). The calculated V_L then was 2.186 µl; approximately only a 2% error (32 nL). Ergo, this demonstrates the importance of aligning the bones to segment them from the lungs in order to accurately measure V_L locally utilizing the technique developed by Kitchen et al. (2008). In the

next section, an overview of image alignment is introduced and different alignment techniques are explored for possible alignment of the bony anatomy of the thoracic cage from PB-PCX images.

3.2 Image Alignment

The process of aligning images begins with identifying matching features (image registration) and transforming the images (image transformation) to align those features. There are many scenarios where image alignment or just image registration is important in medical imaging. For patients with a cancerous lung nodule, alignment of chest images recorded before and after treatment is important in accurately tracking the position and comparing the size of the nodule (Crum et al., 2004). Radiation therapy involves irradiating cancerous tissue with x-rays. During treatment, breathing and other movements made by the patient displaces the cancerous tissue from its initial position. Tracking its motion using image registration can guide the x-ray beam during treatment (Gao et al., 2006). Images of different modalities are also often aligned. For example, positron emission tomography (PET) images depicting a physiological event are aligned to computed tomography (CT) images to put it into anatomical context. These are just some of the many examples of when image alignment is needed.

The aim of this section is not to give a detailed account of all the possible image alignment techniques but to provide an overview of the general problems and approaches associated with aligning chest images. This section is divided into introducing the mathematical overview of image alignment, then discussing image registration and transformation in the context of lung imaging.

3.2.1 Mathematical Notation, Definition and Terminology

While there are a plethora of image alignment techniques, there are four fundamental factors to consider when aligning images:

1. The features to be matched.
2. The algorithm that best matches these features.
3. The method that most accurately transforms the image to align those features.
4. The method of evaluation that best gauges the accuracy of the alignment.

These fundamental factors are affected by the type of images being matched (i.e. two-dimensional (2D) or three-dimensional (3D)), the image modality used (CT, magnetic resonance imaging (MRI),

PET, radiography, PCX imaging) and whether the images being aligned are of the same (intramodal) or different (intermodal) modalities. In the remainder of this section, the mathematical notations will be introduced for aligning 2D images, since the images aligned in this thesis are 2D only.

Let two images be defined by image A and image B, where $\{\mathbf{A}_i\} \in \mathbf{r}_\perp$ are the set of coordinates (control points) relating to M features in image A and $\{\mathbf{B}_i\} \in \mathbf{r}'_\perp$ be a set of coordinates found in image B corresponding to the same features as in image A, both in Euclidean space where $i \in 1, 2...M$. Here, the objective is to align image B to image A. A number of image registration methods have been developed in determining pairs of control points between image A and image B. They can be categorized into feature- and intensity-based image registrations, both are which the topics of interest in the next subsections. The main difference is that the former uses higher level features such as lines and corners whereas the latter uses pixel intensity directly for matching purposes.

After performing image registration to determine the pairs of control points, the next step is to decide the transformation function $\widehat{T}$ to fit to the control points in order to map the coordinates from image B to image A. That is:

$$\widehat{T} : \mathbf{r}'_\perp \mapsto \mathbf{r}_\perp \iff \widehat{T}(\mathbf{r}'_\perp) = \mathbf{r}_\perp. \tag{3.4}$$

Note that $\widehat{T}$ maps the coordinates, and not the intensity, of image B to image A. That is, it does not make image B look like image A by giving a position in the transformed image B, which is denoted $B^{\widehat{T}}(\mathbf{r}_\perp)$, the same intensity as $A(\mathbf{r}_\perp)$. Instead, $\widehat{F}$ is designated to be the function that maps the intensity values between the two images. If the two images are taken from the same modality, then $\widehat{F}$ will be an identity function (i.e. $\widehat{F}[B^{\widehat{T}}(\mathbf{r}_\perp)] = B^{\widehat{T}}(\mathbf{r}_\perp)$).

The ideal transformation model to use depends on the complexity of the coordinate mapping between the two images. These can range from: the simple rigid-body transformation (rotation, reflection and translation); the slightly more general affine transforms (scaling, homothety, similarity transformation, shear mapping in addition to the rigid body transformation); to the more sophisticated non-rigid transformation (examples of which include multi-resolution multi-quadric elastic transformation (Zhang, 2006; Bentoutou et al., 2007)).

The final process of image alignment is evaluating how accurately image A and image $B^{\widehat{T}}$ overlap. In medical imaging, a gold standard technique is often used that is believed to be the best in the particular application area or for the given image type. For the removal of bones in the chest, dual-energy subtraction (DES) is considered the most accurate. It takes the recording of two images at different x-ray energies and exploits the energy dependence of the attenuation coefficient

of constituent materials to separate bone and lung tissue (Ishigaki et al., 1986; Carnibella et al., 2012a). However, DES has yet to be successfully used in dynamic PB-PCX imaging. Without a gold standard technique, accuracy of alignment must instead be performed by visually assessing the subtracted images of image A and image $B^{\widehat{T}}$ to detect the degree of structural artefacts. Although this approach is subjective, it is easy to visually determine when the image alignment has not worked satisfactorily, particularly when using edge-enhanced PB-PCX images.

3.2.2 Image Registration

Image registration can be generalized into two broad approaches: feature- and area-based image registration. The former involves identifying and matching higher order features such as shapes and lines, while the latter is based on pixel intensities. These two approaches are elaborated in section 3.2.2.1 and 3.2.2.2.

3.2.2.1 Feature-based Image Registration

Feature-based image registration utilizes salient and unique features that are found consistently between images to help serve as control points and align the images accurately. In some applications of medical imaging there are clearly defined features that can easily be identified visually. These distinct features can either originate extrinsically (i.e. external markers attached to the patient) or intrinsically (i.e. belonging to the patient). An example of the former is the use of a stereotactic frame screwed onto the patient's skull to align CT, PET and MRI images of the brain (Karger et al., 2003). Alternatively, skin attached markers present a less invasive procedure; however, it carries a greater risk of misregistration caused by the skin moving independently to the head between image acquisitions (Grunert et al., 1998). Extrinsic markers are also used in image guided surgery and radiation therapy to track the movement of tumors (Lunsford et al., 1990; West et al., 1997; DiMaio et al., 2010). For the latter, the success of matching features originating from within the patient depends on the signal strength of those features. The types of intrinsic features that provide strong signals in the human body vary from corners, lines or curves of the bones, to blood vessels, nerves, and brain tissue (Hill et al., 1991; Xie et al., 2009).

In aligning the bony anatomy of the chest from images, extrinsic markers cannot be placed on the chest skin as it moves independently to the bones and inserting markers on the bones is highly invasive. Alternatively, the bones are highly visible in some parts of a chest radiograph. An automated algorithm can then be utilized to delineate and outline the shape of the ribs. One of the earliest works on rib detection was reported by Toriwaki et al. (1973). Their software system was

able to automatically identify the ribs as well as that of other structures including the heart and thorax only after the position of the ribs were marked by the user. However, it broke down where the signal strength along the edges of the ribs were weak, such as the ventral ribs and those ribs that were poorly calcified. There the signal of the ribs is obscured by image noise, geometrical distortions introduced by the detector system and overlapping structures such as the diaphragm, tumors and lung lesions. Moreover, the need to manually identify the rib positions to initiate the software system is time consuming.

Numerous researchers have since worked to expand and improve upon the work of Toriwaki et al. (1973). Most rib segmentation algorithms developed so far are quite elaborate but do share a common framework. They begin with some form of image processing. For example, they typically employ Fourier filtering to suppress lower frequency components and enhance the edges of bone, or take the logarithm of the image to expand the lower valued intensities over a wider range of intensity bins (Wechsler and Fu, 1978). This step is followed by applying edge detector operators such as the Laplacian and Sobel operators to detect bone edges (Toriwaki et al., 1973; Persson, 1976; Wechsler and Fu, 1978; Staal et al., 2007). These edges are filtered to retain those that make up part of the bone from those associated with other structures. However, those edges retained often do not make up the entire bony anatomy of the chest, leaving many gaps where edges of the bone have not been detected. These gaps are filled by imposing separate models on the ribs and vertebral column. Examples of such models that have been tried include the parabolic function fitted using the Hough transform and deformable models such as spline fitting (Wechsler and Fu, 1978; Yue et al., 1995; Zagorchev et al., 2007).

Despite the improvement made on the work of Toriwaki et al. (1973) there has yet to be a truly robust automatic algorithm for detecting the rib borders, particularly for the top and bottom ribs where they are poorly defined in chest radiographs. The algorithm developed by Plourde et al. (2006) is considered to be the most proficient to date. This involves the user identifying four points on each rib; these are used as starting points in a rib detection algorithm that outlines the boundaries of the rib. However, given that it is a semi-automatic approach, it may become laborious when multiple images are analyzed, particularly for dynamic imaging sequences. In light of the frailty and susceptibility of these algorithms against noise and overlapping structures, feature-based image registration may fail in aligning PB-PCX chest images. Although PB-PCX imaging can boost the bone signal, these are also masked by the increased signal of the lungs. In section 3.4, an image alignment method that uses feature-based image registration is developed and tested on aligning the bones of PB-PCX chest images of newborn rabbit kittens.

3.2.2.2 Area-based Image Registration

Area-based image registration involves calculating the degree of similarity between two images directly from their pixel values (or voxel values when using 3D images). The algorithm used to match the features is known as a similarity measure. Small regions of predetermined size in image B are selected and scanned through areas of predefined size in image A to find its closest match. Herein, the small regions in image B are named kernels, which are equal or smaller in size than areas in image A that are termed search areas.

For complex transformations, a main trade-off for area-based image registration is between kernel size and alignment accuracy. This is illustrated in Fig. 3.2 for registering images of the thoracic cage. A decrease in kernel size allows complex transformations to be more accurately mapped, with the downside of reducing the amount of structural information that it holds. Consequently, there is a high probability that the kernel will enclose a non-unique area and subsequently will likely match with multiple regions within the search area. Conversely, increasing the kernel size would elevate its uniqueness to allow a higher chance of a significant match, but loses information on local transformation. Kernels can translate within the search area while also rotating and scaling its size to find its closest matching feature. However, these multiple degrees of freedom require very long computation time and would increase the risk of misregistration. For aligning the chest, it is usually sufficient to translate the kernels only to find its corresponding matching feature in the search area. As will be shown later in section 3.3, this is adequate to produce accurate alignments of chest images.

The following sections will cover three similarity measures: (i) sum of squared differences (SSD); (ii) cross correlation (CC) and; (iii) mutual information (MI). These are by no means the complete repertoire of techniques. For a complete review of intensity-based image registration techniques, please refer to Hill et al. (2001) and Zitová and Jan (2003), as starting points.

Sum of Squared Differences

One of the simplest similarity measures is the SSD between the kernel B' of image B and the search area A' of image A. For N pixels in the region of overlap between A' and B' (or domain $\Omega_{A',B'}$),

$$SSD(\mathbf{r}'_{\perp}) = \frac{1}{N} \sum_{\mathbf{r}_{\perp} \in \Omega_{A',B'}} |A'(\mathbf{r}_{\perp}) - B'(\mathbf{r}_{\perp} - \mathbf{r}'_{\perp})|^2. \tag{3.5}$$

With the center of A' and B' both located at the origin $\mathbf{r}_{\perp} = (0, 0)$, the SSD is computed within the overlapping region of A' and B' as B' is translated across A' by displacement vector $\mathbf{r}'_{\perp}$ pixels.

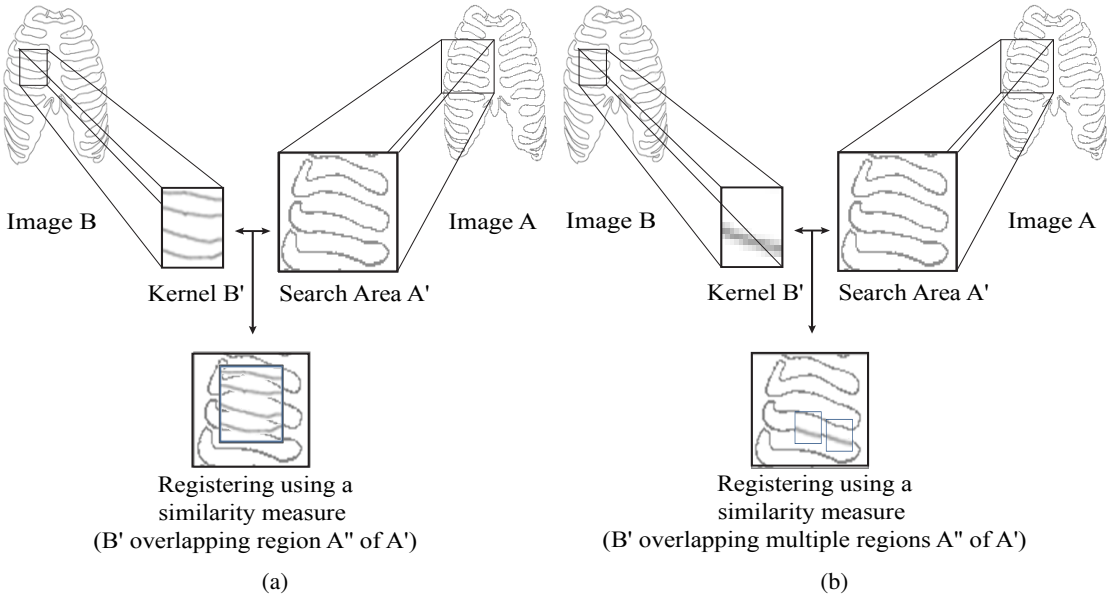

Figure 3.2: Drawbacks of area-based image registration. In these chest images, the bones have undertaken a highly localized expansion transformation. In this situation (a) shows the difficulties in attempting to perfectly match a kernel in image B within a search area in image A, by translating the kernel only, due to localized movements of the ribs within the kernel. (b) To overcome the difficulty in (a), the kernel size is reduced. This is traded-off by the loss of structural detail resulting in multiple regions with which the kernel could be registered.

The vector $\mathbf{r}'_{\perp}$ where SSD is minimized represents the coordinate with respect to the origin in A' where it best matches to B' as the total difference between their intensities within $\Omega_{A',B'}$ is smallest. The pair of control points recorded would then be the coordinate of B' in image B and that of A' in image A plus the vector $\mathbf{r}'_{\perp}$ where SSD is minimized. Due to the presence of the squared term in Eq. 3.5, differences in pixel intensities between the images due to noise are over-represented and can exaggerate the total difference; instead, the squared term can be removed. Consequently, this similarity measure becomes the sum of absolute differences (SAD). Both SSD and SAD are simple to implement, but for registering inter-modal images, they are not ideal as it intrinsically assumes the intensity values between image A and image B are proportional to one another. That is, it assumes $\widehat{F}$ is an identity function and is therefore only applicable to registering intramodal images (see section 3.2.1). SAD has been chosen as one of the similarity measures to be tested on illustrated chest images shown in section 3.2.4.

Cross-Correlation

CC is commonly used in medical image registration for its superior processing time and insensitivity to noise. With the same definitions of the parameters introduced for SSD, the normalized CC (*NCC*) is defined as (Kano et al., 1994):

$$NCC(\mathbf{r}'_\perp) = \frac{1}{N} \sum_{\mathbf{r}_\perp \in \Omega_{A',B'}} \frac{[A(\mathbf{r}_\perp) - \overline{A'}][B'(\mathbf{r}_\perp - \mathbf{r}'_\perp) - \overline{B'}]}{\sigma_{A'}\sigma_{B'}}, \tag{3.6}$$

where

$$\overline{A'} = \frac{1}{N} \sum_{\mathbf{r}_\perp \in \Omega_{A',B'}} A'(\mathbf{r}_\perp), \tag{3.7}$$

$$\overline{B'} = \frac{1}{N} \sum_{\mathbf{r}_\perp \in \Omega_{A',B'}} B'(\mathbf{r}_\perp - \mathbf{r}'_\perp), \tag{3.8}$$

$$\sigma_{A'} = \frac{1}{N} \sum_{\mathbf{r}_\perp \in \Omega_{A',B'}} [A'(\mathbf{r}_\perp) - \overline{A'}], \tag{3.9}$$

and

$$\sigma_{B'} = \frac{1}{N} \sum_{\mathbf{r}_\perp \in \Omega_{A',B'}} [B'(\mathbf{r}_\perp - \mathbf{r}'_\perp) - \overline{B'}]. \tag{3.10}$$

Both A' and B' are subtracted from the mean value within $\Omega_{A',B'}$ of A' and B', denoted $\overline{A'}$ and $\overline{B'}$ to respectively suppress differences in background intensity values, and are subsequently cross-correlated (i.e. summing the products of their intensities). The correlation value is normalized through dividing both by the total number of pixels, N, in $\Omega_{A',B'}$ and the standard deviations, $\sigma_{A'}$ and $\sigma_{B'}$, of A' and B', respectively. The NCC varies from -1 to 1, with 1 representing perfect and 0 completely imperfect match, while <0 represents anti-correlation within $\Omega_{A',B'}$ of A' and B'.

Normalizing the correlation value by $\sigma_{A'}\sigma_{B'}$ is important in making it less susceptible to matching regions simply because they have large intensities. For example, consider a kernel enclosing a unique feature and the corresponding exact same feature in the search area situated at some coordinate. Elsewhere, suppose there is a region with a large intensity spike. The correlation value will form a stronger match to the large intensity spike rather than the feature as the sum of the product of their intensities is greater. However, since the standard deviation of A' containing the intensity spike is significantly higher than that of the region containing the feature, dividing by $\sigma_{A'}$ will reduce the correlation value at the spike and make the kernel match to the feature.

Direct computation of the NCC using Eq. 3.6 is computationally more expensive than SAD (Mori and Kashino, 2010), but the unnormalized CC ($CC = \sigma_{A'}\sigma_{B'}NCC$) can be computed in Fourier space via the convolution theorem:

$$CC(\mathbf{r}'_\perp) = \mathcal{F}^{-1}\left[\mathcal{F}\left\{A'(\mathbf{r}_\perp) - \overline{A'}\right\} \times \mathcal{F}^*\left\{B'(\mathbf{r}_\perp) - \overline{B'}\right\}\right], \tag{3.11}$$

where $\mathcal{F}^*$ is the complex conjugate of $\mathcal{F}$. If the size of B' is not equal to that of A', then B' is zero-padded. Equation 3.11 allows the high numerical computational efficiency of the Fast Fourier transform to be exploited. There is no simple frequency domain expression to incorporate $\sigma_{A'}\sigma_{B'}$ into Eq. 3.11 and calculate NCC. Lewis (1995) developed a fast NCC by pre-computing $\sigma_{A'}\sigma_{B'}$ and applying it to each correlation value calculated using Eq. 3.11. However, since large intensity spikes present in chest images are predominantly attenuation-induced, a method is developed in sections 3.3 and 3.4 to remove attenuation-induced regions of large intensities to offset the need to normalize against $\sigma_{A'}\sigma_{B'}$ before performing CC.

Mutual Information

The MI method is an information theoretic approach to image registration. MI falls under the field of information theory that quantifies the amount of information contained within a data set. Before explaining how this is applied to image registration, information (H) is first defined. Consider an alphabet containing s letters. A one-letter word has s possible letters, hence it contains s quanta of information. Generalizing, an n letter word has s^n quanta of information. With increasing n, the amount of information increases exponentially. However, this is unrealistic in linguistics since there are syntactic rules that specify which combination of letters are permitted. Hartley (1928) imposed a set of conditions, those being that information increases linearly with word length (i.e. $H \propto n$) and that the amount of information is equal if $s_1^{n_1}=s_2^{n_2}$, for two given words of length n_1 and n_2 containing s_1 and s_2 letters, respectively. The only function that satisfies these conditions is:

$$H = \ln s^n. \tag{3.12}$$

Equation 3.12 shows that when there is only one letter in the alphabet ($\ln 1 = 0$), no information is gained because the outcome is already known. It is also a measure of entropy, which is defined as the degree of uncertainty. The more possibilities (information) the greater the uncertainty (entropy). A restrictive condition of Eq. 3.12 is it assumes that all words have an equal occurrence probability. Shannon (1948) uplifted this restriction and expressed information as a sum of all the different possible combinations (i) of letters making up a word, with each combination having occurrence probability p_i:

$$H = -\sum_i p_i \ln p_i. \tag{3.13}$$

Equation 3.13[1] can be redefined in the context of grayscale images. The entropy H is defined

[1]Equation 3.12 can be seen as a special case of Eq. 3.13, where each possible combination of s letters making up

as the amount of information each image contains where $p(i)$ is the probability distribution of their grayscale values (i), which can be approximated by computing their image histogram and dividing by the total number of pixels. The joint entropy is also introduced, where $p(i, j)$ is defined as the joint probability distribution. It represents the likelihood in which a pixel has grayscale intensity value of i in one image and that of j in the corresponding pixel in another image. This can be computed from a 2D joint histogram where two of the axes correspond to the dynamic intensity range of the two images, and the third axis is the frequency of their intensities appearing at the same pixel divided by the total number of pixels. If the images are exactly the same, that is they are perfectly aligned, then their joint histogram will form a sharp line (Fig. 3.3(a)). This indicates no new information is gained between them, hence their joint entropy (uncertainty) is minimal. Conversely, misaligned images form a scattered histogram, consequently increasing their joint entropy (Fig. 3.3(b)). With these definitions, the expression for MI is introduced for a given kernel B' and region A'' within the search area A' of image A (Viola and Wells, 1995):

$$MI(A'', B') = H(A'') + H(B') - H(A'', B'), \tag{3.14}$$

where

$$H(A'') = -\sum_i p_{A''}(i) \ln[p_{A''}(i)], \tag{3.15}$$

$$H(B') = -\sum_j p_{B'}(j) \ln[p_{B'}(j)], \tag{3.16}$$

and

$$H(A'', B') = -\sum_{i,j} p_{A''B'}(i, j) \ln[p_{A''B'}(i, j)]. \tag{3.17}$$

Here, $H(A'')$ and $H(B')$ are the entropy of regions A'' and B', respectively, and $H(A'', B')$ is their joint entropy.

Two regions are most similar when their joint entropy is minimal and consequently their MI would be maximal. Complete misregistrations may still produce small joint entropy values such as two images with uniform background. This is why the first two terms of Eq. 3.14, which are the individual entropy of the two images, are important in differentiating the registering of two images with anatomical structures from those with uniform intensity backgrounds. While in the

a n letter word have equal probability. The total number of possible combinations is s^n. Therefore, each combination have an equal probability $p = 1/s^n$. Substituting this into Eq. 3.13, $H = -\sum_i p_i \ln p_i = -\sum_i \frac{1}{s^n} \ln \frac{1}{s^n} = \ln s^n$, which gives Eq. 3.12.

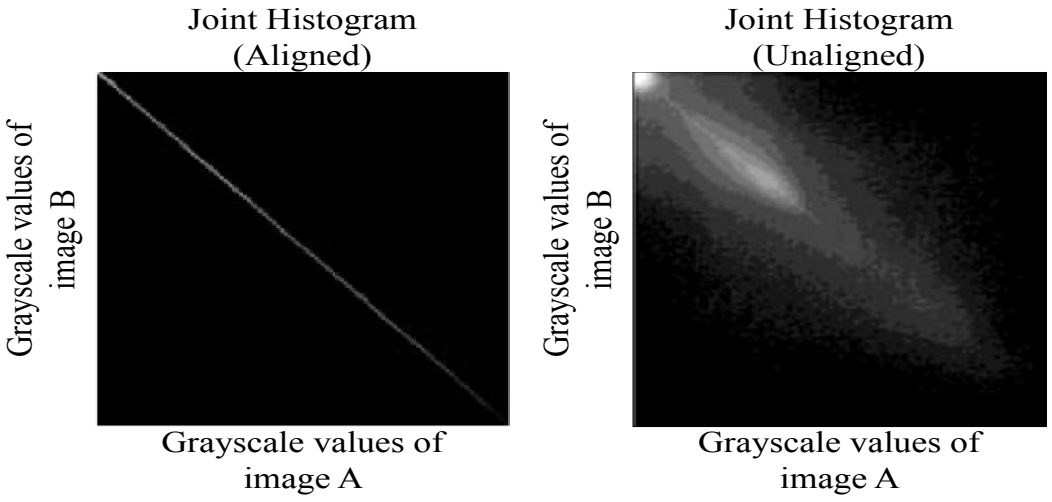

(a) (b)

Figure 3.3: Examples of 2D joint histograms showing two identical images when they are: (a) aligned and (b) misaligned when one of them is rotated by 2° (Pluim et al., 2003).

latter their joint histogram will produce a strong peak, and consequently their joint entropy value will be low, the individual entropy of the two regions are low, hence offsetting the low joint entropy and producing a low MI value.

The presence of noise in medical images causes the joint histogram of $p_{A'',B'}(i, j)$ to disperse. However, as long as the noise is approximately uniform across the image and less than the structural signal enclosed by both images, the maximal MI value will still correspond to the kernel registering with the matching structure.

The main benefit of MI is its ability for inter-modality image registration, in which the registered images would not necessarily correspond to a linear joint histogram ($p_{A'',B'}(i, j)$) but more generally a curve. When the images are not registered, a cluster of non-zero probabilities will appear around the curve. Registration by MI can, therefore, be thought of as trying to maximize the sharpness of the histogram. This is the main reason why MI is ideal for inter-modal registration as it does not assume any relationship of the intensities between the images.

3.2.3 Image Transformation

To determine the transformation function defined in Eq. 3.4, it is necessary to have some prior knowledge of the form of distortion that image B has undergone from image A. For simple transformations that include rotation and translation, the transformation can be determined through solving the Orthogonal Procrustes problem (Hurley and Cattell, 2007). This problem determines

the rotation (R) and translation (t) matrices that minimizes the residual error Σ^2, which is given by:

$$\Sigma^2 = \sum_{\mathbf{r}_\perp \in \Omega_{A,B}} \|\mathbf{B}_\mathrm{i} - (R\mathbf{A}_\mathrm{i} + t)\|^2 , \tag{3.18}$$

where $\mathbf{A}_\mathrm{i}$ and $\mathbf{B}_\mathrm{i}$, the control points corresponding to image A and image B, respectively, are represented as column vectors. R and t are respectively represented by 2-by-2 rotation and translation matrices.

Equation 3.18 was first solved by Schönemann (1966) for the solutions to R and t. This approach is ideal for aligning images of the head as it acts as a rigid object undergoing only rigid transformation. Consequently, it has been useful in multi-modality medical image registration of the head for image guided surgery (Habets et al., 2009). However, for complex distortions beyond the rigid or affine transformation, namely the chest, a transformation function with a higher number of degrees of freedom is needed to model such complicated and localized deformations. Two such functions are the 2D polynomial and 2D spline interpolation functions. In both cases, their functions are fitted to the coordinate relationships between image A and image B:

$$u_1 = T_1(v_1, v_2) \tag{3.19}$$

and

$$u_2 = T_2(v_1, v_2), \tag{3.20}$$

where (u_1, u_2) and (v_1, v_2) are the Euclidean coordinates of image A and image B, respectively. T_1 and T_2 are the functions with which either the polynomial or spline functions will be fitted. How these interpolation functions are solved will be discussed in the following subsections as they will be utilized in transforming PB-PCX images of the thoracic cage.

3.2.3.1 Polynomial interpolation

Polynomial interpolation approximates T_1 and T_2, appearing in Eqs. 3.19 and 3.20, to be in the form of a polynomial:

$$u_1 = \sum_{i=0}^{N} \sum_{j=0}^{N} K_{ij}^1 v_1^i v_2^j \tag{3.21}$$

and

$$u_2 = \sum_{i=0}^{N} \sum_{j=0}^{N} K_{ij}^2 v_1^i v_2^j, \tag{3.22}$$

where K^1 and K^2 are the polynomial coefficients for an N^{th} order polynomial.

From here on the following steps for solving the polynomial coefficient will only be shown for K^1 as similar steps can be made for K^2. Using the M known control point pairs, $\mathbf{A}_\mathrm{i} \rightarrow (u_{1\mathrm{i}}, u_{2\mathrm{i}})$ and $\mathbf{B}_\mathrm{i} \rightarrow (v_{1\mathrm{i}}, v_{2\mathrm{i}})$ where $\mathrm{i} = 1, 2..., M$, these are substituted into Eq. 3.21 and expressed in matrix form between u_1 and (v_1, v_2):

$$\begin{pmatrix} u_{11} \\ u_{12} \\ \vdots \\ u_{1M} \end{pmatrix} = \begin{pmatrix} V'_{21} & v_{11}V'_{21} & v_{11}^2V'_{21} & \cdots & v_{11}^NV'_{21} \\ V'_{22} & v_{12}V'_{22} & v_{12}^2V'_{22} & \cdots & v_{12}^NV'_{22} \\ \vdots & \vdots & \vdots & \ddots & \vdots \\ V'_{2M} & v_{1M}V'_{2M} & v_{1M}^2V'_{21} & \cdots & v_{1M}^NV'_{2M} \end{pmatrix} \begin{pmatrix} K_0^1 \\ K_1^1 \\ \vdots \\ K_N^1 \end{pmatrix}, \tag{3.23}$$

where

$$V'_{2i} = (1, v_{2i}, v_{2i}^2, \cdots, v_{2i}^N) \tag{3.24}$$

and

$$K_i^1 = (K_{i0}^1, K_{i1}^1, \cdots, K_{iN}^1). \tag{3.25}$$

This presents a system of linear equations, and in order to obtain a unique solution for K^1 the number of control point pairs should be equal to or greater than the number of unknown polynomial coefficients. In the above matrix, there are $(N+1)^2$ unknown polynomial coefficients K_i^1, thus there must be at least $M \geq (N+1)^2$ control points. Equation 3.23 can be rewritten in shorthand notation as:

$$\mathbf{u_1} = \mathbf{VK^1}. \tag{3.26}$$

To solve for the coefficients K_{ij}^1 that best fit to the points (v_{1i}, v_{2i}, u_{1i}), the method of least squares is adapted. The coefficients K_{ij}^1 that are chosen return the minimal absolute squared difference between the observed and fitted points, known as the residual error Σ^2. In this case:

$$\begin{aligned} \Sigma^2 &= \sum_{i=1}^{M} |u_1 - T_1(\mathbf{B}_\mathrm{i})|^2 \\ &= \left\| \mathbf{u_1} - \mathbf{VK}^1 \right\|^2, \end{aligned} \tag{3.27}$$

where the coefficients are found through minimizing Σ^2. This is equivalent to finding the zero gradient of Σ^2 with respect to each coefficient K_{ij}^1. Thus, Σ^2 is differentiated in terms of each coefficient K_{ij}^1 and set to zero to solve for K_{ij}^1. Starting from Eq. 3.27:

$$
\begin{aligned}
\Sigma^2 &= (\mathbf{u_1} - \mathbf{V}\mathbf{K^1}) \cdot (\mathbf{u_1} - \mathbf{V}\mathbf{K^1}) \\
&= (\mathbf{u_1} - \mathbf{V}\mathbf{K^1})^\intercal (\mathbf{u_1} - \mathbf{V}\mathbf{K^1}) \\
&= \mathbf{u_1}^\intercal \mathbf{u_1} - \mathbf{K}^{1\intercal}\mathbf{V}^\intercal \mathbf{u_1} - \mathbf{u_1}^\intercal \mathbf{V}\mathbf{K}^1 + \mathbf{K}^{1\intercal}\mathbf{V}^\intercal \mathbf{V}\mathbf{K^1} \\
&= \mathbf{u_1}^\intercal \mathbf{u_1} - 2\mathbf{K}^{1\intercal}\mathbf{V}^\intercal \mathbf{u_1} + \mathbf{K}^{1\intercal}\mathbf{V}^\intercal \mathbf{V}\mathbf{K^1} \qquad (3.28) \\
\nabla_{\mathbf{K^1}}(\Sigma^2) &= -2\mathbf{V}^\intercal \mathbf{u_1} + 2\mathbf{V}^\intercal \mathbf{V}\mathbf{K}^1 \\
&= 0, \\
\mathbf{K^1} &= (\mathbf{V}^\intercal \mathbf{V})^{-1}\mathbf{V}^\intercal \mathbf{u_1}.
\end{aligned}
$$

Here, the matrix transpose is denoted by $^\intercal$. In going from the 3rd to 4th line of Eq. 3.28, notice that $\mathbf{u_1}^\intercal \mathbf{V}\mathbf{K^1} = (\mathbf{K^1}^\intercal \mathbf{V}^\intercal \mathbf{u_1})^\intercal$, and since it is a scalar[2], $(\mathbf{K}^{1\intercal}\mathbf{V}^\intercal \mathbf{u_1})^\intercal = \mathbf{K}^{1\intercal}\mathbf{V}^\intercal \mathbf{u_1}$. If $\mathbf{V}^\intercal \mathbf{V}$ is invertible, then the coefficients $\mathbf{K^1}$ of the polynomial function T_1 can be solved. The expression $(\mathbf{V}^\intercal \mathbf{V})^{-1}\mathbf{V}^\intercal$ is known as the pseudoinverse of V in the case of an over-determined system. Pseudoinverse matrices are a generalization of the inverse square matrix for non-square matrices (Penrose and Todd, 1955).

When the similarity measure SSD was introduced earlier in this section, the importance of the residual error being the absolute difference rather than the absolute squared difference was highlighted to avoid giving disproportionate weighting to large differences in intensity due to noise. In the context of fitting a function, giving greater weighting to larger residual errors can cause over-fitting. This is particularly problematic when using higher order polynomials. Instead of just fitting to the trend of the points, the minor fluctuations due, for example, to misregistrations, are also fitted. Consequently, coordinates between control points will be poorly transformed. However, for polynomial fitting the residual error must be squared, as performed in Eq. 3.27, so that it is continuously differentiable with respect to $\mathbf{K^1}$ everywhere in order to solve for the minima[3].

3.2.3.2 2D spline interpolation

An alternative to using large order polynomials is dividing the coordinate transform maps, (v_1, v_2, u_1) and (v_1, v_2, u_2), into piecewise polynomials of lower order to map complex transformations. For

[2] $\mathbf{K}^{1\intercal}$ is a row matrix, $\mathbf{V}^\intercal$ is a $N \times M$ matrix, and $\mathbf{u_1}$ is a column matrix. The product of their matrices $\mathbf{K^1}^\intercal \mathbf{V}^\intercal \mathbf{u_1}$, therefore returns a scalar quantity.

[3] Consider a differentiable function u with independent variable x and that it crosses the x-axis at $x = h$. The minima of $|u|$ and $|u|^2$ will then both occur at $x = h$. In the context of polynomial fitting, $x = h$ represents the polynomial coefficient that minimizes the residual error $|u|^2$. This is determined by differentiating $|u|^2$ and solving for x at $\frac{\mathrm{d}|u|^2}{\mathrm{d}x} = 0$. It will be shown that $|u|$ cannot instead be defined as the residual error since it is non-differentiable at $x = h$. The proof is as follows: at $|u| \neq 0$, $\frac{\mathrm{d}}{\mathrm{d}x}|u| = \frac{\mathrm{d}}{\mathrm{d}x}(u^2)^{1/2} = \frac{u}{|u|}\frac{\mathrm{d}u}{\mathrm{d}x}$ and therefore is differentiable. However, at $x = h$, $\frac{\mathrm{d}|u|}{\mathrm{d}x}$ is indeterminate $(= \frac{0}{0})$. Instead, the limit can be computed: $\lim_{x\to h^+} \frac{|u|-0}{h} = \frac{|u|}{h}$ and $\lim_{x\to h^-} \frac{|u|-0}{h} = \frac{-|u|}{h}$. Since the limits do not converge to the same value, $|u|$ is non-differentiable at $x = h$. Conversely, the limit of $\frac{\mathrm{d}|u|^2}{\mathrm{d}x}$ exists and therefore $|u|^2$ is differentiable at $x = h$.

this thesis, Delaunay triangulation is employed to divide the coordinate transform maps into triangles, where the control points form the vertices, until maximal planar subdivision (MPS) is achieved (Delaunay, 1934; de Berg et al., 2008). This occurs when adding additional edges (lines linking the vertices) will destroy planarity (crossing of edges). Then the coordinates within each triangle are interpolated to construct the transformation map. Linear interpolation can be employed but so can higher order polynomials. In comparison to the former, the latter returns a smoother transformation function and consequently so too the warped image. This is due to the condition imposed when fitting that higher order polynomials between triangles have equal derivatives. The main disadvantage is it is more time consuming.

An important attribute of Delaunay triangulation is that, although there are multiple ways of achieving MPS, it is able to determine which MPS will return the most accurate transformation map. To demonstrate how this is achieved, consider the set of control points shown in Figure 3.4 that can be triangulated in two different ways to achieve MPS. Looking at the point marked by q, its value is interpolated differently in Figs. 3.4(a) and 3.4(b). In general, the further apart control points used to interpolate are, the greater uncertainty there is about the value at point q, and thus a greater likelihood its interpolated value will return a large error. It can be seen in Fig. 3.4(a) that the triangle MNF (or EMN) formed by the shorter edge MN would likely return a more accurate interpolated value than the triangle EFM (or EFN) formed by the longer edge EF in Fig. 3.4(b). The shorter edge is known as a legal edge as opposed to an illegal edge that formed the skinnier triangle. Delaunay triangulation detects these illegal edges and corrects for them by flipping the edges to form legal edges such as in Fig. 3.4. In reference to Fig. 3.4(a), it detects illegal edges by constructing a circle through the control points in contact with the edge through q (i.e. points M and N) and either E or F. If the fourth control point lies in the interior of the circle then it is an illegal edge, otherwise it is a legal edge (de Berg et al., 2008).

Spline interpolation is generally more stable than polynomial interpolation when fitting to complex transformation maps since it avoids the problem of overfitting and introducing large unwanted oscillations around the edges of the image due to the Runge phenomenon (Runge, 1901). Also, control points that are not accurately registered only affect the alignment accuracy around those control points since the transformation map is independently interpolated in each Delaunay triangle.

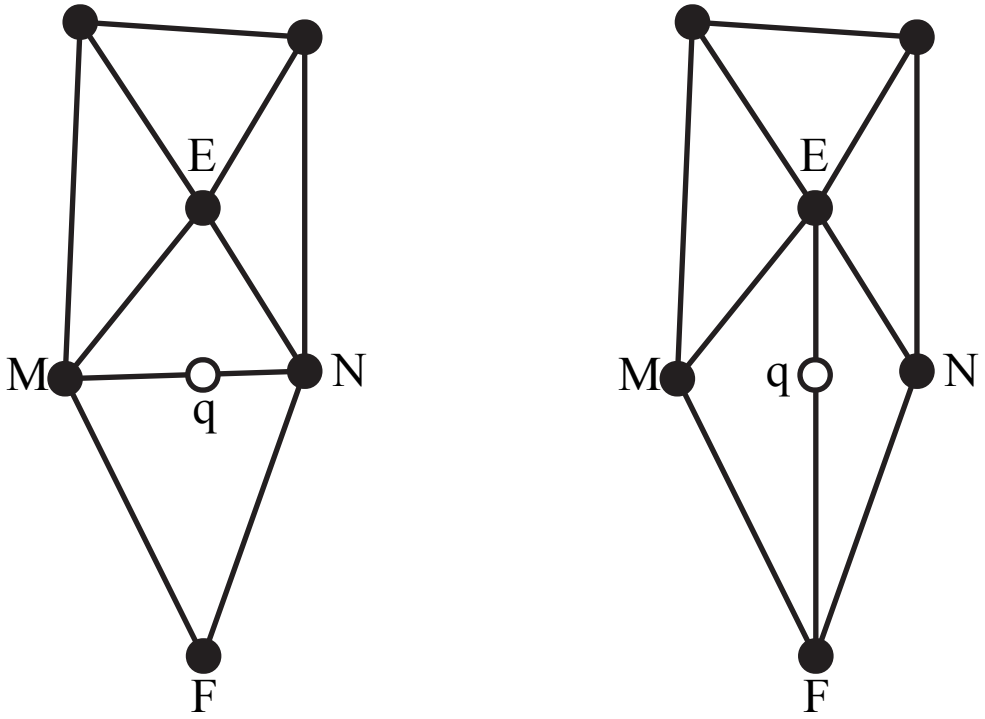

Figure 3.4: Delaunay triangulation. (a) and (b) shows the two possible ways of achieving MPS of the control points (filled circles). (a) is more accurate in interpolating point q than (b) because the line used to interpolate is shorter.

3.2.4 Image Alignment of the Thoracic Cage

Based on the success of previous studies in aligning chest x-ray images utilizing either area- or feature-based image registration, it was considered that the former would likely be more accurate and robust against a weak signal-to-noise ratio (SNR). An appropriate combination of similarity measure and transformation function was then required to provide a high level of accuracy for aligning the thoracic cage without heavy computation constraints. The latter point is important since dynamic imaging returns numerous images, each requiring alignment. Both the similarity measure and transformation function are evaluated together by calculating the relative difference in total intensity (RDTI) between the transformed image $B^{\widehat{T}}$ and image A:

$$RDTI = \left[1 - \frac{\sum_{i=1}^{N}\sum_{j=1}^{M}|B(i,j)^{\widehat{T}} - A(i,j)| - \sum_{i=1}^{N}\sum_{j=1}^{M}|B(i,j)^{\widehat{T}} - B(i,j)|}{\sum_{i=1}^{N}\sum_{j=1}^{M}|B(i,j) - A(i,j)|}\right] \times 100. \tag{3.29}$$

Non-rigid warping does not conserve the total image intensity. Hence, the absolute difference in the total intensity of B and $B^{\widehat{T}}$ was subtracted from the subtracted images of $B^{\widehat{T}}$ and A so that the value of RDTI represented the difference due to misalignment only. A value of 0% means the

alignment of the images has not improved whereas at 100%, the total intensity of the subtracted image is 0, meaning perfect alignment. Negative RDTI indicates worsening of the alignment.

In order to select the most appropriate similarity measure and transformation function for thoracic imaging, tests were performed on an artist's impression of a rib cage, as shown in Fig. 3.5. Figure 3.5(a) shows the original depiction of a chest that was transformed using a barrel distortion to mimic the motion of the ribs during inspiration as shown in Fig. 3.5(b). This was achieved by assigning a number of control points, $\mathbf{A}_i$, equally spaced 25 pixels apart in Fig. 3.5(a). The position of these control points is shown in Fig. 3.5(c). Each column of control points was altered to follow an arc of a circle where the left and right half of the control points followed the left and right arc of a circle, respectively. These are denoted as $\mathbf{B}_i$. To begin, the outermost column of control points was mapped out to a circle of radius 5000 pixels. Each subsequent column of control points traced out a circle of radius 27 pixels less than the previous one such that the curvature of these columns of control points increased gradually towards the center of the image. The final result is shown in Fig. 3.5(d). The image in Fig. 3.5(a) was then transformed from $\mathbf{A}_i$ to $\mathbf{B}_i$ using a 3^{rd} order 2D polynomial to obtain the barrel distorted image shown in Fig. 3.5(b), which increased its size from 764×804 pixels to 807×782 pixels.

Various combinations of similarity measures and transformation function were tested on the barrel distorted image in Fig. 3.5(b) to see how well it aligned back to Fig. 3.5(a). The Interactive Data Language (IDL 7.1) was used to run all in-built and custom-developed similarity measures and transformation functions as well as all other image processing algorithms in the remaining chapters. The in-built functions used here were: *polywarp.pro*, *poly_2D.pro* and *warp_tri.pro*. IDL 7.1 was operated on a PC using an Intel®Core™2 Duo, 3.32GHz CPU with 4 GB of RAM.

For each similarity measure, which are CC, SAD and MI, the kernel and search area size were 64×64 pixel and 128×128 pixel, respectively. Beginning at the top left corner of Figs. 3.5(a) and 3.5(b), a search area and kernel was chosen, respectively, where the initial coordinates of the kernel coincided with the center of the search area. The search area and kernel were then translated in increments of 16 pixels across and 16 pixels down. At each interval the similarity measure was applied to determine the region within the search area that best matched with the kernel. A pair of control point sets, $\mathbf{A}_i$ and $\mathbf{B}_i$, was thus obtained. $\mathbf{B}_i$ represents the coordinates of the central pixel of each kernel in the barrel distorted chest image and $\mathbf{A}_i$ represents the coordinates where the central pixel of each kernel produced the best fit within the search area of the original chest image.

Before fitting a transformation function to the pair of control point sets, certain pairs of control points were removed to ensure the alignment was optimally smooth and accurate. Each pair of

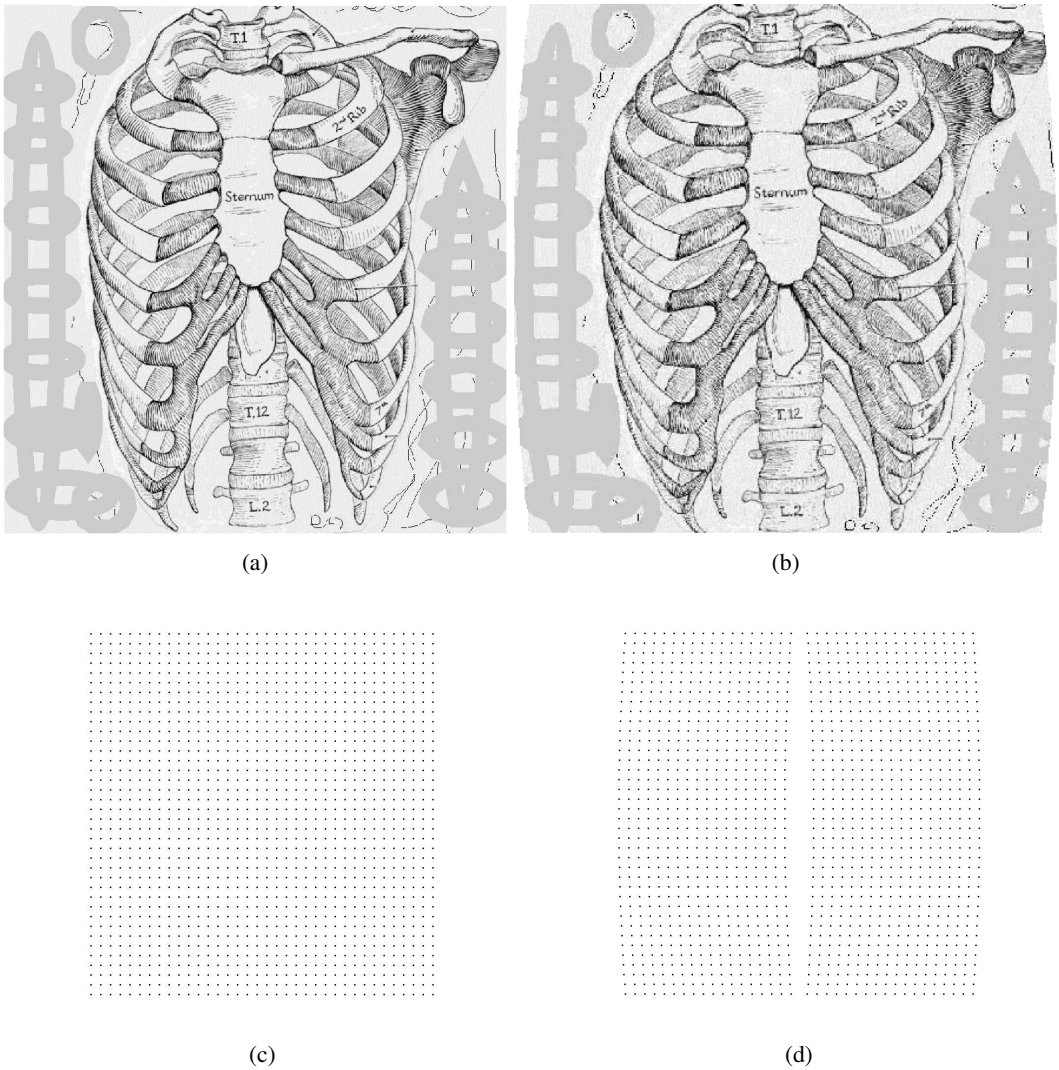

Figure 3.5: An illustration of a chest (a) before and (b) after undergoing a barrel distortion to resemble the movement made during inspiration. While these images look very similar, they can clearly be differentiated from the degree of curvature at the edge of the images. (c) and (d) show the control points used to distort (a) using a 3rd order 2D polynomial function.

control points describes a shift vector, defined as the vector $\mathbf{A}_i$-$\mathbf{B}_i$. Based on knowing what the direction and magnitude of the shift vectors should be, those pointing more than 10^o away from the expected direction and having a magnitude exceeding the known maximum magnitude were discarded. Those that remained will be known as *filtered* control points. For each similarity measure, the filtered control points were used to transform the chest with different orders of 2D polynomials and spline functions.

Figure 3.6 shows the performance of the different area-based alignment techniques. Overall, the SAD method presented the most quantitatively accurate result with MI surprisingly returning the worst results; this latter finding may be due to the use of small kernel sizes. Whilst small

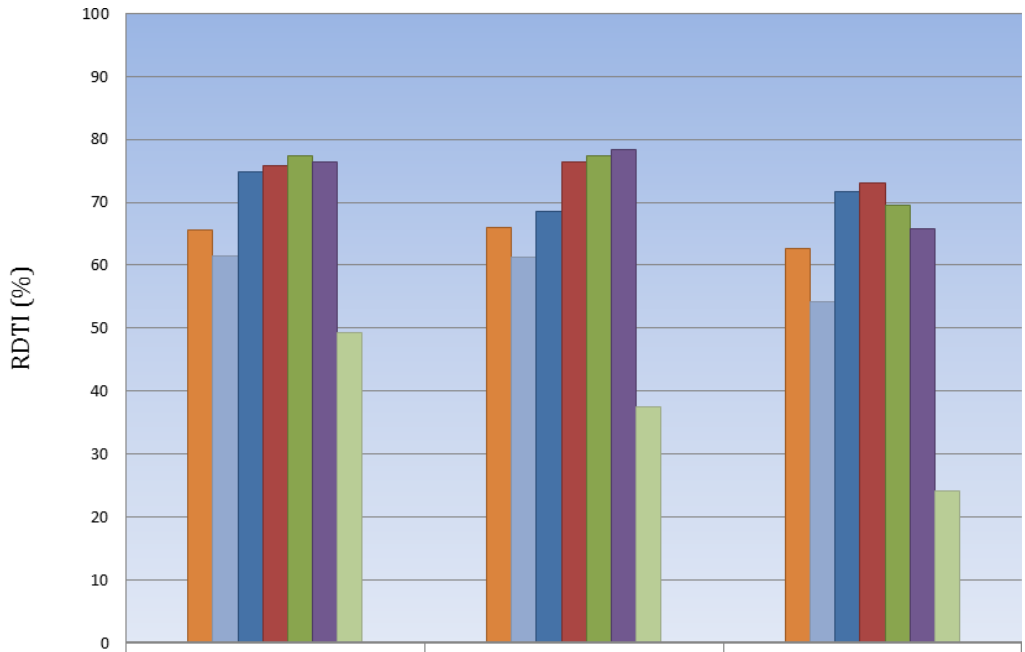

	CC	SAD	MI
Bilinear (%)	65.5	66.0	62.7
Biquintic (%)	61.5	61.3	54.3
2nd order (%)	74.8	68.6	71.6
3rd order (%)	75.8	76.4	73.2
4th order (%)	77.4	77.3	69.5
5th order (%)	76.3	78.5	65.8
6th order (%)	49.2	37.5	24.1
7th order (%)	-48.5	-289.3	-67.5
Avg time taken (mins)	0.5	19.8	1624.4

Figure 3.6: Comparison of different combinations of similarity measures and transformation functions in terms of the RDTI values (%) and average time taken (mins) to align the images in Figs. 3.5(a) and 3.5(b). An RDTI value of 100% represents perfect alignment. The RDTI values calculated for the 7^{th} order 2D polynomial transformation function returned negative values due to over-fitting of control points (not plotted).

kernel sizes affect the performance of all the similarity measures it seems MI has been affected to a larger extent. Unlike the other two similarity measures, MI does not assume a linear relationship between the intensities of the two images. This is a useful property to have when implemented in inter-modality image registration; however, it also increases the probability for a misregistration to occur. For example, if a kernel overlaps a region of the search area that does not resemble the kernel, but as long as there is a strong one-to-one function between the intensities of the images, MI will return a high value since the joint histogram will form a sharp curve and that both the kernel and search area enclose anatomical structures. Misregistration could be minimized using smaller bin sizes for the histogram, but this increases computation time considerably.

The time taken to perform each combination of similarity measures and transformation functions was computed and averaged over the transformation functions (see Fig. 3.6). They were averaged because the time required to perform any of the transformation functions was negligible compared to that of the similarity measures. The SAD method took 20 mins to register all the kernels while CC was completed in less than a minute as a consequence of using the fast Fourier transform (FFT). The MI method required 1624 mins (~27 hours) to align a single image with most of the time spent plotting an intensity histogram for each kernel/search area pair. This time could have been reduced by increasing the histogram bin size, but that was found to significantly decrease the accuracy of the alignment.

Polynomial interpolation provided better alignment compared to spline interpolation for all three similarity measures. This is not surprising as the barrel distortion was generated using a polynomial function. Beyond the 5^{th} order 2D polynomial the alignment accuracy quickly deteriorated due to over-fitting of control points (Runge's phenomenon). Spline interpolation was not as accurate, but still had RDTI values > 60%. Interestingly, biquintic spline interpolation performed much worse than bilinear spline interpolation. This may be due to the former imposing that the transformation function is smooth while sacrificing alignment accuracy.

Considering that the motion of the lung will not follow a perfectly polynomial-shaped distortion in 2D, spline interpolation would be more stable against more elaborate movements. CC is only marginally less accurate but exhibits far greater computational efficiency. Therefore, CC and bilinear spline interpolation were chosen for their time efficiency and robustness while retaining high accuracy. This combination of similarity measure and transformation function was also found to be most accurate in correcting spatial distortions in images recorded for this thesis using x-ray cameras coupled to a tapered fiber optic element (Islam et al., 2010).

3.3 Area-Based Image Alignment Approach

The work presented in this section is based upon that by Leong et al. (2013a). This section describes an area-based (AB) alignment method for segmenting bone from sequences of PB-PCX chest images of breathing rabbit kittens (section 3.3.1). By isolating the image of the lungs from that of the bones, these segmented images enable the calculation of changes in air volume in highly localized regions of the lung. The results showing the accuracy of the alignment and the calculated volumes are presented in section 3.3.2. A discussion on the implications of these results is provided in section 3.3.3.

3.3.1 Methodology

Image acquisition

Imaging experiments were performed in Hutch 3 of beamline 20B2 at the SPring-8 synchrotron radiation source, Japan (Goto et al., 2001). A Si (111) double-bounce monochromator was tuned to 24 keV, which has been shown to provide optimum SNR and bone/soft-tissue contrast for imaging rabbit kittens on this beamline (Kitchen et al., 2008). The relative energy width was $\Delta E/E$~10^{-4} and the photon flux density was ~2×10^8 photons/s/mm^2. The PB-PCX imaging setup was adapted (see Fig. 2.3) with the subject placed approximately $D = 210$ m downstream of the source and the detector positioned a further $L = 3$ m downstream. Newborn rabbit kittens were imaged as part of two experiments. The first group were imaged live at a frame rate of 3 Hz, with a respiratory cycle of 2.5 s. Images were recorded with an exposure time of 40 ms using a high resolution detector comprised of a fiber optic (FOP) taper bonded between the 4000×2672 pixel Hamamatsu CCD camera (C9300-124F21) and a 20 μm thick gadolinium oxysulfide ($Gd_2O_2S:Tb^+$;P43) phosphor. The effective pixel size was 16.2 μm based on the taper ratio of 1.8:1 and a native pixel size of 9 μm. Kittens in the second group were humanely killed via anaesthetic overdose prior to imaging. These kittens were imaged at a frame rate of 1 Hz and exposure time of 40 ms, with a respiratory cycle of ~10 mins, using a 25 μm thick gadolinium oxysulfide phosphor-coupled CCD camera (Hamamatsu, C4742-95HR). A tandem lens system provided an effective pixel size of 22.47 μm (after 2×2 pixel binning).

Sample preparation

All procedures involving animals were approved by the Monash University Animal Ethics Committee and the SPring-8 Animal Care and Use Committee. Pregnant New Zealand white rabbits at 31 days of gestation were anaesthetized by an intravenous injection of propofol (Rapinovet; 12 mg kg^{-1} bolus, 40 mg h^{-1} infusion). Rabbit kittens were delivered by caesarean section, sedated and surgically intubated. The umbilical cord was then cut and the kittens were placed in a water-filled cylindrical polymethyl methacrylate (PMMA) container, with their heads out of the container and sealed by a rubber diaphragm surrounding their necks. A custom-made remotely controlled mechanical ventilator was connected to the endotracheal tube (Kitchen et al., 2010a). At birth and before breathing began for the first time, the lungs are filled with fluid. Several images were recorded of the lungs in their fluid-filled (non-aerated) state before ventilating. Rabbits and rabbit kittens imaged *in vivo* were humanely killed via anaesthetic overdose at the end of each

experiment.

Image processing

For quantitative volumetric analysis, the dark current arising from the detector was subtracted from the images, which were subsequently normalized against the incident beam intensity. This was achieved by first averaging 20 dark field images with the shutter closed and 20 flat field images with the shutter reopened and the object absent at the end of each imaging sequence. Nonlinear spatial distortions arising from the FOP camera, as a result of imperfect alignment of the fiber bundles at each end of the taper, were corrected by the use of Delaunay triangulation with bilinear spline interpolation (Islam et al., 2010). Low frequency trends were then removed to aid the cross correlation process since it is highly sensitive to large transverse gradients in the background intensity (remember that Eq. 3.11 is used to compute CC, which is not normalized against $\sigma_{A'}\sigma_{B'}$ and therefore does not correct for such gradients) and their removal reduced the occurrence of misregistrations. These trends included: (i) the parabolic profile produced by the cylindrical container; (ii) the high energy (harmonic) x-rays reflected by the crystal monochromators creating a narrow horizontal band across the image; and (iii) the low frequency components of the air-filled lungs (which was added back when performing the lung volume analysis). To correct for the parabolic profile, a horizontal rectangular ROI below the lungs was selected along the container, averaged vertically, smoothed, then least-squares fitted with a 6^{th} order one-dimensional (1D) polynomial. The polynomial curve was extruded vertically and subtracted from the images. The higher harmonic contaminants were corrected in the same manner but without polynomial fitting. The low frequency components of the aerated lungs were removed by subtracting a 200×200 pixel boxcar smoothed image of the lungs.

During sequence acquisition the beam intensity was prone to fluctuation due, for example, to the loss and top-up of electrons in the synchrotron storage ring and thermal drifting of the monochromator crystals. This was corrected by rescaling each image to a chosen reference frame using the average intensity in a uniform region somewhere away from the moving kitten.

Image registration

A suitable non-aerated image was selected as the reference image, which was then registered and warped to each aerated image. This was achieved in two steps, where images were corrected first for globally- then locally-induced bone misalignments. The former arise from the movement relating to the kitten floating in the container. Kitchen et al. (2008) corrected for this by tracking the movement of a single vertebra using CC (Eq. 3.11). Here, that approach was extended to

tracking multiple vertebrae as it was found that each moved slightly independently to one another. The sizes and coordinates of the kernels enclosing each vertebra in the non-aerated image were specified by the user. The corresponding search areas were automatically centered at the same coordinates and enlarged by 10%. Each pair of control points was calculated using CC (Eq. 3.11), which were then replicated horizontally to both edges of the image, allowing the images to be transformed in its entirety. This aligned the vertebral column of the two images and enabled the coordinates of regions where the ribs articulated with the vertebra, which will be written in short form as vertebra-rib (VR) points, to be fixed between images when locally aligning the bones to correct for respiratory-related motion, that is, locally-induced bone misalignments (described next).

The thoracic cavity was then partitioned into three regions: left/right lungs and the vertebral column. A series of 64×64 pixel kernels were selected at a sample rate of 32 pixels for the left and right lungs and correlated using CC (Eq. 3.11) with their corresponding 128×128 pixel search areas. This corrected for localized movements associated with the expansion of the thoracic cage. A kernel of this size was chosen as it was sufficiently large to enclose a small segment of at most a single rib as each moves independently. The size of the search area was chosen to account for the largest likely rib displacement. Both the kernel and search area sizes can easily be modified if the parameters of the imaging system, such as magnification and pixel size, are changed.

The pair of control points determined for the left/right lungs underwent a filtration process to remove unrealistic shift vectors. Control points were kept if all three of the following criteria were met: (i) the CC value was above a given threshold value (Keane and Adrian, 1990); (ii) the absolute difference between the angle of the shift vector and average angle of the adjacent shift vectors was less than 20°; and (iii) the absolute difference between the magnitude of the shift vector and average magnitude of the adjacent shift vectors was less than 5 pixels (81 μm). Image noise introduces noise in the CC output images. A threshold value was applied to ensure that only matched regions with CC values significantly greater than that returned by purely noisy regions were accepted. This threshold value was chosen to equal the CC peak value returned when a pair of water-only 64×64 pixel ROIs chosen outside the rabbit, but within the container, were cross-correlated. The angle of 20° and magnitude 5 pixels were selected based on a trial and error approach. These values were found to optimize the ratio of realistic to unrealistic shift vectors for chest images with various degrees of movement, yielding comparatively smooth transformations and one-to-one mapping of the coordinates. The left and right lungs of the non-aerated image were transformed using the filtered control points and recombined together with the vertebral column to construct the registered image. To minimize the computation time required to perform image alignment and phase retrieval,

the region outside the chest, which includes the forelimbs, was masked out.

Image analysis

After aligning the PB-PCX images, SIPRA was used to determine the change in their projected thickness and subsequently that of their V_L utilizing Eq. 2.7. The attenuation coefficient (μ) and refractive index decrement (δ) of water are required as input to SIPRA. The latter was calculated earlier in section 3.1 to be 3.991×10^{-1} (24 keV), while the former was calibrated by isolating a large section of 20 PB-PCX images that contained the water-filled container only. The inner and outer diameter of the container was measured to be 32.0 ± 0.1 mm and 39.0 ± 0.1 mm, respectively. Using the Beer–Lambert law (Eq. 1.35b), the attenuation coefficient of PMMA (μ_{PMMA}=48.91 m^{-1}) obtained from the NIST database (NIST, 2014) and its thickness (7 mm), the attenuation signal of the container was removed. μ was then calculated to be 54.64 ± 0.01 m^{-1} using the Beer–Lambert attenuation law. This is similar to the value 54.735 m^{-1} (24 keV) for water obtained from the NIST database (NIST, 2014). The absolute uncertainty of the measured V_L was determined by measuring the standard deviation (σ) of the volume difference in a water-only ROI between the reference and the set of 2252 aerated images against the ROI size (N × M pixels). The points were fitted with a rational exponent function ($3.543 \times 10^{-7} \times [\text{N} \times \text{M}]^{3/4} + 3.654 \times 10^{-6}$) from which σ can be calculated for any sized ROI[4].

Because of the non-linear dependence between the PB-PCX image intensity and projected material thickness, phase retrieval was performed on the individual images first before subtracting them. The direct subtraction of PB-PCX images shown in the results section (section 3.3.2) are only to display how successfully the images were aligned.

3.3.2 Results

Chest Segmentation

The AB alignment method was successfully tested on several sets of PB-PCX images of rabbit kitten chests during mechanical ventilation. A non-aerated image was chosen as the reference image to have its thoracic cage aligned with that of each image recorded during ventilation. Figure 3.7(a) shows the non-aerated lungs of the reference image from one such dataset. The remaining sequence of images, Fig. 3.7(b-f), shows the lungs during one respiratory cycle. The speckle pattern seen in

[4]It was found that the intensity values between pixels had some degree of correlation. This may arise from crosstalk between pixels. Consequently, the uncertainty of the measured volume in a region is not the quadrature sum of that of the individual pixels within the region. If this was done, the uncertainty in the intensity of a given region would be overestimated. The method described in the main text for calculating the uncertainty in any size region accounts for the intensity correlation between pixels.

the aerated chest images is created by x-rays converging as a consequence of the alveoli mimicking aberrated compound refractive lenses (Kitchen et al., 2004). This will be explained in greater detail in chapter 4. As a consequence of utilizing a non-aerated image, the calculated volume difference is approximately equal to the total V_L in the aerated image; thus, the absolute rather than relative V_L can be measured. Furthermore, the lack of speckles in the non-aerated image means the kernel can treat the speckles in the search area as high frequency noise, against which CC is robust, hence only the bone is registered.

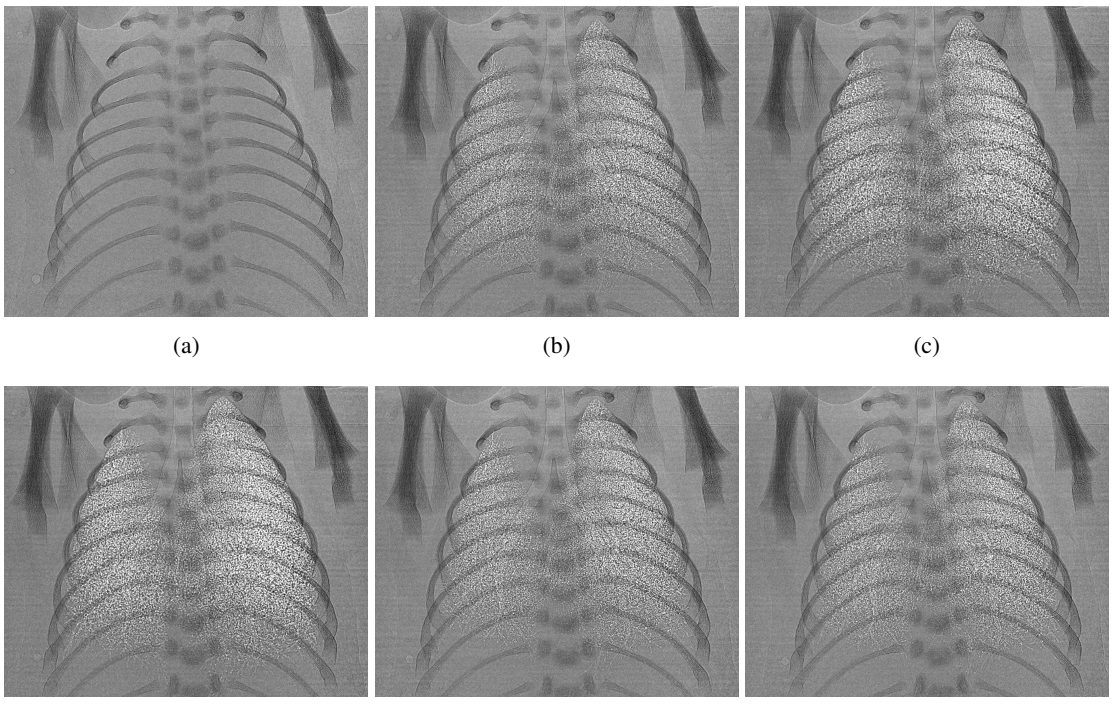

Figure 3.7: A series of 24×21 mm^2 PB-PCX chest images of a newborn rabbit kitten recorded at 3 Hz with (a) fluid-filled lungs and (b-f) over one respiratory cycle, beginning mid-inspiration. The x-ray beam energy was set to 24 keV and the images were recorded at 3 m ODD.

Figure 3.8(a) shows the direct subtraction of Fig. 3.7(a) from Fig. 3.7(c). Due to the expansion of the thoracic cage as the lung fills with air and the movement of the kitten, the bones do not exactly overlap and therefore bone artefacts appear in the subtracted image. The images were then registered to correct for global movement. Here ends the similarity between the AB alignment technique developed herein and preceding work by Kitchen et al. (2008). While in both cases the vertebral column is aligned, the AB alignment technique proceeds to align the ribs, thus forming a fully registered image. Images whose vertebral column only was aligned are denoted as unregistered images. Figure 3.8(b) displays the images subtracted after global correction. This

shows the vertebral column aligned accurately whilst each rib appears to rotate about the side of the connected vertebra. This highlights the assumption made earlier on the VR points being fixed to be a good approximation when aligning the ribs.

Local shift vectors were next calculated for each lung to correct for the rib movement and screened for unrealistic vectors. Figure 3.8(c) shows the resultant shift vectors. Note that only one tenth of the vectors are displayed for clarity. The zero magnitude shift vectors at the VR points are not visible. A histogram showing the distribution of the magnitude of the resultant shift vectors is presented in Fig. 3.8(d). This shows a majority of the magnitudes are realistic since they are approximately consistent with the extent of displacement of the ribs. A small minority of unrealistic shift vectors remain. Although the selection criteria could be altered to become more stringent, too many realistic shift vectors would also be filtered out, thereby adversely affecting accuracy of the alignment.

Using the filtered control points, the reference image was transformed and subtracted from the aerated image, as shown in Fig. 3.8(e). Only small misalignment errors can be seen as faint artefacts predominantly along the outer borders of the chest. Since alignment was restricted to within the chest, strong artefacts are visible outside the chest. The total time taken to perform the image alignment was approximately 7 seconds on the aforementioned PC (see section 3.2.4). Figure 3.8(f) reveals the subtracted phase-retrieved images yielding the projected thickness of air. A ROI of at least a single pixel in size and of any shape could then be chosen from Fig. 3.8(f) to calculate the regional V_L enclosed within it. As stated in the previous section, phase retrieval cannot be performed on Fig. 3.8(e) where the images have already been directly subtracted due to the nonlinear dependence between the intensity and projected material thickness (see Eq. 1.58b).

Lung volume calculations

Figure 3.9(a) shows total V_L calculated using the registered and unregistered reference images during mechanical ventilation of the kitten. That is, the technique developed here is compared to that of Kitchen et al. (2008). Both techniques return almost identical total V_L with the small discrepancies attributed to non-conservation of the total intensity of the image after non-rigid warping of the non-aerated image (as discussed in section 3.2.4). The small discrepancies are well within the uncertainties of both techniques, demonstrating there is negligible detrimental effect of the non-rigid transformation on altering the total volume of the non-aerated image.

The ability of the techniques to measure V_L on a pixel-by-pixel basis was compared. For 1000 sequential PB-PCX images of the same kitten in Fig. 3.8, the V_L was computed at each pixel using

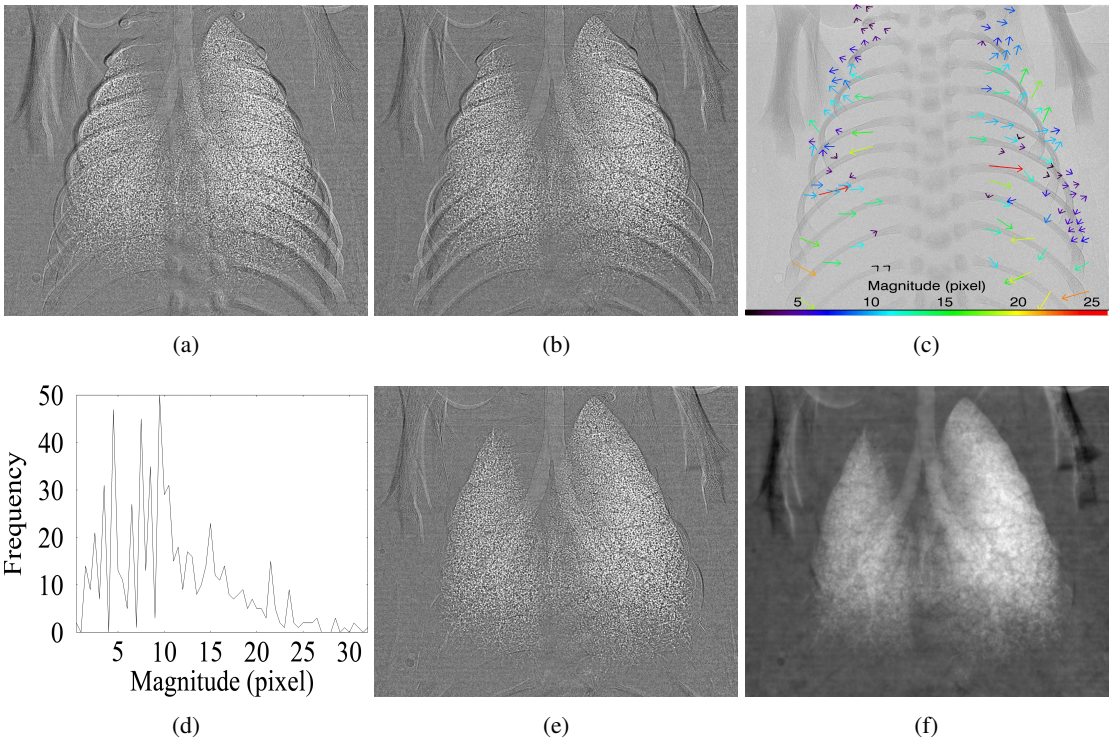

Figure 3.8: Image Alignment. (a) The direct subtraction of the non-aerated (Fig. 3.7(a)) and an aerated (Fig. 3.7(c)) image show the relative movement of the bony structures during image acquisition. (b) Subtraction after alignment of the vertebrae in the non-aerated image with that of the aerated image. (c) After correlating the entire thoracic cage the control point pairs are represented by shift vectors (~ one tenth of the vectors are shown), which enabled the non-aerated image to be transformed using bilinear spline interpolation. (d) A histogram showing the distribution of the magnitude of the shift vectors (the zero magnitude shift vectors have been suppressed). (e) Subtraction of the transformed image from that of the aerated image leaving only the signal due to the air in the lungs (plus artefacts). (f) To perform lung volume analysis, the registered images underwent phase retrieval before subtraction, yielding the change in projected thickness of water at each pixel. Image size: 24×21 mm^2.

the two techniques. The percentage difference in the calculated V_L between the two techniques was calculated at each pixel for the 1000 images and represented as a histogram, as shown in Fig. 3.9(b). The shaded region in Fig. 3.9(b) shows that on average 16% of pixels within the lungs have a volume difference greater than 20%, and given that the fractional uncertainty of the measured change in V_L in each pixel is only ~1%, these differences are significant. The majority of these differences occurred around where the bones were not aligned, as evidenced in Figs. 3.9(c) and 3.9(d). These results show that the bones have a detrimental effect when performing regional V_L analysis and the AB alignment technique is able to effectively remove the bones to accurately measure the V_L on a pixel-by-pixel basis.

A set of PB-PCX chest images attained from the second group (slow inflation rates; ~10 mins) was used to generate an image sequence whose pixel values show the percentage of its maximum

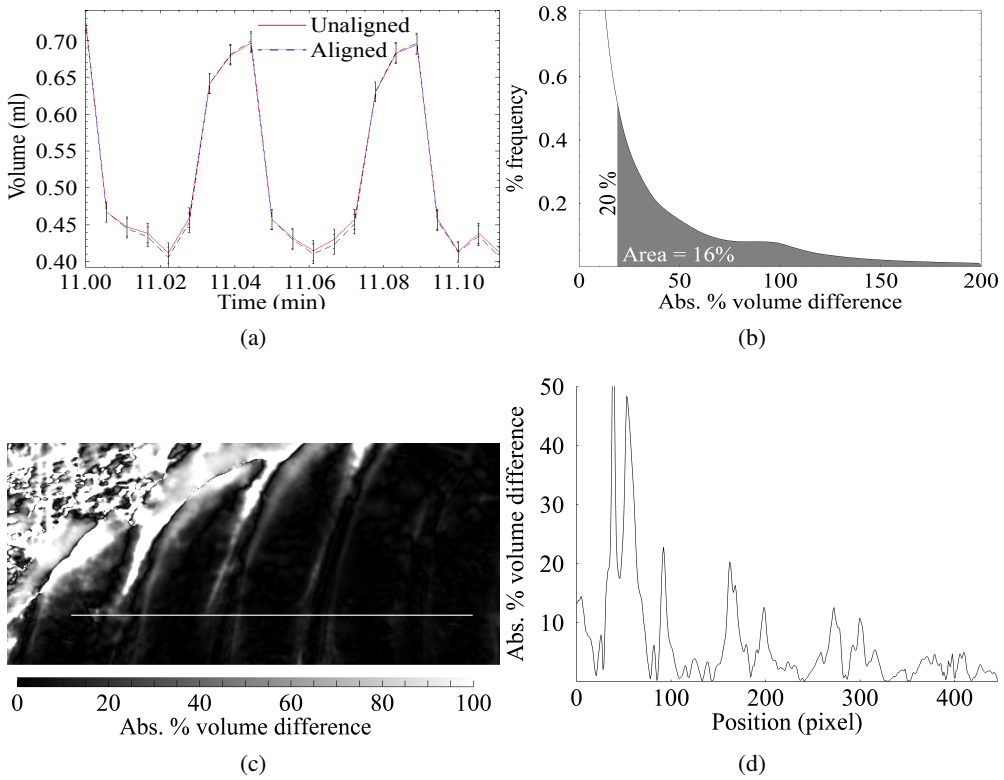

Figure 3.9: Lung air volume analysis. (a) The total V_L was determined over several respiratory cycles, beginning at t=11 mins after initiation of mechanical ventilation, using the misaligned (unregistered) and aligned (registered) non-aerated images. The absolute % volume difference in the calculated pixel-by-pixel V_L from 1000 aerated images using misaligned and aligned non-aerated images are represented in a (b) histogram and as a (c) image of half a lung. The greatest differences are seen at the edge of the chest where the movement of the ribs is largest, as demonstrated in (d), which shows a plot of the line profile indicated by the thick white horizontal line in (c).

V_L capacity. Each aerated image was aligned to the reference (non-aerated) image of the sequence and the change in V_L was computed from each pixel. The volumetric images were stacked to determine the time when each pixel within the lungs reached its maximum air volume. Figure 3.10 shows maps of the time taken for each region of the lungs to reach 10%, 50% and 80% of its maximum air volume, on a pixel-by-pixel basis. It can be seen that the major airways aerated first, as expected, followed by an otherwise relatively uniform aeration up to 10% of maximum volume (Fig. 3.10(a)). However, the left lung (left side of image) then aerated towards 50% maximum air volume more slowly in comparison to the right lung (Fig. 3.10(b)). The peripheral regions of the lungs are also seen to more slowly ventilate during the latter stages of the inspiratory period. At the end of inspiration the lungs asymptoted toward their maximum air volume more uniformly as the applied airway pressure also reached its plateau (Fig. 3.10(c)). Therefore, the combined panels in Fig. 3.10 show that the time constant of aeration is highly localized.

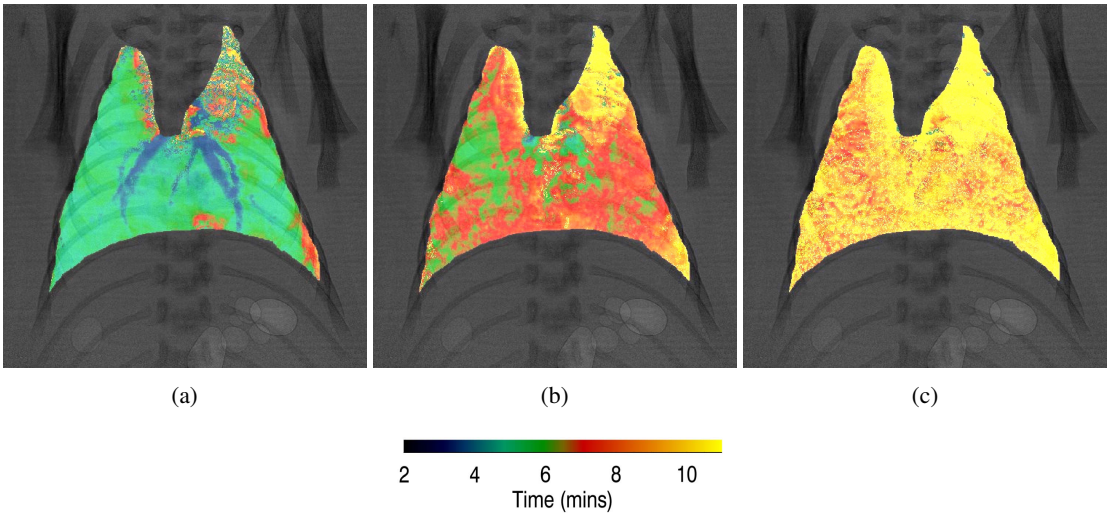

Figure 3.10: Non-uniform lung aeration. A series of maps were produced showing the time taken for each pixel of the lung to reach (a) 10%, (b) 50% and (c) 80% of their maximum air volume. Image size: 24×21 mm^2.

3.3.3 Discussion

This work demonstrates that the technique for measuring V_L, developed by Kitchen et al. (2008), can be extended to more accurately measure regional V_L using the AB alignment method. This method has been able to accurately align PB-PCX chest images with minimal computational cost, primarily by exploiting the use of FFT-based CC. Other similarity measures were investigated, namely MI and SAD on illustrative chest images (see section 3.2.4), and the resultant subtracted images at best showed a marginal improvement compared to CC, based on the visual inspection of artefacts and the calculated RDTI; however, this coincided with a large increase in computation time. These similarity measures were also tested on PB-PCX chest images (not shown) and similarly showed no significant improvement compared to CC in alignment from the resultant subtracted images. Polynomial interpolation was also considered as an alternative to bilinear spline interpolation since it has the ability to produce a smooth transformation; however, the complexity in the motion of the chest requires a higher order polynomial, but is prone to suffering Runge's phenomenon.

Figure 3.10 shows the distribution of gas can be inhomogeneous across the lung. The AB alignment-based volumetric method developed herein can help determine whether this is the norm for healthy lungs and how it differs from lung-related diseases. With the development of high-powered laboratory-based x-ray sources capable of performing PB-PCX imaging, this technique can become a cheap, fast and potentially readily accessible diagnostic tool that can recognize and localize lung-related diseases earlier than conventional x-ray imaging and global lung function tests

(see chapter 2). The ability to study the homogeneity of lung aeration can also be highly beneficial to reducing ventilation-induced lung injury (Hooper et al., 2007). This is particularly important for preterm infant resuscitation. By first using this technique to gain insight into the crucial but transient period of achieving lung aeration at birth, ventilation strategies can be optimized accordingly.

Compared to conventional x-ray imaging, PB-PCX images of the chest can enhance the edges of the conducting zone that contains the trachea, bronchi and bronchioles, and the respiratory zone, which includes the alveoli (Kitchen et al., 2005). This is most prominent from the alveoli, which produces a speckle signal (see Fig. 3.7). However, in aligning the bones, the signals from these structures weaken that of the bone. Consequently, during image registration the kernels selected in those parts of the lungs enclosing strong phase contrast from these structures either weakly correlated or misregistered. This resulted in a moderate portion of shift vectors rejected in the central areas of the lungs where a majority of those structure resided, as shown in Fig. 3.8(c) by the lack of shift vectors. Despite this, the movement of the medial segment of the ribs during breathing is closely restricted to rotating around their corresponding VR point. This was adequately accounted for by the piecewise bilinear spline interpolation between the zero magnitude VR points and their closest lateral control point.

At increasing differential movement of the chest, the AB alignment method became decreasingly accurate. This was attributed to two factors: the increasingly inaccurate assumption that the medial segment of the ribs is just rotating around their corresponding VR point, and the increasing angular rotation of the ribs in the sagittal plane (i.e., the plane perpendicular to that of the PB-PCX chest image). The latter causes the degree of overlap of the ribs between images to change, which cannot be account for by the AB alignment method, since it assumes a one-to-one coordinate mapping. The latter is also responsible for attributing to the former factor. A measurable indicator of the degree of differential movement was the V_L change. It was found, on average, that for total V_L changes less than 0.60 ml, the alignment was quite accurate but gradually deteriorated beyond this volume as the movement of the thoracic cage became overly complex (see CD attached to this thesis). Given that the average weight of a rabbit kitten was 30 g, the maximum volume change per unit mass of 0.60/.03=20 ml/kg, which is considered to be a large volume change (Wilson et al., 2012). Therefore, this technique could be applied to measure a range of V_L in patients.

A non-aerated reference image may not always be available or possible to obtain in some studies. Alternatively, an aerated PB-PCX chest image could be used as a reference image. While this will instead provide relative volumetric measurements, which still carries much important respiratory information, a more problematic issue is that cross-correlating ROIs that have speckles

present in both is likely to increase the prevalence of misregistrations as the speckles weaken the signal intensity of the bone. Moreover, the speckles may correlate more strongly with each other than the bones themselves. Consequently, the AB alignment method may not be as robust in using an aerated chest image as a reference image to measure relative changes in V_L.

Regardless of whether the reference image is an aerated or non-aerated chest image, the maximum accurately measurable volume change could be increased either through modifying the method or image acquisition process. More shift vectors could be retained by correcting rather than rejecting them. These corrections could be made based on preserving the continuity and smoothness of the transformation (see e.g. Li et al. (2000)). Smaller sized kernels were trialled to better handle the localized lung movement, but the structural information it enclosed was less unique and became more prone to misregistrations. Shortening the object-to-detector propagation distance to reduce or remove the phase contrast could improve the bone contrast relative to the speckle contrast to reduce the occurrence of misregistrations. Finally, if the reference image was an aerated PB-PCX chest image, then it could be chosen to be the image with the least lung aeration (i.e. least speckle contrast).

3.4 Feature and Area-Based Hybrid Image Alignment Approach

The AB alignment method presented in the previous section is completely automated and requires no *a priori* knowledge about the structure of the chest. The kernels are sampled evenly throughout the image and correlated within their respective search areas. However, many of the shift vectors are rejected for being unrealistic and not all of those that are accepted by the filter are realistic. Herein, a feature and area-based hybrid (FAH) alignment method is described in section 3.4.1 that is more selective in which kernels are used to perform CC and the shift vectors are corrected based on *a priori* knowledge of the thoracic cage. It was hypothesized that this would significantly reduce the computation time and improve the alignment, particularly at high lung volumes. The results showing the accuracy of the alignment and how it compares with the AB alignment method are presented in section 3.4.2. A discussion on its drawbacks and possible improvements is provided in section 3.4.3.

3.4.1 Methodology

Consider a non-aerated and aerated PB-PCX chest image of the lung such as those seen in Fig. 3.7. The steps outlined below are applied after the images are pre-processed and their vertebral column are aligned as described in section 3.3.1. These steps are designed to track each rib in those images to help guide the selection of kernels (in the non-aerate image) and search areas (in the aerated image). This process considerably reduces the computation time since the number of kernels to be registered is notably reduced. The steps outlined below are demonstrated on the aerated image in Fig. 3.7(c) and displayed in Fig. 3.11.

1. A threshold is applied to isolate the signal of the bone and create a binary image (Fig. 3.11(a)).

2. The binary image undergoes morphological 'opening'[5] using a structure element with dimensions comparable to the known width of the ribs to fill any gaps between segments that are part of the same rib and remove any signals that are not that of bone (Fig. 3.11(b)).

3. A small horizontal rectangle is created for each rib with one end positioned at the VR point that is provided by the user during alignment of the vertebral column. The other end protrudes away from the vertebrae and is rotated until it overlaps with the rib. The degree of overlap is measured by implementing CC between the rectangle and rib in polar coordinates (Fig. 3.11(c)).

4. A 32×32 pixel box is then created at each of the VR coordinates and moved away at intervals of 32 pixels from the vertebrae along their respective ribs in the direction at which the horizontal rectangle is angled. At every interval, the central coordinate of the box is recorded and stored as a control point for that rib. The direction is adjusted whenever it moves away from the rib, which is indicated by a significant change in the mean intensity of the pixels enclosed in the box. Since the ribs overlap, there is the possibility that the box may track one rib and continue onto the rib below it. To avoid this, the lowest rib in the chest is tracked first. There a 2^{nd} order 1D polynomial is fitted to the control points of that rib as a lower bound for tracking the rib above. An upper bound is also set. Since the ribs are slanted downwards, the upper bound for each rib is set to equal the y-coordinate of their corresponding VR point (Fig. 3.11(d)).

[5]Morphological operators alter the structures within a given image utilizing a structure element. The structure element is an image shape that probes the given image. In morphological opening, the structure element acts to reduce the size of and remove any structures smaller than its size. It then expands those remaining structures to restore their size. It can be realized then that morphological opening is useful in removing noisy signals and small structures from images. More details are provided in section 5.10 on morphological operators. See Shih (2009) for a more detailed description of morphological operators.

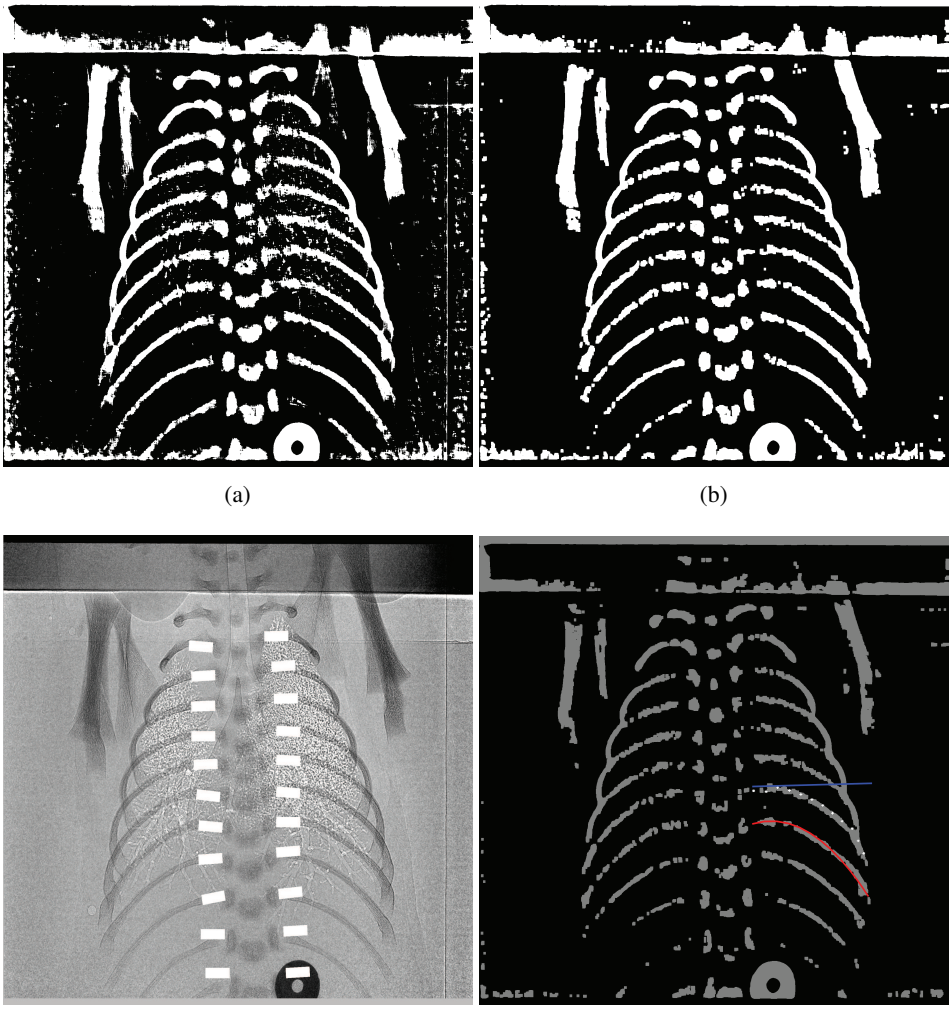

(a) (b)

(c) (d)

Figure 3.11: Tracking of the ribs was done in the following order: (a) creating a binary image of the bones; (b) applying the morphological operator 'open' to enhance signal of bone and remove signals not of bone (for example, lung speckle); (c) determining the initial direction of each rib from the VR point; and (d) applying an upper (blue) and lower (red) boundary for tracking each rib. Images: 24.4×20.9 mm^2.

Kernels of size 64×64 pixels were created at each control point of the rib that were tracked in the non-aerated image and cross-correlated (Eq. 3.11) with their corresponding 128×128 pixel size search area located at the control points tracked in the aerated image. For each control point the returned shift vector was replicated twice, once above and once below it, in the direction normal to the tangent line of the 2$^{\text{nd}}$ order 1D polynomial function (fitted during step 4 outlined above) at the control point. These replicated shift vectors can be seen in Fig. 3.12(c) as a trio of shift vectors. Each of these span the width of the ribs to ensure each rib is independently warped. That is, each rib warped is not influenced by those adjacent to it.

The set of shift vectors for each rib underwent a correction phase. It is assumed that the rib movement is purely rotation-based (i.e., it rotates around its corresponding VR point) and that the curvature of the ribs is approximately quadratic. Thus, the amplitude and angle of each set of shift vectors should increase quadratically and remain constant, respectively, along the rib away from the VR point. To enforce this, the amplitudes of the shift vectors along each rib were weighted fitted with a 2^{nd} order 1D polynomial . Those shift vectors whose amplitude differ more than three standard deviations from that of the fitted polynomial was replaced by that of the polynomial. The weighting assigned to the control points was proportional to the distance between the position of the shift vectors and the VR point. More weighting was provided to those furthest away from the VR point as the bone signal is not masked by lung speckle and is therefore most likely to return correct shift vectors. Constraining the angle of the shift vectors to be constant is not an entirely accurate assumption. While the rib movement is rotation-based, it rotates three dimensionally. Consequently, its 2D projected image would not necessarily show the angle of the shift vectors to be constant along a rib. Instead, the angles of the shift vectors were smoothed using a four pixel boxcar average to ensure smoothness of the transformation. Finally, the non-aerated image is transformed to align with the aerated image using bilinear spline interpolation.

3.4.2 Results

Figure 3.12 demonstrates the FAH alignment method applied to the same pair of images aligned using the AB method in Fig. 3.8 (i.e. Figs. 3.7(a) and 3.7(c)). The FAH alignment method took place after their vertebral columns were aligned, as shown in Fig. 3.8(b). Both images were thresholded to create a binary image, then underwent morphological opening to remove non-bony signals and to fill in the gaps between segments that were part of the same rib. The resultant binary images are shown in Fig. 3.11(b) and Fig. 3.12(a) for the aerated and non-aerated images, respectively. Both images show the bones successfully isolated and, importantly, that the lung speckle signal was removed from the aerated image. The ribs at the bottom of the image could not be entirely recovered as they were only partially calcified. Before calcification, bone is made of cartilage tissue that have similar complex refractive indices to lung tissue (Gilbert, 2010, ch. 14). Consequently the signal of partially calcified bone cannot be differentiated from that of lung tissue. However, the remaining ribs were successfully isolated and tracked. This is shown for the non-aerated image in Fig. 3.12(a) with white markers overlaid on top of the binary image representing the control points of the ribs. The aerated lungs also had its ribs successfully isolated and tracked (not shown). The shift vectors generated after image registration are presented in

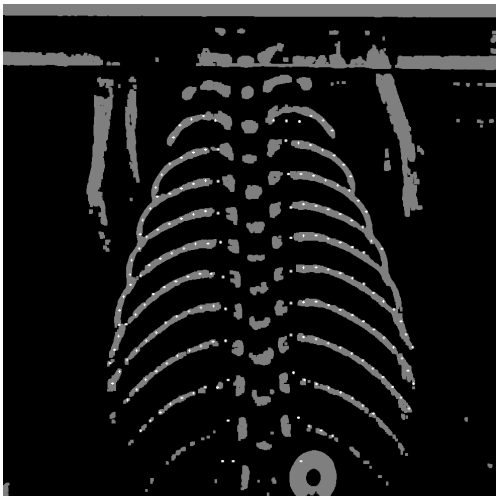

(a)

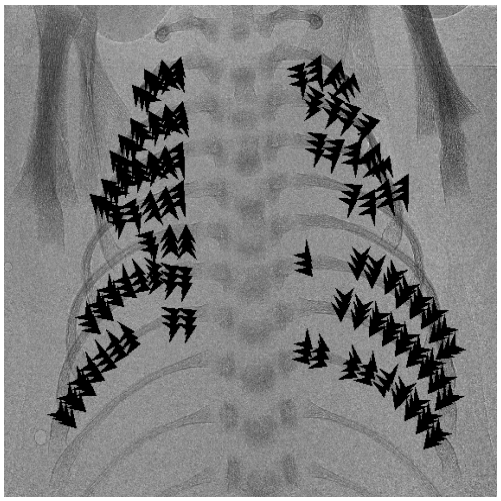

(b)

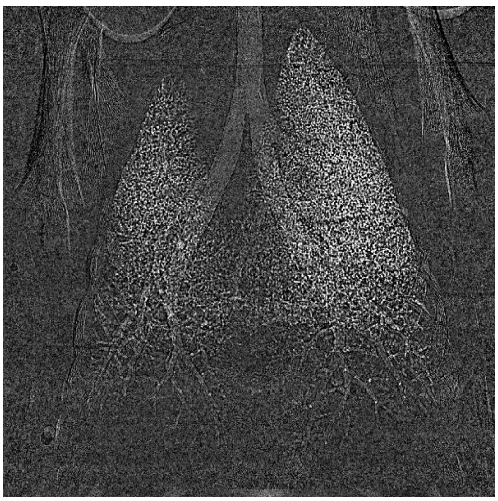

(c)

Figure 3.12: Feature and area-based hybrid alignment method. (a) Using the steps demonstrated in Fig. 3.11, the ribs were tracked in both images, but only that of the non-aerated lungs is shown. (b) After correlating the entire thoracic cage the control point pairs are represented by shift vectors, which enabled the non-aerated image to be transformed using bilinear spline interpolation. (c) The transformed image is subtracted from the air-filled image, thus isolating the signal of water. Images: 24.4×20.9 mm^2.

Fig. 3.12(b). After applying the bilinear spline transformation function to the non-aerated chest image, this was subtracted from the aerated image as shown in Fig. 3.12(c).

The total time taken to run the FAH alignment method on a 1480×1296 pixel image pair was ~7 seconds using a PC with identical specifications as that used to run the AB alignment method. The computation time is similar to that of the AB method, which also took ~7 seconds to align the same pair of images. The amount of time saved by reducing the number of kernels was offset by the time taken to track the ribs. However, this time includes tracking both images. This only needs

to be done once on the non-aerated image, after which only the aerated images are tracked. The total computation time where one image is tracked was then reduced to ~5 seconds.

To compare the accuracy of the AB and FAH alignment techniques, a panel of subtracted images is presented in Fig. 3.13. At low V_L, there is small differential bone movement and both techniques accurately align the ribs, as shown in Fig. 3.13(a) and 3.13(b). At a higher air volume where there was larger differential bone movement the FAH alignment method produced more bone artefacts in the subtracted image (Fig. 3.13(c)) than the AB alignment method (Fig. 3.13(d)). A video clip comparing the two techniques for an image sequence showing the ventilation of a newborn rabbit kitten in the CD accompanying this thesis.

3.4.3 Discussion

In section 3.3 an AB alignment method was presented that involved kernels and search areas being evenly sampled across two images for image registration. It was found to be highly accurate in aligning PB-PCX chest images over a large range of V_L. A drawback to this method was that a large number of shift vectors returned were deemed unrealistic and were therefore rejected. This prompted the development of a FAH alignment method that isolates the bony signal beforehand then performing image registration only of the bony signal, where realistic shift vectors are most likely returned. The aim was to reduce the computation time and improve the alignment accuracy. Since there are only a small number of shift vectors per selected rib, filtering them based on their surrounding shift vectors would likely detrimentally affect the alignment accuracy than improve it. Instead, the ribs were modeled using 2^{nd} order 1D polynomials to correct the size and direction of shift vectors that are considered unrealistic. Both the AB and FAH algorithms worked well at low V_L, but the former was more accurate than the latter at high V_L. It is likely that, in the FAH alignment method, modeling the amplitude of the shift vectors as a 2^{nd} order 1D polynomial was overly simplistic at high V_L. Higher order polynomials were trialled but were found to produce unwanted oscillations along a rib after warping due to over-fitting. Alternatively, 2D splines can be fitted. Whilst this would provide a greater degree of freedom for fitting to the control points, it was found to cause non-smooth warping of the ribs (data not shown).

Even at low V_L where modeling the amplitude of the shift vectors as a 2^{nd} order 2D polynomial appeared sufficient, bone artefacts still appeared at times. This is likely due to the over-reliance on too few realistic shift vectors. That is, fitting a polynomial function on only a few control points can become heavily influenced by one or two unrealistic control points. Consequently, the entire rib can become inaccurately aligned. Conversely, unrealistic shift vectors in the AB alignment

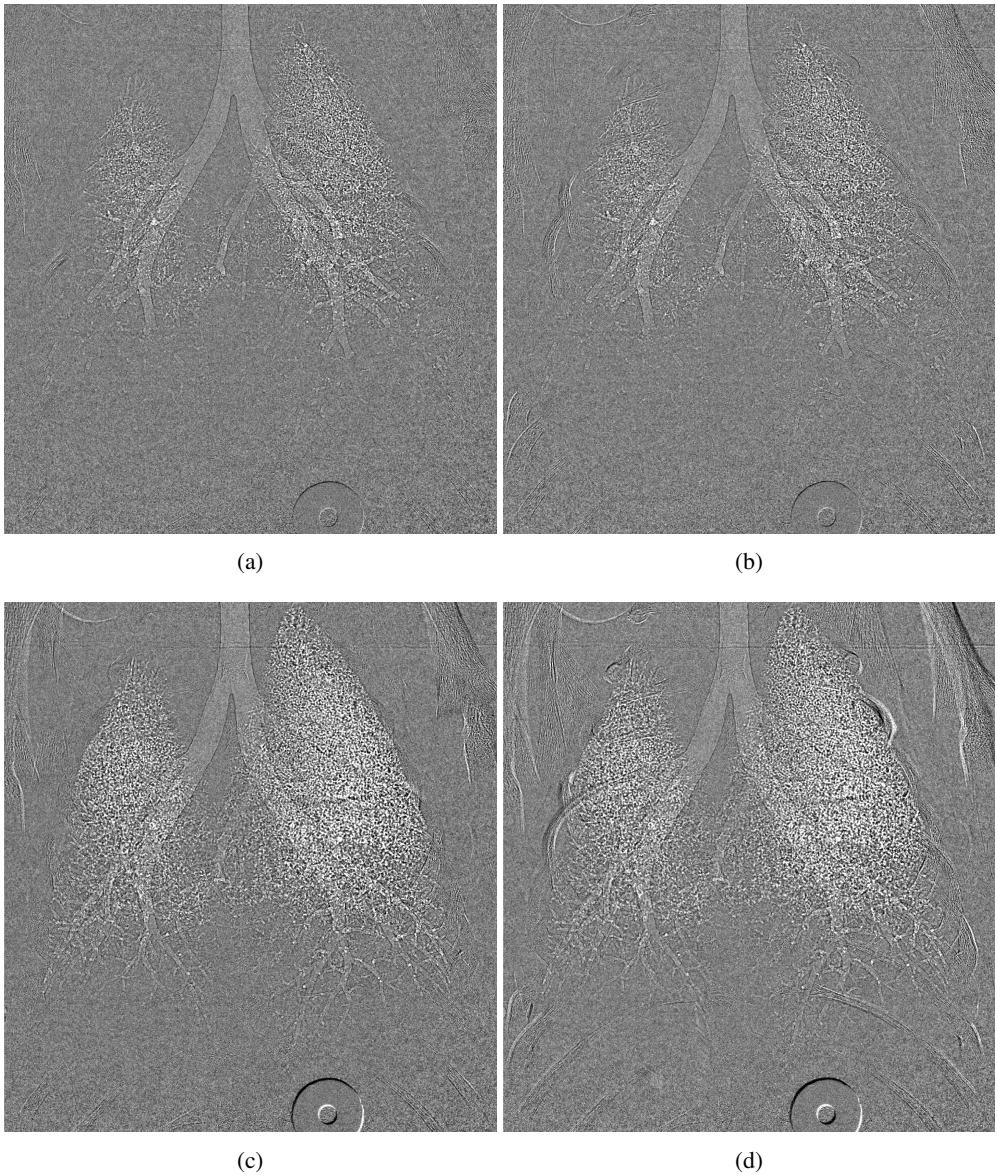

(a) (b)

(c) (d)

Figure 3.13: Two aerated PB-PCX chest images, at low and high lung air volume, are aligned and subtracted from a non-aerated PB-PCX chest image using the AB [(a) and (c)] and FAH [(b) and (d)] alignment algorithms. The top and bottom panel of images correspond to the lungs at low and high air volumes, respectively. Images: 24.4×20.9 mm^2.

method only affect a small region of the chest. Since the AB alignment method was found to be more robust than the FAH alignment method, only the results of the AB alignment method were reported in the paper by Leong et al. (2013a).

3.5 Concluding Remarks

Accurately measuring the homogeneity of lung aeration is likely to be highly beneficial to studying and diagnosing child and adult lung-related disease and for optimizing mechanical ventilation strategies for preterm infants. Herein, two alignment algorithms were developed to segment the bony anatomy from 2D PB-PCX images of the chest to isolate the lungs. Then, using SIPRA, the change in air volumes between localized regions of the lung, down to the micron scale pixel size, could be measured. However, since the FAH alignment method was found to be less robust than the AB alignment method and was accurate over smaller changes in lung volumes, the AB alignment method was chosen to perform localized V_L measurements.

The total V_L measured with and without segmenting the bones using the AB alignment method agreed. This showed that the total volume in the non-aerated chest image after image warping with a non-rigid transformation function was negligibly altered compared to the uncertainty in the total volume. In analyzing the V_L regionally, there was significant improvement compared to images that were not aligned, primarily in areas where there was large differential movement of the bones. However, when the differential movement of the bones becomes overly complex the alignment accuracy reduced. Therefore, the AB alignment method is capable of isolating the lungs and providing high spatiotemporal resolution measures of lung aeration from 2D PB-PCX images, without the use of contrast agents that are required in other image-based volumetric techniques.

4 Measurement of Absolute Regional Lung Air Volumes from Near-Field X-ray Speckles

4.1 Introduction

In chapter 3 a method for performing regional measurements of lung air volume (V_L) was introduced. To reiterate, that method aligns the bony anatomy between two propagation-based phase contrast x-ray (PB-PCX) chest images to remove the bones and isolate the image of lungs before applying the single image phase retrieval algorithm (SIPRA) to measure changes in V_L between them. Removal of the bones is what enables accurate volumetric analysis on small regions of the lungs. However, perfect alignment of the bones is impossible to achieve because the chest moves three-dimensionally while alignment is performed on the two-dimensional (2D) projection. The ribs appear to move relative to one another and the amount of overlap between them can change from one image to the next. The transformation function utilized for warping the chest images is one-to-one and does not account for such complex motion. While image transformation functions need not be one-to-one, it is necessary to avoid unrealistic transformation of the chest such as shearing and folding (Samant et al., 2013). This shortcoming is pronounced when the differential movement of the bones is large, particularly at high volumes, which limits regional measurement of V_L to low volumes.

Another major drawback to the method in chapter 3, and the other phase contrast x-ray (PCX) imaging-based techniques described in section 2.2, is that the chest must be immersed in water. This considerably complicates the experimental setup and greatly reduces the signal-to-noise ratio (SNR) due to extra attenuation of the x-rays by the water bath. Whilst SNR can be improved by increasing the intensity of the x-ray source, a concomitant increase in radiation dose ensues. Moreover, that technique is limited to measuring changes in V_L, rather than absolute V_L, unless an image of a non-aerated lung is available; this is not always easily obtained. The functional residual capacity (FRC)[1] for example, is an important physiological parameter that can only be determined

[1]The total lung air volume at the end of passive expiration.

from measures of absolute V_L.

Notice that in Fig. 3.7, PB-PCX chest images have the appearance of a speckle pattern, characterized by bright and dark intensity variation, whose contrast appears synchronized with the volume of air in the lungs. Figure 4.1 zooms in on Fig. 3.7(f) to show the lung speckles in more detail. In this chapter, a novel approach for measuring regional V_L from PB-PCX images is described that relates lung speckle contrast directly to V_L. As lung speckle is made of intensity peaks and troughs that vary randomly over a given range of length scales, representing it in Fourier space by taking the magnitude of its Fourier transform (power spectrum) produces peaks revealing the dominant band of spatial frequencies (length scales) of the speckle. The area (optical power) contained under those peaks is how speckle contrast will be quantified. A generalized overview of the current literature on the origin and characteristics of speckle patterns is provided in section 4.2, followed by a derivation relating the area under the power spectra of lung speckle to V_L in sections 4.3-4.5. This method is tested and validated on simulated lung tissue (section 4.6) and then on the lungs of rabbit kittens (section 4.7). The results and discussion are presented in sections 4.6 and 4.7 with concluding remarks given in section 4.8. This chapter is an expanded version of the work published in *Optics Express* (Leong et al., 2013b).

4.2 The Origin of Lung X-ray Speckles

Spatially random samples such as particles suspended in liquid (colloids) and optically rough surfaces of textured materials contain rapid spatial fluctuations in complex refractive index (Giglio et al., 2001; Fricke-Begemann and Hinsch, 2004; Kirkpatrick et al., 2007; Mishchenko, 2008; Goodman, 2010; Carnibella et al., 2012b). The phase of an incident wavefield is randomly altered as it traverses through or reflects off such an object (Goodman, 2010). For a partially coherent wavefield, the intensity downstream of the exit surface of the object exhibits bright and dark spots, known as speckles, formed by constructive and destructive interference of coherently scattered electromagnetic waves. The speckles can be viewed as many Fresnel fringes arising from multiple interferences between the incident and scattered waves. This highlights that a non-zero degree of spatial coherence is required for speckles to manifest since Fresnel fringes also require such coherence. However, this is not the case for temporal coherence as Wilkins et al. (1996) shows a high degree of temporal coherence is not required to produce Fresnel fringes and therefore to produce speckle.

Given the conditions for the formation of speckle provided above, namely sufficient spatial

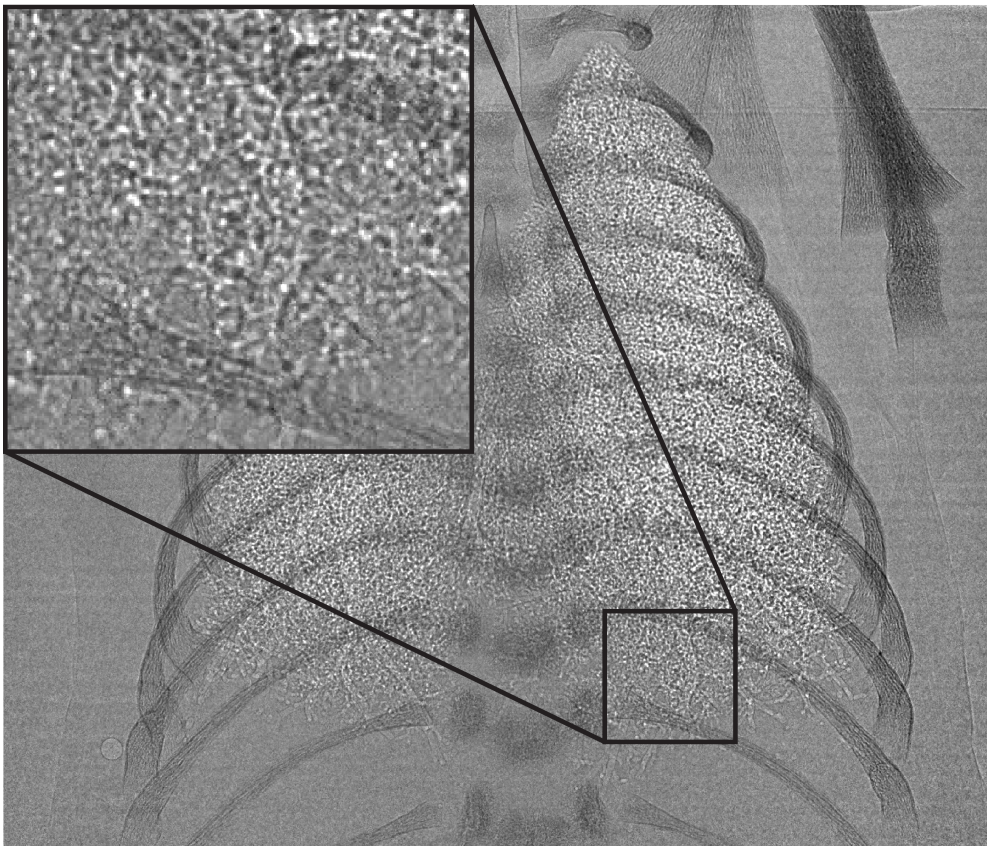

Figure 4.1: A PB-PCX aerated chest image, as was shown in Fig. 3.7(d), with a small part of the chest magnified (inset image size: 6.48×6.48 mm^2) to show the speckled pattern of the lung in greater detail.

coherence and scattering from a rough structure, it is not surprising that speckle is observed in PB-PCX images of the lungs. First, PB-PCX imaging utilizes a partially spatially coherent x-ray source with a coherence area of several microns, enough to form Fresnel fringes (see section 1.3). Second, the lung is a spatially random medium that contains many air-filled alveoli that are uniformly pseudo-randomly distributed and enclosed by thin regions of tissue. This forms many tissue-air interfaces that cause x-rays to coherently scatter in many directions, dictated by the laws of refraction and diffraction, and interfere with the incident wavefield to form bright and dark intensity variations (i.e., speckles).

Yagi et al. (1999) were one of the first to encounter lung speckle, which was observed using PB-PCX chest images of a mouse. They hypothesized that speckles formed as a consequence of alveoli being present in the lungs since the speckles were of similar size to the alveoli. Suzuki et al. (2002) also observed lung speckle and attributed it to refraction off multiple alveoli superimposed in an image. They found that the object-to-detector propagation distance (ODD) and x-ray energy can be optimized to achieve maximal lung speckle contrast by providing sufficient refraction for

edge enhancement but not too much such that it blurs the image. Kitchen et al. (2004) investigated the origin of these speckles by simulating PB-PCX images of lung tissue. Here they modeled lung tissue as voids randomly embedded in water. PB-PCX images were generated by first calculating the wavefield at the exit plane utilizing the projection approximation. Second, the exit plane wavefield was numerically propagated to the detector plane using the angular spectrum formalism of scalar wave optics, as described in section 1.9. Speckles similar to those seen in PB-PCX chest images of a rabbit kitten were observed. They hypothesized that alveoli act locally as aberrated compound refractive lenses, causing rays to gradually become more focused and form bright intensity spots as part of the speckle pattern.

An additional feature seen in simulated lung speckle, as performed by Kitchen et al. (2004), was the appearance of screw-type singularities in the wavefield phase beyond the near-field regime. In accordance with the work by Berry and Dennis (2000), random phase screens (which lungs can be categorized as) do lead to a type of singularity known as phase vortices. These are characterized as having points of zero intensity around which the phase changes by an integer multiple of 2π. That is, a closed line integral over the phase map that encloses the zero intensity pixel is non-zero. This necessarily means the phase around the vortex is discontinuous, exhibiting a screw-type character. Therefore, beyond the near-field regime, the speckled intensity field due to x-ray scattering from the lungs will have zero intensities associated with phase vortices. Within the near-field regime and under the projection approximation no phase vortices should appear (Schmalz et al., 2011), provided that there are no structural vortices such as a spiral staircase phase plate, which in general will hold true for imaging the lungs (Kitchen et al., 2004). It is possible then that the presence (or lack of) phase vortices could help determine if the lung is imaged within the near-field regime. The PB-PCX chest images recorded for this thesis possess no phase singularities but this fact does not necessarily mean it was recorded within the near-field regime. The spatial resolution may have been insufficient to resolve the zero intensities[2] or that phase singularities did not manifest. Kitchen et al. (2004) demonstrated the effects of spatial resolution on phase vortices by observing that they appear in simulated sub-micron pixel size PB-PCX lung tissue images but disappeared when the images were binned to a pixel size of the order of microns.

[2]If spatial resolution is sufficiently low such that diffraction effects can be ignored and therefore operate within the formalism of geometrical optics, phase vortices (or more generally phase singularities) do not appear and instead one has infinite intensities known as caustics. For example, consider parallel rays illuminating a lens. According to geometrical optics, these rays will converge to the focal point of the lens where it predicts there is infinite intensity, but no phase singularities. Scalar wave optics instead predicts an Airy disk of peaked but non-infinite intensity that *softens* the caustics. Airy disks produce phase singularities in the form of concentric rings with zero intensities and associated discontinuous phase jumps of π (Basistiy et al., 1995). Phase vortices in lung speckles can therefore be seen if there is sufficient spatial resolution to resolve the intensity minima.

4.3 Structural Dependency Between Scatterer and its Speckle Pattern

Speckle possesses statistical properties that depend upon that of the scattering object within the near-field regime. An example of such dependency is discussed by Goodman (2010, sec 4.5.5), where an expression is derived relating speckle contrast, defined as the ratio between the standard deviation and mean of the speckle intensity, to surface roughness (standard deviation of surface height). This is further developed by Tchvialeva et al. (2010) and Jeyapoovan et al. (2012). The importance of measuring surface roughness ranges from designing commercial products (for example, touchpads (Mizuhara et al., 2013)) to studying geological materials (for example, soil erosion (Zheng et al., 2014)).

Brogioli (2009) and Cerbino et al. (2008) expanded the work by Goodman (2010) for colloids. Cerbino et al. (2008) showed that the scattered intensity distribution depends on the particle sizes present in colloidal samples. Brogioli (2009) was able to extract size distribution and relative concentrations of particles in colloids encoded in the scattered intensity distribution. This was achieved iteratively by generating scattered intensity distributions using Mie theory[3] for a range of simulated colloidal samples until they converged to that experimentally attained. Similarly, Carnibella et al. (2012b) developed an iterative method for measuring size distribution and relative concentrations of particles from colloidal samples, but from the autocorrelation function[4] of speckled intensity patterns. Autocorrelation functions of colloidal samples were simulated utilizing the angular spectrum formalism described in section 1.9.

All the methods, including that by Cerbino et al. (2008), Brogioli (2009) and Goodman (2010), developed thus far on relating speckle patterns to the object are valid only in the near-field regime. However, the definition of their near-field regime differs from that defined here towards the end of section 1.7.1. Their definition defines the regime to be where the properties of the speckled intensity downstream of the object depends only on that of the random object. Beyond this regime (i.e. for larger ODDs), the properties of the speckled wavefield become altered due to the finite source size from which the incident wavefield was generated. The near-field regime defined in this thesis is the regime over which near-field intensity equation (NFIE) (Eq. 1.55) is valid. This

[3]Mie theory gives exact solutions to Maxwell's equations (Eqs. 1.1-1.4) for wavefields scattering off a sphere (Mie, 1908). Although, the solutions are non-trivial and take the form of an infinite series of basis functions. Consequently, it would be difficult to directly extract structural information of the particles from the scattered intensity using Mie theory.

[4]For a given 2D image $I(\mathbf{r}_\perp)$, its autocorrelation (A) is defined as $A(\Delta\mathbf{r}_\perp) = \int I(\mathbf{r}_\perp)I(\mathbf{r}_\perp + \Delta\mathbf{r}_\perp)\mathrm{d}\mathbf{r}_\perp$. Alternatively, the autocorrelation of $I(\mathbf{r}_\perp)$ can be calculated by taking the inverse Fourier transform of its power spectrum. The autocorrelation function encodes much structurally-dependent information such as the arrangement of particles and their sizes.

equation breaks down well before the finite source size affects the wavefield and therefore the near-field regime defined in this thesis is far more stringent than the other. The method developed by Carnibella et al. (2012b) is, however, valid beyond both near-field regimes as speckle images were simulated beyond those regimes and were successfully used to determine particle size distributions of colloidal samples from their experimentally recorded speckles.

The colloidal samples studied by Brogioli (2009) and Cerbino et al. (2008) contain suspended particles of sizes that range from nanometers to a few microns, which are comparable to the wavelength of the incident wavefield, hence justifying utilizing the Mie theory to accurately model the scattered intensity of the particles and therefore extract its size and concentration. However, alveolar sizes are typically many orders larger than the wavelength (~0.1Å) of the incident x-ray wavefield, ranging from 100-200 μm. In this case, simpler alternatives to Mie theory can be employed, as is the focus of the next section, where a mathematical model is developed to relate the lung speckle contrast from PB-PCX images in the near-field regime to the structural properties of the lung. In this chapter, the mathematical method is applied to measure V_L and, in chapter 5, to measure the dominant alveolar size and number.

4.4 Power spectrum of a near-field 2D intensity map of a 3D random distribution of identical voids

Consider a medium composed of a single material of projected thickness $T(\mathbf{r}_\perp)$ enclosing N non-absorbing voids (i.e. $\beta_{void} = \delta_{void} = 0$) of radius R, as shown in Fig. 4.2. The void sizes that are of interest to this study (i.e., the alveolus) are around six order of magnitude larger than the wavelength and impart relatively weak phase gradients. These facts culminate in allowing the projection approximation to be made where it neglects the effects of transverse scattering within the sample (see Eq. 1.37). Hence, for a paraxial monochromatic wavefield propagating along the z direction, the transmitted intensity ($I(\mathbf{r}_\perp, z = 0)$) and phase shift ($\varphi(\mathbf{r}_\perp, z = 0)$) at the exit surface of the homogeneous medium are:

$$I(\mathbf{r}_\perp, z = 0) = \exp[-2k\beta T(\mathbf{r}_\perp)] \tag{4.1}$$

and

$$\varphi(\mathbf{r}_\perp, z = 0) = -k\delta T(\mathbf{r}_\perp). \tag{4.2}$$

In the near-field regime ($N_F \geq \max\{1, |\varphi|_{max}\}$), NFIE was provided in Eq. 1.55. Substituting Eqs. 4.1 and 4.2 into Eq. 1.55 gives:

$$\frac{I(\mathbf{r}_\perp, z = L)}{I(\mathbf{r}_\perp, z = 0)} - 1 = L\delta\left[\nabla_\perp^2 T(\mathbf{r}_\perp) - \mu\,|\nabla_\perp T(\mathbf{r}_\perp)|^2\right], \tag{4.3}$$

with all terms as originally defined and $\mu = 2k\beta$. Note that ω has been dropped from Eq. 1.55 for notational simplicity.

The two approximations, namely the projection approximation and the near-field condition, made to derive the last equation have similar conditions governing their validity range. For the near-field condition, it is $N_F \geq \max\{\pi, |\varphi|_{max}\}$, and for the projection approximation it is Eq. 1.37. If in Eq. 1.37, the following substitutions are made, $|\nabla_\perp \varphi|_{\max} \simeq \frac{|\varphi|_{\max}}{a}$ and $\Delta x \simeq a$, then it can be seen that if the near-field condition holds then generally so does the projection approximation, provided that $T < L$. This inequality is true for all the phase contrast imaging data shown in this thesis, and therefore ensured that the projection approximation was always satisfied whenever the images were recorded within the near-field regime.

To remove any dependency on attenuation in Eq. 4.3, the second term on the RHS can be neglected if $\mu\,|\nabla_\perp T(\mathbf{r}_\perp)|^2 \ll \left|\nabla_\perp^2 T(\mathbf{r}_\perp)\right|$. This was justified by Paganin (2006, p. 297) by stating that this was possible if the *'transverse intensity gradient and/or transverse phase gradient is not too strong'*. Here, it is explicitly shown when this is true. The following substitutions are made: $|\nabla_\perp T| \simeq |\Delta T|/a$ where $|\Delta T|$ is the maximum magnitude of the difference in projected thickness across the characteristic length a over which T varies appreciably in the $\mathbf{r}_\perp$ plane, and $\left|\nabla_\perp^2 T\right| \simeq |\Delta T|/a^2$. This simplifies the inequality to $\mu|\Delta T(\mathbf{r}_\perp)| \ll 1$. The lung tissue projected

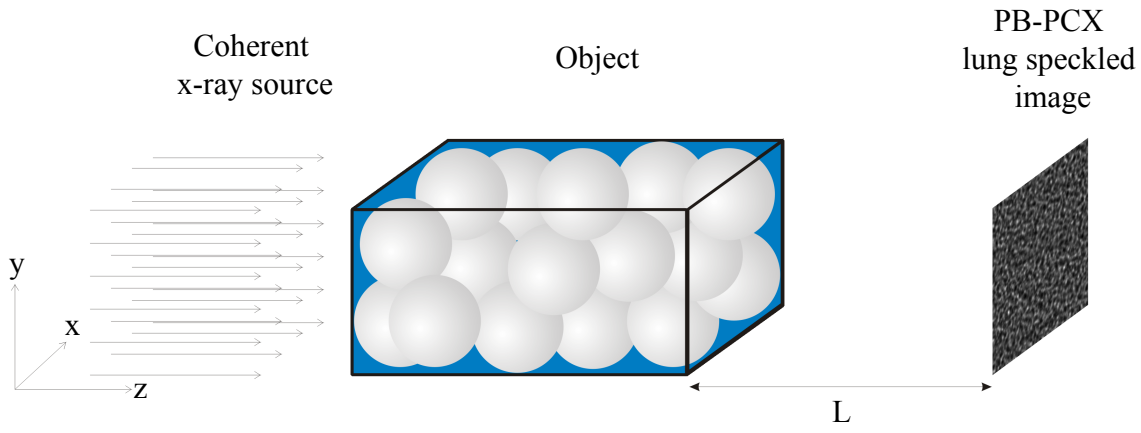

Figure 4.2: Alveoli in lung tissue, modeled by voids uniformly randomly embedded within an absorbing medium, are illuminated by a coherent x-ray source and a speckled PB-PCX image is recorded a distance L from the exit surface of the object.

thickness in rabbit kittens varies on average ~1 mm between adjacent pixels and as all lung imaging was done at 24 keV, $\mu = 54.7\ \mathrm{m}^{-1}$ (NIST, 2014), thus $\mu|\Delta T(\mathbf{r}_\perp)| \approx 0.055$. Consequently, the second term on the RHS of Eq. 4.3 can be ignored, hence the absolute square of the Fourier transform of Eq. 4.3 gives the power spectrum:

$$\left|\mathcal{F}\left\{\frac{I(\mathbf{r}_\perp, z = L)}{I(\mathbf{r}_\perp, z = 0)} - 1\right\}\right|^2 = L^2\delta^2 k_\perp^4 \left|\mathcal{F}\left\{T(\mathbf{r}_\perp)\right\}\right|^2 . \tag{4.4}$$

Here the Fourier derivative theorem was utilized to replace the Fourier transform of $\nabla_\perp^2$ with $-k_\perp^2 = -(k_x^2 + k_y^2)$ (Paganin, 2006, sec. A.4). Returning to the object of interest, for a uniformly random distribution of N air-filled spherical voids with radius R, each described by the object function $\tilde{G}(\mathbf{r})$ where $\tilde{G}(\mathbf{r}) = 1$ for $|\mathbf{r}| \leq R$ and $\tilde{G}(\mathbf{r}) = 0$ elsewhere, embedded in an absorbing medium ($V(\mathbf{r})$ is equal to unity everywhere in the volume and zero everywhere else), the object can be expressed as a sum of convolutions:

$$\tilde{T}(\mathbf{r}) = V(\mathbf{r}) - \sum_{n=0}^{N} \delta(\mathbf{r} - \mathbf{r}_n) \otimes \tilde{G}(\mathbf{r}), \tag{4.5}$$

where δ's are Dirac delta functions and $\mathbf{r}_n$ represents the random position of the n^{th} void within the dimensions of the absorbing medium. The integral of the modeled lung $\tilde{T}(\mathbf{r})$ along the optic axis z gives the projected thickness $T(\mathbf{r}_\perp)$. For simplicity, the first term on the RHS of Eq. 4.5 will be dropped as it affects only the zero spatial frequency in its corresponding power spectrum, which is unimportant for the analysis performed in this thesis. Generally, the random positions of the voids are unknown but the expectation value of the power spectrum of $\tilde{T}(\mathbf{r})$ can be evaluated without this information. Since the voids are uniformly randomly distributed, any coordinate within the absorbing medium has an equal probability of a void being found there. Thus, the expectation value of the power spectrum of $\tilde{T}(\mathbf{r})$ is (Talbot, 1966):

$$\left\langle \left|\mathcal{F}\left\{\tilde{T}(\mathbf{r})\right\}\right|^2 \right\rangle = \left[N^2\hat{\delta}(0,0,0) + N\right] \left|\mathcal{F}\left\{\tilde{G}(\mathbf{r})\right\}\right|^2 , \tag{4.6}$$

where $\hat{\delta}(0,0,0)$ has a value of unity at (0,0,0) and zero elsewhere (Kronecker delta). The expectation value operation will be dropped for notational simplicity and the first term inside the square brackets of Eq. 4.6 will also be dropped as it too only affects the zero spatial frequency. It can then be seen that the power spectrum of the random distribution of voids is N times the power spectrum of a single void for $k_\perp \neq 0$. This remains valid if the voids are uniformly randomly positioned and do not overlap with neighboring voids (Talbot, 1966).

To determine $T(\mathbf{r}_\perp) = \int_z \tilde{T}(\mathbf{r})dz$, the Fourier slice theorem is employed (Hseigh, 2003, sec. 3.5):

$$\left|\mathcal{F}\left\{\tilde{T}(\mathbf{r})\right\}\right|^2(\mathbf{k}_\perp, 0) = \left|\mathcal{F}\left\{\int_z \tilde{T}(\mathbf{r})\mathrm{d}z\right\}\right|^2(\mathbf{k}_\perp) = \left|\mathcal{F}\left\{T(\mathbf{r}_\perp)\right\}\right|^2(\mathbf{k}_\perp), \tag{4.7}$$

with a similar conclusion made for $|\mathcal{F}\{G(\mathbf{r}_\perp)\}|^2$. The 2D vectors in Fourier space are presented by $\mathbf{k}_\perp = (k_x, k_y)$. If $\tilde{T}(\mathbf{r})$ is rotationally symmetric then $T(\mathbf{r}_\perp)$ is independent of the orientation of $\tilde{T}(\mathbf{r})$. For $\tilde{T}(\mathbf{r})$ to be rotationally symmetric, so too must be $\tilde{G}(\mathbf{r})$ (i.e. for spherical particles). If $\tilde{G}(\mathbf{r})$ is not symmetric, but is randomly orientated, then $\left\langle\left|\mathcal{F}\left\{\tilde{T}(\mathbf{r})\right\}\right|^2\right\rangle$ is approximately rotationally symmetric with $\left|\mathcal{F}\left\{\tilde{G}(\mathbf{r})\right\}\right|^2$ being the azimuthal and polar average of the power spectrum of a single void extruded in the azimuthal and polar directions. Thus, Eq. (4.6) can be reduced to 2D:

$$|\mathcal{F}\{T(\mathbf{r}_\perp)\}|^2 = N\,|\mathcal{F}\{G(\mathbf{r}_\perp)\}|^2\,, \tag{4.8}$$

which is independent of object orientation.

Equation 4.8 shows that even though increasing the number of voids results in an increase in the amount of overlap seen between them in the projected thickness image, the power spectrum only changes by a multiplicative factor. This may seem counter-intuitive as the more voids there are the shorter the characteristic length scale of the image, which would be expected to preferentially amplify high spatial frequencies in the image. However, this is untrue so long as there is no physical overlap between neighboring voids in three-dimensional (3D) space and the positions of the voids are sufficiently random.

To determine $|\mathcal{F}\{G(\mathbf{r}_\perp)\}|^2$, the power spectrum of a 2D projected image of a sphere of radius R, the following integral was solved:

$$\left|\mathcal{F}\left\{\tilde{G}(\mathbf{r})\right\}\right|^2 = \left|\int_V \tilde{G}(\mathbf{r})\exp(-2\pi i\mathbf{k}\cdot\mathbf{r})\mathrm{d}\mathbf{r}\right|^2, \tag{4.9}$$

where $\mathbf{k} = (k_x, k_y, k_z)$ are 3D vectors in Fourier space. The evaluation of Eq. 4.9 is simplified by the rotational invariance of $\tilde{G}(\mathbf{r})$, which effectively reduces it to a one dimensional problem. The integral in Eq. 4.9 can then be expressed analytically by first expanding then evaluating the exponential term as a Taylor series to give an exact solution (Sykora, 2008):

$$\left|\mathcal{F}\left\{\tilde{G}(\mathbf{r})\right\}\right|^2 = \left|V\frac{3}{(kR)^2}\left[\frac{\sin(kR)}{kR} - \cos(kR)\right]\right|^2, \tag{4.10}$$

where $k = |\mathbf{k}| = \sqrt{k_x^2 + k_y^2 + k_z^2}$ and $V = \frac{4}{3}\pi R^3$ is the volume of a sphere.

Again, utilizing the Fourier slice theorem, the 2D power spectrum of a projected sphere is a slice of its 3D power spectrum through the origin. Since the 3D power spectrum is rotationally symmetric, the equation of the 2D power spectrum is identical to Eq. (4.10) but the z-coordinate is dropped and k is redefined as $k_\perp$.

The 2D version of Eq. 4.10, Eq. 4.8 and Eq. 4.4 are combined to arrive at the power spectrum of the near-field 2D intensity map of a 3D random distribution of identical voids normalized against its attenuation image[5]:

$$\left|\mathcal{F}\left\{\frac{I(x,y,z=L)}{I(x,y,z=0)}-1\right\}\right|^2 = L^2\delta^2k_\perp^4N\left|V\frac{3}{(k_\perp R)^2}\left[\frac{\sin(k_\perp R)}{k_\perp R}-\cos(k_\perp R)\right]\right|^2. \tag{4.11}$$

Here, $I(\mathbf{r}_\perp, z=0)$ can be recovered using SIPRA given in Eq. 1.60.

4.5 Determination of Lung Air Volume from Near-Field X-ray Speckle

Hooper et al. (2007) showed a prominent peak could be seen in azimuthally averaged PB-PCX power spectra of aerated rabbit kitten lungs and that the area (optical power) under the peak showed a dependence on V_L. The appearance of a prominent peak is consistent with Eq. 4.11 as it is a damped oscillator function. The observed dependance between the prominent peak and V_L is now not surprising as both Eq. 4.11 and V_L depend on the number and size of alveoli. The objective of this section is to quantify this dependence, starting with Eq. 4.11. To determine the area under the power spectrum (PS_{Area}), Eq. 4.11 is integrated over a select band of radial spatial frequencies, $k_{\perp 0} \leq |k_\perp| \leq k_{\perp N}$, and over the azimuthal angles $[0, 2\pi)$, then $\xi = k_\perp R$ is substituted to give:

$$PS_{Area} = 16\pi^2L^2\delta^2NR\int_{\xi_0/R}^{\xi_N/R}\left|\left[\frac{\sin(\xi)}{\xi}-\cos(\xi)\right]\right|^2 \mathrm{d}\xi. \tag{4.12}$$

The limits of the integral in Eq. 4.12 are dependent on R. However, under experimental conditions, the higher order peaks of the oscillatory function inside the integral are suppressed by the detector point spread function (PSF) and penumbral blurring, which explains why only a single peak was seen by Hooper et al. (2007)[6]. Consequently, the measured PS_{Area} will be dominated

[5]The derivation presented here also holds for absorbing particles in a non-absorbing medium. In this case, δ in Eq. 4.4 will correspond to the absorbing particle. To see this, the power spectrum of a near-field 2D intensity map of a 3D random distribution of identical voids was shown in Eq. 1.50 to be dependent on its Fraunhofer diffraction pattern (i.e. Fourier transform of its object function). Babinet's principle states that the Fraunhofer diffraction pattern from an opaque body is identical to that of an aperture of the same shape, except the zero frequency component, which is not relevant to our analysis (Born and Wolf, 2000, sec. 8.3.2). Hence, their power spectra in the near-field will also be identical.

[6]The detector PSF indicates the degree of blurring of the image caused by the detector. The detectors utilized in this thesis are scintillator-based where x-rays are converted into visible light by a material that absorbs x-rays and re-emits

by the lowest order peak. This effect is demonstrated using simulated data in the results section (Fig. 4.4(a)). Therefore, the limits of the integral from experimental images can be fixed so long as it includes the first order peak. The area under it is equal to the integral of Eq. 4.12 over its first order peak, bounded by the minima at $\xi = 0$ and $\xi = 4.493$ (these are the first two positive solutions to Eq. 4.12), yielding:

$$PS_{Area} = 34\pi^2 L^2 \delta^2 NR. \tag{4.13}$$

There are additional factors that have not entirely been accounted for in deriving Eq. 4.13, namely penumbral blurring, the detector PSF and asymmetrically shaped alveoli. These factors affect the area under all peaks in the power spectra. If the imaging setup remains unchanged between recordings over time, then the power spectra are equally affected by penumbral blurring and the detector PSF. While alveoli are not perfectly spherical, but more resemble polyhedra, they are uniformly randomly positioned and oriented. Consequently, the derivation above is still valid and PS_{Area} maintains its proportionality with R. For polyhedra, R holds a different definition to that of a sphere as will be revealed in the following proof. To prove PS_{Area} is proportional to R for any arbitrarily-shaped voids, Eq. 4.9 is generalized for a polyhedron with a value of unity in the domain $\Omega(\mathbf{r})$ of its shape function and 0 elsewhere:

$$\left|\mathcal{F}\left\{\tilde{G}(x,y,z)\right\}\right|^2 = \left|\int_{\Omega(\mathbf{r})} \exp(-2\pi i \mathbf{k}\cdot\mathbf{r})\mathrm{d}\mathbf{r}\right|^2. \tag{4.14}$$

For simplicity, Eq. 4.14 is re-defined in spherical coordinates:

$$\left|\mathcal{F}\left\{\tilde{G}(r,\theta_r,\varphi_r)\right\}(k,\theta_k,\varphi_k)\right|^2 = \left|\int_r\int_{\theta_r}\int_{\varphi_r} \exp(-2\pi i \mathbf{k}\cdot\mathbf{r})\sin\theta_r r^2 \mathrm{d}r\mathrm{d}\theta_r\mathrm{d}\varphi_r\right|^2, \tag{4.15}$$

where (r,θ_r,ϕ_r) and (k,θ_k,ϕ_k) are the spherical coordinates of $\mathbf{r}$ and $\mathbf{k}$, respectively. Note that the subscripts do not indicate dependence on them; they serve to differentiate which angles are associated with which coordinate space. To determine the spherical form of the exponential term in Eq. 4.15, note that it is a plane wave and is a solution to the wave equation defined in Eq. 1.5. By re-expressing the wave equation in spherical coordinates and then solving it to obtain the plane wave solution, the spherical form of the exponential term is (Qang et al., 2008):

---

them as visible light. The visible light is re-emitted with angular divergence that increases with scintillator thickness, causing blurring of the image. In addition, penumbral blurring arises from the finite x-ray source size and is related to the degree of spatial coherence described in section 1.3. In footnote 7 of chapter 1, an analogy was given of Young's double slit where an increasing source size gradually blurred the fringe contrast until it was completely washed out, which in Fourier space is equivalent to applying a low-pass filter.

$$\exp(-i2\pi\mathbf{k}\cdot\mathbf{r}) = (2\pi)^3 \sum_{l=0}^{\infty}\sum_{m=-l}^{l}(-1)^l j_l(kr)Y_l^m(\theta_k,\varphi_k)\overline{Y_l^m(\theta_r,\varphi_r)}, \tag{4.16}$$

where $j_l(kr)$ are spherical Bessel functions of order l, $Y_l^m(\theta_k,\phi_k)$ are spherical harmonic functions of degree l and order m, and the overline represents the complex conjugate.

Substituting Eq. 4.16 into Eq. 4.15 gives:

$$\left|\mathcal{F}\left\{\tilde{G}(r,\theta_r,\varphi_r)\right\}(k,\theta_k,\varphi_k)\right|^2 = \left|\int_r\int_{\theta_r}\int_{\varphi_r}(2\pi)^3\sum_{l=0}^{\infty}\sum_{m=-l}^{l}(-1)^l j_l(kr)Y_l^m(\theta_k,\varphi_k)\overline{Y_l^m(\theta_r,\varphi_r)}\sin(\theta_r)r^2\mathrm{d}r\mathrm{d}\theta_r\mathrm{d}\varphi_r\right|^2. \tag{4.17}$$

Equation 4.17 is first integrated with respect to r as it is implicitly dependent on θ_r and φ_r. This can be seen by rewriting $r = RG(\theta_r,\varphi_r)$, where R is defined as the inradius that corresponds to the radius of the largest circle that can be drawn within $\Omega(\mathbf{r})$ of the polyhedron. $G(\theta_r,\varphi_r)$ is an arbitrary function defined the shape of the void. Thus, integrating the terms that include r:

$$A(r) = \int_r j_l(kr)r^2\mathrm{d}r. \tag{4.18}$$

A change of variables is made to bring out k by letting $a = kr$:

$$\begin{aligned} A(a) &= \frac{1}{k^3}\int_a j_l(a)a^2\mathrm{d}a \\ &= \frac{1}{k^3}B(a) \\ &= \frac{1}{k^3}B(kRG(\theta_r,\varphi_r)), \end{aligned} \tag{4.19}$$

where $B(a) = \int_a j_l(a)a^2da$. The exact form of $B(a)$ is not important in this proof.

Substituting Eqs. 4.19, 4.17 and 4.8 into Eq. 1.50, the power spectrum of a near-field 2D image, normalized against its attenuation image, of a 3D random distribution of identical arbitrarily shaped polyhedron voids is attained:

$$\left|\mathcal{F}\left\{\frac{I(x,y,z=L)}{I(x,y,z=0)}-1\right\}\right|^2 = L^2\delta^2k_\perp^4 \times\left|\frac{1}{k_\perp^3}\int_{\theta_r}\int_{\varphi_r}(2\pi)^3\sum_{l=0}^{\infty}\sum_{m=-l}^{l}(-1)^l Y_l^m(\theta_k,\varphi_k)\overline{Y_l^m(\theta_r,\varphi_r)}\mathrm{d}B(k_\perp RG(\theta_r,\varphi_r))\theta_r\mathrm{d}\varphi_r\right|^2. \tag{4.20}$$

Here, the Fourier slice theorem was again utilized where the 2D power spectrum of an arbitrarily shaped void is a slice of its 3D power spectrum through its origin, this is assuming that the voids

are uniformly randomly distributed and orientated for its 3D power spectrum to be rotationally symmetric. To determine PS_{Area}, Eq. 4.20 is integrated over the first order peak and $\xi = k_{\perp}R$ is substituted to give:

$$PS_{Area} = L^2\delta^2 NR\times \int_{\xi}\left|\int_{\theta_r}\int_{\varphi_r}(2\pi)^3\sum_{l=0}^{\infty}\sum_{m=-l}^{l}(-1)^l Y_l^m(\theta_k,\varphi_k)\overline{Y_l^m(\theta_r,\varphi_r)}B(\xi G(\theta_r,\varphi_r))\mathrm{d}\theta_r\mathrm{d}\varphi_r\right|^2 d\xi. \quad (4.21)$$

Equation 4.21 shows that for any arbitrarily shaped polyhedron voids, which are uniformly randomly distributed and orientated, the area under the 2D power spectrum of its near-field image, normalized against its attenuation image, is proportional to R. Evaluation of the triple integral term in Eq. 4.21 would equal different values for different shaped polyhedra. For a sphere, it would equal to $34\pi^2$ and therefore Eq. 4.21 reduces to Eq. 4.13. The alveoli were modeled as spheres because a simple analytic solution for Eq. 4.10 exists. If the overall shape of the alveoli is non-spherical and is known then an exact solution for PS_{Area} can be solved.

Returning to the main objective of this section in relating PS_{Area} to V_L, since 90% of V_L can be accounted for in the alveoli, the remainder being the volume of the airways of the lungs (this includes the trachea, bronchi and bronchioles) (Weibel, 1963), V_L can be expressed as:

$$V_L \propto NR^3. \quad (4.22)$$

This expression is true for any arbitrarily shaped polyhedra[7].

The relationship between V_L and PS_{Area} will depend on how N and R vary with time (t). That is, if N and R were parametrized by $N = at^n$ and $R = bt^r$, respectively[8], where n, r, a, b are constants, and substituted in Eqs 4.13 and 4.22 it is easy to show that:

$$V_L \propto PS_{Area}^{\frac{n+3r}{n+r}}. \quad (4.23)$$

[7]To prove Eq. 4.22 is true for all polyhedra, the following triple integral is written to determine the total volume of N arbitrarily shaped polyhedra: $V = N\int_{\Omega(\mathbf{r})}\mathrm{d}\mathbf{r}$, where $\Omega(\mathbf{r})$ is the domain of its shape function. This integral is converted into spherical coordinates, i.e. $V = N\int_r\int_\theta\int_\varphi \sin(\theta)r^2\mathrm{d}\mathbf{r}$, and as was similarly argued just after Eq. 4.17, r can be expressed as $r = RG(\theta,\varphi)$. Substituting this expression into the integral and integrating over R, the following expression is obtained: $V = \frac{1}{3}NR^3\int_\theta\int_\varphi \sin(\theta)G^3(\theta,\varphi)\mathrm{d}\theta\mathrm{d}\varphi$. This proves that $V \propto NR^3$ as required. If the polyhedron was assumed to be a sphere, then $G(\theta,\varphi)$ would be independent of θ and φ, and be equal to unity. This reduces the expression for V to that of N spheres, $V = \frac{4}{3}NR^3$.

[8]These *ad hoc* parametrization with respect to time of the alveolar number and size as a power law are supported by other studies (Suki et al., 1994; Barabási et al., 1996). Many of the possible physiological events that take place in the lung can be adequately described by a power law relationship. For instance, the beginning of inspiration can be marked by $t = 0$, making a and b represent the initial number and size of alveoli. During inspiration, n and r can take on some non-zero value to signify recruitment of alveoli and increase in their size. Then, during expiration, n and r can take on some negative value along with different values for a and b to signify de-recruitment and decrease in size.

In section 4.6, the expression given for PS_{Area} (Eq. 4.13) is first validated from simulations of PB-PCX images of colloids. Directly measuring V_L from PS_{Area} using Eq. 4.23 is not possible unless the alveolar shape, detector PSF and penumbral blurring are accounted for, and that n, r, a, and b are known. Instead, in section 4.7, PS_{Area} will be calibrated against known values of V_L to account for these factors, which is then used to measure unknown values of V_L from PB-PCX chest images. The known V_L values were calculated utilizing the method described in section 2.2.1 (Kitchen et al., 2008).

4.6 Validation of the Power Spectrum of a Random 3D Distribution of Identical Voids

4.6.1 Methodology

To validate the relationship between the PS_{Area} with N and R in Eq. 4.13, simulations were performed with conditions set similarly to that of imaging real lung tissue. First the lung tissue was simulated by creating a projected thickness image of uniformly randomly positioned spherical voids within a uniform slab of tissue. Next the projection approximation was used to calculate the amplitude and phase shift at the exit surface using Eqs. 1.35a and 1.35b to form the exit surface wavefield. This was propagated using the angular spectrum formalism of scalar wave optics described in section 1.9 to obtain the PB-PCX image. These steps are described in detail below and the specific conditions for these simulations are summarized in Table 4.1.

Projected lung thickness images of size 11.8×11.8 mm^2, with pixel size 0.59μm, were produced by first creating a projected thickness map with a positive constant value set across the image to represent the lung thickness. The position of each void was created using the Box-Muller method to generate random 2D coordinates (Wilks, 2011). If including the void into the image resulted in the maximum thickness of voids at any one pixel exceeding that of the lungs, then an alternate coordinate would be generated until this was not the case. Due to the images being discretely sampled, they were convolved with a Gaussian kernel, with full width half max (FWHM) B=16 μm to soften the jagged edges of the discretely sampled voids. This served to minimize the number of pixels with $|\nabla_\perp \varphi| > \frac{\pi}{2}$ radians per pixel so that the phase map at the exit surface was sufficiently sampled.

Three different sets of projected thickness lung samples were generated. The range of void sizes chosen for the lung samples corresponded to that of the alveoli observed in computed tomography (CT) reconstructions of rabbit kitten lungs (see section 5.4, Figs 5.7(c) and 5.7(d)) and also in

Pixel size (μm)	0.59
Mean alveolar radius (μm)	30, 35, 40, 45, 50, 55, 60, 65, 70, 75
Alveolar radius standard deviation (μm)	5.9
SOD (m; D)	∞
ODD (m; L)	1, 3
Attenuation coefficient (μ_w(NIST, 2014))	54.735 m^{-1} (at 24 keV)
Refractive index decrement (δ_w(NIST, 2014))	3.99×10^{-7} (at 24 keV)
Maximum volume packing fraction (%)	75
Lung thickness (mm)	10

Table 4.1: Parameters used for simulating PB-PCX images of lung tissue.

other studies (Kovar et al., 2002; Hooper et al., 2007; Bickenbach et al., 2009). Also, from the CT reconstructions of rabbit kitten lungs, the volume packing density of alveoli was measured to be as high as 76% and on average 54%. In the first set, 65 μm radius voids were uniformly randomly packed in a 10 mm thick sample at 54% volume packing density. Several PB-PCX images were simulated from this sample at different ODD to determine the optimal ODD at which to image the kittens for calibrating V_L against PS_{Area} in section 4.7. In the second set of samples, the same lung sample was generated as in the first set but with a 1 mm thick sample. Several such samples were generated and stacked to achieve different sample thicknesses. This was to simulate lung tissue with varying N while R was fixed. In the third set of samples, for each of the different mean sized voids, 5900 voids were suspended in a 10 mm thick sample. In contrast to the first set, this was to simulate lung tissue with varying R while keeping N fixed. A maximum volume packing fraction of 75% was achieved from the sample with the largest mean radius void (75 μm).

All simulated PB-PCX images were convolved with a Gaussian PSF of FWHM $B = SL/D$ to account for penumbral blurring (Gureyev et al., 2009). The source size S was set to 150×10 μm^2 and the source-to-object distance (SOD) $D = 210$ m. These parameters were those of the synchrotron beamline used for experimental studies reported in section 4.7.1. The detector PSF was accounted for by increasing the FWHM of the Gaussian PSF by 20 μm. The value of 20 μm was determined from measuring the PSF of the detectors used to image kittens in section 4.7. PS_{Area} was calculated by integrating their power spectra from $k_o = 0.85$ mm^{-1} (this was the smallest non-zero spatial frequency sampled) to k_N =Nyquist frequency.

4.6.2 Results

Before quantitatively validating the theory presented in section 4.4, simulated lung speckles were qualitatively compared with experimental lung speckles in both real and reciprocal space. The

experimental lung speckles are from a rabbit kitten imaged at 24 keV, 3 m ODD and with a pixel size of 16.2 μm (see section 4.7.1 for details of the experimental conditions). The simulated lung speckles were from the first sample set whose PB-PCX images was produced under those same experimental conditions. The real and simulated speckles respectively shown in Fig. 4.3(a) and 4.3(b) appear very similar. This is reflected in their azimuthally averaged power spectra shown in Fig. 4.3(c) and Fig. 4.3(d), respectively, with a dominant peak over a similar band of spatial frequencies. This shows that modeling lung tissue as voids randomly embedded in an absorbing material to be a highly accurate model.

While very similar, there were slight discrepancies between the real and simulated speckle image. The intensity contrast of real speckles shown in Fig. 4.3(a) is lower than that of simulated speckles in Fig. 4.3(b). This is reflected in their azimuthally averaged power spectra, where for real lungs (Fig. 4.3(c)) the peak is broader and weaker than that of simulated lungs (Fig. 4.3(d)). There are a number of possible reasons: (1) the lung samples are not exactly the same in regards to the alveoli/void shape, size distribution and volume packing density, (2) the detector PSF and penumbral blurring were inaccurately accounted for, (3) there was incoherent scattering by lung tissue and air between the object and detector, (4) the alveoli are closely packed rather than uniformly randomly distributed (the effect of close packing on lung speckle will be discussed in section 5.4), and (5) the projection approximation is enforced in simulations, but this may be significantly violated in real experiments. The term significant was used as there will always be some transverse scattering within the lungs that results in the exit surface wavefield deviating from that predicted by the projection approximation.

Next, to verify the theory presented in section 4.4, namely Eq. 4.11, the power spectrum of a simulated lung speckle image, normalized against its attenuation image, was plotted with that expected using Eq. 4.11 (see Fig. 4.4(a)). The speckled image corresponded to voids with mean radius 65 μm that were packed uniformly randomly in a 1 mm water-filled container at 1 m ODD. Both power spectra show similar first order peaks. The position of their first order peaks are not exactly aligned because the lung speckles were simulated from a Gaussian distribution of different sized voids while the analytic solution assumed single sized voids equal to the mean size. Also, the detector PSF and penumbral blurring was applied only to the simulated lung speckle, causing its peak to shift to lower spatial frequencies. These are also responsible for partially suppressing its second order peak and completely suppressing the remaining higher order peaks. In summary, the similarity between the power spectra in Fig. 4.4(a) validates Eq. 4.11 up to the first order peak, which is what the power spectrum is integrated over to calculate PS_{Area} (see Eqs. 4.12 and 4.13).

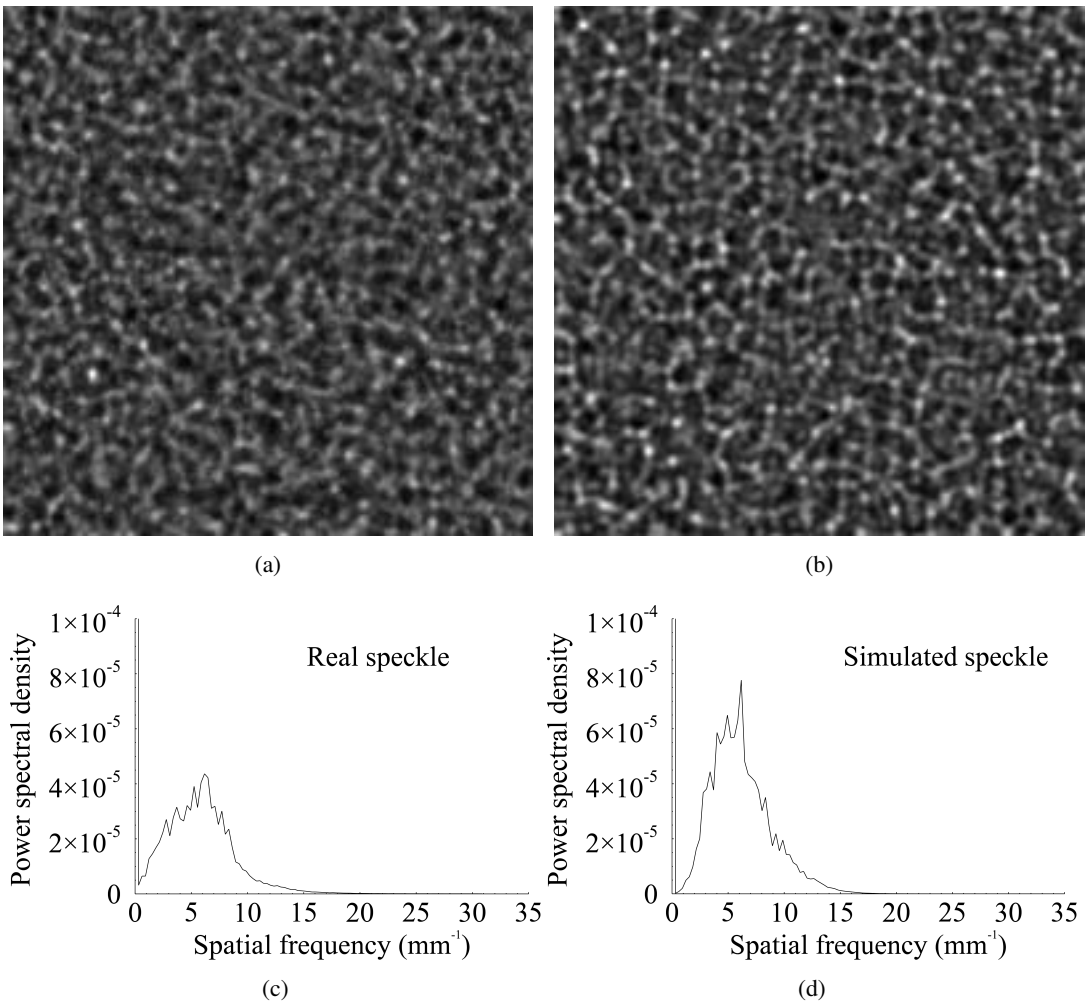

Figure 4.3: PB-PCX images of a ~10 mm thick sample (a) of real and (b) simulated (mean radius of 65 μm) lung tissue normalized by their phase retrieved attenuation image (image dimensions: 3.24 × 3.24 mm^2). Their corresponding power spectra are shown in (c) and (d), respectively.

To verify the linear relationship between PS_{Area} and N, as predicted by Eq. 4.11, PS_{Area} (normalized against the ODD) was plotted against the sample thickness of simulated lung tissue from the second sample set at 1 m and 3 m ODD (see Fig. 4.4(b)). The sample thickness is essentially proportional to N since the total volume fraction was made approximately constant throughout the sample. At 1 m ODD, PS_{Area} was directly proportional to N for all lung thicknesses. However, at 3 m ODD, Fig. 4.4(a) shows N at first varies linearly with PS_{Area} but begins to break down at $N = 3000$ as N_F approached, then became less than, $\max\{1, |\varphi|_{max}\}$.

The dependence between R and PS_{Area} was investigated by plotting PS_{Area} (normalized against the ODD) against R of simulated lung tissue from the third sample set at 1 m and 3 m ODD, as shown in Fig. 4.4(c). As predicted by Eq. 4.11, PS_{Area} varies linearly with R. Surprisingly, this is

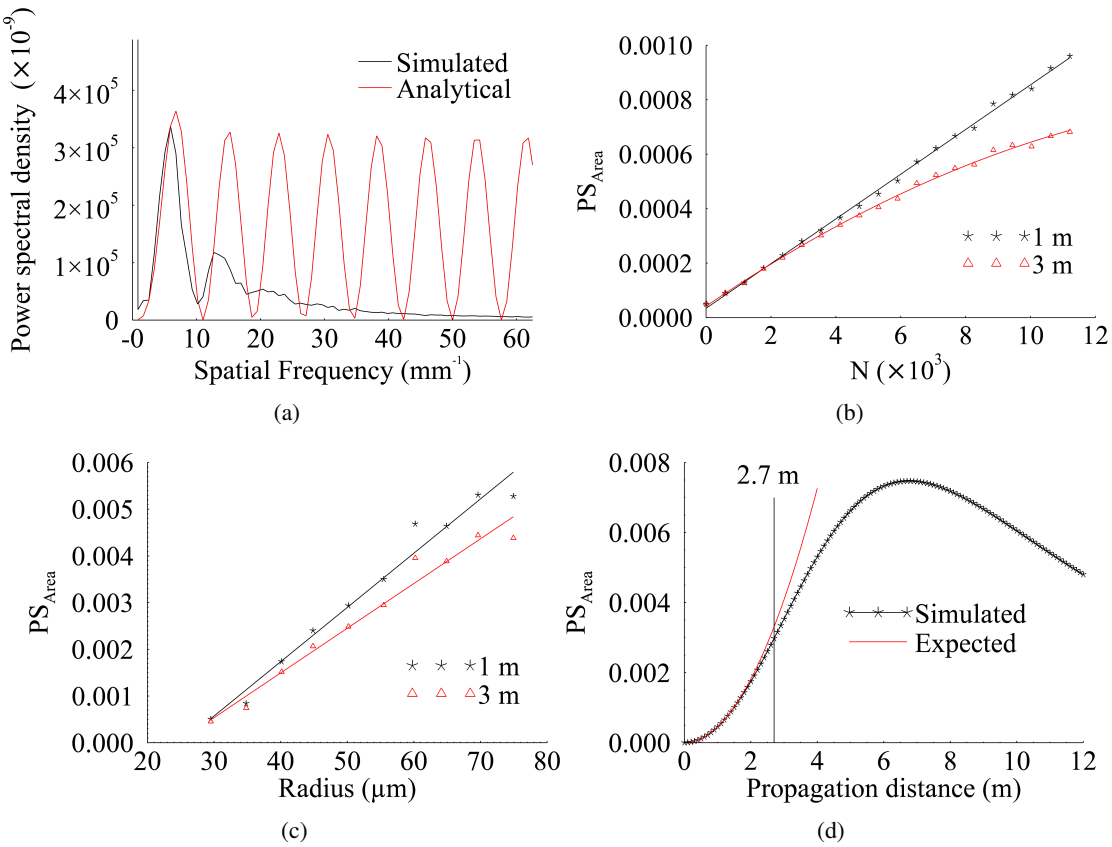

Figure 4.4: (a) Comparison of simulated power spectra of lung tissue, normalized against their attenuation images, versus that given by Eq. 4.11, for voids of 65 μm radius at 1 m ODD. Plots of PS_{Area}, normalized against the ODD, of simulated lung tissue versus (b) number of voids, of radius 65 μm, and (c) void radius with a maximum volume packing density of 75%; all at an energy of 24 keV, and at 1 m and 3 m ODD. (d) A plot displaying the PS_{Area} of 65 μm radius voids packed in a 10 mm thick water-filled container against ODD compared with that calculated from Eq. 4.11.

true even at 3 m ODD when N_F is less than $\max\{1, |\varphi|_{max}\}$.

Figure 4.4(d) compares the PS_{Area} calculated from the power spectra of simulated PB-PCX images from the third sample set, normalized against their attenuation images, and that expected using Eq. 4.13 over a range of ODD values. Setting an upper limit on the discrepancy between the PS_{Area} values at 10%, the near-field regime was found to extend at up to ~2.7 m ODD (marked in Fig. 4.4(d)). The maximum ODD within the near-field regime calculated from $N_F = \max\{1, |\varphi|_{max}\}$ was found to be 0.83 m. Here, $|\varphi|_{max}$ represented the average phase excursion of the exit surface wavefield instead of the maximum phase excursion to form a better statistical representation of whether the PB-PCX image was within the near-field regime. The lack of agreement between the maximum ODDs is likely due to the discrepancy threshold being set to 10%. Reducing the discrepancy threshold would result in better agreement. However, a 10% error in PS_{Area} is sufficiently accurate for the work presented in this thesis. PB-PCX images of rabbit kittens in

section 4.7 were therefore recorded at 3 m ODD. While choosing the ODD to be less than 2.7 m would ensure the near-field condition was well satisfied, it was found that the contrast-to-noise ratio (CNR) ratio of lung speckles was small and weakened the correlation between V_L and PS_{Area}. This is elaborated upon in section 4.7.3.

4.6.3 Discussion

The theory presented in section 4.4 that relates speckle contrast to the size and number of voids uniformly randomly distributed in water from simulations of their PB-PCX images has been validated. The concentration and size of voids were chosen to resemble that of alveoli to determine the optimal experimental conditions for imaging lungs under which the theory is approximately valid.

The simulations performed herein employed the projection approximation to calculate exit surface wavefields before determining the validity range of the near-field condition. In real experiments, however, x-rays undergo transverse scattering within the sample and hence the projection approximation is not always satisfied. Possible future work in addressing this issue is provided in section 6.2.

The tissue thickness chosen to simulate lungs was similar to that of newborn rabbits. Human lungs are, however, significantly thicker than that of rabbits with similar sized alveoli of 90-104 μm in radius and there are many times more of them (Ochs et al., 2004). To remain within the validity of the projection approximation and near-field condition, the x-ray source energy could be increased. This is possible because, as shown in Fig. 1.10, high refractive index decrement values, and therefore strong phase contrast, can be maintained at high energies relative to attenuation contrast. Alternatively, an analytical relationship between speckle contrast and the structural properties of the lungs could be derived beyond the validity of the projection approximation and near-field condition, but the relationship will unlikely be simple.

4.7 Measuring Lung Air Volume from Near-field X-ray Speckle

4.7.1 Methodology

To reiterate from section 4.5, the theory presented does not allow V_L to be measured directly from PS_{Area} unless the detector PSF, penumbral blurring, alveolar shape and the coefficients introduced in Eq. 4.23 are known. While the former two can easily be measured and incorporated into the theory, this is not so for the latter two factors. The theory assumes that the alveoli are spherically

shaped, which from CT reconstructions of the lungs is not correct (they are more like polyhedrons). Moreover, they exist in a range of shapes and sizes. Determining the coefficients introduced in Eq. 4.23 requires understanding of alveolar mechanics. While it is currently a topic of high interest, and is explored in chapter 5, these coefficients are difficult to measure since they would be different between animals and experiment settings. In this section, all these factors are accounted for by measuring the PS_{Area} and V_L simultaneously using PB-PCX images of rabbit kittens to create a calibration curve. This curve would enable regional measures of PS_{Area} to be converted into V_L.

The image acquisition, sample preparation and image processing are similar to that described in section 3.3.1, However, there are sufficient differences that it is necessary to describe most of the methods here in full.

Image acquisition and sample preparation

All imaging experiments took place in Hutch 3 of beamline 20B2 at the SPring-8 synchrotron in Japan with a Si (111) double-bounce monochromator tuned to 24 keV (Goto et al., 2001). The x-ray SOD was set at D = 210 m. All animal procedures were conducted in accordance with the protocol approved by the Monash University Animal Ethics Committee and the SPring-8 Animal Care and Use Committee. At 31 days of gestation, pregnant New Zealand white rabbits were anesthetized initially by an intravenous injection (Rapinovet [Schering-Plough Animal Health, USA]; 12 mg kg^{-1} bolus, 40 mg h^{-1} infusion) and anaesthesia was maintained via isoflurane inhalation (1.5– 4%; Isoflurane, Delvet Pty. Ltd., Australia).

Kittens were delivered by caesarean section, sedated and surgically intubated. Those in the first group (Group-Water, n = 15) were immersed in a water-filled cylindrical poly-methyl methacrylate container (plethysmograph) with their head out and the chamber sealed with a rubber diaphragm enclosing their necks. See Fig. 2.3 in chapter 2 for a schematic diagram of the setup. The lungs in their fluid-filled state were required to calculate absolute V_L using the volumetric technique developed by Kitchen et al. (2008), and so imaging was performed immediately after birth when the lungs are initially non-aerated. The kittens were humanely killed at the end of each experiment via anesthetic overdose of Nembutal (Abbott Laboratories, USA, 100 mg/kg). Kittens in the second group (Group-Air, n=3) were humanely killed immediately after birth via anesthetic overdose. The deceased kittens were supported in an upright position and connected to a pneumotach (flowmeter) to measure differential airflow at the mouth opening throughout each respiratory cycle.

Two different detectors were used to acquire PB-PCX images: (i) a large format (4000×2672 pixels) Hamamatsu CCD camera (C9300-124F21) with a tapered fiber optic (FOP) coupling the

sensor to a 20 μm thick gadolinium oxysulfide ($Gd_2O_2S:Tb^+$; P43) phosphor (this is the same detector utilized for the work shown in section 3.3), and (ii) a tandem lens-coupled scientific-CMOS (sCMOS) imaging sensor coupled to a 25 μm thick gadolinium oxysulfide ($Gd_2O_2S:Tb^+$; P43) phosphor (pco.edge; 2560×2160 pixels). The effective pixel sizes for these two detectors were 16.2 μm, based on the taper ratio of 1.8:1, and 15.23 μm, respectively. In both groups, imaging sequences were respiratory gated, with timing controlled by a custom-designed pressure-controlled ventilator (as used for the work shown in section 3.3) (Kitchen et al., 2010b) with a respiratory cycle of 2.5 s and exposure time of 40 ms. In Group-Water, the kittens were immersed in water and imaged at a frame rate of 3 Hz using both detectors while for those in Group-Air only the sCMOS camera was used and imaged at a frame rate of 10 Hz.

Image processing and analysis

All PB-PCX images were flat and dark field corrected and distortion corrected as described in section 3.3.1.

In constructing the calibration curve, each PB-PCX chest image of the kittens from Group-Water was divided into quadrants. Quadrants were created by partitioning the chest along the spinal column to separate the left and right lungs and also partitioning along the seventh rib down from the neck to separate the apical and basal lobes. This increased the number of (V_L, PS_{Area}) points and also helped ensure that variability in the lung thickness between quadrants did not affect the calibration curve. V_L was calculated utilizing the technique developed by Kitchen et al. (2008). PS_{Area} was calculated using the LHS of Eq. 4.11 and integrating from $k_o = 2\,\mathrm{mm}^{-1}$ to k_N =Nyquist frequency. Given the experimental conditions it was found that this k_o value optimized the correlation strength of the $PS_{Area} - V_L$ curves between kittens and quadrants. Evidence for this can be seen in section 4.7.2 (Fig. 4.6(c)), which shows low frequency components up to $2\,\mathrm{mm}^{-1}$ being noticeably contaminated by remnant low frequency trends arising predominately from the bone and skin signal. For those kittens from Group-Air a flowmeter (pneumotach), which measures the rate of air flowing in and out of the lungs, was employed to validate the calibration curve. Both PS_{Area} and V_L were normalized against the number of pixels so that PS_{Area} measured from a region-of-interest (ROI) of any size can be directly converted to V_L.

From Eq. 4.11, the attenuation image ($I(x, y, z = 0)$) is required to calculate PS_{Area}. This was estimated using SIPRA given in Eq. 1.60 with $\mu = 54.74\ \mathrm{m}^{-1}$ and $\delta = 3.99 \times 10^{-7}$ set for water at 24 keV as given in section 3.3.1. As demonstrated in section 2.2.1, and by Beltran et al. (2011), SIPRA will accurately reverse the lung tissue-induced phase contrast, but will over-smooth regions

where there is bone. Therefore, dividing PB-PCX chest images by their attenuation image (using SIPRA) will accurately remove the attenuation contrast of lung tissue but not entirely in regions where there is bone, particularly along the edges of the bone. Nevertheless, its contribution to the power spectra is small compared to the lung speckle signal.

4.7.2 Results

A $PS_{Area} - V_L$ calibration curve was generated from the 15 newborn rabbit kittens in Group-Water. Two cameras were used that had slightly dissimilar spatial frequency responses, or modulation transfer functions (MTFs). The MTF is the power spectrum of the detector PSF. It represents the ability of the detector to accurately preserve the amplitudes of each of the spatial frequencies in an image and this depends on its design. Two distinct calibration curves were measured for the different cameras, which differed by a multiplicative factor of 3.35. Such a difference is not surprising given the different phosphor thicknesses and optical coupling systems. PS_{Area} measurements calculated using the sCMOS camera were multiplied by 3.35 to align with the calibration curve attained from the FOP camera. While this highlights the need to produce a calibration curve for each of the detectors, a calibration curve would also be needed for different experimental configurations. This includes different types of animals due to variability in lung morphology and the choice of x-ray energy and ODD since the power spectrum of the speckle produced would be affected by such factors. A direct plot of V_L against PS_{Area} showed a non-linear relationship. It was found that raising V_L to the power $\frac{n+r}{n+3r} = \frac{3}{4}$ best linearized the curve based on the chi-square goodness-of-fit test.

A linearized $PS_{Area} - V_L$ calibration curve is plotted, of which 10% of the data points are shown in Fig. 4.5(a). A weighted linear trend ($V_L^{3/4} = a \times PS_{Area} + b$) was fitted with coefficients $a = (1.345 \pm 0.001) \times 10^{-4}$ and $b = (-6.84 \pm 0.02) \times 10^{-7}$. The uncertainty in $V_L^{3/4}$ was determined using the rational exponent function derived in section 3.3.1 that relates the uncertainty in V_L to the ROI size. The uncertainty in PS_{Area} was determined from the standard deviation of PS_{Area} values measured from several water-only ROIs selected from PB-PCX images. A $PS_{Area} - V_L$ curve from the quadrants from one of the kittens used for Fig. 4.5(a) is plotted in Fig. 4.5(b). This shows the $PS_{Area} - V_L$ curve from the quadrants diverge slightly from each other at large V_L. This divergence was observed in other kittens at different V_L that depended on their total lung capacity. The possible causes for this are discussed in section 4.7.3. While there would be a slight reduction in accuracy, the curve fits the majority of points extremely well overall, as Fig. 4.5(a) shows and also that the Pearson product-moment correlation coefficient $R^2 = 0.97$ for the fitted curve.

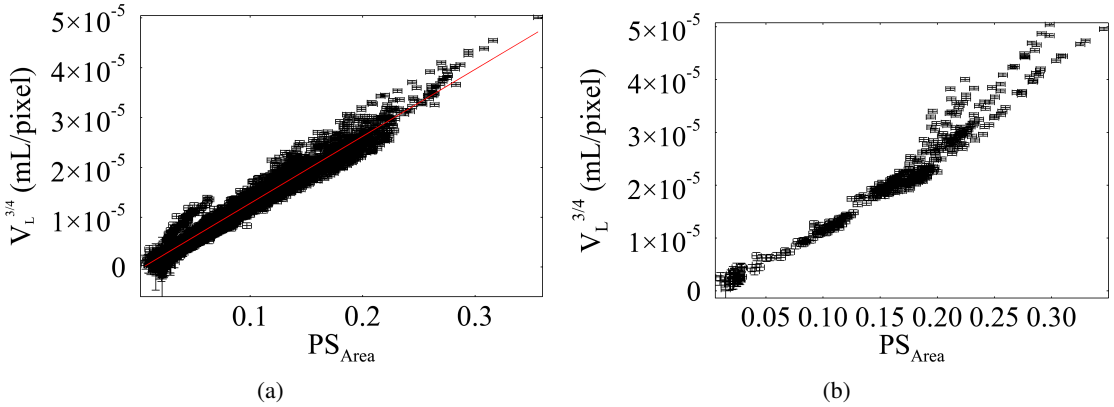

Figure 4.5: A calibration curve between V_L and the PS_{Area} from PB-PCX chest images divided into quadrants showing data from (a) 15 kittens, with only a subset of points ($\sim$ 10%) displayed for clarity, and (b) a single kitten. A weighted linear fit was performed on the entire set of points on the calibration curve and is shown in (a) as a red line.

The PB-PCX images of a kitten immersed in water and air after dividing by their attenuation image are displayed in Figs. 4.6(a) and 4.6(b), respectively. These show how the attenuation-induced intensity trends are removed. Their corresponding power spectra in Fig. 4.6(c) reveal a large spike between frequencies 0 mm^{-1} and 2 mm^{-1}. For the kitten in water, this is attributed predominantly to the phase contrast of bone. An even larger spike between those frequencies is seen for the kitten in air due to the enhanced boundary of the skin and bone. To show that the amplitude between those frequencies are dominated by bone and/or skin, the power spectra are subtracted from that of the same kitten but with no lung aeration. Figure 4.6(d) shows the resultant power spectra and the disappearance of the large spike between spatial frequencies 0 mm^{-1} and 2 mm^{-1}. Beyond the frequency 2 mm^{-1}, the power is dominated by that arising from the high contrast lung speckle, which was the range over which PS_{Area} was calculated. However, the power spectra correspond to very similar changes in lung air volume (water: 0.272 ml and air: 0.274 ml), yet their PS_{Area} are evidently different. A number of possible reasons are suggested and discussed in section 4.7.3. Nonetheless, it was found that the power spectra in air and water consistently differed by a multiplicative factor of 5.37 when using the same detector, which enables volumetric measures to be made by simply accounting for this factor.

The calibration curve in Fig. 4.5(a) generated from kittens imaged in water was multiplied by the factor of 5.37 before measuring the total change in V_L of three kittens imaged in air. This was then compared with that measured using a flowmeter (see Fig. 4.7(a)). A straight line was fitted to Fig. 4.7(a) with a gradient of 1.06±0.06 (R^2= 0.978). This shows the calibration curve to be a highly accurate tool for determining the total change in V_L without needing to immerse the

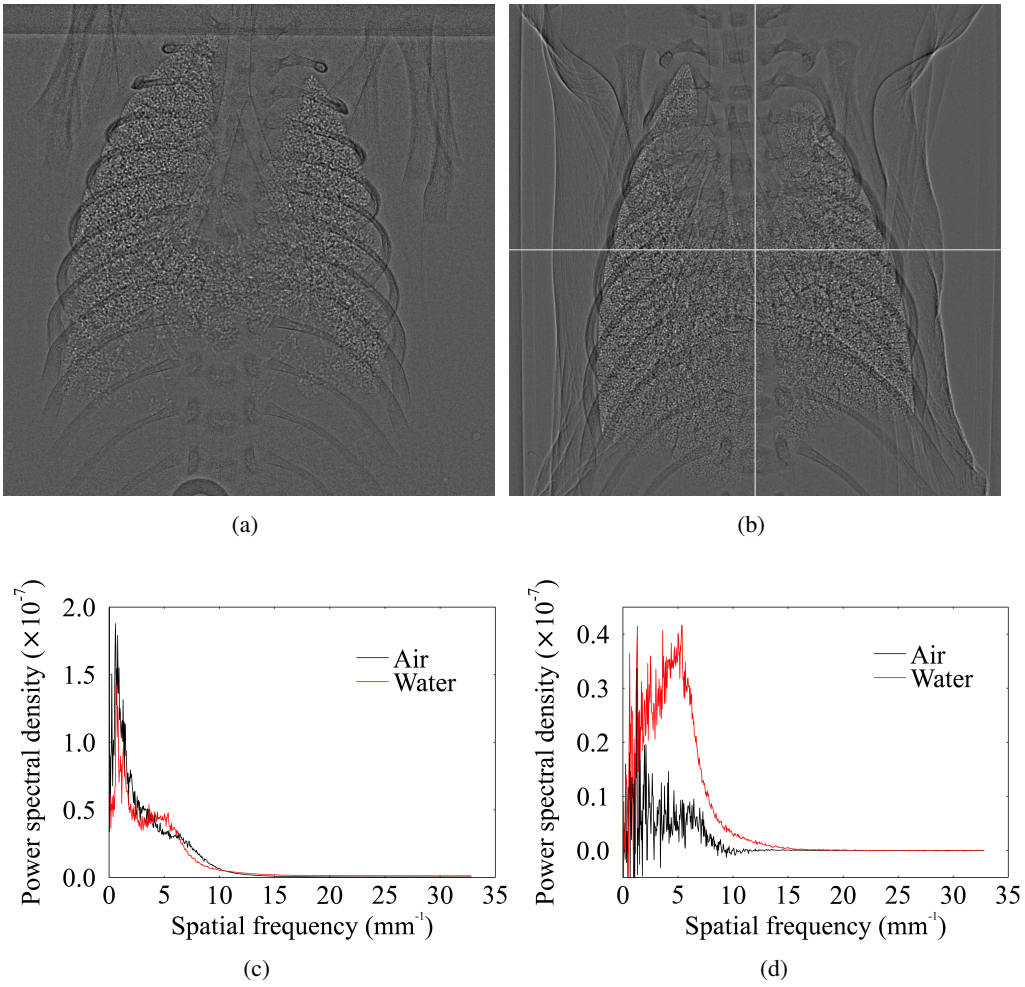

Figure 4.6: A pair of 24×21 mm^2 PB-PCX chest images of a newborn rabbit kitten in (a) a water-filled tube and in (b) air. (c) shows their respective power spectra after dividing by their attenuation image reconstructed using phase retrieval. (d) shows the power spectra in (c) after subtracting from that of their corresponding non-aerated PB-PCX image.

animal in water and, moreover not requiring a PB-PCX image of the lungs in their fluid-filled state. This gives confidence the calibration curve can be used for retrieving accurate regional volumetric information.

A quadrant-based analysis of a single kitten imaged in air (Fig. 4.7) reveals non-uniform lung aeration. Figure 4.6(b) shows how the quadrants were delineated, indicated by the white lines. As expected, the volumetric curves of each quadrant oscillate in phase with the mechanical ventilation cycle. However, there are subtle but important physiological differences between quadrants. The lower quadrants show a larger increase in tidal volume[9] than in the upper quadrants, while the upper right quadrant is the only quadrant showing a significant increase in FRC from its initial FRC. These differences could be attributed to inhomogeneous lung compliance and airway resistance,

[9]The difference in lung air volume at end-inspiration and end-expiration during normal breathing

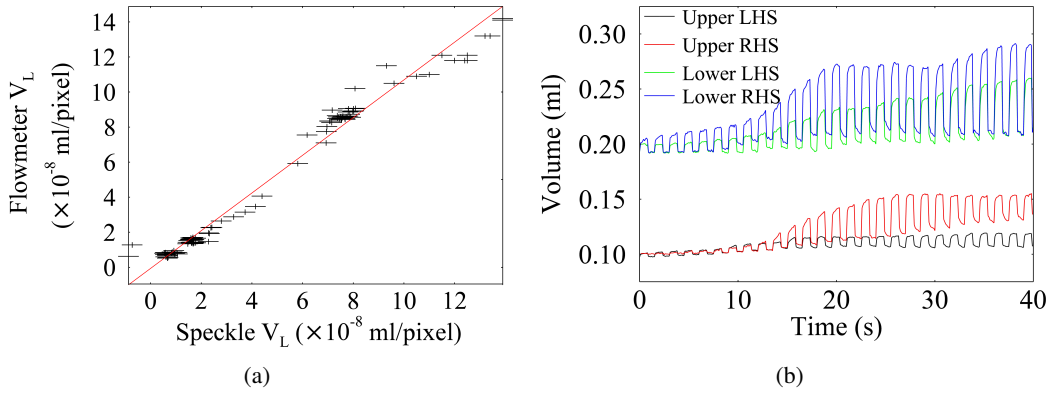

(a) (b)

Figure 4.7: (a) A representation of the accuracy of using the calibration curve to measure the change in total V_L of kittens imaged in air in comparison to using a flowmeter. The red line is the line of best fit. (b) Regional V_L measurements from a lung image sequence after partitioning the images into quadrants. Note that the lower quadrant curves have been offset by 0.1 ml to better distinguish them from the upper quadrant curves.

which are related to lung tissue structure. This quantification of non-uniform aeration using regional analysis is critical for assessing the efficacy of resuscitation strategies for newborn infants and detecting local abnormalities in the lungs (Pillow et al., 2006; Kitchen et al., 2014; Tingay et al., 2014).

Next, the ability of the technique developed herein to build a pixel-by-pixel map of V_L is demonstrated using 128 x 128 pixel ROIs to measure V_L from the speckle texture. The calibration curve (Fig. 4.5(a)) was used to convert PS_{Area} measured from the speckle pattern into V_L in each ROI. This was performed on pairs of images where each pair was a PB-PCX chest image of a kitten recorded at end-inspiration and at end-expiration. A volumetric map was constructed for each image of each pair and the difference was taken between them to give the tidal volume at each pixel. At a low tidal volume, Fig. 4.8(a) shows lung aeration to be highly localized where the greatest change in V_L is at the bifurcation of the left/right main bronchi into tertiary bronchi. As the tidal volume increased (see Figs. 4.8(b) and 4.8(c)), the flow of air became more apparent at the peripheral regions where lung expansion occurred. Summation of the pixels in Fig. 4.8 gave the total change in V_L (Fig. 4.8(a): 0.15 ml, Fig. 4.8(b): 0.27 ml, Fig. 4.8(c): 0.37 ml), which agreed closely with that from calculating PS_{Area} of the total lung (Fig. 4.8(a): 0.12 ml, Fig. 4.8(b): 0.24 ml, Fig. 4.8(c): 0.36 ml). These values respectively correspond to a percentage difference of 4.6%, 2.7% and 1.3%. These small differences predominantly arise due to having a discrete frequency domain for the power spectrum analysis. Since different sized ROIs sample the frequency domain differently, a small error is introduced into V_L. Accuracy can be improved by interpolating the

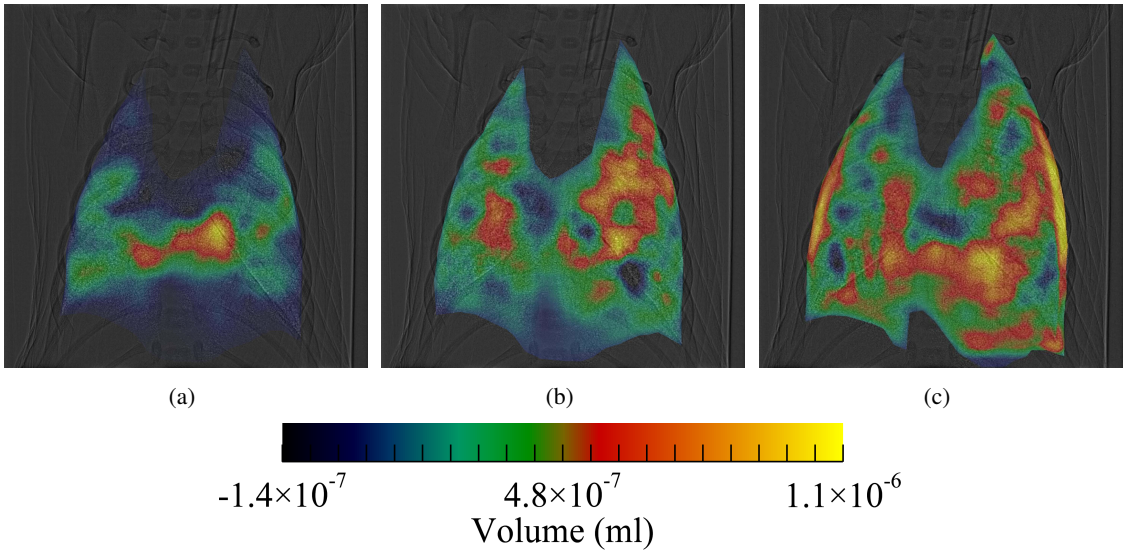

Figure 4.8: Regional volumetric maps of dimensions 14.6×14.6 mm^2 from a mechanically ventilated rabbit kitten in air ventilated using three different tidal volumes: (a) 0.12 ml, (b) 0.24 ml and (c) 0.35 ml. These maps of regional tidal volumes demonstrate the distribution of air when it enters the lung.

discrete spatial frequencies.

4.7.3 Discussion

The technique outlined here presents a novel approach to measuring V_L regionally from PB-PCX chest images without requiring the use of a contrast agent. Imaging modalities such as positron emission tomography (PET) or magnetic resonance imaging (MRI) require a medium to be injected inside the lungs with which to measure V_L while water acts as a contrast agent for previously developed techniques that use PCX modalities. Here, no such contrast agent was required. Instead, the air inside the lungs, combined with their complex structure, served to provide a speckle pattern whose statistical properties are directly related to the airway morphology, thereby enabling V_L to be measured non-invasively from 2D projections.

There are three limitations that can be foreseen in this technique: (i) motion blur, (ii) the multi-valued relationship between PS_{Area} and V_L, and (iii) the minimum size of the region from which V_L can be measured. The motion of the chest wall causes blurring of the images, which results in a reduction in PS_{Area} (Goodman, 2010, sec. 4.6). The zero spatial frequency is, however, largely unchanged, which is why those techniques previously discussed that measure V_L from the intensity of pixels are minimally affected by motion blur. Reducing the exposure time can reduce the degree of motion blur, but this coincides with a decrease in SNR. This can be offset by improvements in detector technology that have greater quantum efficiency and produce less

noisy images. Alternatively, there are techniques that could measure and correct for motion blur (Wang et al., 2005). However, respiratory-induced motion blur is non-linear and difficult to correct. Motion blur can also be avoided through patient breath holds or taking measurements towards the end of inspiration/expiration when there is minimal chest motion.

The relationship between V_L and PS_{Area} was introduced in Eq. 4.23 as a power law relationship: $V_L \propto PS_{Area}^{\frac{n+3r}{n+r}}$. The calibration curve in Fig. 4.5(a) showed PS_{Area} was approximately proportional to $V_L^{3/4}$ and therefore the exponent $\frac{n+3r}{n+r} = \frac{4}{3}$. For the exponent to be > 1, both n and r must be > 0 during inspiration and < 0 during expiration. This means alveoli are being recruited and increasing in size during inspiration, and vice versa during expiration. However, the study of $PS_{Area} - V_L$ curves of a single rabbit kitten lungs during ventilation displayed subtle deviations in the exponent away from the value $\frac{4}{3}$ during breathing (see Fig. 4.5(b)). This effect was masked in the calibration curve as it was made up of multiple single breath curves from kittens mechanically ventilated with different positive inspiratory and positive end-expiratory pressures. This allowed a single calibration curve to approximate V_L. Furthermore, at large volumes ($\geq$10 ml/kg), the exponent between quadrants sometimes diverged, as seen in Fig. 4.5(b). These deviations in the exponent may be due to the variable relationship between $V_L$and PS_{Area}. That is, the constants making up the exponent may not be a constant, which means the lungs behave differently, over space or time. This is investigated in greater detail in chapter 5. Alternatively, the variable exponent may be caused by the break down of the near-field condition. As the lungs respire, the alveolar size and number change and therefore the Fresnel number N_F may decrease towards or below unity. Across the lungs, the average projected thickness between quadrants is different in that the apical region of the lungs is thinner than that adjacent to the diaphragm. Thus, the phase gradients and consequently N_F would also be different between quadrants.

When performing regional V_L analysis, the region must be large enough to sufficiently sample the spatial frequencies of a power spectrum. As detector technology continues to improve, it is expected that detectors with larger numbers of pixels producing lower noise coupled with better detector spatial resolution will become available. Hence V_L will be able to be measured in smaller ROIs in the future. Another major benefit of having lower noise level detectors is a reduced ODD. The ODD was set at up to 3 m to produce a sufficiently strong speckle SNR, but this distance was found to be at the edge of the near-field regime (section 4.6.2). Hence, PB-PCX chest images were also recorded at 1.5 m ODD but were not included in this thesis because V_L weakly correlated with PS_{Area} due to the weak CNR of the speckle. Thus, a lower detector noise level will allow PB-PCX images to be recorded at shorter ODD while still having a short exposure time to minimize

chest-induced motion blur.

Since the technique presented herein does not require the subject to be immersed in water like the techniques described in chapter 3, the improved SNR allows significant reduction in the exposure time and avoids the practical difficulty of imaging animals in water. The SNR of an image of a rabbit kitten imaged in air was measured to be $\sim 1.4\times$ larger than a kitten imaged in water. The region chosen in calculating SNR was at the thickest (central) portion of the body below the lungs. This improvement in SNR will be important for translating this research for use with lower powered laboratory-based x-ray machines (Tuohimaa et al., 2007; Ewald et al., 2011; Garson et al., 2013).

Despite reducing the SNR, immersing the chest in water may be important in removing the skin-air interface, which can reduce lung speckle contrast. The loss of speckle contrast in air was accounted for empirically in this work by comparing the power spectra of rabbit kittens imaged in air and water at different V_L. It would be interesting in future work to determine the source of this reduction. The skin may act as a random phase diffuser that causes a reduction in speckle contrast. This was initially argued to be due to a loss of coherence in the x-ray beam resulting in this effect to be labeled as 'decoherence' (Robinson et al., 2003; Vartanyants and Robinson, 2003; Han et al., 2004; Xiao and Voelz, 2006). However, Nugent et al. (2003) highlighted that according to Liouville's theorem, coherence cannot be destroyed and that decoherence in this context is a misnomer. The apparent loss in coherence, and therefore the reduction in speckle contrast, may be attributed to the limited spatial resolution of the detector to resolve the small variations in the skin. This leads to blurring of speckles, which mimics what would occur if the x-ray source actually lost coherence. Nesterets (2008) simulated objects comprised of features that a detector can and cannot resolve, and showed the contrast of the resolvable features degraded. Using wave-optics, they showed the unresolvable features acted as a damping factor that attenuates the contrast of resolvable features. Results from preliminary investigations into decoherence are presented in section 6.2.

4.8 Concluding remarks

This chapter describes an entirely novel approach to measuring V_L regionally by generating a calibration curve between lung speckle, quantified by the area under its power spectrum, and lung air volume. This approach is a significant improvement over other imaging-based volumetric techniques that require either a large radiation dose (e.g. CT), potentially harmful contrast agents (e.g. SPECT, PET and MRI), or alignment of bone (chapter 3). While PB-PCX imaging does

involve the use of radiation, the associated dose is minimal compared to CT and can be performed in real-time.

Unlike the previous PB-PCX imaging-based techniques of measuring V_L from two-dimensional images, the subject does not need to be immersed in water, which significantly boosts the SNR of the image and makes this technique more practical to implement. This has a two-fold advantage; the exposure time can be reduced to minimize both motion blur and radiation dose. Also, an image of a lung in its fluid-filled state is not required to perform absolute measurement of V_L. The theory underlying this method was first tested on simulated lung tissues and was found to be accurate and robust against a range of lung tissue thicknesses and particle sizes. Then, the method was tested on several newborn rabbit kittens for measuring both the total and regional changes in V_L, and successfully validated against other proven techniques.

5 Real-time Measurement of Alveolar Size and Population Using PB-PCX Imaging

Measuring alveolar population and size would allow the lung mechanics of a healthy lung to be directly studied, which is currently poorly understood. Better understanding of this would lead to abnormalities in the lung being more readily recognized and for optimizing mechanical ventilators to minimize the risk of ventilation-induced lung injury (VILI). The importance of studying the dynamics of alveolar morphology is elaborated in section 5.1. A review of techniques for imaging alveoli and their drawbacks is presented in section 5.2. Some of the image processing techniques utilized for studying alveolar morphology are described in section 5.3.

In the previous chapter, a generalized theory was introduced relating lung speckle contrast in the near-field regime, which was quantified by the area under the power spectrum (PS_{Area}), to alveolar population and size for the purpose of measuring lung air volume (V_L). That theory was validated on simulated lung tissue. This chapter (sections 5.4 and 5.5) presents a novel technique for measuring alveolar population and size utilizing that theory and is an expansion on the paper published in *Biomedical Optics Express* (Leong et al., 2014).

5.1 The Importance of Studying the Dynamics of Alveolar Morphology

The dynamics of alveolar morphology are not yet very well understood, partly due to the inherently complicated interconnecting nature of alveoli, but also because previous studies used different experimental techniques, animal subjects and techniques for morphometric analysis (Carney et al., 1999; Escolar and Escolar, 2004). Understanding how alveoli change in shape and size during respiration can help in the recognition of abnormal behaviors and appearances that lead to VILI and other diseases of the lung. To elaborate, studies have proposed that over-distension of alveoli and continual collapsing and re-inflating of alveoli when under mechanical ventilation induce shear

stress along the alveolar wall leading to VILI (Muscedere et al., 1994; Hubmayr, 2002). Lung related diseases such as emphysema can alter the molecular structure of the lungs and have been shown to affect the mechanical behaviour of the alveoli (Faffe and Zin, 2009).

Lung pressure-volume (PV) curves have been an important tool for describing the behavior of the alveoli during respiration. These are a plot of the transpulmonary (for spontaneously breathing) or airway (for mechanical ventilation) pressure against the total volume change of air in the lungs during a single respiration cycle. A typical PV curve of a healthy lung is shown in Fig. 5.1(a), which shows a hysteresis between the inspiration and expiration curves. This hysteresis represents the difference in energy required to inflate and deflate the lungs. The reason for this discrepancy in energy is still under debate. For a long time it was believed that the lungs accommodated the flow of air from the total isotropic expansion and contraction of individual alveoli. This was supported by direct visualization of the alveoli that showed their total surface area varied with V_L raised to the power $\frac{2}{3}$ (Dunnill, 1967; Forrest, 1970; D'Angelo, 1972). The hysteresis is then the sum of that of the individual alveoli, which may arise from their viscoelastic properties[1] (Sugihara et al., 1972). Alternatively, or also, concentration of surfactant may differ during inspiration and expiration[2] (Hellmuth and Lima, 2012). However, inflating the lungs with saline to remove the air-liquid interface (i.e., surface tension) significantly reduces the hysteresis (see Fig. 5.1(b)). Hence, the viscoelastic property of the alveoli only makes a small contribution to the hysteresis of the PV curve. Figure 5.1(b) also shows that the hysteresis size remains largely unchanged after inflating the lungs with air without the presence of surfactant. The only significant change is that lung compliance ($\frac{\Delta V}{\Delta P}$) is reduced as expected since surface tension is increased.

There have been studies that have shown the hysteresis in the PV curve may be instead due to the sequential recruitment/derecruitment of alveoli (Smaldone et al., 1983; Carney et al., 1999; Brancazio et al., 2001; Frazer et al., 2004). At the beginning of inspiration, Fig. 5.1(a) shows that lung compliance is poor, suggesting that many of the alveoli may be inflated from a collapsed

[1] Materials that revert to their original state after being deformed are elastic and do not dissipate energy. Those that form a resistance to deformation are viscous. Therefore, a viscoelastic material subjected to deformation will resist but eventually alter to the final state that it would have reached if it was elastic. This resistance is what causes energy to dissipate. The alveoli are a viscoelastic material such that when air enters them they do not immediately respond by inflating. Similarly, when air exits they deflate back to their original size but in a delayed manner. This viscoelastic property lies in the arrangement of the molecular bonds changing to accommodate the deforming material but encounters resistive forces such as friction between molecules. The energy lost from resistive forces contributes to the hysteresis in lung PV curves.

[2] Surfactant lowers the surface tension created by the air-liquid interface lining the inner layer of the alveolus. Surface tension greatly affects the internal pressure of the lung and therefore the lung PV curve. During respiration, surfactant is dynamically secreted and absorbed. This may cause the concentration of surfactant to be uneven during inspiration and expiration, thereby contributing to the hysteresis in the lung PV curve.

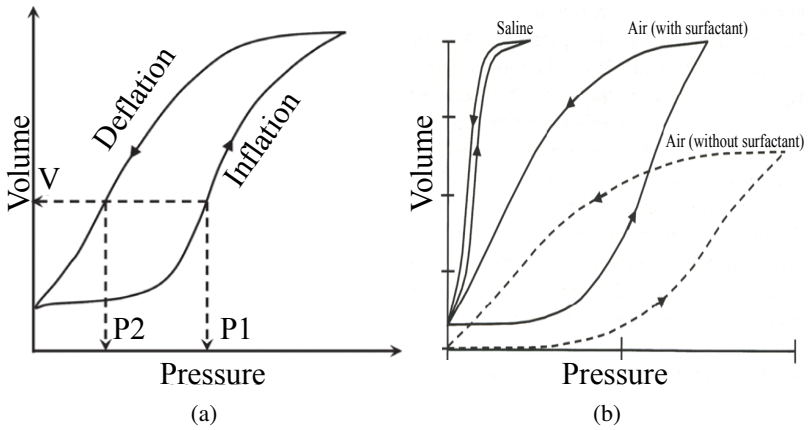

Figure 5.1: (a) A typical PV curve of the lung during inspiration and expiration and (b) several PV curves of the lung under different conditions during breathing (Orgeig et al., 2014).

state[3] to overcome the opposing force from surface tension. This is known as alveolar recruitment. As the alveoli increase in size, the same increase in pressure produces larger increases in volume. The expiration curve follows a different path to that during inspiration because the inflated alveoli simply decrease in size together. In other words it is believed that during expiration there will be more alveoli open, but they will be smaller in size than at an equivalent volume during inspiration. Towards the end of expiration, some alveoli collapse, or de-recruit. One opposing argument against alveolar recruitment/derecruitment is that the apparent change in the number of alveoli may be due to alveoli becoming filled with fluid instead of collapsing (Hubmayr, 2002).

Despite the ambiguity about the information lung PV curves convey, they have been useful in optimizing mechanical ventilators. Mechanical ventilators assist in breathing by creating a pressure gradient across the lung to draw air into the lungs for gas exchange. A pressure gradient can be created by lowering the internal pressure of the lung (negative pressure mechanical ventilator) or raising the pressure at the opening airway above that of the lung (positive pressure mechanical ventilator) to draw air in. It is important that the pressure gradient set is not too steep so as to over-distend the alveoli or inflate too rapidly. That pressure gradient is reversed to push air out of the lungs by either lowering or raising the pressure at the opening airway or the lungs, respectively. However, setting the internal pressure back to atmospheric for certain individuals can cause alveoli to collapse and injure the lung. For example, the alveoli of premature infants are prone to collapsing since they lack surfactant to lower surface tension. To prevent this, the internal pressure of the lungs are set slightly higher than normal by the mechanical ventilator. Particular features of the PV curve, such as the knee point along the inflation curve in Fig. 5.1(a), have been used to help set the

[3]Consider a balloon. From everyday experiences, more work is required to blow into the balloon, i.e., it has low compliance, initially than when it is at a larger size. This effect was proven and quantified by James and Guth (1996).

lower and upper pressure limits to avoid alveolar collapse and over-distension, respectively (Lu and Rouby, 2000).

Although lung PV curves are not commonly utilized clinically these days for many reasons such as a lack of a standardized procedure to measure it, it can help diagnose and establish severity of chronic obstructive pulmonary disease such as asthma and emphysema (Harris, 2005). Salazar and Knowles (1964) developed an exponential-based model to fit to lung PV curves, which Greaves and Colebatch (1980) utilized and found one of the factors in that model was significantly different between healthy and emphysematous lungs. This factor was found to correlate with the average alveolar size, the difference in the factor showing emphysema patients exhibit larger than average alveolar sizes, which is in agreement with what is known about emphysema (Smith et al., 2012).

The interpretation of lung PV curves can often be muddled by the methodology adopted. For example, the supersyringe (Matamis, 1984), constant flow (Suratt et al., 1980) and multiple-occlusion (Goetz et al., 2001) methods can produce different PV curves of the same lung (Harris, 2005). This makes it less reliable in inferring the structure and behavior of the lungs. Furthermore, lung PV curves provide only global insight of the lung and not regional mechanical differences, which can be very beneficial to clinicians. Regardless, lung PV curves have indicated that alveolar mechanics is rather complicated but may be a more sensitive indicator to respiratory diseases than static chest x-ray images and pulmonary tests, and help reduce the risk of VILI. These underlie the motivation for directly measuring the morphology of the lung and its mechanics locally. In the next section, different imaging-based techniques that directly study the behavior of alveoli are surveyed.

5.2 Current Techniques for Imaging Alveoli

Directly studying lung structure at the alveolar scale can be performed *ex vivo* through histological imaging. There the lungs are inflated and immediately fixed chemically or frozen to preserve their structural integrity. They are then cut into thin slices for viewing under a light microscope (Braber et al., 2010; Arab et al., 2011; Schwenninger et al., 2011). Histological images have high spatial resolution to resolve the alveoli and its supporting features, but their main advantage is the ability to stain particular features of interest such as the alveolar walls. This has proven useful in correlating alveolar structure to different lung conditions that are associated with disease or aging. For example, aging was found to be associated with enlargement of the alveoli as elastin, which is responsible for maintaining shape, is gradually lost (Yamamoto et al., 2003). Kyphoscoliosis describes an abnormal curvature of the spine that hampers the alveolar development during the early stages of birth. Consequently, these patients have fewer but larger alveoli (Berend and Marlin,

1979).

While lung histology provides highly detailed images of the lungs *ex vivo*, it is limited to postmortem and biopsy studies. It is also highly invasive and localized, which makes it unsuitable as a first choice diagnostic tool for live subjects. Tomographic-based imaging modalities provide a non-invasive and more global approach to studying alveolar mechanics. Section 5.4 provides such results in an animal model using synchrotron radiation, as seen in Figs. 5.7(c) and 5.7(d). Alveolar analysis using computed tomography (CT) has also been demonstrated elsewhere (Watz et al., 2005; Roth-Kleiner et al., 2014). A major drawback to CT of the chest is the high exposure to ionizing x-ray radiation (Bushberg et al., 2012, p. 399). Diffusion magnetic resonance imaging (MRI) has insufficient spatial resolution to resolve alveoli but can infer their size by exploiting the material-dependent diffusion of the contrast agent ^{3}He that is administered before imaging (Fichele et al., 2004). The acquisition times for both of these modalities are long compared to the length of a single spontaneous breathing cycle, which makes dynamic imaging of the alveoli in real-time unfeasible due to motion artefacts. Although there has been progress towards improving the imaging acquisition frame rate, this is traded-off against poor spatial resolution and signal-to-noise ratio (SNR) to resolve the alveoli (Li et al., 2007; Tsao, 2010). Alternatively, prospectively gating, where projections (CT) or pulsed signals (MRI) from similar time points in the respiratory cycle are grouped together during post-processing, allows multiple reconstructions per respiratory cycle with comparable temporal resolution to x-ray imaging, but requires relatively consistent simultaneous measures of V_L for sorting (Low et al., 2003; Nieman et al., 2009; Dubsky et al., 2012).

To overcome the poor temporal resolution of tomographic-based imaging, investigation of lung structure at the alveolar scale in real-time has been done via several other lung imaging techniques that do not use ionizing radiation, including optical coherence tomography (OCT), confocal laser scanning microscopy (CLSM) and ultrasound (Ossant et al., 2001; Bickenbach et al., 2009; Meissner et al., 2009; Unglert et al., 2012; Chang et al., 2013). OCT uses a partially coherent visible light source and a Michelson interferometer to produce three-dimensional (3D) images (see Fig. 5.2). A Michelson interferometer works on a similar principle to the Bonse-Hart interferometer shown in Fig. 1.15. The light source is split into two arms, the reference and sample arm, by a beam splitter, where each are reflected off a mirror, and recombined to form a fringe pattern at the detector. A fringe pattern forms from a low coherence light source only when the optical path difference between the two arms is less than the coherence length of the source (see section 1.3); essentially the two arms must be close to having equal optical path lengths. By replacing one of the mirrors with a sample, light is reflected off the interfaces (as shown in Fig. 5.2) within the object

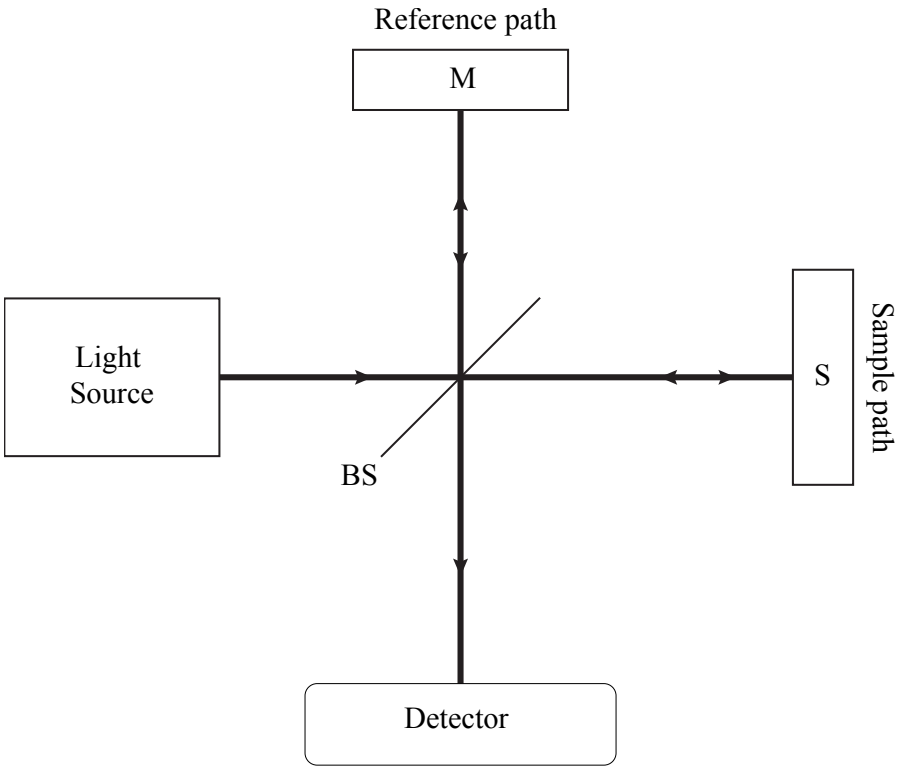

Figure 5.2: A schematic diagram of an OCT setup. BS=Beam splitter. M=Mirror. S=Sample. (Fujimoto et al., 2000).

and recombined with the beam from the reference path. Since a fringe pattern only forms when the two arms have almost equal optical path length, the depth of the interfaces can be deduced. A 3D map of the sample can be constructed with the intensity values representing the maximum fringe amplitude. In turn, the fringe amplitude represents that of the reflected wave that is dependent on the refraction index gradient across the interface. The reconstructed 3D image is then similar to a PCX image with enhanced edges along the boundaries. This makes OCT ideal for imaging the alveoli, which are air-filled cavities surrounded by tissue, that produces strong refractive index gradients. However, OCT has a depth of focus of several millimeters that is insufficient to penetrate the skin and into the lungs (Raffel et al., 2007). Invasive maneuvers must then be performed to image alveoli. For example, fiber optic cameras can be inserted via tracheal intubation (McLaughlin et al., 2012; Kirsten et al., 2013).

In CLSM, a visible light source is reduced to a small point using a pinhole and, with a lens, is focused onto a plane within the sample as shown in Fig. 5.3. A second lens is positioned with its focal point coinciding with the focused plane. The light scattered from the sample is refocused by the second lens. A pinhole is positioned at the focal point of the second lens to reject light scattered from unfocused planes and remove diffraction rings. Diffraction rings arise from the finite size of

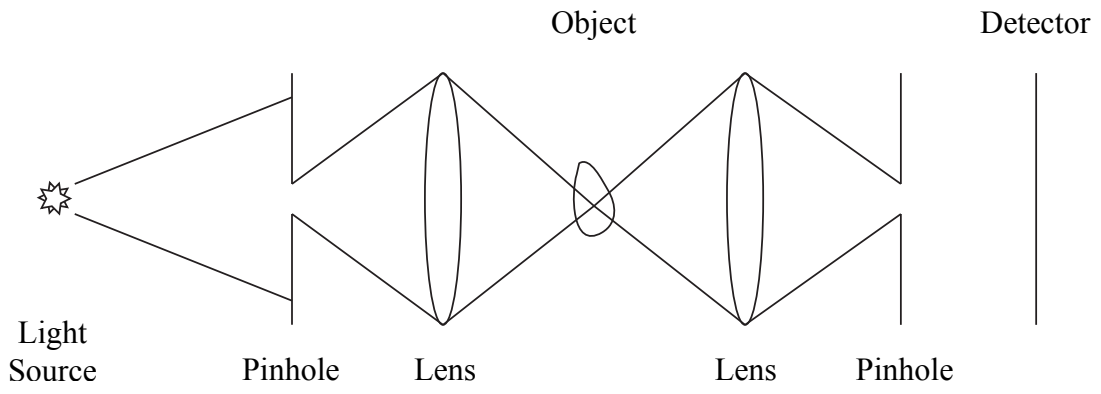

Figure 5.3: A schematic diagram of a CLSM setup.

the lens, which reduces the spatial resolution (Hecht, 2002, secs. 10.2.5-6). Shifting the position of the lens along the optic axis allows imaging of different planes within the object to build a 3D image. Similar to OCT, it renders highly detailed images of alveoli but has limited penetrative power due to visible light being highly scattering in soft tissue (Namati et al., 2008). To overcome this limitation, CLSM has been engineered into an endoscope and inserted into the airways to directly visualize the alveoli (Schwenninger et al., 2008). However, that was shown to alter the intraplueral pressure and subsequently artificially changed the alveolar morphology (Unglert et al., 2012). Unlike OCT, CLSM can provide fluorescence imaging when the lungs are stained with a fluorescent dye, which increases the contrast of the alveoli (Gaertner et al., 2012). While using a single pinhole to scan across the object is very slow, the latest microscopes have multiple pinholes that increase the frame rate to as much as 100 Hz. However, this technology is still restricted to a field-of-view (FOV) of the order tens of microns (Sisan et al., 2006; McAllister et al., 2008).

Ultrasound produces 3D images using pulsed ultrasonic waves. It works under a very similar principle to OCT, but because sound waves travel significantly slower than light its phase can be directly measured; hence there is no need to interfere with a reference wave to recover the phase. Sound waves are generated from a piezoelectric crystal, which converts an electrical current into pulsed sound waves, illuminates the object, and reflects off the interfaces. A piezoelectric crystal working in reverse converts the reflected sound waves into an electric signal to construct an image that, like PCX images, reveal the boundaries of the materials. Depth information is recovered from the time taken for the pulsed sound wave to reflect from the object. While the spatial resolution (typically on the order of mm) of ultrasound is insufficient to directly visualize the alveoli, the distribution of the scattered sound waves could potentially be used to recover alveolar size. Insana et al. (1990) developed a technique to measure particle sizes by relating the scattered sound waves

to a model based on the first Born approximation[4] and assumes a uniformly random distribution of spheres/voids. The model is very similar to that in section 4.4 but theirs was derived in the context of the interactions between sound waves and matter, which not only depends on the density (i.e., the refractive index) but also the compressibility of the medium. This technique has only been tested on glass particles and tumors from which their sizes were accurately recovered (Insana et al., 1990; Chen et al., 1998; Anderson et al., 2010). Application of this technique has yet to be trialled on animal models, but the images obtained from ultrasound would encode scattering sizes of structures other than the lung airways such as bone and collagen (Insana et al., 1990). A method to delineate these components may then need to be developed.

The aforementioned alveolar imaging techniques provide either only a snapshot (poor temporal resolution) and/or a small 3D region (small FOV and/or penetrative depth) of how alveoli behave during breathing. In section 5.4, a novel technique is introduced that can measure both the number of alveoli and their average size regionally across from speckled propagation-based phase contrast x-ray (PB-PCX) chest images. This technique is validated using a morphometric alveolar analysis technique on CT images. Two such morphemtric analysis techniques that were employed are presented and compared below before introducing the novel technique in section 5.4.

5.3 Morphometric Alveolar Dimensional Analysis Techniques

5.3.1 Granulometry

Granulometry is a particle sizing technique that utilizes the morphological opening operator, which is the erosion followed by dilation of an image (f) with a structure element (S). Granulometry can be performed on any n-dimensional image f. A structure element is an n-dimensional image of an object of a certain size and shape used to probe for similar objects in f. Mathematically, granulometry is defined as a function representing the relative frequency ($RelF$) of objects with size R:

$$RelF(R) = \frac{\mathrm{d}}{\mathrm{d}R}[f \ominus S(R)] \oplus S(R), \tag{5.1}$$

where the morphological erosion operator is represented by:

[4]The first Born approximation provides a solution to the reflected wavefield. It expresses the reflected wavefield as the sum of the incident wavefield and the wavefield that results from single scattering events between the incident wavefield and point scatterers within the medium. The first Born approximation and the Fresnel propagation equation (Eq. 1.50) converge to the same expressions for the reflected wavefield, when both assume wavefield paraxiality and a weakly scattering object (Giewekemeyer, 2011, sec. 3.2.5).

$$[f \ominus S](\mathbf{r}) = \min_{\mathbf{r}' \in S}\{f(\mathbf{r} + \mathbf{r}')\}, \tag{5.2}$$

and the morphological dilation operator is represented by:

$$[f \oplus S](\mathbf{r}) = \max_{\mathbf{r}' \in S}\{f(\mathbf{r} + \mathbf{r}')\}. \tag{5.3}$$

To understand Eq. 5.1, Eqs. 5.2 and 5.3 are first explained. In erosion and dilation, the center of the structure element S is defined as the origin in coordinate space $\mathbf{r}'$. It is centered at each point in $\mathbf{r}$ of the image f and the value of that point is replaced by the minimum (erosion) or maximum (dilation) value of f coincident with S.

To demonstrate how granulometry measures object sizes, consider the following panel of images in Fig. 5.4. Figure 5.4(a) encloses three different sized circular particles. In granulometry, circular structure elements of differing sizes are cycled through; for each structure element, erosion is first completed followed by dilation. First consider the structure element size to be less than the smallest sized particle in Fig. 5.4(a). As can be seen from Fig 5.4(b), erosion acts to reduce the size of the particles by the size of the structure element. Utilizing the same size structure element, Fig. 5.4(b) undergoes dilation to restore the particles to their original sizes as shown in Fig. 5.4(c). If the structure element size is increased to be just greater than the smallest particle in Fig. 5.4(a), the smallest particle becomes completely eroded as shown in Fig. 5.4(d). Therefore, it cannot be restored when Fig. 5.4(d) undergoes dilation, as shown in Fig. 5.4(e). The total intensity of Fig. 5.4(e) is reduced, in comparison to Fig. 5.4(a), but when the structure element size was less than that of the smallest particle the total image intensity (Fig. 5.4(c)) remained unchanged. After cycling through different size structure elements and measuring the resulting total image intensity, the derivative of the total image intensity with respect to the structure element size (in this case defined to be the radius) is computed. This will be known as a granulometry plot. Figure 5.4(f) reveals sudden changes in the total intensity, where the radius corresponding to those sudden changes equal that of the particles. Note that the amplitudes do not represent the relative number of particles of that size, rather they represent the total intensity enclosed by the particles of that size.

Figure 5.4 demonstrates the principle of granulometry on an image with particles being the same shape as that of the structure element. However, alveoli have a range of shapes and some are linked together by a common airway (see Fig. 5.5). Consequently, alveoli are not completely bounded. Despite this, granulometry is still able to identify and measure the alveolar size. The

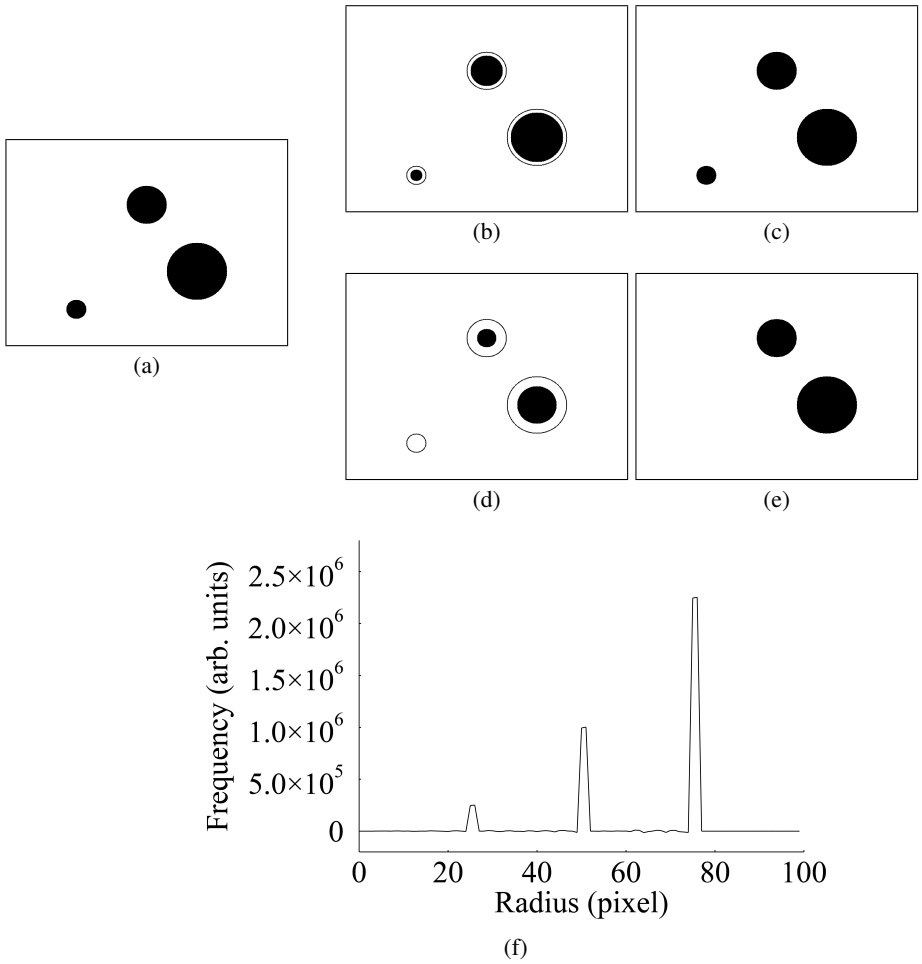

Figure 5.4: Principle of granulometry. The morphological opening operator is applied on image (a) to determine the radius of the three circular particles enclosed within, using a range of differently sized circular structure elements. (b) and (c) show (a) after erosion then dilation, respectively, using a structure element of radius less than the smallest circle in (a). Similarly, (d) and (e) are images of (b) and (c), respectively, but having used a structure element just larger than the smallest particle. Note that circular outlines are drawn in (b) and (d) to help compare the size of the particles with their original sizes before erosion. (f) represents a granulometry plot, which is the derivative of the total intensity of (a) after having undergone erosion then dilation against the structure element radius.

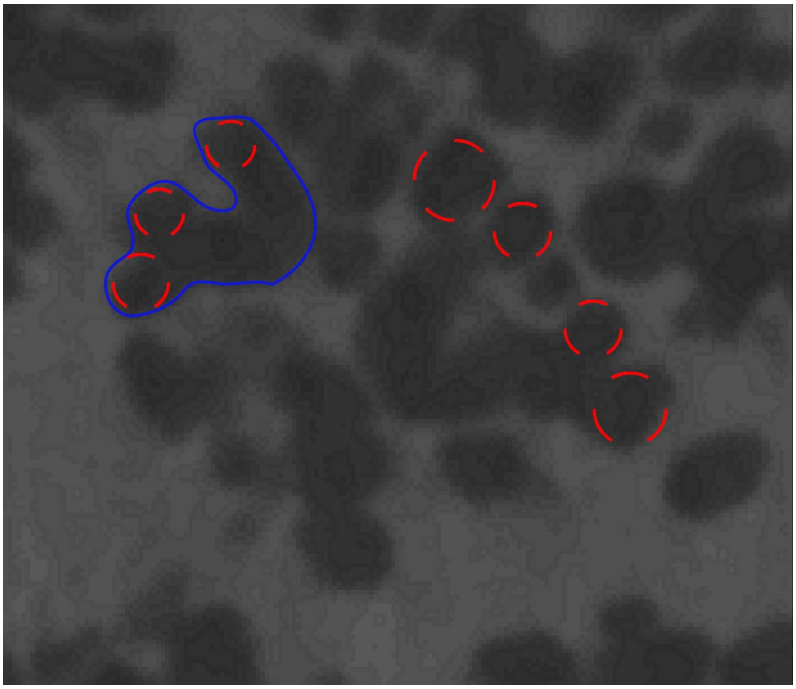

(a)

Figure 5.5: Transaxial 17.7×15.3 μm^2 CT slice of the lungs of a rabbit kitten highlighting some of the alveoli (outlined in red). Some alveoli are part of a common airway (outlined in blue).

measured sizes correspond to their inradius, highlighted as red circles in Fig. 5.5[5]. The following panel of images in Fig. 5.6 demonstrate this by showing the same CT slice as in Fig. 5.5 after applying the morphological opening operator with different size circular structure elements. Note that the CT slices displayed are thresholded to make the airways easier to discern. Accompanying the CT slices are plots showing the dominant sizes of the airways represented as peaks. The sequence of panels shows that the sizes of the individual alveoli protruding from the small airways are able to be measured. Note, however, that the first prominent peak at diameter of 8 pixels is due to noisy pixels around the edges of the airways. Attached to the CD accompanying this thesis is a complete video clip of Fig. 5.6.

[5] As an example, consider an alveolus shaped as a cuboid and with a spherical structure element being employed for granulometry. As explained, granulometry uses the morphological opening operator and cycles through structure elements of increasing size and the size that causes a change in the total intensity would correspond to that of the alveolus. By the definition provided for the morphological erosion operator, the structure element would first completely erode the cuboid alveolus when its radius is just greater than the inradius of the alveolus, since the structure element of that size begins to include the background. Therefore, the alveolus is not restored after dilation and a change in the total intensity occurs.

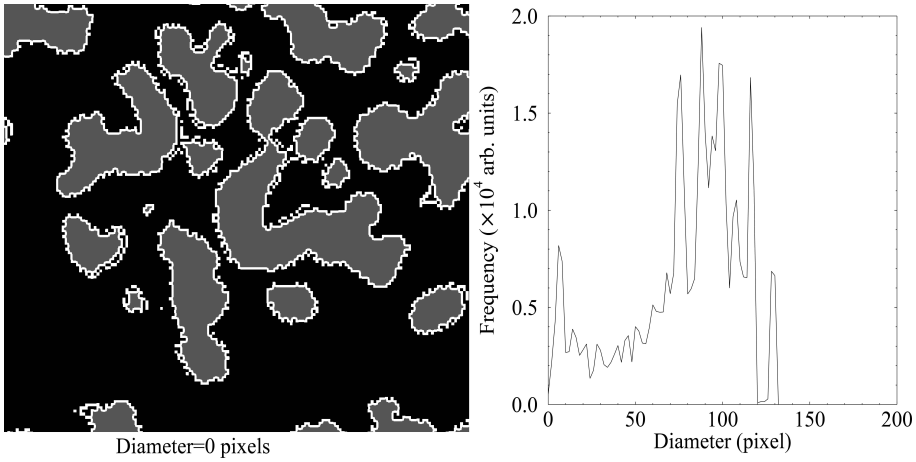

(a) 0 pixels

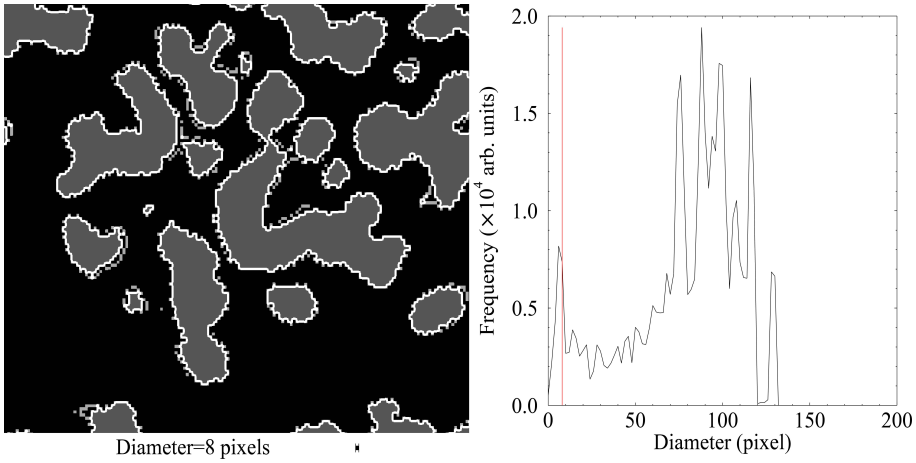

(b) 8 pixels

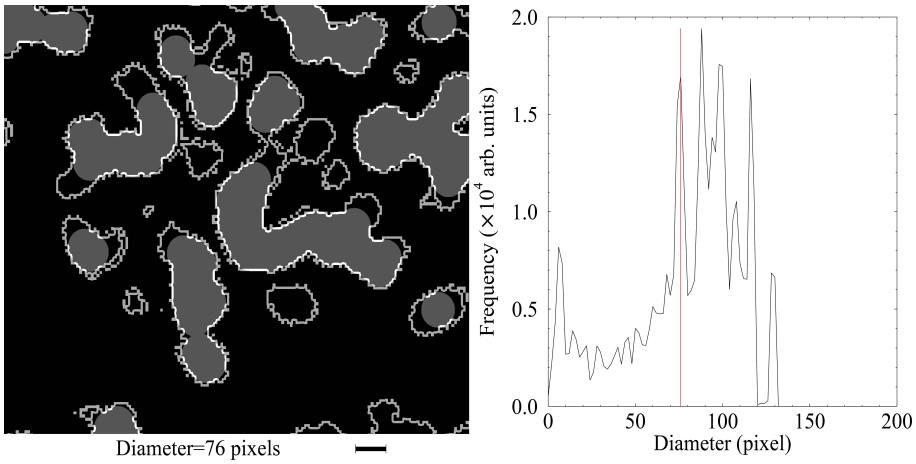

(c) 76 pixels

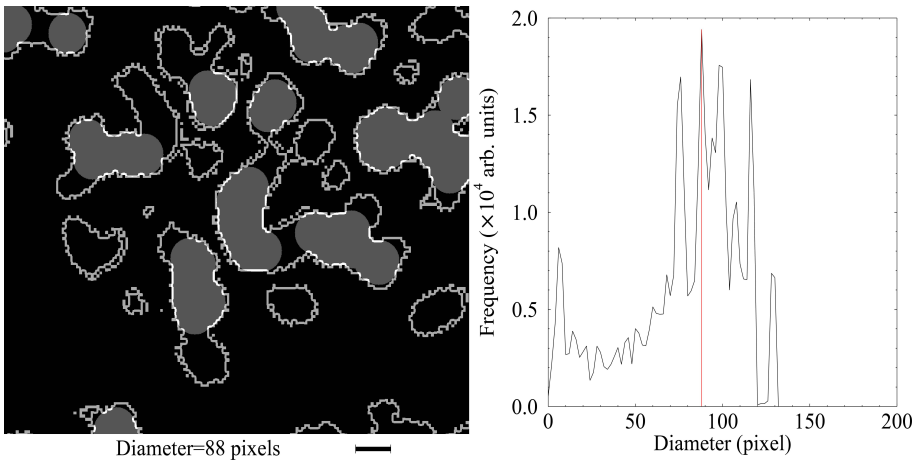

(d) 88 pixels

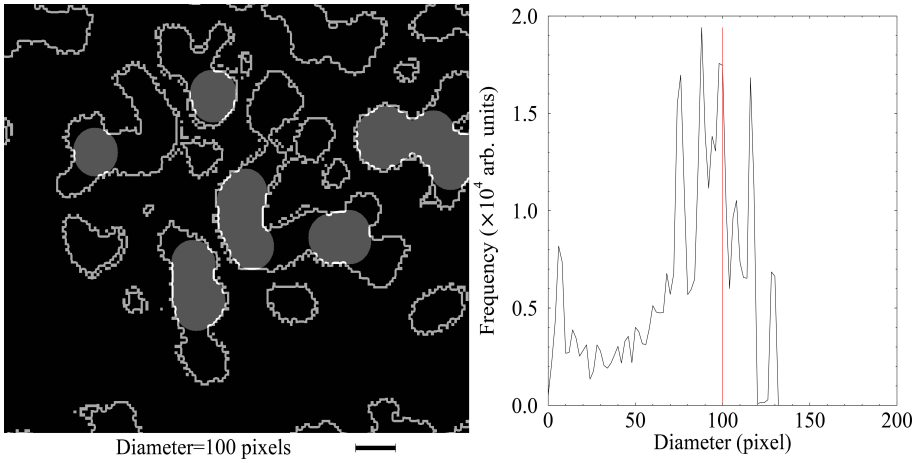

(e) 100 pixels

Figure 5.6: Image of a CT slice displayed in Fig. 5.5 after morphological opening with a spherical structure element with diameter (a) 0 pixels, (b) 8 pixels, (c) 76 pixels, (d) 88 pixels, and (e) 100 pixels. The original outlines of the airways are over-plotted on each image as a way to show which parts of the airway have been measured. A scale bar is provided indicating the diameter of the structure element. A granulometry plot accompanies each image to show which peaks correspond to which parts of the airways.

5.3.2 Watershedding and its Comparison Against Granulometry

Watershedding is another particle sizing technique that offers a greater number of degrees of freedom in detecting and sorting particle sizes than granulometry. Particles are located using a local maximum search algorithm followed by expanding the maxima (akin to filling a series of valleys with water) until it hits an adjacent maximum or a predefined minimum threshold intensity value to form blobs. Parameters can be defined to control how far maxima are expanded (i.e. the blob size), which maxima are significant and, for those that are not, whether they should be discarded or

merged with an adjacent blob.

The flexibility provided by watershedding in allowing different parameters to be set makes it prone to noise, intensity changes in the image background and particles with poorly defined boundaries. The presence of noise results in the detection of many irrelevant local maxima, which also significantly increases computation time. Noise can be smoothed but over-smoothing expands the boundaries of the particles and leads to overestimating their size. Careful setting of the minimum threshold intensity value is important to correctly measure the particle size. This is difficult to set with a varying background intensity. Particles packed closely may appear partially merged together, namely because of finite sampling and the detector point spread function (PSF). Furthermore, as previously mentioned, some alveoli do not have an entirely defined boundary because they are linked together by a small airway (see Fig. 5.5). Watershedding is unable to delineate such alveoli or particles.

The main advantages of watershedding over granulometry are: computational speed; ability to measure the number of particles; provision of information on the particle shape; and provision of subpixel measurements of particle size. Granulometry is significantly slower since at each coordinate of the image the pixel values enclosed by the structure element are sorted to determine the maximum and minimum value when dilating and eroding, respectively. Also, granulometry cannot return the total number of particles as it only calculates the total change in intensity, and since the structure element is of a set shape, no information is returned on the true shape of the particles. Furthermore, the structure element size can only grow in increments of the pixel size, hence the relative size increments will depend upon how well the image space is sampled. Although the image can be expanded to improve sampling, there is a large concomitant increase in computation time. Conversely, in watershedding, particle size can be measured from that of the blob, for example its mean chord length, with subpixel accuracy. Alternatively, a simplified way of measuring their size is to impose spherical model on the blobs. The formula for the volume of a sphere can be used to determine the radius of the blob with subpixel accuracy from the total volume enclosed within it.

After rigorous testing of both particle sizing techniques on CT slices of lung alveoli, granulomtery was found to be more robust against variability in background intensity across the image and conjoining alveoli. Despite watershedding providing more information about the alveoli, it was found to be less robust as parameters optimized for one CT lung image were regularly sub-optimal for others. The lower computation time required for watershedding in comparison to granulometry was offset by the time taken to optimize the watershedding parameters for each CT lung image set.

In light of these findings, granulometry was employed as a gold standard for a newly developed technique to particle sizing and counting that is presented in section 5.4.

5.4 A Theory for Extracting Lung Morphology from Near-Field X-ray Speckles

This section shows how the alveolar size and population can be determined from lung speckle patterns in PB-PCX chest images if the V_L is known. This derivation closely follows that developed in section 4.4, but in that derivation alveoli were assumed to be uniformly randomly distributed, which may not always be true. For instance, two PB-PCX chest images were recorded at low (Fig. 5.7(a)) and high (Fig. 5.7(b)) V_L, which is clearly evidenced by the amount of air seen in their corresponding CT chest slices, shown in Figs. 5.7(c) and 5.7(d), respectively. At the larger volume, it can be seen that the alveoli become more closely packed and less uniformly randomly distributed. The following subsections reveal how short-range-order (SRO) arising from close packing can significantly alter the power spectra of particulate images[6]. Hence this section modifies the derivation in section 4.4 to account for SRO. As was shown in section 4.4, for a single material object the power spectrum of its PB-PCX image ($I(\mathbf{r}_\perp, z = L)$) normalized against its attenuation image ($I(\mathbf{r}_\perp, z = 0)$) can be expressed as:

$$\left|\mathcal{F}\left\{\frac{I(\mathbf{r}_\perp, z = L)}{I(\mathbf{r}_\perp, z = 0)} - 1\right\}\right|^2 = L^2\delta^2 k_\perp^4 \left|\mathcal{F}\left\{T(\mathbf{r}_\perp)\right\}\right|^2, \tag{5.4}$$

where all the symbols are as defined in section 4.4.

The functional form of a distribution of voids $\tilde{G}(\mathbf{r})$ enclosed in $V(\mathbf{r})$ is also reintroduced from section 4.4:

$$\tilde{T}(\mathbf{r}) = V(\mathbf{r}) - \sum_{n=0}^{N} \delta(\mathbf{r} - \mathbf{r}_n) \otimes \tilde{G}(\mathbf{r}), \tag{5.5}$$

where all the symbols are as defined in section 4.4. In that section, its power spectrum was evaluated to be N times $\left|\mathcal{F}\left\{\tilde{G}(\mathbf{r})\right\}\right|^2$ for non-zero spatial frequencies by assuming $\tilde{G}(\mathbf{r})$ to be

[6]The degree of order refers to the distance over which the correlation between particles remains significantly above zero (zero representing no correlation). Crystals have long-range-order since they are made up of atoms arranged in a periodic manner over a large region. This means the position of one particle can be used to determine that of another from afar. SRO refers to when the correlation is high only between adjacent alveoli. That is, the position of one particle can accurately predict the position of another particle close to it. SRO occurs when the particles are randomly closely packed (Kachan and Ponyavina, 2002). In the lungs, the alveoli are quite closely packed and may therefore exhibit SRO. Medium-range-order describes objects with properties between that of short- and long-range-order. One example is powdered crystals. However, there has yet to be clear boundary defined separating short-, medium- and long-range-ordering.

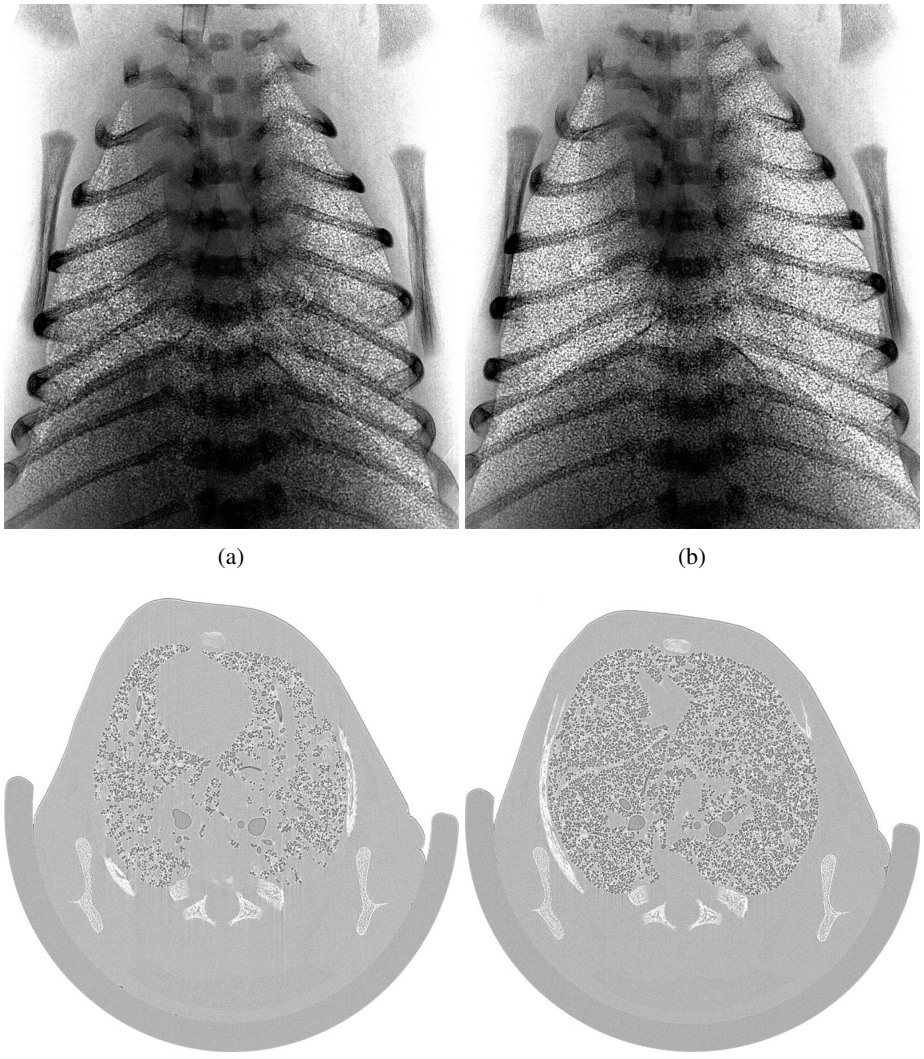

Figure 5.7: PB-PCX image of the chest at (a) low and (b) high lung air volume of the same rabbit kitten (image size: 19.8×22.8 mm^2). These PB-PCX images were one of 1800 projections used to reconstruct 27.6×26.4 mm^2 CT slices as shown in (c) and (d), respectively. Note that the bones appear black in the projection image since the image represents the attenuated intensity and white in the CT slices since the slice represents the linear attenuation coefficient. ODD = 1 m. Energy = 24 keV. Exposure time per projection = 50 ms.

uniformly randomly distributed. However, it will be shown herein that this expression is incorrect for closely packed spheres by first explicitly expressing $\left|\mathcal{F}\left\{\tilde{T}(\mathbf{r})\right\}\right|^2$ as:

$$\left|\mathcal{F}\left\{\tilde{T}(\mathbf{r})\right\}\right|^2 = \left|\int_V \tilde{T}(\mathbf{r})\exp(-i2\pi\mathbf{k}\cdot\mathbf{r})\mathrm{d}\mathbf{r}\right|^2, \tag{5.6}$$

where $\mathbf{k} = (k_x, k_y, k_z)$ are vectors in 3D Fourier space.

The first term of Eq. 5.5 is a constant function and so contributes only to the zero spatial frequency. The zero frequency, however, is not relevant to this study and will be ignored hereafter. To derive an analytic solution to the integral in Eq. 5.6, and hence obtain explicit dependence on N and R, Eq. 5.5 (minus $V(\mathbf{r})$) is substituted into Eq. 5.6. Then after making use of the convolution theorem and the sifting property of the unit impulse, the following expression is yielded (Guinier, 1994):

$$\left|\mathcal{F}\left\{\tilde{T}(\mathbf{r})\right\}\right|^2 = \left|\mathcal{F}\left\{\tilde{G}(\mathbf{r})\right\}\right|^2\left[N + \sum_{m=1}^{m\neq n}\sum_{n=1}\cos(2\pi\mathbf{k}\cdot\mathbf{D}_{mn})\right], \tag{5.7}$$

where $\mathbf{D}_{mn}$ is the vector from the center of sphere m to the center of sphere n. The voids are assumed to be macroscopically isotropic[7], much like alveoli, making their power spectra rotationally symmetric. Thus, both $|\mathcal{F}\{G(\mathbf{r})\}|^2$ and the cosine term in Eq. 5.7 can be rotationally averaged. This is done for the cosine term by averaging over the polar angle defined between $k = |\mathbf{k}|$ and $D_{mn} = |\mathbf{D}_{mn}|$, and the azimuthal angle formed by the plane containing $\mathbf{k}$ and $\mathbf{D}_{mn}$ with an arbitrary plane. Thus, Eq. 5.7 reduces into one-dimensional (1D) form with independent variable k and distance D_{mn}, to give a result equivalent to the Debye scattering formula, which was derived for predicting the diffraction patterns of gases and liquids (Debye, 1915):

$$\overline{\left|\mathcal{F}\left\{\tilde{T}(\mathbf{r})\right\}\right|^2} = \overline{\left|\mathcal{F}\left\{\tilde{G}(\mathbf{r})\right\}\right|^2}\left[N + \sum_{m=1}^{m\neq n}\sum_{n=1}\frac{\sin(2\pi kD_{mn})}{2\pi kD_{mn}}\right]. \tag{5.8}$$

The overbar represents the rotational average, which hereafter will be dropped for notational simplicity. According to the Fourier slice theorem, $\left|\mathcal{F}\left\{\tilde{T}(\mathbf{r})\right\}\right|^2(\mathbf{k}_\perp, 0) = \left|\mathcal{F}\left\{\int_z \tilde{T}(\mathbf{r})\mathrm{d}z\right\}\right|^2(\mathbf{k}_\perp) = |\mathcal{F}\{T(\mathbf{r}_\perp)\}|^2(\mathbf{k}_\perp)$. This is also true for $|\mathcal{F}\{G(\mathbf{r})\}|^2$ and therefore allows k to be replaced with $k_\perp$ in Eq. 5.8 to give an expression for the power spectrum of the projected object thickness $T(\mathbf{r}_\perp)$. Substituting this 1D form of Eq. 5.8 into Eq. 5.4, and with $|\mathcal{F}\{G(\mathbf{r})\}|^2$ assumed to be the power spectrum of a sphere, which is given in Eq. 4.10, gives the main equation of this chapter, the PB-PCX speckle image power spectrum with SRO:

[7]That is, the voids are randomly orientated and the degree of order in their spatial distribution is similar in all directions.

$$\left|\mathcal{F}\left\{\frac{I(\mathbf{r}_\perp, z=L)}{I(\mathbf{r}_\perp, z=0)}-1\right\}\right|^2 = L^2\delta^2k_\perp^4N\left|\frac{4\pi R^3}{(k_\perp R)^2}\left[\frac{\sin(k_\perp R)}{k_\perp R}-\cos(k_\perp R)\right]\right|^2 \times\left[1+\int_V\rho(D)\frac{\sin(2\pi k_\perp D)}{2\pi k_\perp D}\mathrm{d}V\right]. \quad (5.9)$$

Here, the summation term in Eq. 5.8 has been rewritten as an integral, over the volume $V(\mathbf{r})$, weighted by the function $\rho(D)$ that is defined as the occurrence frequency of alveoli separated by distance D. The area under the power spectrum of Eq. 5.9 ($PS_{Area-order}$) over its first order peak bounded by the same adjacent minima as defined for Eq. 4.12 is given by:

$$PS_{Area-order} = L^2\delta^2N\left\{34\pi^2R+\int_{k_\perp}\left|4\pi R\left[\frac{\sin(k_\perp R)}{k_\perp R}-\cos(k_\perp R)\right]\right|^2 \times\int_V\rho(D)\frac{\sin(2\pi k_\perp D)}{2\pi k_\perp D}\mathrm{d}V\mathrm{d}k_\perp\right\}. \quad (5.10)$$

It can be shown that Eq. 5.10 reduces to Eq. 4.12 if there is no SRO, that is, the alveoli are uniformly randomly distributed. This occurs when $\rho(D)$ = constant, which means there is equal probability within $V(\mathbf{r})$ that an alveolus will be separated by any distance D from another. The integral over V in Eq. 5.10 becomes the Fourier transform of $V(\mathbf{r})$ (as shown by Guinier (1994, sec. 2.5)). If the ratio of the sphere size $G(\mathbf{r})$ to the dimension of $V(\mathbf{r})$ is much less than unity then the dominant spatial frequencies of the integral term is confined towards $k_\perp = 0$ and away from the first order peak. The second term in the curly brackets of Eq. 5.10 vanishes, hence Eq. 5.10 reduces to Eq. 4.12.

As mentioned in section 4.5, since 90% of the volume corresponding to V_L can be accounted for in the alveoli, each of which is approximated as N isolated spheres of radius R, then:

$$V_L = \frac{4}{3}\pi NR^3. \quad (5.11)$$

If V_L and the $PS_{Area-order}$ are known, Eqs. 5.10 and 5.11 can be used to simultaneously solve for N and R. This method will hereon be labeled as the speckle-based alveolar analysis method (SAAM). However, to use Eq. 5.10, $\rho(D)$ must be known, which is difficult to determine for alveoli. Therefore, SAAM was first tested under the assumption that the alveoli were uniformly randomly distributed by utilizing Eq. 4.12, instead of Eq. 5.10, together with Eq. 5.11 to measure N and R. This method is much simpler to employ as only δ needs to be known, which can be readily calculated for a given material at a given x-ray energy using the National Institute of Standards and Technology (NIST) database (NIST, 2014).

An alternative method is using the position of the first order peak in the power spectrum (PS_{Peak}) where, under the assumption that the alveoli is uniformly distributed, it is located at $PS_{Peak} = \frac{2.74}{R}$ (this is solved from Eq. 4.11) to calculate R. N could then be calculated from the measured PS_{Area} or V_L, but in section 5.5, V_L was utilized.

Both SAAM and the alternative method assume the alveoli are uniformly randomly distributed, but Figs 5.7(c) and 5.7(d) indicate that the alveoli may have some significant degree of packing order at increasing V_L. Consequently, both methods may not be sufficiently accurate to calculate N and R of alveoli in those images. To realize this, observe that both Eq. 5.9 and Eq. 4.11 are oscillatory functions in Fourier space. As the packing fraction increases, their first order peaks differ in position as does the area under the peaks. In the next section, the effect of ordering on the accuracy of SAAM and using PS_{Peak} is explored by testing them on PB-PCX images of soda lime glass (SLG) microspheres, uniformly randomly arranged and closely packed, and comparing the measured values of N and R with their known values. As will be shown, the alternative method was found to be less robust to SRO compared to SAAM.

5.5 Measure of Glass Particle and Alveolar Morphology

SAAM is validated using colloidal SLG microspheres, which closely resemble alveoli in size and shape, and is then applied to rabbit kittens to measure alveolar dimensions. These measurements are then compared with a gold standard measurement of alveolar size from high-resolution CT images (see section 5.5.1 for details). The results and analysis from both microspheres and rabbit lungs is presented in section 5.5.2. The prospect of applying this work to human patients forms part of the discussion in section 5.5.3.

5.5.1 Methodology

Image acquisition

PB-PCX images were acquired, flat field corrected and, for long image sequences (>2 mins), the intensity of each frame was normalized to the first frame, as described in section 3.3.1.

Two detectors were used in this study: a 2560×2160 pixel scientific (sCMOS) tandem lens-coupled scientific-CMOS (sCMOS) imaging sensor (pco.edge; PCO AG, Germany) coupled to a 25 μm thick gadolinium oxysulfide (Gd2O2S:Tb;P43) powdered phosphor (this was the same detector utilized for the work presented in section 4.7), and a 2040×2040 pixel sCMOS imaging sensor (ORCA-Flash4.0; Hamamatsu, Japan) with a direct fiber optic coupling the sensor to a

150 μm thick columnar CsI scintillator. Their effective pixel sizes were 15.23 μm and 6.38 μm, respectively.

Glass particles

SLG microspheres (Whitehouse Scientific, Ltd.) were imaged at 30 keV using both detectors to test the robustness of SAAM for extracting their average R and N against detection system. 150-180 μm sized microspheres were sprinkled onto a cover slip to produce a sparse random distribution and then sealed with another cover slip placed on top. A hollow step-wedge made of polymethyl methacrylate was designed with the depth (i.e. thickness) of the steps at 1 mm, 2 mm, 5 mm, 10 mm and 20 mm. The hollow step-wedge was separately filled with closely packed microspheres of sizes 43-55 μm, 63-75 μm, 75-90 μm, 90-106 μm, 106-125 μm, 150-180 μm, 180-212 μm and 250-300 μm.

Rabbit kittens

All animal experiments performed were approved by the Monash University Animal Ethics Committee and the SPring-8 Animal Care and Use Committee. Pregnant New Zealand white rabbits (27-30 days of gestation, term=31-32 days; n=4) were anaesthetized initially using propofol (i.v; 12 mg/kg bolus, 150-500 mg/h infusion), then via inhalation following intubation (Isoflurane 1.5-4%). Rabbit kittens (n=10) were delivered by caesarean section, then humanely killed using an overdose of sodium pentabarbitone (>100 mg/kg i.p.). The experimental setup shown in Fig. 2.3 was employed here. Before ventilation, several non-aerated images of the chest were recorded. Thereafter ventilation was initiated with an airway pressure (AP) of 16 cmH_2O. AP was then gradually increased to 27 cmH_2O and decreased back to 16 cmH_2O via 1 cmH_2O increments, each of which was held for 5 s. The images were recorded at 24 keV with a frame rate of 20 Hz, 40 ms exposure time, and 1 m ODD. Only the pco.edge detector was used because, of the detectors available at the time of experiments, only it had a sufficiently large FOV to image the entire chest of a rabbit kitten in a single exposure. The ODD of 1 m seems to contradict what was found in chapter 4, in that with the same detector and exposure time employed, the contrast-to-noise ratio (CNR) of lung speckle at 1.5 m ODD was too weak to accurately quantify lung structure. Fortunately, it was discovered that the pco.edge detector, being a lens-based system, was not optimally focused at that time. Rectifying this significantly boosted the lung speckle CNR sufficiently to allow imaging at 1 m ODD and consequently be well within the near-field regime.

The ventilator was disconnected with AP last set at 2 cmH_2O. High resolution CT images (1800 projections from 0°-180° with 50 ms exposures and 1 m ODD) were then acquired for a

gold standard comparison. Additional CT images were then recorded after the kitten's lungs were filled with 100% N_2 at 29 cmH_2O AP with the intubation tube then tied off to prevent lung collapse. Each rabbit kitten was fixed in a test tube filled with 2% agarose solution to reduce motion blur. PB-PCX images of a rabbit kitten were also recorded at different ODDs to measure the degree of validity of Eq. 5.4 at increasing ODD.

Image analysis

The power spectrum of a speckled PB-PCX lung image given by Eq. 4.11 does not account for the detector PSF and penumbral blurring. Given that the synchrotron source size of the beamline used for this study was 150×10 μm^2, the source-to-object distance was D =210 m, and the maximum ODD set was 3 m, penumbral blurring is less than a pixel width for both detectors (see e.g. Gureyev et al. (2009) for method to calculate penumbral blur). However, the detector PSF varies significantly between detectors, and was therefore measured and corrected for each PB-PCX image before subsequent image analysis. The detector PSF was determined by first having the edge spread function (ESF) measured both vertically and horizontally using a 5.25 mm thick lead block. The spatial derivatives of the ESFs were averaged, extruded azimuthally to construct the detector PSF, and fitted with a 2D Pearson type VII distribution function (PVII) (Hall Jnr et al., 1977). The Wiener deconvolution algorithm was used to deconvolve the PB-PCX images with the fitted detector PSF (Stewart, 2006). This algorithm is most stable against the input parameter, the SNR of the deconvolved image, at low spatial frequencies where the first order peak of the power spectrum of lung speckle presides, thus it need not be known exactly. An optimal SNR value of 500 was found to provide consistent values of N and R for microspheres and alveoli. Wiener deconvolution amplifies high frequency noise but the degree of noise amplification is similar between frames of the same animal. To suppress this effect, the power spectra of images without speckle (e.g. the non-aerated lung images) were subtracted from that of the speckled image (e.g. aerated lung images).

As is required to calculate PS_{Area}, PB-PCX images were divided by their attenuation image using the single image phase retrieval algorithm (SIPRA), which requires μ and δ as inputs for the filter. These were for SLG microspheres (30 keV), $\mu_{SLG} = 197\ m^{-1}$ and $\delta_{SLG} = 5.09 \times 10^{-7}$, and for lung tissue (24 keV), $\mu_{LT} = 54.74\ m^{-1}$ and $\delta_{LT} = 3.99 \times 10^{-7}$ (as determined previously for the work in section 4.7).

To summarize, PS_{Area} was calculated using the following sequence of steps applied to the PB-PCX lung speckle image: (i) deconvolving the detector PSF, (ii) dividing by its attenuation

image, (iii) computing its azimuthally averaged power spectrum, (iv) subtracting from that of its non-aerated PB-PCX image, and (v) integrating between 2 mm^{-1} and the Nyquist frequency. As justified in section 4.6.2, the spatial frequencies above 2 mm^{-1} includes the first order peak and those below are contaminated by bone and skin.

3D granulometry (described in section 5.3.1) was chosen as the 'gold standard' to evaluate the accuracy of SAAM for measuring alveolar dimensions. Spheres of various sizes were created as structure elements to survey the lung for alveoli of similar size using the morphological opening operator on 7.5 mm^3 CT volumes of rabbit kitten lungs. The CT volumes were magnified by a factor of 4 and bilinearly interpolated beforehand to increase the spatial sampling rate. Alveolar dimensions were calculated using SAAM from one of the corresponding CT projection images. V_L was calculated, as required to use SAAM, by intensity thresholding the CT images to segment the airways before counting the total voxels within them.

5.5.2 Results

Three types of 150-180 μm microsphere samples were investigated: single and multiple microspheres uniformly randomly dispersed between cover slips, and a hollow step-wedge filled with microspheres. These samples were recorded at 15 cm ODD using the pco.edge detector and are shown in Figs. 5.8(a-c). Both N and R were calculated using Eqs. 5.11 and 4.13. N and R were also determined from the position of the first order peak in the speckle power spectrum, that is, PS_{Peak}. The calculated values of N and R along with their expected values are presented in Table 5.1.

Table 5.1: The number and mean radius of SLG microspheres calculated from the propagation-based phase contrast x-ray images in Fig. 5.8(a-c) and compared with the expected values shown in brackets.

	Number		Radius (μm)	
Microspheres	PS_{Area}	PS_{Peak}	PS_{Area}	PS_{Peak}
Single (Fig. 5.8a)	0.67±.03(1)	2.7±0.1	96±4(83±8)	59.55±0.01
Multiple (Fig. 5.8b)	52±3(59)	59.63±0.08	87±4(83±8)	83.47±0.08
Packed (Fig. 5.8c)	3732±460(3600±800)	7500±1600	82±9(83±8)	64.90±0.01

For single and multiple microspheres placed between cover slips, V_L was calculated using Eq. 5.11 with N and an average value for R measured directly from their images. The calculated and expected values of N and R for a single microsphere agree poorly because the image noise masked its signal (see Fig. 5.8(d)). However, as the number of microspheres increased, a clear peak in the power spectrum became evident above the noise in Fig. 5.8(d). This resulted in excellent

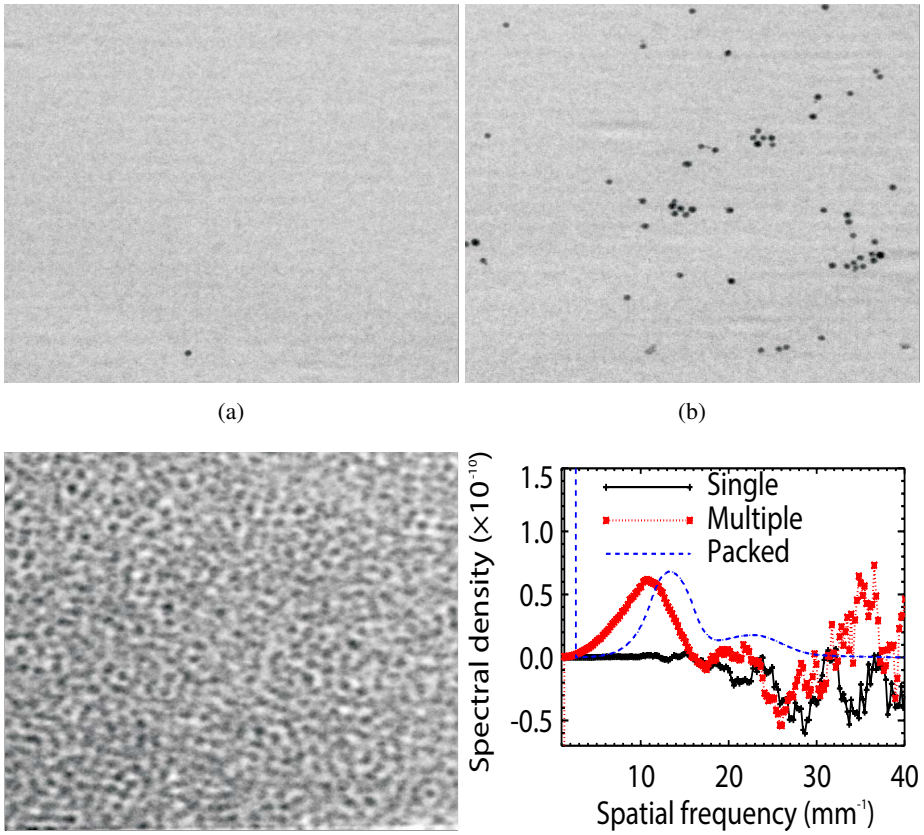

Figure 5.8: Propagation-based phase contrast x-ray images of 150-180 μm sized microspheres, showing (a) a single glass particle, (b) multiple glass particles and (c) a 1 mm thick container of glass particles with volume packing density ≈ 55% (Image dimensions: 3.83×3.83 mm^2). (d) shows the corresponding power spectra of (a)-(c), after deconvolving to remove the detector point spread function, dividing by their attenuation contrast image, normalizing against the total pixels in the image and the number of microspheres. ODD = 15 cm. Energy = 30 keV. Exposure time = 1 s.

agreement between the calculated and expected values of N and R using both the PS_{Area} and PS_{Peak} (Table 5.1). The uncertainties in N and R calculated from PS_{Area} and PS_{Peak} were propagated from the uncertainty in V_L, which is the difference in V_L calculated from using the mean R and the mean of R plus one standard deviation measured manually from the images. However, the uncertainty in R calculated from PS_{Peak} was determined differently and was based upon fitting a PVII function to the centroid. Comparing the uncertainties in N and R, at low packing fraction, they are more precisely measured from PS_{Peak} than from PS_{Area} as PS_{Peak} does not depend on how precisely V_L is measured.

Microspheres poured into a container inevitably stack on top of one another to produce some SRO. V_L was determined using SIPRA to calculate the projected thickness of glass at each pixel then summed and multiplied by the pixel area (Paganin et al., 2002). Surprisingly, the presence

of SRO did not adversely affect the calculation of N and R using PS_{Area}. Their uncertainty was propagated from that of V_L, which was determined using the rational exponent function derived in section 3.3.1 that relates the uncertainty in V_L to the region-of-interest (ROI) size (Leong et al., 2013a). Conversely, PS_{Peak} shifted to higher frequencies (see Fig. 5.8(d)), thereby underestimating R and overestimating N. Again, the uncertainty of the former was determined from weighted fitting of a PVII function to the centroid while that of the latter was determined in a similar manner to N that was calculated from PS_{Area}. Two important and consequential points arise from these findings: (1) there is SRO in closely packed particles as indicated by the shift in PS_{Peak}, and (2) despite this, Eqs. 4.22 and 4.13 can still accurately calculate N and R. Figure 5.8(d) provides a clue to why Eqs. 5.11 and 4.13 remain valid. There we see that the shape and position of the first order peak is altered by SRO, but the area under the curve remains virtually unchanged. This presents a favorable outcome, since the packing density of alveoli will vary during respiration.

PB-PCX images of the 1 mm thick region of the step-wedge, each containing different sized microspheres, were recorded using the ORCA detector to better resolve the smaller sized microspheres. N and R were calculated for each and are plotted in Fig. 5.9(a), which show that they are in close agreement with the expected values. However, at increasing sample thickness (that is, at increasing $|\varphi|_{max}$) and ODD, large errors accumulated in the calculation of R as N_F reduces below $\max\{1, |\varphi|_{max}\}$. This is shown in Fig. 5.9(b). A similar trend (not shown) was found when plotting N as a function of ODD. The accuracy of calculating R of a single layer of particles also decreases despite the fact that $N_F \geq \max\{1, |\varphi|_{max}\}$ for up to 2 m ODD ($R \approx 165$ μm, $|\varphi|_{max} = |-k\delta_{SLG}2R| = 13.5$, $L = 2$ m, $a = 2R$, $N_F = 61.6$). The consistent overestimation of PS_{Area} with respect to that obtained experimentally, which is denoted in this thesis as the large-distance error, could be due to a number of possible effects. A complete study of these competing effects is warranted, but was beyond the scope of this thesis. Nevertheless, an extended discussion on these effects is given in section 5.5.3.

Considering that the typical alveolar radius and projected thickness of a fully aerated lung of a rabbit kitten are 75 μm and 10 mm, respectively, and given that the ODD used in these experiments was 1 m, $N_F = 435$ and $|\varphi|_{max} = |-k\delta_{SLG}2R| = 363$. Since $N_F \geq \max\{1, |\varphi|_{max}\}$, this shows the PB-PCX lung images recorded in this study satisfy the near-field condition. However, as was shown for SLG microspheres, there exists an increasing large-distance error at increasing ODD. From Fig. 5.9(b), the degree of the large-distance error is similar at 1 m ODD for increasing projected thickness of up to 10 mm. Therefore, a single factor can be applied to the images to account for the large-distance error. To determine this factor for the lungs, many rabbit kittens were aerated to

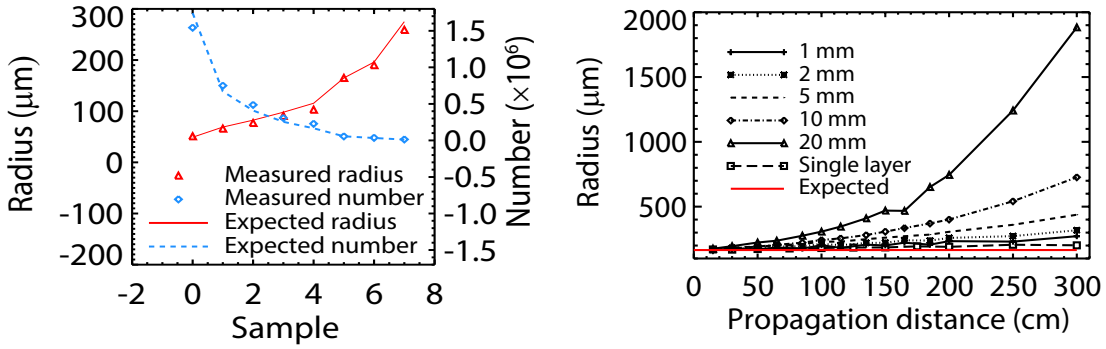

Figure 5.9: Evaluating the accuracy of calculating the number and mean radius of microspheres from propagation-based phase contrast x-ray images of (a) a 1 mm thick container filled separately with different sized microspheres at 15 cm ODD and (b) containers of variable thickness filled with 150-180 μm sized microspheres at various ODDs. Energy = 30 keV. Exposure time = 1.2 s.

various V_L and imaged at different ODDs. The PS_{Area} was calculated at each ODD and compared with the expected PS_{Area}, which was determined by assuming the calculated PS_{Area} at the lowest ODD of 15 cm was accurate and subsequent PS_{Area} were extrapolated to larger ODD using Eq. 5.4. This was done for several rabbit kittens at 1 m ODD and on average their calculated PS_{Area} differed by a factor of 2.3±0.6 from the expected value. This factor was accounted for in all PB-PCX rabbit kitten images recorded at 1 m to give a more reliable measure of the alveolar dimensions and population.

3D granulometry was utilized to test the accuracy of measuring alveolar dimensions from PS_{Area} and PS_{Peak}, although it does not yield their number, N. Figure 5.10(a) shows typical granulometry curves that correspond to a 7.5 mm^3 ROI that includes the CT slices shown in Figs. 5.7(c) and 5.7(d). The maximum value represents the dominant alveolar dimension. 3D granulometry was performed on several more rabbit kittens and compared with PS_{Area} and PS_{Peak} (see Fig. 5.10(b)). The uncertainty in R measured from 3D granulometry was determined by the width of the flat top of the peak while that measured from PS_{Area} was propagated from the largest source of uncertainty, that being the factor, 2.3±0.6, used to correct for the large-distance error. The uncertainty in PS_{Peak}, determined from weighted fitting to the PVII function was negligible (< 1 μm). The gradients for PS_{Area} and PS_{Peak} against 3D granulometry were 0.9±0.3 (Pearson product-moment correlation coefficient R^2= 0.6) and 0.2±0.1 (R^2= 0.3), respectively. The gradient of the latter indicates the insensitivity of PS_{Peak} with R, which is likely caused by short-range-ordering of alveoli affecting the measured size (see section 5.4), while the former shows a strong positive correlation. From the results of the SLG microspheres, this further demonstrates the fact that utilizing PS_{Area} is immune to short-range-ordering effects.

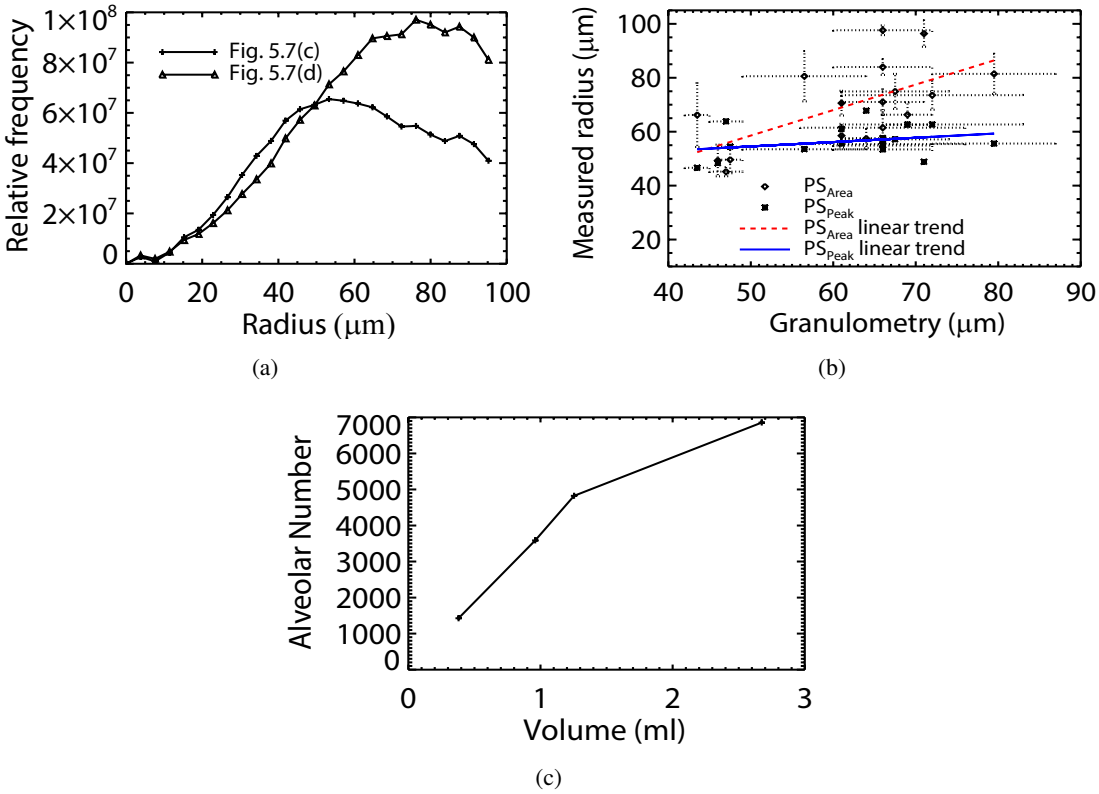

Figure 5.10: (a) Distribution of alveolar dimensions determined from regions centered about the two CT slices in Figs. 5.7(c) and 5.7(d), respectively, using 3D granulometry. (b) The average alveolus size was measured both from PS_{Area} and PS_{Peak} and was compared with that measured from 3D granulometry for several rabbit kittens. (c) The alveolar number was approximated by manually counting the number of alveolar surface profiles from one transaxial slice per CT of a ventilating kitten and plotted against the total lung air volume determined by intensity thresholding the entire CT reconstruction.

To demonstrate the presence of alveolar recruitment and de-recruitment, the number of alveoli was manually counted from a transaxial slice for each CT (similar to those shown in Fig. 5.7(c) and 5.7(d)) recorded of a kitten at different stages of respiration, which in stereology shows that it is approximately proportional to the alveolar number in 3D (Miyomoto, 1994). The transaxial slices were chosen to be approximately at the same axial position in the lung for each animal. Figure 5.10(c) shows alveolar number correlates with the total V_L of the entire CT.

The ability of the technique presented herein to dynamically measure N and R during ventilation is demonstrated in Fig. 5.11; from the first breath of the rabbit kitten to several respiratory cycles later. From the first breath (Fig. 5.11(a)) N (calculated from PS_{Area}) was measured to first increase before reaching a plateau after $t = 5$ s as Fig. 5.11(b) shows. This increase in N coincides with the clearing of fetal lung liquid and consequent recruitment of aerated alveoli. An increase in R, computed from PS_{Area}, follows the same trend as V_L. Conversely, R that was derived from PS_{Peak}

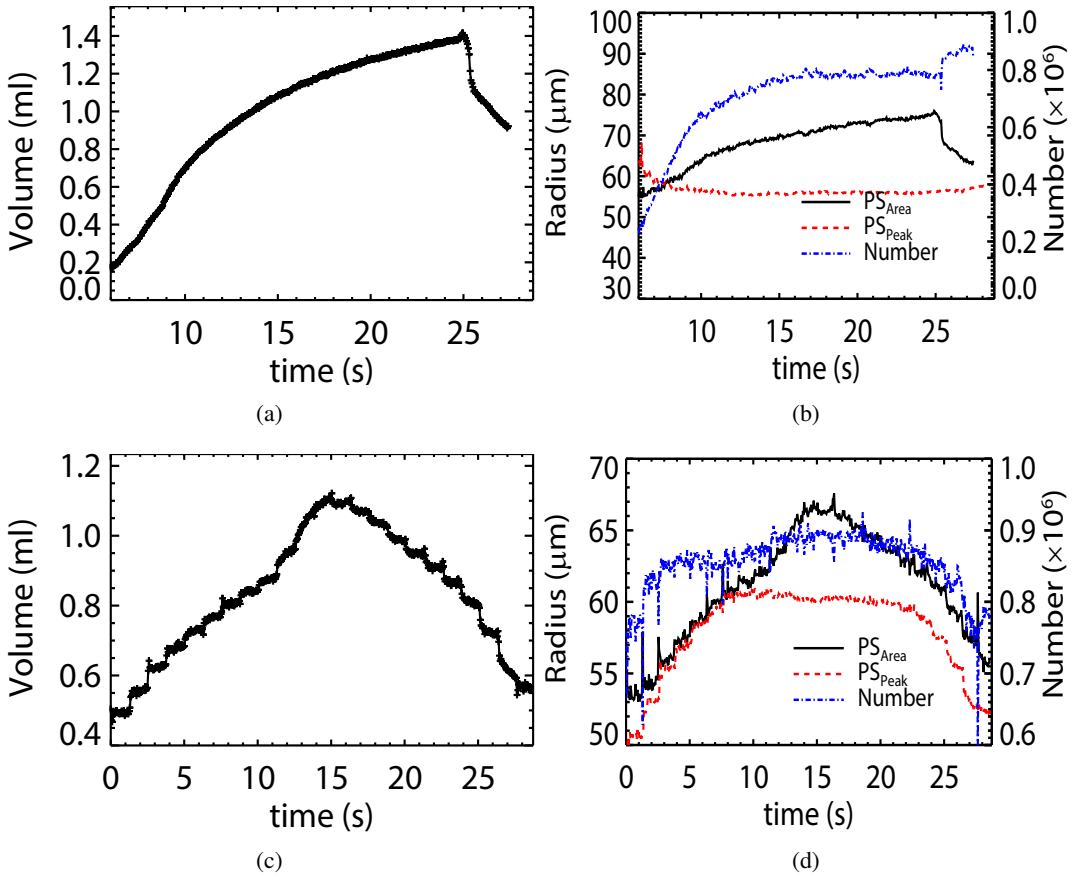

Figure 5.11: Lung air volumes from PB-PCX chest images of a kitten mechanically ventilated (a) from its first breath, and (c) over a single respiratory cycle several breaths after its first. The corresponding calculation of number and mean radius of alveoli are shown in (b) and (d), respectively.

remains largely unchanged, which may be caused by alveoli becoming more closely packed. At $t \geq 27$ s, a sudden drop in V_L sees R decreasing (calculated from PS_{Area}), but interestingly N concomitantly increased. The increase in N may be caused by the trapping of air as the airways collapse to produce the appearance of additional alveoli in the form of air bubbles. During a respiratory cycle of a well-ventilated lung (Fig. 5.11(c)), the independent calculations of R shown in Fig. 5.11(d) initially closely agree, but after $t \geq 6$ s they diverge again. This is likely due to effects of SRO affecting peak position. N (calculated from PS_{Area}) remains approximately constant throughout except at the beginning and end of the respiratory cycle. This shows evidence of alveolar recruitment followed by de-recruitment.

The same two respiratory cycles plotted in Figs. 5.11(a) and 5.11(c) are plotted against airway pressure (AP) to present their pressure-volume (PV) curves given in Figs. 5.12(a) and 5.12(b), respectively. In section 5.1, it was suggested that the hysteresis between the inspiration and

expiration curve was caused by alveolar recruitment and de-recruitment occurring at different pressures. These results support this hypothesis that the hysteresis is caused by differences in alveolar structure during inspiration and expiration. In Fig. 5.12(a), a large degree of hysteresis can be seen, which is reflected in the alveolar number and radius not being equal at the same AP during inspiration and expiration. Note that this is expected for an infant taking its very first breath, during which lung fluid is cleared and alveoli are recruited for the first time to increase the functional residual capacity (FRC). Several breaths later, when the lungs are well aerated, Fig. 5.12(b) shows the hysteresis remains; albeit, to a smaller extent. This is reflected also in the smaller differences in alveolar morphology between inspiration and expiration.

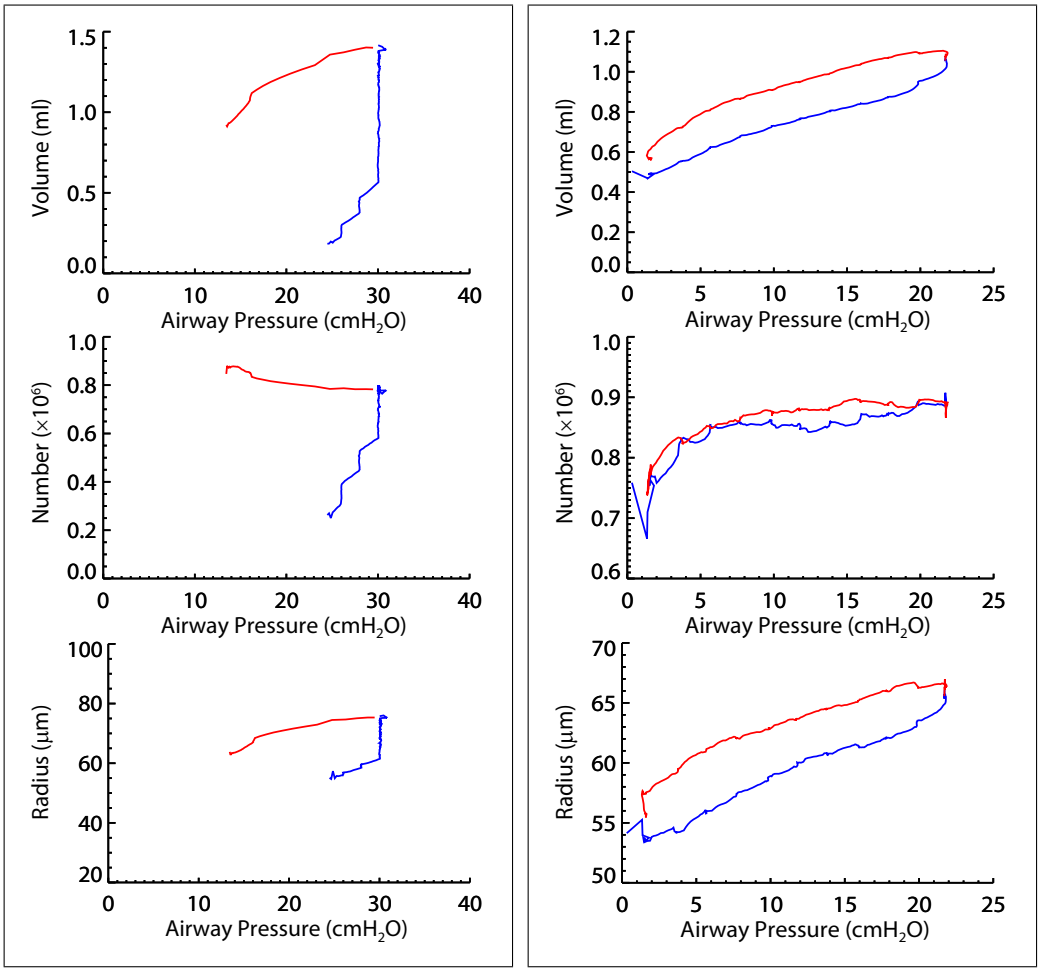

Figure 5.12: AP is plotted with total lung air volume, alveolar number and radius from (a) first breath (the same as in Fig. 5.11(a)) and (b) over a single respiratory cycle several breaths after its first (the same as in Fig. 5.11(c)). The blue and red curves represent points corresponding to inspiration and expiration, respectively.

5.5.3 Discussion

The structural and functional complexity of the lung makes it both intriguing to understand yet difficult to study. Many lung imaging techniques are limited to studying only small regions of the lungs accessible to invasive instruments, or lungs that are effectively motionless, thereby precluding the extraction of functional information. Here, the theoretical derivations developed in section 5.4 were applied to measure the number (N) and radius (R) of alveoli from the speckle patterns of PB-PCX ventilated chest images. Highly spatially resolved PB-PCX images can be recorded in real-time during a respiratory cycle by using intense and coherent synchrotron light coupled with detectors having high spatial resolution and quantum efficiency. This technique can therefore provide valuable insight into the structural lung changes during respiration.

In this study, N and R were measured for the whole lungs. However, a key benefit of this technique is its ability to also measure N and R locally, which requires PS_{Area} and V_L to also be regionally measured. The minimum size of the ROI that V_L can be measured from, using the technique adopted in this study (i.e., Kitchen et al. (2008)), is limited by the differential movement of the bone. However, the technique developed in chapter 3 can be utilized here to measure V_L on a pixel-by-pixel basis (Leong et al., 2013a). For calculating PS_{Area}, the ROI must be large enough to adequately sample the power spectrum. Given the detector pixel size of 15.23 μm and typical alveolar size of 150 μm, N and R can be calculated from a ROI as small as ~0.5 mm^2 compared to that of the entire lung being ~230 mm^2. This would be important in optimizing ventilation strategies to ensure all parts of the lung are adequately aerated without over-distending the alveoli that can lead to conditions such as ventilation-induced lung injury and bronchopulmonary dysplasia. Diagnosis and treatment of respiratory diseases including emphysema could also benefit by better localizing and targeting the diseased region.

Non-aerated PB-PCX images of the lungs are required for the technique presented herein but are not always accessible, particularly for studying subjects that are not newborn. One alternative is intensity thresholding a low dose chest CT image reconstructed from phase retrieved PB-PCX images (using SIPRA) to remove the aerated alveoli, with the resulting image Radon-transformed then propagated using the angular spectrum described in section 1.9 to obtain the non-aerated PB-PCX chest image. While CT can provide information on N and R, the technique presented herein can achieve this using single projections. Consequently, the temporal resolution of this technique is far superior in allowing dynamic measures at a significantly lower radiation dose than CT. Similarity in anatomical structure of the chest within a species should also make it possible to use a non-aerated PB-PCX image for different subjects of the same species. This would avoid

doing CT and imparting unnecessary radiation dose to every subject.

The large-distance error was associated with the loss of speckle contrast at large ODDs despite remaining within the near-field regime and was accounted for empirically in this work by imaging rabbit kittens at different ODDs. It would be interesting in future work to determine the source of this large-distance error. It could be due to the partial coherence of the x-ray source, which blurs speckle contrast. Synchrotron x-rays, however, are extremely coherent as the use of a crystal monochromator produces a small frequency bandwidth and the source size was shown to be sufficiently small that it did not adversely affect the speckle contrast at the ODD employed. Another possible reason for the reduction in speckle contrast is decoherence, which was introduced in section 4.7.3. While the rabbit kittens were imaged in water, there are objects other than the skin that possess random unresolvable small-scaled defects that cause a reduction in speckle contrast. These include optical elements such as beryllium windows and features within the chest[8].

5.6 Concluding Remarks

This chapter has highlighted the many alveolar imaging techniques with their associated advantages and disadvantages. For dynamically studying the mechanical behavior of lung alveoli *in vivo*, these imaging techniques are not feasible due to either their insufficient temporal resolution, FOV or penetrative depth. A non-invasive low dose in situ PB-PCX imaging-based technique was herein introduced that was able to accurately quantify the number and average size of alveoli in real-time. This technique was first tested on lung phantoms that were made of microspheres. It was shown to accurately calculate the size and number of microspheres, of various sizes and filled in containers of different thicknesses, from recordings of their PB-PCX images. Then the technique was applied on rabbit kittens undergoing mechanical ventilation, which robustly produced dynamic quantitative information on the alveolar number and their average size. This revealed the recruitment and de-recruitment of alveoli. 3D grayscale granulometry was employed as a gold standard for alveolar dimensions and agreed well with our technique. The number of alveoli counted from CT slices of different degrees of aeration confirmed the presence of recruitment/de-recruitment.

The technique presented herein does not require any contrast agents or radionuclides and, because planar imaging is performed, subjects are exposed to much less radiation than from

[8]For the lungs, some of these unresolvable features may include tiny capillaries and the overall aperiodic arrangement of the individual components of the lung such as collagen. For microspheres, it is not so apparent what the unresolvable features are. However, PB-PCX imaging of the same samples of microspheres as used for the work presented in this chapter was performed at beamline Bl20XU, at submicron resolution. The images (not shown here) revealed that the microspheres were contaminated by tiny air pockets and water droplets within the microphores.

high resolution CT imaging. As well as furthering the conceptual understanding of the structural behaviour of the lung, this technique has potential to be performed with a laboratory-based x-ray source and consequently applied to clinical diagnosis of respiratory diseases, evaluating the effect of therapeutic treatments, and monitoring of assisted ventilation.

6 Summary and Future Work

This thesis has described theoretical developments in propagation-based phase contrast x-ray (PB-PCX) imaging of the lungs that were implemented towards performing quantitative lung measurements. A summary of the key results regarding three such developments described in this thesis is presented in section 6.1, along with ideas for improving their performance and employing them outside of synchrotrons in section 6.2.

6.1 Summary of Work

Chapter 3 described a phase retrieval-based method for measuring regional changes in lung air volumes from PB-PCX chest images involving alignment then segmentation of the bones. Image alignment is certainly not new and has long been employed in aligning medical images recorded at different time points and from different imaging modalities. However, to the knowledge of this author, this was the first time image alignment for segmentation purposes was performed on PB-PCX chest images. Two image alignment algorithms were developed: area-based (AB) and feature- and area-based hybrid algorithms. While slightly computationally less efficient, the former was found to be more robust and accurate than the latter, particularly at large lung air volumes. This was attributed to the latter being over-reliant on too few realistic translation vectors and imposing a model on the lungs that became over-simplistic at high lung air volumes. Adopting the area-based approach, changes in lung air volume (V_L) were accurately measured from regions as small as the detector pixel size. It was also found that the non-conservation of the total intensity, caused by the employment of a non-rigid transformation function, negligibly affected the accuracy of the measured V_L. The main advantage discovered in aligning PB-PCX chest images was that the added phase contrast on top of the absorption contrast of the bones significantly decreased the rate of misregistrations.

The focus of this thesis then shifted to the study of lung speckle observed in PB-PCX chest

images of an aerated lung. An analytic expression for the power spectrum of lung speckle within the near-field regime was derived in the first half of chapter 4 by modeling the lungs as a uniformly random distribution of spherical voids embedded in lung tissue. This was validated with PB-PCX lung images simulated utilizing the angular spectrum formalism. Simulations revealed that many properties of the lungs were encoded in the area under the power spectrum (PS_{Area}) of the speckled image. One of the advantages of studying lung speckle in Fourier space was that the bone and lung speckle signals dominated different spatial frequencies and hence lung speckle could be exclusively studied.

One aspect of the lung deciphered from PS_{Area} was V_L. This was tested in the second half of chapter 4, where lung speckle power spectra were computed from recorded PB-PCX chest images of rabbit kittens immersed in water and calibrated against V_L, which was measured separately utilizing a phase retrieval-based method. A one-to-one correlation between the two parameters was found, thereby validating their relationship. The fact that the relationship was one-to-one alleviated a potential problem in that the relationship may have varied significantly between rabbit kittens and breathing/ventilation strategy (for e.g. small and large tidal volumes). This calibration curve was successfully utilized to measure total changes in V_L from PB-PCX chest images of rabbit kittens immersed in air. The results agreed well with those measured using a flowmeter. The advantage of this method is that the bone and lung signal are separated in Fourier space and consequently allow absolute measures of V_L. To achieve this utilizing the method described in chapter 3, both the chest immersed in water and a PB-PCX non-aerated chest image are required. Consequently, the signal-to-noise ratio (SNR) is significantly boosted, which becomes important when working with lower powered laboratory-based x-ray sources.

Another aspect lung speckle encodes is the alveolar population and their average size. In chapter 5, a method was developed, called the speckle-based alveolar analysis method (SAAM), for extracting these structural parameters based on the theory developed in chapter 4. This was tested on lung phantoms, constructed using microspheres, and was capable of accurately measuring their size and number provided that the near-field condition was satisfied. Microspheres uniformly randomly distributed and closely packed were also tested and SAAM was found to be accurate for both. This is despite the fact that SAAM assumes uniformly randomly arranged particles. It was found that the power spectrum of speckled images of particles randomly arranged and closely packed differed in shape but negligibly under their area. This was an important result as the alveoli become closely packed at high V_L. Applying this method to imaging the aerating lungs of newborn rabbit kittens revealed the presence of recruitment and de-recruitment of alveoli, which provides

an explanation for the presence of the hysteresis seen in lung pressure-volume (PV) curves. 3D granulometry was employed as a gold standard for measuring the alveolar dimensions and agreed well with the method presented, while the number of alveoli counted from computed tomography (CT) slices confirmed the presence of recruitment/de-recruitment. The topic of how alveoli behave and how this relates to the shape of PV curves has been of great interest in the literature. The method developed here should prove to be a decisive tool towards addressing this highly debated topic.

6.2 Future Work on Quantitative Phase Contrast X-ray Imaging

This section will begin with possible ways of addressing individual limitations of each quantitative PB-PCX imaging-based method summarized above. Subsequently, a discussion on what areas of additional investigation are required to successfully employ these methods using lab-based x-ray sources is given and what currently available clinical methods with which it could be combined.

In chapter 3, the AB alignment algorithm developed for measuring regional changes in V_L was accurate at up to a volume change per unit mass of around 20 mL/kg. This was due to the increasing complexity in the motion of the chest and differential degree of overlapping of ribs between chest images caused by the angular rotation of the ribs perpendicular to that of the x-ray chest image plane. However, many of the animals ventilated in our studies surpass 20 mL/kg. Moreover, compared to newborn rabbits, the ribs of matured chests are completely calcified along their entire segment, potentially resulting in greater differences in the degree of bone overlapping between chest images. A means to increase the range over which V_L can be measured accurately from this method could be to offset the angle of the chest in the sagittal plane before recording. This would reduce the degree of rib movement and the amount of overlapping bones remains unchanged between chest images. As an extreme example, viewing a hand waving in the plane perpendicular to the line of sight has more differential movement than viewing it along the plane that the hand is waving in.

Another cause for the decrease in accuracy of the AB alignment algorithm is the use of a non-rigid transformation function. While it was shown that this had a negligible effect on the measured total change in V_L, that may not be true for local measures of V_L. To ascertain the extent to which the non-conserving volume contributes regionally, the AB alignment algorithm could be compared with other regional volumetric techniques discussed in chapter 2, such as CT and the

analyzer-based phase contrast x-ray (AB-PCX)-based technique developed by Kitchen et al. (2011). If the transformation function was found to have a significant effect, calculating the Jacobian of the transformation function could be used to locally correct for the intensity of the transformed image[1].

In chapters 4 and 5, the methods developed for extracting structural and functional information from lung speckle are based on the theory developed in section 4.4. It was found that theory broke down by incorrectly predicting the lung speckle contrast at increasing object-to-detector propagation distance (ODD) despite remaining within the near-field regime. One reason given in section 4.7.3 was the limited detector spatial resolution (decoherence). A preliminary investigation into decoherence (not performed in chapter 5) was performed using two detectors, with pixel size 15.23 μm (pco.edge) and 6.38 μm (ORCA Flash) (their features were described in section 5.5.1). A stepwedge packed with 150-180 μm microspheres was imaged using the two detectors under the same experimental conditions. The area under the power spectra (PS_{Area}) (defined in Eq. 4.13) was computed from each detector at different ODDs and is shown in Fig. 6.1(a). Their uncertainties were determined by calculating the standard deviation of PS_{Area} from multiple recordings of the stepwedge. This is plotted with the results presented in Fig. 6.1, but since the fractional uncertainty was ~0.01%, this uncertainty is too small to be seen. At 15 cm ODD, PS_{Area} measured by the ORCA Flash is in close agreement with the expected values, but not so using the pco.edge due to lung speckle contrast decreasing (Fig. 6.1(a)). The expected values were calculated by assuming the PS_{Area} value from the 1 mm thick part of the stepwedge imaged at 15 cm ODD was accurate, and subsequent PS_{Area} values at increasing thickness were extrapolated using Eq. 5.4. Hence, Fig. 6.1(a) supports the notion that decreasing spatial resolution reduces the visibility of phase contrast.

Repeating the experiments described above for studying decoherence but at 1 m ODD, the PS_{Area} measured using ORCA Flash does not agree with the expected value (Fig. 6.1(b)). This is inconsistent with the proof given by Nesterets (2008) in that the degree of decoherence is independent of ODD. It is possible that the lack of agreement in the PS_{Area} is due instead to the breakdown of the near-field condition. Even though according to $N_F \geq \max\{1, |\varphi|_{max}\}$, the near-field condition at 1 m ODD is satisfied, it was relaxed from the more stringent condition, $N_F \gg \max\{1, |\varphi|_{max}\}$ defined by Gureyev et al. (2008). This may be have been incorrect to do so in the first place. Alternatively, $|\varphi|_{max}$ may have been underestimated. This may be due to the

[1]Transformation functions map the coordinate system of one image onto another. This may involve shrinking, expanding, etc. between the coordinate systems. The Jacobian of the transformation function represents these changes by taking the absolute value of the determinant of the matrix of partial derivatives of the coordinates of one system with respect to the other system. Transforming coordinate systems alters the local intensity. The Jacobian represents the degree of change in the intensity between transformed images.

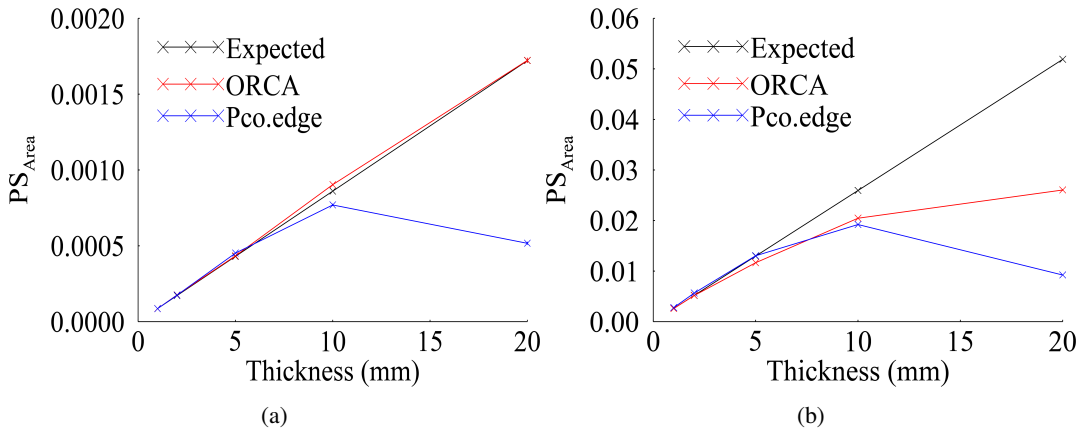

Figure 6.1: A stepwedge packed with 150-180 μm microspheres is imaged using the ORCA Flash and pco.edge detector at (a) 15 cm and (b) 1 m ODD.

discrete sampling of the wavefield, which inevitably smoothes the wavefield. It could also be due to $|\varphi|_{max}$ being computed from the projected phase map when it should be computed from its three-dimensional phase map. Consequently, the maximum ODD of ~2.7 m determined for lung tissue may have been overestimated. A deeper investigation into the near-field condition could be performed to better define the near-field regime.

The lack of agreement between the PS_{Area} shown in Fig. 6.1(a) could also arise from the breakdown of the projection approximation. In this study it was approximated that if the near-field condition ($N_F \geq \max\{1, |\varphi|_{max}\}$) was satisfied then so too is the projection approximation (Eq. 1.37) since $T < L$ and $\Delta x \approx a$. However, Δx is equal to the pixel size, which is generally much smaller than a, this being the characteristic length scale of the object imaged. Consequently, the validity range of the projection approximation may be more narrow than the near-field condition. Simulation and experimental studies on the validity of the projection approximation have only been performed for simple objects such as a single cylinder and millimeter sized object (Martz, Jr. et al., 2007; Morgan et al., 2010a,b). For more complex micron-sized objects such as the alveoli, a generalized scattering formalism, such as the multi-slice approximation[2], can be incorporated into the simulations presented in chapter 4 to study the validity range of the projection approximation and how it affects lung speckle contrast.

[2]In the multi-slice approximation an object is divided into slices of thickness Δz. The projection approximation is used to relate the wavefield at the planes z_0 to that at $z_0 + \Delta z$. Since the projection approximation ignores free-space propagation, the angular spectrum formulation of scalar diffraction integrals is utilized to propagate the wavefield having undergone phase and amplitude shifts under the projection approximation from planes z_0 to $z_0 + \Delta z$. These steps are applied recursively to propagate the resultant wavefield from plane $z_0 + \Delta z$ to $z_0 + 2\Delta z$, and so forth until arriving at the exit surface of the object (Cowley, 1995; Paganin, 2006). The multi-slice approximation provides a more accurate representation of the exit-surface wavefield compared to that given by the projection approximation as it accounts for scattering within the object.

All three of the quantitative methods developed in this thesis are capable of performing local measures of lung function. To correctly do this, the expansion and deflation of the lungs should be taken into account rather than using a fixed sized region of interest in a two-dimensional (2D) image. Christensen et al. (2007) showed that lungs do not expand or relax uniformly but in a local manner. Fouras et al. (2012) developed a particle image velocimetry-based algorithm that is able to measure regional expansion of the lungs by tracking the motion of the lung-induced speckles. Future studies could be performed by adapting some of their work to further increase the accuracy of the techniques developed here.

It would be ideal if the three quantitative methods can be employed utilizing laboratory-based x-ray generators so that they become more widely accessible for researchers and for clinicians to test on humans. Since such generators are typically orders of magnitude lower powered than synchrotrons, filtering the beam to make it monochromatic is ill-afforded. However, these quantitative methods are valid only with monochromatic x-rays and consequently would need to be generalized for a polychromatic source. Gureyev and Wilkins (1998) showed that the near-field intensity equation (NFIE) (Eq. 1.55), the underlying equation for all three of the quantitative methods, can be generalized for a polychromatic x-ray source so long as the projection approximation remains valid across the x-ray energy spectrum. Typical spectra from laboratory-based x-ray sources range from 15-70 keV, which for lung tissue of small animals is sufficiently weakly scattering for the projection approximation to remain valid within this energy range (Hemberg, 2004). For larger animals this may not be true at lower energies. In that case the x-rays can be beam hardened to filter out the lower energies. Additional information is required in order to use the generalized form of NFIE, namely the x-ray beam intensity profile and its energy spectrum. These can be measured by imaging the direct beam profile and utilizing an energy sensitive detector.

Partial spatial coherence may also need to be accounted for when utilizing lower powered laboratory-based x-ray generators as the source-to-object distance (SOD) will most likely be much less than that in a synchrotron. Consequently, it has a significant blurring affect on recorded PB-PCX images. For all the work performed in this thesis, the blurring effect was quantified using the method described by Gureyev et al. (2009). However, this method may not be applicable for lab-based x-ray sources since it assumes that the x-rays at the source plane are delta correlated. While this assumption is mostly true for synchrotron sources, even if the x-rays at the source plane are not delta correlated, the large ODDs allows the wavefield to evolve to what it would be if the x-rays were delta correlated (Cerbino, 2007). Therefore for lab-based x-ray sources, a more rigorous derivation incorporating partial spatial coherence may be needed to accurately recover

lung information. Some leads into studying the blurring effects of partially coherent x-rays can be found in Gureyev et al. (2006) and Petruccelli et al. (2013).

If the quantitative techniques become successful using lab-based sources, then they could be tested on humans. In regards to the exposure of x-ray radiation dose humans would receive, in this work, the skin entrance radiation dose of x-rays measured on the animals was ~1 mGy per PB-PCX image while the SNR (mean/standard deviation of image intensity) was ~10. The latter was measured from several regions that were away from the rabbit kitten but within the water-filled cylinder. This radiation dose is only slightly more than the standard chest x-ray image, but the spatial resolution is significantly higher and is still much lower than a standard chest CT (Bushberg et al., 2012, Ch. 11). However, the same SNR may not be achievable with human lungs under the same experimental conditions as they are much larger and consequently more attenuating than that of rabbit kittens. The SNR could be improved by increasing the x-ray energy to reduce the degree of attenuation while achieving high phase contrast since it decreases less rapidly. How much the x-ray energy would need to be increased by must also be determined.

The volumetric techniques (described in chapters 3 and 4) can potentially be combined with perfusion tests to measure gas exchange efficiency[3]. Currently, ventilation and perfusion tests are done separately through SPECT and angiography[4], respectively. Combining the techniques described herein with angiography, which has successfully been performed using PB-PCX imaging (Lang et al., 2014), allows ventilation/perfusion test to be done simultaneously and potentially better resolve regions with poor gas exchange.

The work done in this thesis proves that phase contrast x-ray (PCX) imaging provides much more than enhancing soft tissue contrast to produce aesthetically pleasing images. PCX imaging-based quantitative techniques were developed and gave insight into the dynamics of lung mechanics. From fundamental research regarding the energy proficiency of the lungs to matters of clinical significance such as detecting respiratory diseases in their early stage where treatment is more efficacious, the techniques developed herein can lend important contribution to addressing these issues and more.

[3]For an animal to function normally, it requires a sufficient supply of oxygen (ventilation) met with a sufficient blood supply (perfusion) to take up the oxygen. Deviation from the norm is indicated by a mismatch in ventilation and perfusion. This is measured clinically using scintigraphy and is commonly referred to as a ventilation/perfusion scan.

[4]Angiography is an imaging technique where a radioactive isotope or contrast agent (for example, Technetiumand (Zöphel et al., 2009) and iodine (Sarnelli et al., 2005), respectively) is injected into the pulmonary circulatory system from which its activity can be quantified.

References

G. S. Agarwal, G. Gbur, and E. Wolf. Coherence properties of sunlight. *Opt. Lett.*, 29(5):459, 2004. (p 15)

L. Allen and M. Oxley. Phase retrieval from series of images obtained by defocus variation. *Opt. Commun.*, 199(1-4):65–75, 2001. (p 41)

J. J. Anderson, M.-T. Herd, M. R. King, A. Haak, Z. T. Hafez, J. Song, M. L. Oelze, E. L. Madsen, J. A. Zagzebski, W. D. O'Brien, and T. J. Hall. Interlaboratory comparison of backscatter coefficient estimates for tissue-mimicking phantoms. *Ultrason. Imaging*, 32(1):48–64, 2010. (p 138)

M. R. Arab, M. H. Heidari, R. Mashhadi, R. Mirzaei, and M. Jahantigh. Histological study of the toxic effects of solder fumes on spermatogenesis in rats. *Cell J.*, 13(1):5–10, 2011. (p 134)

I. Arad, N. Simanovsky, and R. Braunstein. Exposure of extremely low birth weight infants to diagnostic x-rays: a longitudinal study. *Acta Paediatr.*, 98(2):266–269, 2009. (p 50)

F. Arfelli, D. Pelliccia, A. Cedola, A. Astolfo, I. Bukreeva, P. Cardarelli, D. Dreossi, S. Lagomarsino, R. Longo, L. Rigon, N. Sodini, and R. H. Menk. Recent developments on techniques for differential phase imaging at the medical beamline of ELETTRA. *J. Instrum.*, 8(06):C06001, 2013. (p 38)

A.-L. Barabási, S. Buldyrev, H. Stanley, and B. Suki. Avalanches in the lung: A statistical mechanical model. *Phys. Rev. Lett.*, 76(12):2192–2195, 1996. (p 113)

A. Barty. *Quantitative phase-amplitude microscopy*. PhD thesis, The University of Melbourne, 2000. (p 44)

I. V. Basistiy, M. S. Soskin, and M. V. Vasnetsov. Optical wavefront dislocations and their properties. *Opt. Commun.*, 119(5-6):604–612, 1995. (p 104)

J. H. T. Bates. *Lung Mechanics: An Inverse Modeling Approach*. Cambridge University Press, Cambridge, 2009. (p 1)

G. Bauman, M. Puderbach, M. Deimling, V. Jellus, C. Chefd'hotel, J. Dinkel, C. Hintze, H.-U. Kauczor, and L. R. Schad. Non-contrast-enhanced perfusion and ventilation assessment of the human lung by means of fourier decomposition in proton MRI. *Magn. Reson. Med.*, 62(3): 656–664, 2009. (p 54)

M. Bech, A. Tapfer, A. Velroyen, A. Yaroshenko, B. Pauwels, J. Hostens, P. Bruyndonckx, A. Sasov, and F. Pfeiffer. In-vivo dark-field and phase-contrast x-ray imaging. *Sci. Rep.*, 3:3209, 2013. (p 39)

M. Beister, D. Kolditz, and W. A. Kalender. Iterative reconstruction methods in x-ray CT. *Phys. Medica*, 28(2):94–108, 2012. (p 50)

P. Beltrame, E. Bolle, A. Braem, C. Casella, E. Chesi, N. Clinthorne, R. De Leo, G. Dissertori, L. Djambazov, V. Fanti, M. Heller, C. Joram, H. Kagan, W. Lustermann, F. Meddi, E. Nappi, F. Nessi-Tedaldi, J. Oliver, F. Pauss, M. Rafecas, D. Renker, A. Rudge, D. Schinzel, T. Schneider, J. Séguinot, P. Solevi, S. Stapnes, and P. Weilhammer. The AX-PET demonstrator-Design, construction and characterization. *Nucl. Instrum. Meth. A*, 654(1):546–559, 2011. (p 52)

M. A. Beltran, D. M. Paganin, K. Uesugi, and M. J. Kitchen. 2D and 3D X-ray phase retrieval of multi-material objects using a single defocus distance. *Opt. Express*, 18(7):6423–36, 2010. (p 56, 63)

M. A. Beltran, D. M. Paganin, K. K. W. Siu, A. Fouras, S. B. Hooper, D. H. Reser, and M. J. Kitchen. Interface-specific x-ray phase retrieval tomography of complex biological organs. *Phys. Med. Biol.*, 56(23):7353–7369, 2011. (p 121)

Y. Bentoutou, N. Taleb, A. Bounoua, K. Kpalma, and J. Ronsin. Feature-based registration of satellite images. In *2007 15th Int. Conf. Digit. Signal Process.*, pages 419–422. IEEE, 2007. (p 65)

N. Berend and G. E. Marlin. Arrest of alveolar multiplication in kyphoscoliosis. *Pathology*, 11(3): 485–491, 1979. (p 134)

M. V. Berry and M. R. Dennis. Phase singularities in isotropic random waves. *P. R. Soc. A*, 456 (2001):2059–2079, 2000. (p 104)

J. Bickenbach, R. Dembinski, M. Czaplik, S. Meissner, A. Tabuchi, M. Mertens, L. Knels, W. Schroeder, P. Pelosi, E. Koch, W. M. Kuebler, R. Rossaint, and R. Kuhlen. Compari-

son of two in vivo microscopy techniques to visualize alveolar mechanics. *J. Clin. Monitor Comp.*, 23(5):323–32, 2009. (p 115, 135)

J. Biederer. General Requirements of MRI of the Lung and Suggested Standard Protocol. In *MRI Lung*, chapter 1, pages 3–16. Springer Science & Business Media, Heidelberg, 2009. (p 54)

J. A. Blokland, P. Trindev, M. P. Stokkel, and E. K. Pauwels. Positron emission tomography: a technical introduction for clinicians. *Eur. J. Radiol.*, 44(1):70–75, 2002. (p 52)

U. Bonse and M. Hart. An x-ray interferometer. *Appl. Phys. Lett.*, 6(8):155–156, 1965. (p 38)

M. Born and E. Wolf. *Principles of Optics: Electromagnetic Theory of Propagation, Interference and Diffraction of light*. CUP Archive, Cambridge, 7th edition, 1999. (p 28)

M. Born and E. Wolf. *Principles of Optics: Electromagnetic Theory of Propagation, Interference and Diffraction of Light*. CUP Archive, Cambridge, 2000. (p 110)

S. Braber, K. A. T. Verheijden, P. A. J. Henricks, A. D. Kraneveld, and G. Folkerts. A comparison of fixation methods on lung morphology in a murine model of emphysema. *Am. J. Pysiol.-Lung C.*, 299(6):L843–851, 2010. (p 134)

W. L. Bragg. The diffraction of short electromagnetic waves by a crystal. In *Proc. Camb. Philol. Soc.*, volume 17, pages 43–57, 1913. (p 36)

L. Brancazio, G. N. Franz, E. L. Petsonk, and D. G. Frazer. Lung area-volume models in relation to the recruitment-derecruitment of individual lung units. *Ann. Biomed. Eng.*, 29(3):252–262, 2001. (p 132)

D. Briedis, K. K. W. Siu, D. M. Paganin, K. M. Pavlov, and R. A. Lewis. Analyser-based mammography using single-image reconstruction. *Phys. Med. Biol.*, 50(15):3599–3611, 2005. (p 2)

D. Brogioli. *Near Field Speckles*. PhD thesis, Cornell university, 2009. (p 105, 106)

D. J. G. Buch. *Pharmacology ReCap 2.0 for Bachelor of Dentistry Students*. Quick Review of Pharmacology, Rajkot, 2010. (p 2)

A. Burian, P. Kuosmanen, J. Saarinen, and C. Rusu. Two dimensional phase retrieval using neural networks. In *Neural Networks Signal Process. X. Proc. 2000 IEEE Signal Process. Soc. Work. (Cat. No.00TH8501)*, volume 2, pages 652–661. IEEE, 2000. (p 41)

A. Burvall, U. Lundström, P. A. C. Takman, D. H. Larsson, and H. M. Hertz. Phase retrieval in x-ray phase-contrast imaging suitable for tomography. *Opt. Express*, 19(11):10359–76, 2011. (p 43)

J. T. Bushberg, J. A. Seibert, E. M. Leidholdt, and J. M. Boone. *The Essential Physics of Medical Imaging*. Lippincott Williams & Wilkins, Philadelphia, 3rd edition, 2012. (p 9, 10, 16, 17, 52, 53, 135, 169)

J. Callahan, M. S. Hofman, S. Siva, T. Kron, M. E. Schneider, D. Binns, P. Eu, and R. J. Hicks. High-resolution imaging of pulmonary ventilation and perfusion with 68Ga-VQ respiratory gated (4-D) PET/CT. *Eur. J. Nucl. Med. Mol. I.*, 41(2):343–9, 2014. (p 50)

Cancer Research UK. Worldwide Cancer Statistics, 2014. URL `http://www.cancerresearchuk.org/cancer-info/cancerstats/world/`. (p 4)

D. E. Carney, C. E. Bredenberg, H. J. Schiller, A. L. Picone, U. G. McCann, L. A. Gatto, G. Bailey, M. Fillinger, and G. F. Nieman. The mechanism of lung volume change during mechanical ventilation. *Am. J. Resp. Crit. Care*, 160(5):1697–1702, 1999. (p 131, 132)

R. P. Carnibella, A. Fouras, and M. J. Kitchen. Single-exposure dual-energy-subtraction x-ray imaging using a synchrotron source. *J. Synchrotron Radiat.*, 19(Pt 6):954–959, 2012a. (p 66)

R. P. Carnibella, M. J. Kitchen, and A. Fouras. Determining particle size distributions from a single projection image. *Opt. Express*, 20(14):15962–15968, 2012b. (p 102, 105, 106)

R. Cerbino, L. Peverini, M. A. C. Potenza, A. Robert, P. Bösecke, and M. Giglio. X-ray-scattering information obtained from near-field speckle. *Nat. Phys.*, 4(3):238–243, 2008. (p 105, 106)

R. Cerbino. Correlations of light in the deep Fresnel region: An extended Van Cittert and Zernike theorem. *Phys. Rev. A*, 75(5):053815, 2007. (p 168)

E. J. Chae, J. B. Seo, H. W. Goo, N. Kim, K.-S. Song, S. D. Lee, S.-J. Hong, and B. Krauss. Xenon ventilation CT with a dual-energy technique of dual-source CT: initial experience. *Radiology*, 248(2):615–624, 2008. (p 50)

S. Chang, N. Kwon, B. M. Weon, J. Kim, C. K. Rhee, H. S. Choi, Y. Kohmura, M. Yamamoto, T. Ishikawa, and J. H. Je. Tracking x-ray microscopy for alveolar dynamics in live intact mice. *Sci. Rep.*, 3:1304, 2013. (p 135)

J. F. Chen, J. A. Zagzebski, F. Dong, and E. L. Madsen. Estimating the spatial autocorrelation function for ultrasound scatterers in isotropic media. *Med. Phys.*, 25(5):648–655, 1998. (p 138)

S. R. Cherry, J. A. Sorenson, and M. E. Phelps. *Physics in Nuclear Medicine*. Elsevier Health Sciences, Philadelphia, 2012. (p 51, 52)

P. R. Chess, L. Toia, and J. N. Finkelstein. Mechanical strain-induced proliferation and signaling in pulmonary epithelial H441 cells. *Am J Physiol Lung Cell Mol Physiol*, 279(1):L43–51, 2000. (p 4)

G. E. Christensen, J. H. Song, W. Lu, I. El Naqa, and D. A. Low. Tracking lung tissue motion and expansion/compression with inverse consistent image registration and spirometry. *Med. Phys.*, 34(6):2155–2163, 2007. (p 168)

P. Coan, A. Wagner, A. Bravin, P. C. Diemoz, J. Keyriläinen, and J. Mollenhauer. In vivo x-ray phase contrast analyzer-based imaging for longitudinal osteoarthritis studies in guinea pigs. *Phys. Med. Biol.*, 55(24):7649–7662, 2010. (p 2)

A. Compton. A quantum theory of the scattering of X-rays by light elements. *Phys. Rev.*, 21(5): 483–502, 1923. (p 9, 18)

D. M. Connor, E. B. Cole, Z. Zhong, C. A. Parham, and E. D. Pisano. Preliminary performance measurements from a second generation diffraction enhanced imaging system. In N. J. Pelc, R. M. Nishikawa, and B. R. Whiting, editors, *SPIE Med. Imaging*, page 83134G. International Society for Optics and Photonics, 2012. (p 38)

J. Conway. Lung imaging-two dimensional gamma scintigraphy, SPECT, CT and PET. *Adv. Drug Deliv. Rev.*, 64(4):357–368, 2012. (p 52)

J. M. Cowley. *Diffraction Physics*. Elsevier, Amsterdam, 3rd edition, 1995. (p 39, 167)

J. T. Cremer. *Advances in Imaging and Electron Physics*, volume 172 of *Advances in Imaging and Electron Physics*. Elsevier, Massachusetts, 2012. (p 19)

J. T. Cremer Jnr. *Neutron and X-ray Optics*. Elsevier, London, 2013. (p 21)

W. R. Crum, T. Hartkens, and D. L. G. Hill. Non-rigid image registration: theory and practice. *Brit. J. Radiol.*, 77(Spec No 2):S140–S153, 2004. (p 64)

B. D. Daly, G. E. Parks, C. H. Edmonds, C. Hibbs, and J. C. Norman. Dynamic alveolar mechanics as studied by videomicroscopy. *Respir. Physiol.*, 24(2):217–231, 1975. (p 1)

E. D'Angelo. Local alveolar size and transpulmonary pressure in situ and in isolated lungs. *Respir. Physiol.*, 14(3):251–266, 1972. (p 132)

C. Darwin. XXXIV. The theory of X-ray reflexion. *Philos. Mag.*, 27(158):315–333, 1914. (p 36)

C. David, B. Nöhammer, H. H. Solak, and E. Ziegler. Differential x-ray phase contrast imaging using a shearing interferometer. *Appl. Phys. Lett.*, 81(17):3287, 2002. (p 39)

T. J. Davis, D. Gao, T. E. Gureyev, A. W. Stevenson, and S. W. Wilkins. Phase-contrast imaging of weakly absorbing materials using hard x-rays. *Nature*, 373(6515):595–598, 1995. (p 36)

M. de Berg, O. Cheong, M. van Kreveld, and M. Overmars. Delaunay Triangulations. In *Comput. Geom. Algorithms Appl.*, chapter 9, pages 191–215. Springer Science & Business Media, Berlin, 3rd edition, 2008. (p 77)

P. Debye. Zerstreuung von Röntgenstrahlen. *Ann. Phys.-Berlin*, 351(6):809–823, 1915. (p 147)

B. Delaunay. Sur la sphère vide. A la mémoire de Georges Voronoï. *Bull. l'Académie des Sci. l'URSS*, 7(6):793–800, 1934. (p 77)

C. J. DiMaio, S. Nagula, K. A. Goodman, A. Y. Ho, A. J. Markowitz, M. A. Schattner, and H. Gerdes. EUS-guided fiducial placement for image-guided radiation therapy in GI malignancies by using a 22-gauge needle (with videos). *Gastrointest. Endosc.*, 71(7):1204–1210, 2010. (p 66)

P. A. M. Dirac. The Quantum Theory of the Electron. *P. R. Soc. A*, 117(778):610–624, 1928. (p 52)

G. Dixit, J. Slowik, and R. Santra. Proposed imaging of the ultrafast electronic motion in samples using X-ray phase contrast. *Phys. Rev. Lett.*, 110(13):137403, 2013. (p 9)

Y. Du, J. Huang, D. Lin, and H. Niu. Analysis of field of view limited by a multi-line x-ray source and its improvement for grating interferometry. *Anal. Bioanal. Chem.*, 404(3):793–797, 2012. (p 41)

S. Dubsky, S. B. Hooper, K. K. W. Siu, and A. Fouras. Synchrotron-based dynamic computed tomography of tissue motion for regional lung function measurement. *J. Roy. Soc. Interface*, 9 (74):2213–2224, 2012. (p 135)

M. S. Dunnill. Effect of lung inflation on alveolar surface area in the dog. *Nature*, 214(5092): 1013–1014, 1967. (p 132)

A. R. Edmonds. *Angular Momentum in Quantum Mechanics*. Princeton University Press, Princeton, 1996. (p 53)

A. Einstein. *Relativity, the Special and the General Theory: A Popular Exposition.* Ryerson Press, Canada, third edition, 1920. (p 24)

J. D. Escolar and A. Escolar. Lung hysteresis: a morphological view. *Histol. Histopathol.*, 19(1): 159–166, 2004. (p 131)

J. Ewald, T. Wilhein, I. McNulty, C. Eyberger, and B. Lai. Source size characterization of a microfocus x-ray tube used for in-line phase-contrast imaging. *10th Int. Conf. x-ray Microsc.*, 1365(1):81–83, 2011. (p 128)

P. P. Ewald. Introduction to the dynamical theory of x-ray diffraction. *Acta. Crystall. A-Crys.*, 25 (1):103–108, 1969. (p 36)

D. S. Faffe and W. A. Zin. Lung parenchymal mechanics in health and disease. *Physiol. Rev.*, 89 (3):759–75, 2009. (p 132)

R. P. Feynman, R. B. Leighton, and M. Sands. *The Feynman Lectures on Physics*, volume 2. Basic Books, New York, millennium edition, 2013. (p 25)

S. Fichele, N. Woodhouse, A. J. Swift, Z. Said, M. N. J. Paley, L. Kasuboski, G. H. Mills, E. J. R. van Beek, and J. M. Wild. MRI of helium-3 gas in healthy lungs: posture related variations of alveolar size. *JMRI-J. Magn. Reson. Im.*, 20(2):331–335, 2004. (p 135)

M. Fizeau. Determination of the velocity of light by experiment. *J. Frankl. Inst.*, 48(6):452–453, 1849. (p 7)

J. B. Forrest. The effect of changes in lung volume on the size and shape of alveoli. *J. Physiol.*, 210(3):533–547, 1970. (p 132)

A. Fouras, B. J. Allison, M. J. Kitchen, S. Dubsky, J. Nguyen, K. Hourigan, K. K. W. Siu, R. A. Lewis, M. J. Wallace, and S. B. Hooper. Altered lung motion is a sensitive indicator of regional lung disease. *Ann. Biomed. Eng.*, 40(5):1160–1169, 2012. (p 4, 168)

D. G. Frazer, W. G. Lindsley, K. Rosenberry, W. McKinney, W. T. Goldsmith, J. S. Reynolds, S. Tomblyn, and A. Afshari. Model predictions of the recruitment of lung units and the lung surface area-volume relationship during inflation. *Ann. Biomed. Eng.*, 32(5):756–763, 2004. (p 132)

T. Fricke-Begemann and K. D. Hinsch. Measurement of random processes at rough surfaces with digital speckle correlation. *J. Opt. Soc. Am. A*, 21(2):252–262, 2004. (p 102)

W. Friedrich. Die Geschichte der Auffindung der Röntgenstrahlinterferenzen. *Naturwissenschaften*, 10(16):363–366, 1922. (p 36)

J. G. Fujimoto, C. Pitris, S. A. Boppart, and M. E. Brezinski. Optical coherence tomography: an emerging technology for biomedical imaging and optical biopsy. *Neoplasia*, 2(1-2):9–25, 2000. (p 136)

M. Gaertner, P. Cimalla, S. Meissner, W. M. Kuebler, and E. Koch. Three-dimensional simultaneous optical coherence tomography and confocal fluorescence microscopy for investigation of lung tissue. *J. Biomed. Opt.*, 17(7):071310, 2012. (p 2, 137)

S. Gao, L. Zhang, H. Wang, R. de Crevoisier, D. D. Kuban, R. Mohan, and L. Dong. A deformable image registration method to handle distended rectums in prostate cancer radiotherapy. *Med. Phys.*, 33(9):3304–3312, 2006. (p 64)

C. Garcia, L. Prota, M. Morales, P. Romero, W. Zin, and P. Rocco. Understanding the mechanisms of lung mechanical stress. *Braz. J. Med. Biol. Res.*, 39(6):697–706, 2006. (p 4)

A. B. Garson, E. W. Izaguirre, S. G. Price, and M. A. Anastasio. Characterization of speckle in lung images acquired with a benchtop in-line x-ray phase-contrast system. *Phys. Med. Biol.*, 58 (12):4237–4253, 2013. (p 17, 128)

Y. Ge, K. Li, J. Garrett, and G.-H. Chen. Grating based x-ray differential phase contrast imaging without mechanical phase stepping. *Opt. Express*, 22(12):14246–14252, 2014. (p 41)

R. W. Gerchberg and W. O. Saxton. Phase determination from image and diffraction plane pictures in the electron-microscope. *Optiko*, 34:275–284, 1971. (p 41)

R. W. Gerchberg and W. O. Saxton. A practical algorithm for the determination of phase from image and diffraction plane pictures. *Optik*, 35:277–246, 1972. (p 41)

K. Giewekemeyer. *A Study on New Approaches in Coherent X-ray Microscopy of Biological Specimens*. Universitätsverlag Göttingen, Göttingen, 2011. (p 138)

M. Giglio, M. Carpineti, A. Vailati, and D. Brogioli. Near-field intensity correlations of scattered light. *Appl. Optics*, 40(24):4036–4040, 2001. (p 102)

S. F. Gilbert. *Developmental Biology*. Sinauer Associates, Massachusetts, 2010. (p 96)

A. A. Ginde, A. Foianini, D. M. Renner, M. Valley, and C. A. Camargo. Availability and quality of computed tomography and magnetic resonance imaging equipment in U.S. emergency departments. *Acad. Emerg. Med.*, 15(8):780–783, 2008. (p 54)

I. Goetz, A. Hoo, S. Lum, and J. Stocks. Assessment of passive respiratory mechanics in infants: double versus single occlusion? *Eur. Respir. J.*, 17(3):449–455, 2001. (p 134)

M. Gomez, A. Nogales, M. C. Garcia-Gutierrez, and T. A. Ezquerra, editors. *Applications of Synchrotron Light to Scattering and Diffraction in Materials and Life Sciences*, volume 776 of *Lecture Notes in Physics*. Springer, Berlin, 2009. (p 5)

J. W. Goodman. *Speckle Phenomena in Optics: Theory and Applications*. Roberts & Company, Colorado, 2010. (p 102, 105, 126)

S. Goto, K. Takeshita, Y. Suzuki, H. Ohashi, Y. Asano, H. Kimura, T. Matsushita, N. Yagi, M. Isshiki, H. Yamazaki, Y. Yoneda, K. Umetani, and T. Ishikawa. Construction and commissioning of a 215-m-long beamline at SPring-8. *Nucl. Instrum. Meth. A*, 467-468:682–685, 2001. (p 16, 83, 120)

I. A. Greaves and H. J. Colebatch. Elastic behavior and structure of normal and emphysematous lungs post mortem. *Am. Rev. Respir. Dis.*, 121(1):127–136, 1980. (p 134)

H. S. Green and E. Wolf. A scalar representation of electromagnetic fields. *Proc. Phys. Soc. A*, 66 (12):1129–1137, 1953. (p 10)

P. Grunert, W. Müller-Forell, K. Darabi, R. Reisch, C. Busert, N. Hopf, and A. Perneczky. Basic principles and clinical applications of neuronavigation and intraoperative computed tomography. *Comput. Aided Surg.*, 3(4):166–173, 1998. (p 66)

A. Guinier. *X-ray Diffraction in Crystals, Imperfect Crystals, and Amorphous Bodies*. Courier Corporation, New York, 1994. (p 147, 148)

O. Gundogdu, E. Nirgianaki, E. Che Ismail, P. M. Jenneson, and D. A. Bradley. Benchtop phase-contrast x-ray imaging. *Appl. Radiat. Isotopes*, 65(12):1337–1344, 2007. (p 16)

T. E. Gureyev and K. A. Nugent. Phase retrieval with the transport-of-intensity equation. II. Orthogonal series solution for nonuniform illumination. *J. Opt. Soc. Am. A*, 13(8):1670–1682, 1996. (p 41)

T. E. Gureyev and S. W. Wilkins. On x-ray phase retrieval from polychromatic images. *Opt. Commun.*, 147(4-6):229–232, 1998. (p 168)

T. E. Gureyev, C. Raven, A. Snigirev, I. Snigireva, and S. W. Wilkins. Hard x-ray quantitative non-interferometric phase-contrast microscopy. *J. Phys. D. Appl. Phys.*, 32(5):563–567, 1999. (p 41)

T. E. Gureyev, Y. I. Nesterets, D. M. Paganin, A. Pogany, and S. W. Wilkins. Linear algorithms for phase retrieval in the Fresnel region. 2. Partially coherent illumination. *Opt. Commun.*, 259(2): 569–580, 2006. (p 169)

T. E. Gureyev, Y. I. Nesterets, A. W. Stevenson, P. R. Miller, A. Pogany, and S. W. Wilkins. Some simple rules for contrast, signal-to-noise and resolution in in-line x-ray phase-contrast imaging. *Opt. Express*, 16(5):3223–3241, 2008. (p 35, 166)

T. E. Gureyev, S. C. Mayo, D. E. Myers, Y. Nesterets, D. M. Paganin, A. Pogany, A. W. Stevenson, and S. W. Wilkins. Refracting Röntgen's rays: propagation-based x-ray phase contrast for biomedical imaging. *J. Appl. Phys.*, 105(10):102005, 2009. (p 115, 151, 168)

D. F. Habets, S. I. Pollmann, X. Yuan, T. M. Peters, and D. W. Holdsworth. Error analysis of marker-based object localization using a single-plane XRII. *Med. Phys.*, 36(1):190–200, 2009. (p 74)

M. M. Hall Jnr, V. G. Veeraraghavan, H. Rubin, and P. G. Winchell. The approximation of symmetric x-ray peaks by Pearson type VII distributions. *J. Appl. Crystallogr.*, 10(1):66–68, 1977. (p 151)

S. Han, H. Yu, J. Cheng, C. Gao, and Z. Luo. Contrast and resolution in direct Fresnel diffraction phase-contrast imaging with partially coherent x-ray source. *Rev. Sci. Instrum.*, 75(10):3146–3151, 2004. (p 128)

R. S. Harris. Pressure-volume curves of the respiratory system. *Respir. Care*, 50(1):78–99, 2005. (p 134)

R. V. L. Hartley. Transmission of information. *Bell Syst. Tech. J.*, 7(3):535–563, 1928. (p 71)

R. H. Hashemi, W. G. Bradley, and C. J. Lisanti. *MRI: The Basics*. Lippincott Williams & Wilkins, Philadelphia, 2012. (p 54)

E. Hecht. *Optics*. Addison Wesley Longman, Boston, 2002. (p 19, 22, 25, 137)

R. A. P. Hellmuth and R. G. Lima. Contact Finite Element with Surface Tension Adhesion. In J. Natal, M. Renato, T. João, M. R. S., M. Pinotti, Barbosa, and A. Slade, editors, *Technol. Med. Sci.*, Lecture Notes in Computational Vision and Biomechanics, pages 19–38. Springer Netherlands, 2012. (p 132)

O. Hemberg, M. Otendal, and H. M. Hertz. Liquid-metal-jet anode electron-impact x-ray source. *Appl. Phys. Lett.*, 83(7):1483–1485, 2003. (p 17)

O. Hemberg. Liquid-metal-jet anode x-ray tube. *Opt. Eng.*, 43(7):1682–1688, 2004. (p 168)

D. L. Hill, D. J. Hawkes, J. E. Crossman, M. J. Gleeson, T. C. Cox, E. E. Bracey, A. J. Strong, and P. Graves. Registration of MR and CT images for skull base surgery using point-like anatomical features. *Brit. J. Radiol.*, 64(767):1030–1035, 1991. (p 66)

D. L. Hill, P. G. Batchelor, M. Holden, and D. J. Hawkes. Medical image registration. *Phys. Med. Biol.*, 46(3):R1–45, 2001. (p 68)

N. H. Hillman, T. J. M. Moss, S. G. Kallapur, C. Bachurski, J. J. Pillow, G. R. Polglase, I. Nitsos, B. W. Kramer, and A. H. Jobe. Brief, large tidal volume ventilation initiates lung injury and a systemic response in fetal sheep. *Am. J. Resp. Crit. Care*, 176(6):575–581, 2007. (p 4)

S. B. Hooper, M. J. Kitchen, M. J. Wallace, N. Yagi, K. Uesugi, M. J. Morgan, C. Hall, K. K. W. Siu, I. M. Williams, M. Siew, S. C. Irvine, K. Pavlov, and R. A. Lewis. Imaging lung aeration and lung liquid clearance at birth. *FASEB J.*, 21(12):3329–3337, 2007. (p 92, 110, 115)

S. B. Hooper, M. J. Kitchen, A. Fouras, M. J. Wallace, S. Dubsky, K. K. W. Siu, M. L. Siew, N. Yagi, K. Uesugi, and R. A. Lewis. Combined lung imaging and respiratory physiology research at SPring-8. *Synchrotron Radiat. News*, 24(2):19–23, 2011. (p 4)

S. B. Hooper, M. J. Kitchen, M. L. L. Siew, R. A. Lewis, A. Fouras, A. B. te Pas, K. K. W. Siu, N. Yagi, K. Uesugi, and M. J. Wallace. Imaging lung aeration and lung liquid clearance at birth using phase contrast x-ray imaging. *Clin. Exp. Pharmacol. Physiol.*, 36(1):117–25, 2009. (p 4)

J. Hseigh. *Computed Tomography: Principles, Design, Artifacts, and Recent Advances*. SPIE Press, Washington, 2003. (p 109)

C. Hu, T. Zhao, L. Zhang, H. Li, X. Zhao, and S. Luo. Information extraction and CT reconstruction of liver images based on diffraction enhanced imaging. *Prog. Nat. Sci.*, 19(8):955–962, 2009. (p 56)

J. H. Hubbell. Photon cross sections, attenuation coefficients and energy absorption coefficients from 10 keV to 100 GeV. *Natl. Stand. Ref. Data Ser. Nat Bur. Stand.*, 29:1–85, 1969. (p 17, 20)

R. D. Hubmayr. Perspective on lung injury and recruitment: a skeptical look at the opening and collapse story. *Am. J. Resp. Crit. Care*, 165(12):1647–1653, 2002. (p 132, 133)

F. Hüe, J. M. Rodenburg, A. M. Maiden, F. Sweeney, and P. A. Midgley. Wave-front phase retrieval in transmission electron microscopy via ptychography. *Phys. Rev. B*, 82(12):121415, 2010. (p 41)

J. R. Hurley and R. B. Cattell. The procrustes program: producing direct rotation to test a hypothesized factor structure. *Behav. Sci.*, 7(2):258–262, 2007. (p 73)

V. N. Ingal and E. A. Beliaevskaya. X-ray plane-wave topography observation of the phase contrast from a non-crystalline object. *J. Phys. D. Appl. Phys.*, 28(11):2314–2317, 1995. (p 36)

M. F. Insana, R. F. Wagner, D. G. Brown, and T. J. Hall. Describing small-scale structure in random media using pulse-echo ultrasound. *J. Acoust. Soc. Am.*, 87(1):179–192, 1990. (p 2, 137, 138)

T. Ishigaki, S. Sakuma, Y. Horikawa, M. Ikeda, and H. Yamaguchi. One-shot dual-energy subtraction imaging. *Radiology*, 161(1):271–273, 1986. (p 66)

M. S. Islam, R. A. Lewis, K. Uesugi, and M. J. Kitchen. A high precision recipe for correcting images distorted by a tapered fiber optic. *J. Instrum.*, 5(09):P09008, 2010. (p 82, 84)

E. C. Ismail, W. Kaabar, D. Garrity, O. Gundogdu, O. Bunk, F. Pfeiffer, M. J. Farquharson, and D. A. Bradley. X-ray phase contrast imaging of the bone-cartilage interface. *Appl. Radiat. Isotopes*, 68(4-5):767–771, 2010. (p 2)

J. C. Jackson, W. E. Truog, T. A. Standaert, S. E. Juul, J. H. Murphy, E. Y. Chi, A. P. Mackenzie, and W. A. Hodson. Effect of high-frequency ventilation on the development of alveolar edema in premature monkeys at risk for hyaline membrane disease. *Am. Rev. Respir. Dis.*, 143(4 Pt 1): 865–871, 1991. (p 4)

B. Jähne. *Digital Image Processing*. Springer Science & Business Media, Berlin, 6th edition, 2005. (p 48)

H. M. James and E. Guth. Simple presentation of network theory of rubber, with a discussion of other theories. *J. Polym. Sci. Pol. Phys.*, 34(1):7–36, 1996. (p 133)

J. Jauch and F. Rohrlich. *Theory of Photons & Electrons*. Addison-Wesley publishing Company, Massachusetts, 1955. (p 19)

T. Jeyapoovan, M. Murugan, and B. C. Bovas. Statistical analysis of surface roughness measurements using laser speckle images. In *2012 World Congr. Inf. Commun. Technol.*, pages 378–382. IEEE, 2012. (p 105)

S. Kachan and A. Ponyavina. The spatial ordering effect on spectral properties of close-packed metallic nanoparticle monolayers. *Surf. Sci.*, 507-510:603–608, 2002. (p 145)

A. Kano, K. Doi, H. MacMahon, D. D. Hassell, and M. L. Giger. Digital image subtraction of temporally sequential chest images for detection of interval change. *Med. Phys.*, 21(3):453–461, 1994. (p 69)

C. P. Karger, P. Hipp, M. Henze, G. Echner, A. Höss, L. Schad, and G. H. Hartmann. Stereotactic imaging for radiotherapy: accuracy of CT, MRI, PET and SPECT. *Phys. Med. Biol.*, 48(2): 211–221, 2003. (p 66)

H.-U. Kauczor and A. A. Bankier, editors. *Functional Imaging of the Chest*. Springer Science & Business Media, New York, 2004. (p 4)

R. D. Keane and R. J. Adrian. Optimization of particle image velocimeters. I. Double pulsed systems. *Meas. Sci. Technol.*, 1(11):1202–1215, 1990. (p 85)

J. B. Keller. Geometrical theory of diffraction. *J. Opt. Soc. Am.*, 52(2):116, 1962. (p 26)

Khandpur. *Handbook of Biomedical Instrumentation*. Tata McGraw-Hill Education, New Delhi, 2nd edition, 2003. (p 47)

P. S. Khare. *Modern Physics*. Rastogi Publications, New Delhi, 2006. (p 19)

W. W. Kim, C. H. Lee, J. M. Goo, S. J. Park, J. H. Kim, E.-A. Park, and S.-H. Cho. Xenon-enhanced dual-energy CT of patients with asthma: dynamic ventilation changes after methacholine and salbutamol inhalation. *Am. J. Roentgenol.*, 199(5):975–81, 2012. (p 50)

S. J. Kirkpatrick, D. D. Duncan, R. K. Wang, and M. T. Hinds. Quantitative temporal speckle contrast imaging for tissue mechanics. *J. Opt. Soc. Am. A. Opt. Image Sci. Vis.*, 24(12):3728–3734, 2007. (p 102)

L. Kirsten, M. Gaertner, C. Schnabel, S. Meissner, and E. Koch. Four-dimensional imaging of murine subpleural alveoli using high-speed optical coherence tomography. *J. Biophotonics*, 6(2): 148–52, 2013. (p 136)

M. J. Kitchen, D. Paganin, R. A. Lewis, N. Yagi, K. Uesugi, and S. T. Mudie. On the origin of speckle in x-ray phase contrast images of lung tissue. *Phys. Med. Biol.*, 49(18):4335–4348, 2004. (p 87, 104)

M. J. Kitchen, R. A. Lewis, N. Yagi, K. Uesugi, D. Paganin, S. B. Hooper, G. Adams, S. Jureczek, J. Singh, C. R. Christensen, A. P. Hufton, C. J. Hall, K. C. Cheung, and K. M. Pavlov. Phase contrast x-ray imaging of mice and rabbit lungs: a comparative study. *Brit. J. Radiol.*, 78(935): 1018–1027, 2005. (p 92)

M. J. Kitchen, R. A. Lewis, M. J. Morgan, M. J. Wallace, M. L. Siew, K. K. W. Siu, A. Habib, A. Fouras, N. Yagi, K. Uesugi, and S. B. Hooper. Dynamic measures of regional lung air volume using phase contrast x-ray imaging. *Phys. Med. Biol.*, 53(21):6065–6077, 2008. (p 4, 45, 46, 55, 56, 61, 63, 83, 84, 87, 88, 91, 114, 120, 121, 159)

M. J. Kitchen, A. Habib, A. Fouras, S. Dubsky, R. A. Lewis, M. J. Wallace, and S. B. Hooper. A new design for high stability pressure-controlled ventilation for small animal lung imaging. *J. Instrum.*, 5(02):T02002, 2010a. (p 83)

M. J. Kitchen, D. M. Paganin, K. Uesugi, B. J. Allison, R. A. Lewis, S. B. Hooper, and K. M. Pavlov. X-ray phase, absorption and scatter retrieval using two or more phase contrast images. *Opt. Express*, 18(19):19994–20012, 2010b. (p 121)

M. J. Kitchen, D. M. Paganin, K. Uesugi, B. J. Allison, R. A. Lewis, S. B. Hooper, and K. M. Pavlov. Phase contrast image segmentation using a Laue analyser crystal. *Phys. Med. Biol.*, 56 (3):515–534, 2011. (p 4, 57, 58, 166)

M. J. Kitchen, M. L. Siew, M. J. Wallace, A. Fouras, R. A. Lewis, N. Yagi, K. Uesugi, A. B. Te Pas, and S. B. Hooper. Changes in positive end-expiratory pressure alter the distribution of ventilation within the lung immediately after birth in newborn rabbits. *PLoS One*, 9(4):e93391, 2014. (p 125)

O. Klein and Y. Nishina. Über die Streuung von Strahlung durch freie Elektronen nach der neuen relativistischen Quantendynamik von Dirac. *Zeitschrift für Phys.*, 52(11-12):853–868, 1929. (p 20)

C. Kottler, C. David, F. Pfeiffer, and O. Bunk. A two-directional approach for grating based differential phase contrast imaging using hard x-rays. *Opt. Express*, 15(3):1175–1181, 2007. (p 41)

J. Kovar, P. D. Sly, and K. E. Willet. Postnatal alveolar development of the rabbit. *J. Appl. Physiol.*, 93(2):629–635, 2002. (p 115)

A. A. Kumar. *Signals and Systems*. PHI Learning Pvt. Ltd., Delhi, 3rd edition, 2013. (p 58)

V. Kuperman. *Magnetic Resonance Imaging: Physical Principles and Applications*. Academic Press, London, 2000. (p 53)

A. Kyriazis, I. Rodriguez, N. Nin, J. L. Izquierdo-Garcia, J. A. Lorente, J. M. Perez-Sanchez, J. Pesic, L. E. Olsson, and J. Ruiz-Cabello. Dynamic ventilation 3He MRI for the quantification of disease in the rat lung. *IEEE Trans. Biomed. Eng.*, 59(3):777–786, 2012. (p 2, 54)

J. A. R. Lang, J. T. Pearson, A. B. Te Pas, M. J. Wallace, M. L.-L. Siew, M. J. Kitchen, A. Fouras, R. A. Lewis, K. Wheeler, G. R. Polglase, M. Shirai, T. Sonobe, and S. B. Hooper. Ventilation/perfusion mismatch during lung aeration at birth. *J. Appl. Physiol.*, 117(5):535–543, 2014. (p 169)

E. M. Law, A. F. Little, and J. C. Salanitri. Non-vascular intervention with real-time CT fluoroscopy. *Australas. Radiol.*, 45(2):109–112, 2001. (p 50)

A. F. T. Leong, A. Fouras, M. S. Islam, M. J. Wallace, S. B. Hooper, and M. J. Kitchen. High spatiotemporal resolution measurement of regional lung air volumes from 2D phase contrast x-ray images. *Med. Phys.*, 40(4):041909, 2013a. (p 45, 55, 61, 82, 100, 154, 159)

A. F. T. Leong, D. M. Paganin, S. B. Hooper, M. L. Siew, and M. J. Kitchen. Measurement of absolute regional lung air volumes from near-field x-ray speckles. *Opt. Express*, 21(23):777–786, 2013b. (p 46, 102)

A. F. T. Leong, G. A. Buckley, D. M. Paganin, S. B. Hooper, M. J. Wallace, and M. J. Kitchen. Real-time measurement of alveolar size and population using phase contrast x-ray imaging. *Biomed. Opt. Express*, 5(11):4024–4038, 2014. (p 46, 131)

J. P. Lewis. Fast normalized cross-correlation. *Vis. Interface*, pages 120–123, 1995. (p 71)

R. A. Lewis, N. Yagi, M. J. Kitchen, M. J. Morgan, D. Paganin, K. K. W. Siu, K. Pavlov, I. Williams, K. Uesugi, M. J. Wallace, C. J. Hall, J. Whitley, and S. B. Hooper. Dynamic imaging of the lungs using x-ray phase contrast. *Phys. Med. Biol.*, 50(21):5031–5040, 2005. (p 4)

B. Li, G. B. Avinash, and J. Hsieh. Resolution and noise trade-off analysis for volumetric CT. *Med. Phys.*, 34(10):3732, 2007. (p 135)

Q. Li, S. Katsuragawa, and K. Doi. Improved contralateral subtraction images by use of elastic matching technique. *Med. Phys.*, 27(8):1934–1942, 2000. (p 93)

D. A. Lichtenstein. Lung ultrasound in the critically ill. *Ann. Intensive Care*, 4(1):1, 2014. (p 2)

B. J. Liu and H. K. Huang. Principles of x-ray Anatomical Imaging Modalities. In A. P. Dhawan, H. K. Huang, and D.-S. Kim, editors, *Princ. Adv. Methods Med. Imaging Image Anal.*, pages 29–61. World Scientific, Singapore, 2008. (p 48)

P. Liu, J. Sun, Y. Guan, G. Zhang, and L. X. Xu. Detection of lung cancer with phase-contrast x-ray imaging using synchrotron radiation. *Conf. Proc. IEEE Eng. Med. Biol. Soc.*, 1:2001–2004, 2006. (p 2)

R. Loudon. *The Quantum Theory of Light*. Oxford University Press, Oxford, 2000. (p 13)

D. A. Low, M. Nystrom, E. Kalinin, P. Parikh, J. F. Dempsey, J. D. Bradley, S. Mutic, S. H. Wahab, T. Islam, G. Christensen, D. G. Politte, and B. R. Whiting. A method for the reconstruction of four-dimensional synchronized CT scans acquired during free breathing. *Med. Phys.*, 30(6): 1254–63, 2003. (p 135)

Q. Lu and J. J. Rouby. Measurement of pressure-volume curves in patients on mechanical ventilation: methods and significance. *Minerva Anestesiol.*, 4(2):91–100, 2000. (p 134)

L. D. Lunsford, R. J. Coffey, T. Cojocaru, and D. Leksell. Image-guided stereotactic surgery: a 10-year evolutionary experience. *Stereot. Funct. Neuros.*, 54-55:375–387, 1990. (p 66)

M. Lyra and A. Ploussi. Filtering in SPECT Image Reconstruction. *Int. J. Biomed. Imaging*, 2011: 693795, 2011. (p 50)

M. A. Macovei. Measuring photon-photon interactions via photon detection. *Phys. Rev. A*, 82(6): 063815, 2010. (p 17)

D. Mahieu-Caputo, P. Sonigo, M. Dommergues, J. C. Fournet, J. C. Thalabard, C. Abarca, A. Benachi, F. Brunelle, and Y. Dumez. Fetal lung volume measurement by magnetic resonance imaging in congenital diaphragmatic hernia. *BJOG-Int. J. Obstet. Gy.*, 108(8):863–868, 2001. (p 53, 54)

M. Marenzana, C. K. Hagen, P. D. N. Borges, M. Endrizzi, M. B. Szafraniec, T. L. Vincent, L. Rigon, F. Arfelli, R.-H. Menk, and A. Olivo. Synchrotron- and laboratory-based x-ray phase-contrast imaging for imaging mouse articular cartilage in the absence of radiopaque contrast agents. *Philos. T. R. Soc. A*, 372(2010):20130127, 2014. (p 16)

G. Margaritondo. *Elements Of Synchrotron Light for Biology, Chemistry, & Medical Research*. Oxford University Press, Oxford, 2002. (p 14, 33)

R. Marks II. *Handbook of Fourier Analysis & Its Applications*. Oxford University Press, Oxford, 2008. (p 43)

H. E. Martz, Jr., B. J. Kozioziemski, S. K. Lehman, S. Hau-Riege, D. J. Schneberk, and A. Barty. Validation of radiographic simulation codes including x-ray phase effects for millimeter-size objects with micrometer structures. *J. Opt. Soc. Am. A*, 24(1):169, 2007. (p 167)

D. Matamis. Total respiratory pressure-volume curves in the adult respiratory distress syndrome. *Chest*, 86(1):58–66, 1984. (p 134)

J. C. Maxwell. A dynamical theory of the electromagnetic field. *Philos. T. R. Soc. A*, 155:460–512, 1865. (p 5)

S. Mayo, T. Davis, T. Gureyev, P. Miller, D. Paganin, a. Pogany, a. Stevenson, and S. Wilkins. X-ray phase-contrast microscopy and microtomography. *Opt. Express*, 11(19):2289–302, 2003. (p 35)

S. C. Mayo, P. R. Miller, S. W. Wilkins, T. J. Davis, D. Gao, T. E. Gureyev, D. Paganin, D. J. Parry, A. Pogany, and A. W. Stevenson. Quantitative x-ray projection microscopy: phase-contrast and multi-spectral imaging. *J. Microsc.*, 207(2):79–96, 2002. (p 35)

R. G. McAllister, D. R. Sisan, and J. S. Urbach. Design and optimization of a high-speed, high-sensitivity, spinning disk confocal microscopy system. *J. Biomed. Opt.*, 13(5):054058, 2008. (p 137)

R. A. McLaughlin, X. Yang, B. C. Quirk, D. Lorenser, R. W. Kirk, P. B. Noble, and D. D. Sampson. Static and dynamic imaging of alveoli using optical coherence tomography needle probes. *J. Appl. Physiol.*, 113(6):967–974, 2012. (p 136)

S. Meissner, L. Knels, and M. Mertens. Three-dimensional imaging of subpleural alveoli by fourier domain optical coherence tomography. In *4th Eur. Conf. Int. Fed. Med. Biol. Eng.*, pages 2035–2039, 2009. (p 135)

G. Mie. Beiträge zur Optik trüber Medien, speziell kolloidaler Metallösungen. *Ann. Phys.-Berlin*, 330(3):377–445, 1908. (p 105)

R. P. Millane. Phase retrieval in crystallography and optics. *J. Opt. Soc. Am. A*, 7(3):394–411, 1990. (p 41)

M. I. Mishchenko. Multiple scattering by particles embedded in an absorbing medium. 1. Foldy-Lax equations, order-of-scattering expansion, and coherent field. *Opt. Express*, 16(3):2288–2301, 2008. (p 102)

E. J. Mittemeijer. *Fundamentals of Materials Science: The Microstructure-Property Relationship Using Metals as Model Systems*. Springer Science & Business Media, London, 2010. (p 37)

K. Miyomoto. *Particle Number and Sizes Estimated from Sections*, pages 507–516. KTK Scientific Publishers, Meguro-ku, 1994. (p 156)

K. Mizuhara, H. Hatano, and K. Washio. The effect of friction on the usability of touchpad. *Tribol. Int.*, 65:326–335, 2013. (p 105)

A. Momose. Phase-contrast x-ray imaging based on interferometry. *J. Synchrotron Radiat.*, 9(3): 136–142, 2002. (p 39)

A. Momose, T. Takeda, Y. Itai, and K. Hirano. Phase-contrast x-ray computed tomography for observing biological soft tissues. *Nat. Med.*, 2(4):473–475, 1996. (p 2)

A. Momose, S. Kawamoto, I. Koyama, Y. Hamaishi, K. Takai, and Y. Suzuki. Demonstration of x-ray talbot interferometry. *Jpn. J. Appl. Phys.*, 42(Part 2, No. 7B):L866–L868, 2003. (p 39)

K. S. Morgan, K. K. W. Siu, and D. M. Paganin. The projection approximation and edge contrast for x-ray propagation-based phase contrast imaging of a cylindrical edge. *Opt. Express*, 18(10): 9865–9878, 2010a. (p 167)

K. S. Morgan, K. K. Siu, and D. M. Paganin. The projection approximation versus an exact solution for x-ray phase contrast imaging, with a plane wave scattered by a dielectric cylinder. *Opt. Commun.*, 283(23):4601–4608, 2010b. (p 29, 167)

M. Mori and K. Kashino. Fast Template Matching Based on Normalized Cross Correlation Using Adaptive Block Partitioning and Initial Threshold Estimation. In *2010 IEEE Int. Symp. Multimed.*, pages 196–203. IEEE, 2010. (p 70)

S. Moser, S. Nau, M. Salk, and K. Thoma. In situ flash x-ray high-speed computed tomography for the quantitative analysis of highly dynamic processes. *Meas. Sci. Technol.*, 25(2):025009, 2014. (p 50)

W. W. Moses. Fundamental limits of spatial resolution in PET. *Nucl. Instrum. Meth. A*, 648: S236–S240, 2011. (p 52)

A. Muecke, J. P. Rachen, R. Engel, R. J. Protheroe, and T. Stanev. Photomeson production in astrophysical sources, 1999. URL `http://arxiv.org/abs/astro-ph/9905153`. (p 17)

J. G. Muscedere, J. B. Mullen, K. Gan, and A. S. Slutsky. Tidal ventilation at low airway pressures can augment lung injury. *Am. J. Resp. Crit. Care*, 149(5):1327–1334, 1994. (p 132)

E. Namati, J. Thiesse, J. de Ryk, and G. McLennan. Alveolar dynamics during respiration: are the pores of Kohn a pathway to recruitment? *Am. J. Respir. Cell Mol. Biol.*, 38(5):572–578, 2008. (p 137)

I. Nesch, D. P. Fogarty, T. Tzvetkov, B. Reinhart, A. C. Walus, G. Khelashvili, C. Muehleman, and D. Chapman. The design and application of an in-laboratory diffraction-enhanced x-ray imaging instrument. *Rev. Sci. Instrum.*, 80(9):093702, 2009. (p 38)

Y. Nesterets. On the origins of decoherence and extinction contrast in phase-contrast imaging. *Opt. Commun.*, 281(4):533–542, 2008. (p 128, 166)

B. J. Nieman, K. U. Szulc, and D. H. Turnbull. Three-dimensional, in vivo MRI with self-gating and image coregistration in the mouse. *Magn. Reson. Med.*, 61(5):1148–1157, 2009. (p 135)

NIST. National Institute of Standards and Technology, Physical Reference Data, 2014. URL `http://www.nist.gov/pml/data/`. (p 20, 62, 86, 108, 115, 148)

K. Nugent, C. Tran, and A. Roberts. Coherence transport through imperfect x-ray optical systems. *Opt. Express*, 11(19):2323–2328, 2003. (p 128)

M. Ochs, J. R. Nyengaard, A. Jung, L. Knudsen, M. Voigt, T. Wahlers, J. Richter, and H. J. G. Gundersen. The number of alveoli in the human lung. *Am. J. Resp. Crit. Care*, 169(1):120–124, 2004. (p 1, 119)

S. Orgeig, J. L. Morrison, L. C. Sullivan, and C. B. Daniels. Development of the Pulmonary Surfactant System. In *Lung Dev. Aging Environ.*, chapter 9, pages 183–200. Academic Press, Massachusetts, 2nd edition, 2014. (p 133)

F. Ossant, M. Lebertre, L. Pourcelot, and F. Patat. Ultrasonic characterization of maturation of fetal lung microstructure: an animal study. *Ultrasound Med. Biol.*, 27(2):157–169, 2001. (p 135)

D. Paganin and K. Nugent. Noninterferometric phase imaging with partially coherent light. *Phys. Rev. Lett.*, 80(12):2586–2589, 1998. (p 41)

D. Paganin, S. C. Mayo, T. E. Gureyev, P. R. Miller, and S. W. Wilkins. Simultaneous phase and amplitude extraction from a single defocused image of a homogeneous object. *J. Microsc.*, 206 (Pt 1):33–40, 2002. (p 41, 153)

D. Paganin. *Coherent X-Ray Optics*. Oxford University Press, Oxford, 2006. (p 8, 10, 12, 15, 18, 21, 28, 31, 33, 39, 49, 107, 108, 167)

C. Parham, Z. Zhong, D. M. Connor, L. D. Chapman, and E. D. Pisano. Design and implementation of a compact low-dose diffraction enhanced medical imaging system. *Acad. Radiol.*, 16(8): 911–917, 2009. (p 38)

R. Penrose and J. A. Todd. A generalized inverse for matrices. *Math. Proc. Cambridge*, 51(03): 406–413, 1955. (p 76)

E. Persson. A new edge detection algorithm and its applications in picture processing. *Comput. Vision Graph*, 5(4):425–446, 1976. (p 67)

J. C. Petruccelli, L. Tian, and G. Barbastathis. The transport of intensity equation for optical path length recovery using partially coherent illumination. *Opt. Express*, 21(12):14430–14441, 2013. (p 169)

J. J. Pillow, I. Frerichs, and J. Stocks. Lung function tests in neonates and infants with chronic lung disease: global and regional ventilation inhomogeneity. *Pediatr. Pulm.*, 41(2):105–121, 2006. (p 125)

F. Plourde, F. Cheriet, and J. Dansereau. Semi-automatic detection of scoliotic rib borders using chest radiographs. In *Stud. Health Technol. Inform.*, volume 123, pages 533–537, 2006. (p 67)

J. P. W. Pluim, J. B. A. Maintz, and M. A. Viergever. Mutual-information-based registration of medical images: a survey. *IEEE T. Med. Imaging*, 22(8):986–1004, 2003. (p 73)

M. Polacci, L. Mancini, and D. R. Baker. The contribution of synchrotron x-ray computed microtomography to understanding volcanic processes. *J. Synchrotron Radiat.*, 17(2):215–221, 2010. (p 5)

L. Porra, S. Monfraix, G. Berruyer, G. Le Duc, C. Nemoz, W. Thomlinson, P. Suortti, A. R. A. Sovijärvi, and S. Bayat. Effect of tidal volume on distribution of ventilation assessed by synchrotron radiation CT in rabbit. *J. Appl. Physiol.*, 96(5):1899–1908, 2004. (p 50, 52)

M. Poustchi-Amin, S. A. Mirowitz, J. J. Brown, R. C. McKinstry, and T. Li. Principles and applications of echo-planar imaging: a review for the general radiologist. *Radiographics*, 21(3): 767–779, 2013. (p 54)

Q. Qang, O. Ronneberger, and H. Burkhardt. Fourier Analysis in Polar and Spherical Coordinates. Technical report, IIF-LMB, Computer Science Department, University of Freiburg, Germany, 2008. (p 111)

C. Raffel, G. J. Tearney, B. E. Bouma, and I.-K. Jang. OCT imaging of vulnerable plaque: the Massachusetts General Hospital experience. In E. Regar, A. Van Leeuwen, and P. W. Serruys, editors, *Opt. Coherence Tomogr. Cardiovasc. Res.*, chapter 14, pages 121–130. CRC Press, London, 2007. (p 136)

A. Rahmim and H. Zaidi. PET versus SPECT: strengths, limitations and challenges. *Nucl. Med. Commun.*, 29(3):193–207, 2008. (p 52)

K. R. Rao, D. N. Kim, and J. J. Hwang. *Fast Fourier Transform - Algorithms and Applications: Algorithms and Applications*. Springer Science & Business Media, Heidelberg, 2011. (p 33)

M. Reed Teague. Deterministic phase retrieval: a Green's function solution. *J. Opt. Soc. Am.*, 73 (11):1434–1441, 1983. (p 34, 41)

C. G. Rhodes, S. O. Valind, L. H. Brudin, P. E. Wollmer, T. Jones, P. D. Buckingham, and J. M. Hughes. Quantification of regional V/Q ratios in humans by use of PET. II. Procedure and normal values. *J. Appl. Physiol.*, 66(4):1905–1913, 1989a. (p 52)

C. G. Rhodes, S. O. Valind, L. H. Brudin, P. E. Wollmer, T. Jones, and J. M. Hughes. Quantification of regional V/Q ratios in humans by use of PET. I. Theory. *J. Appl. Physiol.*, 66(4):1896–1904, 1989b. (p 52)

J.-C. Richard, M. Janier, F. Lavenne, C. Tourvieille, D. Le Bars, N. Costes, G. Gimenez, and C. Guerin. Quantitative assessment of regional alveolar ventilation and gas volume using 13N-N2 washout and PET. *J. Nucl. Med.*, 46(8):1375–1383, 2005. (p 52)

L. Rigon, H.-J. Besch, F. Arfelli, R.-H. Menk, G. Heitner, and H. Plothow-Besch. A new DEI algorithm capable of investigating sub-pixel structures. *J. Phys. D. Appl. Phys.*, 36(10A): A107–A112, 2003. (p 36, 38)

L. Rigon, A. Astolfo, F. Arfelli, and R.-H. Menk. Generalized diffraction enhanced imaging: application to tomography. *Eur. J. Radiol.*, 68(3 Suppl):S3–7, 2008. (p 36)

I. Robinson, C. Kenney-Benson, and I. Vartanyants. Sources of decoherence in beamline optics. *Physica B*, 336(1-2):56–62, 2003. (p 128)

M. Roth-Kleiner, T. M. Berger, S. Gremlich, S. A. Tschanz, S. I. Mund, M. Post, M. Stampanoni, and J. C. Schittny. Neonatal steroids induce a down-regulation of tenascin-C and elastin and cause a deceleration of the first phase and an acceleration of the second phase of lung alveolarization. *Histochem. Cell Biol.*, 141(1):75–84, 2014. (p 135)

C. Runge. Über empirische Funktionen und die Interpolation zwischen äquidistanten Ordinaten. *Zeitschrift für Math. und Phys.*, 46:224–243, 1901. (p 77)

E. Saccocio and A. Zajac. Simultaneous diffraction of x-rays and the Borrmann effect. *Phys. Rev.*, 139(1A):A255–A264, 1965. (p 39)

E. Salazar and J. H. Knowles. An analysis of pressure-volume characteristics of the lungs. *J. Appl. Physiol.*, 19(1):97–104, 1964. (p 134)

S. S. Samant, J. Wu, J. Xia, and A. Gopal. Optimization in Image Registration. In *Image Process. Radiat. Ther.*, chapter 8, page 286. CRC Press, Florida, 2013. (p 101)

A. Sarnelli, C. Nemoz, H. Elleaume, F. Estève, B. Bertrand, and A. Bravin. Quantitative analysis of synchrotron radiation intravenous angiographic images. *Phys. Med. Biol.*, 50(4):725–740, 2005. (p 169)

J. A. Schmalz, T. E. Gureyev, D. M. Paganin, and K. M. Pavlov. Phase retrieval using radiation and matter-wave fields: validity of Teague's method for solution of the transport-of-intensity equation. *Phys. Rev. A*, 84(2):023808, 2011. (p 41, 104)

P. H. Schönemann. A generalized solution of the orthogonal procrustes problem. *Psychometrika*, 31(1):1–10, 1966. (p 74)

D. Schwenninger, A. Endoscopic, K. Moller, H. Lui, H. Runck, C. Stahl, S. Schumann, and J. Guttmann. Determining alveolar dynamics by automatic tracing of area changes within microscopy videos. In *2008 2nd Int. Conf. Bioinforma. Biomed. Eng.*, pages 2335–2338. IEEE, 2008. (p 137)

D. Schwenninger, H. Runck, S. Schumann, J. Haberstroh, S. Meissner, E. Koch, and J. Guttmann. Intravital microscopy of subpleural alveoli via transthoracic endoscopy. *J. Biomed. Opt.*, 16(4): 046002, 2011. (p 134)

J. C. Segen and J. Wade. *The Patient's Guide to Medical Tests: Everything You Need to Know about the Tests Your Doctor Orders*. Infobase Publishing, New York, 2nd edition, 2002. (p 2)

D. Sengupta and T. Sarkar. Maxwell, Hertz, the Maxwellians, and the early history of electromagnetic waves. *IEEE Antenn Propag. M.*, 45(2):13–19, 2003. (p 5)

V. B. Serikov, M. S. Rumm, K. Kambara, M. I. Bootomo, A. R. Osmack, and N. C. Staub. Application of respiratory heat exchange for the measurement of lung water. *J Appl Physiol*, 72 (3):944–953, 1992. (p 1)

C. E. Shannon. A mathematical theory of communication. *Bell Syst. Tech. J.*, 27(3):379–423, 1948. (p 71)

K. K. Sharma. *Optics: Principles and Applications*. Academic Press, London, 2006. (p 14)

F. Y. Shih. *Image Processing and Mathematical Morphology: Fundamentals and Applications*. CRC Press, Florida, 2009. (p 94)

M. Shinohara, T. Yamashita, H. Tawa, M. Takeda, N. Sasaki, T. Takaya, R. Toh, A. Takeuchi, T. Ohigashi, K. Shinohara, S. Kawashima, M. Yokoyama, K. Hirata, and A. Momose. Atherosclerotic plaque imaging using phase-contrast x-ray computed tomography. *Am. J. Pysiol.-Heart C.*, 294(2):H1094–H1100, 2008. (p 2)

E. V. Shtykova, L. A. Baratova, N. V. Fedorova, V. A. Radyukhin, A. L. Ksenofontov, V. V. Volkov, A. V. Shishkov, A. A. Dolgov, L. A. Shilova, O. V. Batishchev, C. M. Jeffries, and D. I. Svergun. Structural analysis of influenza A virus matrix protein M1 and its self-assemblies at low pH. *PLoS One*, 8(12):e82431, 2013. (p 5)

B. A. Simon. Non-invasive imaging of regional lung function using x-ray computed tomography. *J. Clin. Monitor Comp.*, 16(5-6):433–442, 2000. (p 1, 50)

D. R. Sisan, R. Arevalo, C. Graves, R. McAllister, and J. S. Urbach. Spatially resolved fluorescence correlation spectroscopy using a spinning disk confocal microscope. *Biophys. J.*, 91(11):4241–4252, 2006. (p 137)

J. M. Slowik and R. Santra. X-ray phase-contrast imaging: the quantum perspective. *J. Phys. B-At. Mol. Opt.*, 46(16):164016, 2013. (p 9)

G. C. Smaldone, W. Mitzner, and H. Itoh. Role of alveolar recruitment in lung inflation: influence on pressure-volume hysteresis. *J. Appl. Physiol.*, 55(4):1321–1332, 1983. (p 132)

B. M. Smith, L. Pinto, N. Ezer, N. Sverzellati, S. Muro, and K. Schwartzman. Emphysema detected on computed tomography and risk of lung cancer: a systematic review and meta-analysis. *Lung Cancer*, 77(1):58–63, 2012. (p 134)

S.-K. Son, H. N. Chapman, and R. Santra. Multi-wavelength anomalous diffraction at high x-ray intensity. *Phys. Rev. Lett.*, 107:218102, 2011. (p 41)

E. Spiller. *Soft X-ray Optics*. SPIE Press, Washington, 1994. (p 24)

J. Staal, B. van Ginneken, and M. A. Viergever. Automatic rib segmentation and labeling in computed tomography scans using a general framework for detection, recognition and segmentation of objects in volumetric data. *Med. Image Anal.*, 11(1):35–46, 2007. (p 67)

M. Stewart. Signal Processing. In L. Hogben, editor, *Handb. Linear Algebr.*, chapter 64, page 1400. CRC Press, Florida, 2006. (p 151)

L. Storm and H. I. Israel. Photon cross sections from 1 keV to 100 MeV for elements Z=1 to Z=100. *Atom. Data Nucl. Data*, 7(6):565–681, 1970. (p 20)

K. Suga, K. Yasuhiko, M. Zaki, T. Yamashita, A. Seto, T. Matsumoto, and N. Matsunaga. Assessment of regional lung functional impairment with co-registered respiratory-gated ventila-

tion/perfusion SPET-CT images: initial experiences. *Eur. J. Nucl. Med. Mol. I.*, 31(2):240–9, 2004. (p 50)

T. Sugihara, J. Hildebrandt, and C. J. Martin. Viscoelastic properties of alveolar wall. *J Appl Physiol*, 33(1):93–98, 1972. (p 132)

B. Suki, A. L. Barabási, Z. Hantos, F. Peták, and H. E. Stanley. Avalanches and power-law behaviour in lung inflation. *Nature*, 368(6472):615–618, 1994. (p 113)

P. M. Suratt, D. H. Owens, W. T. Kilgore, R. R. Harry, and H. S. Hsiao. A pulse method of measuring respiratory system compliance. *J. Appl. Physiol.*, 49(6):1116–1121, 1980. (p 134)

Y. Suzuki, N. Yagi, and K. Uesugi. X-ray refraction-enhanced imaging and a method for phase retrieval for a simple object. *J. Synchrotron Radiat.*, 9(3):160–165, 2002. (p 103)

S. Sykora. Generalized Sinc Functions, 2008. URL `http://www.ebyte.it/library/docs/math07/SincN.html`. (p 109)

M. Takeda, H. Ina, and S. Kobayashi. Fourier-transform method of fringe-pattern analysis for computer-based topography and interferometry. *J. Opt. Soc. Am.*, 72(1):156–160, 1982. (p 39)

J. H. Talbot. Fraunhofer diffraction pattern of a random distribution of identical apertures in a plane screen. *P. Phys. Soc.*, 89(4):1043–1053, 1966. (p 108)

G. L. Taylor. Introduction to phasing. *Acta Crystallogr. Sect. D*, 66(Pt 4):325–38, 2010. (p 41)

L. Tchvialeva, I. Markhvida, H. Zeng, D. I. McLean, H. Lui, and T. K. Lee. Surface roughness measurement by speckle contrast under the illumination of light with arbitrary spectral profile. *Opt. Laser Eng.*, 48(7-8):774–778, 2010. (p 105)

U. Thome, A. Töpfer, P. Schaller, and F. Pohlandt. Comparison of lung volume measurements by antero-posterior chest x-ray and the SF6 washout technique in mechanically ventilated infants. *Pediatr. Pulm.*, 26(4):265–272, 1998. (p 50)

S. J. J. Thomson. *Conduction of electricity through gases*. University press, Cambridge, 2nd edition, 1906. (p 19)

D. G. Tingay, M. J. Wallace, R. Bhatia, G. M. Schmölzer, V. A. Zahra, M. J. Dolan, S. B. Hooper, and P. G. Davis. Surfactant before the first inflation at birth improves spatial distribution of ventilation and reduces lung injury in preterm lambs. *J. Appl. Physiol.*, 116(3):251–258, 2014. (p 125)

J.-I. Toriwaki, Y. Suenaga, T. Negoro, and T. Fukumura. Pattern recognition of chest x-ray images. *Comput. Vision Graph*, 2(3-4):252–271, 1973. (p 66, 67)

X. Trepat, L. Deng, S. S. An, D. Navajas, D. J. Tschumperlin, W. T. Gerthoffer, J. P. Butler, and J. J. Fredberg. Universal physical responses to stretch in the living cell. *Nature*, 447(7144):592–595, 2007. (p 4)

J. Tsao. Ultrafast imaging: principles, pitfalls, solutions, and applications. *JMRI-J. Magn. Reson. Im.*, 32(2):252–266, 2010. (p 135)

T. Tuohimaa, M. Otendal, and H. M. Hertz. Phase-contrast x-ray imaging with a liquid-metal-jet-anode microfocus source. *Appl. Phys. Lett.*, 91(7):074104, 2007. (p 17, 128)

M. Uecker, S. Zhang, D. Voit, A. Karaus, K.-D. Merboldt, and J. Frahm. Real-time MRI at a resolution of 20 ms. *NMR Biomed.*, 23(8):986–994, 2010. (p 54)

C. I. Unglert, W. C. Warger, J. Hostens, E. Namati, R. Birngruber, B. E. Bouma, and G. J. Tearney. Validation of two-dimensional and three-dimensional measurements of subpleural alveolar size parameters by optical coherence tomography. *J. Biomed. Opt.*, 17(12):126015, 2012. (p 135, 137)

A. N. van Daatselaar, P. F. van der Stelt, and J. Weenen. Effect of number of projections on image quality of local CT. *Dentomaxillofac Radiol.*, 33(6):361–369, 2004. (p 50)

I. Vartanyants and I. Robinson. Origins of decoherence in coherent x-ray diffraction experiments. *Opt. Commun.*, 222(1-6):29–50, 2003. (p 128)

P. Verbeek. A class of sampling-error free measures in oversampled band-limited images. *Pattern Recogn. Lett.*, 3(4):287–292, 1985. (p 43)

A. Vignaud, X. Maître, G. Guillot, E. Durand, L. de Rochefort, P. Robert, V. Vivès, R. Santus, and L. Darrasse. Magnetic susceptibility matching at the air-tissue interface in rat lung by using a superparamagnetic intravascular contrast agent: Influence on transverse relaxation time of hyperpolarized helium-3. *Magn. Reson. Med.*, 54(1):28–33, 2005. (p 54)

D. J. Vine, D. M. Paganin, K. M. Pavlov, J. Kräuß lich, O. Wehrhan, I. Uschmann, and E. Förster. Analyzer-based phase contrast imaging and phase retrieval using a rotating anode x-ray source. *Appl. Phys. Lett.*, 91(25):254110, 2007. (p 16)

P. Viola and W. Wells. Alignment by maximization of mutual information. In *Proc. IEEE Int. Conf. Comput. Vis.*, pages 16–23. IEEE Comput. Soc. Press, 1995. (p 72)

J. Wang, G. Wang, and M. Jiang. IOS Press Blind deblurring of spiral CT images Based on ENR and Wiener filter. *J. X-ray. Sci. Technol.*, 13:49–60, 2005. (p 127)

Z. Wang, K. Gao, X. Ge, Z. Wu, H. Chen, S. Wang, P. Zhu, Q. Yuan, W. Huang, K. Zhang, and Z. Wu. X-ray phase radiography and tomography with grating interferometry and the reverse projection technique. *J. Phys. D. Appl. Phys.*, 46(49):494003, 2013. (p 41)

H. Watz, A. Breithecker, W. S. Rau, and A. Kriete. Micro-CT of the human lung: Imaging of alveoli and virtual endoscopy of an alveolar duct in a normal lung and in a lung with centrilobular emphysema–initial observations. *Radiology*, 236(3):1053–1058, 2005. (p 135)

W. Weber and R. Kohlrausch. Ueber die Elektricitätsmenge, welche bei galvanischen Strömen durch den Querschnitt der Kette fliesst. *Ann. Phys.-Berlin*, 175(9):10–25, 1856. (p 7)

H. Wechsler and K. Fu. Image processing algorithms applied to rib boundary detection in chest radiographs. *Comput. Vision Graph*, 7(3):375–390, 1978. (p 67)

E. R. Weibel. *Morphometry of the human lung*. Academic Press, Massachusetts, 1963. (p 113)

S. Weinberg. *The Quantum Theory of Fields: Volume 2, Modern Applications*. Cambridge University Press, Cambridge, 1996. (p 17)

T. J. Wellman, T. Winkler, E. L. V. Costa, G. Musch, R. S. Harris, J. G. Venegas, and M. F. V. Melo. Measurement of regional specific lung volume change using respiratory-gated PET of inhaled 13N-nitrogen. *J. Nucl. Med.*, 51(4):646–653, 2010. (p 2)

H. Wen, A. A. Gomella, A. Patel, S. K. Lynch, N. Y. Morgan, S. A. Anderson, E. E. Bennett, X. Xiao, C. Liu, and D. E. Wolfe. Subnanoradian x-ray phase-contrast imaging using a far-field interferometer of nanometric phase gratings. *Nat. Commun.*, 4:2659, 2013. (p 39)

M. N. Wernick, O. Wirjadi, D. Chapman, Z. Zhong, N. P. Galatsanos, Y. Yang, J. G. Brankov, O. Oltulu, M. A. Anastasio, and C. Muehleman. Multiple-image radiography. *Phys. Med. Biol.*, 48(23):3875–3895, 2003. (p 57)

J. West, J. M. Fitzpatrick, M. Y. Wang, B. M. Dawant, C. R. Maurer, R. M. Kessler, R. J. Maciunas, C. Barillot, D. Lemoine, A. Collignon, F. Maes, P. Suetens, D. Vandermeulen, P. A. van den Elsen, S. Napel, T. S. Sumanaweera, B. Harkness, P. F. Hemler, D. L. Hill, D. J. Hawkes,

C. Studholme, J. B. Maintz, M. A. Viergever, G. Malandain, and R. P. Woods. Comparison and evaluation of retrospective intermodality brain image registration techniques. *J. Comput. Assist. Tomo.*, 21(4):554–566, 1997. (p 66)

J. M. Wild. MRI of Pulmonary Ventilation. In *MRI Lung*, chapter 4, pages 35–90. Springer Science & Business Media, Heidelberg, 2009. (p 54)

S. W. Wilkins, T. E. Gureyev, D. Gao, A. Pogany, and A. W. Stevenson. Phase-contrast imaging using polychromatic hard x-rays. *Nature*, 384(6607):335–338, 1996. (p 30, 36, 102)

D. S. Wilks. *Statistical Methods in the Atmospheric Sciences*. Academic Press, Oxford, 2011. (p 114)

M. R. Wilson, B. V. Patel, and M. Takata. Ventilation with "clinically relevant" high tidal volumes does not promote stretch-induced injury in the lungs of healthy mice. *Crit. Care Med.*, 40(10): 2850–2857, 2012. (p 92)

W. H. Wolrld Health Organization. *The Global Burden of Disease: 2004 Update*. World Health Organization, 2008. (p 4)

X. Xiao and D. Voelz. Wave optics simulation approach for partial spatially coherent beams. *Opt. Express*, 14(16):6986–6992, 2006. (p 128)

T. Xie, W. E. Bolch, C. Lee, and H. Zaidi. Pediatric radiation dosimetry for positron-emitting radionuclides using anthropomorphic phantoms. *Med. Phys.*, 40(10):102502, 2013. (p 52)

Y. Xie, M. Chao, and L. Xing. Tissue feature-based and segmented deformable image registration for improved modeling of shear movement of lungs. *Int. J. Radiat. Oncol.*, 74(4):1256–1265, 2009. (p 66)

N. Yagi, Y. Suzuki, K. Umetani, Y. Kohmura, and K. Yamasaki. Refraction-enhanced x-ray imaging of mouse lung using synchrotron radiation source. *Med. Phys.*, 26(10):2190–2193, 1999. (p 103)

T. Yamamoto, S. Kabus, T. Klinder, C. Lorenz, J. von Berg, T. Blaffert, B. W. Loo, and P. J. Keall. Investigation of four-dimensional computed tomography-based pulmonary ventilation imaging in patients with emphysematous lung regions. *Phys. Med. Biol.*, 56(7):2279–2298, 2011. (p 50)

Y. Yamamoto, A. Tanaka, A. Kanamaru, S. Tanaka, H. Tsubone, Y. Atoji, and Y. Suzuki. Morphology of aging lung in F344/N rat: alveolar size, connective tissue, and smooth muscle cell markers. *Anat. Rec. Part A.*, 272(2):538–547, 2003. (p 134)

H. Yang, R.-J. Xuan, C.-H. Hu, and J.-H. Duan. Improvement and error analysis of quantitative information extraction in diffraction-enhanced imaging. *Chinese Phys. B*, 23(4):048701, 2014. (p 56)

A. T. Young. Rayleigh scattering. *Phys. Today*, 35(1):42, 1982. (p 19)

Z. Yue, A. Goshtasby, and L. V. Ackerman. Automatic detection of rib borders in chest radiographs. *IEEE T. Med. Imaging*, 14(3):525–536, 1995. (p 67)

L. Zagorchev, A. Goshtasby, and M. Satter. R-snakes. *Image Vision Comput.*, 25(6):945–959, 2007. (p 67)

F. Zernike. The concept of degree of coherence and its application to optical problems. *Physica*, 5 (8):785–795, 1938. (p 14)

L. Zhang, D. Li, and S. Luo. Non-invasive microstructure and morphology investigation of the mouse lung: qualitative description and quantitative measurement. *PLoS One*, 6(2):e17400, 2011. (p 2)

Y.-l. Zhang. Coarse-to-fine image registration for sweep fingerprint sensors. *Opt. Eng.*, 45(6): 060501, 2006. (p 65)

Z.-C. Zheng, S.-Q. He, and F.-Q. Wu. Changes of soil surface roughness under water erosion process. *Hydrol. Process.*, 28(12):3919–3929, 2014. (p 105)

S.-A. Zhou and A. Brahme. Development of phase-contrast x-ray imaging techniques and potential medical applications. *Phys. Medica*, 24(3):129–148, 2008. (p 3, 36, 37, 41, 59)

B. Zitová and F. Jan. Image registration methods: a survey. *Image Vision Comput.*, 21:977–1000, 2003. (p 68)

K. Zöphel, C. Bacher-Stier, J. Pinkert, and J. Kropp. Ventilation/perfusion lung scintigraphy: what is still needed? A review considering technetium-99m-labeled macro-aggregates of albumin. *Ann. Nucl. Med.*, 23(1):1–16, 2009. (p 169)

A. Zwijnenburg, A. Klumper, C. M. Roos, H. M. Jansen, J. B. van der Schoot, N. van Zandwijk, and H. R. Marcuse. Lung volume calculations from 81 Kr m SPECT for the quantification of regional ventilation. *Clin. Phys. Physiol. M.*, 9(2):147–154, 1988. (p 52)

Appendices: Supporting Publications

Appendix A

High spatiotemporal resolution measurement of regional lung air volumes from 2D phase contrast x-ray images

by A. F. T. Leong, A. Fouras, M. S. Islam, M. J. Wallace, S. B. Hooper, M. J. Kitchen.

Published in Medical Physics **40**, p. 041909, 2013.

Medical Physics
The International Journal of Medical Physics Research and Practice

High spatiotemporal resolution measurement of regional lung air volumes from 2D phase contrast x-ray images

Andrew F. T. Leong, Andreas Fouras, M. Sirajul Islam, Megan J. Wallace, Stuart B. Hooper, and Marcus J. Kitchen

Citation: Medical Physics **40**, 041909 (2013); doi: 10.1118/1.4794926
View online: http://dx.doi.org/10.1118/1.4794926
View Table of Contents: http://scitation.aip.org/content/aapm/journal/medphys/40/4?ver=pdfcov
Published by the American Association of Physicists in Medicine

High spatiotemporal resolution measurement of regional lung air volumes from 2D phase contrast x-ray images

Andrew F. T. Leong[a)]
School of Physics, Monash University, Victoria 3800, Australia

Andreas Fouras
Division of Biological Engineering, Monash University, Victoria 3800, Australia

M. Sirajul Islam
School of Physics, Monash University, Victoria 3800, Australia

Megan J. Wallace and Stuart B. Hooper
The Ritchie Centre and Department of Obstetrics and Gynaecology, Monash Institute of Medical Research, Monash University, Victoria 3168, Australia

Marcus J. Kitchen
School of Physics, Monash University, Victoria 3800, Australia

(Received 27 November 2012; revised 11 February 2013; accepted for publication 24 February 2013; published 19 March 2013)

Purpose: Described herein is a new technique for measuring regional lung air volumes from two-dimensional propagation-based phase contrast x-ray (PBI) images at very high spatial and temporal resolution. Phase contrast dramatically increases lung visibility and the outlined volumetric reconstruction technique quantifies dynamic changes in respiratory function. These methods can be used for assessing pulmonary disease and injury and for optimizing mechanical ventilation techniques for preterm infants using animal models.
Methods: The volumetric reconstruction combines the algorithms of temporal subtraction and single image phase retrieval (SIPR) to isolate the image of the lungs from the thoracic cage in order to measure regional lung air volumes. The SIPR algorithm was used to recover the change in projected thickness of the lungs on a pixel-by-pixel basis (pixel dimensions $\sim$16.2 μm). The technique has been validated using numerical simulation and compared results of measuring regional lung air volumes with and without the use of temporal subtraction for removing the thoracic cage. To test this approach, a series of PBI images of newborn rabbit pups mechanically ventilated at different frequencies was employed.
Results: Regional lung air volumes measured from PBI images of newborn rabbit pups showed on average an improvement of at least 20% in 16% of pixels within the lungs in comparison to that measured without the use of temporal subtraction. The majority of pixels that showed an improvement was found to be in regions occupied by bone. Applying the volumetric technique to sequences of PBI images of newborn rabbit pups, it is shown that lung aeration at birth can be highly heterogeneous.
Conclusions: This paper presents an image segmentation technique based on temporal subtraction that has successfully been used to isolate the lungs from PBI chest images, allowing the change in lung air volume to be measured over regions as small as the pixel size. Using this technique, it is possible to measure changes in regional lung volume at high spatial and temporal resolution during breathing at much lower x-ray dose than would be required using computed tomography.
 [http://dx.doi.org/10.1118/1.4794926]

Key words: phase contrast x-ray imaging, regional lung volume, image registration, thoracic cage segmentation, temporal subtraction

I. INTRODUCTION

Dynamic changes in regional lung air volumes and their derivatives (e.g., regional lung air flow and time constant) are key measures of regional lung mechanics and may indicate localized regions of disease well before the pathogenic changes are sufficient to cause global changes in lung function.[1] Consequently, many techniques have been developed to analyze regional lung volumes using various types of tomography-based imaging modalities (see, e.g., Refs. 2–4). Although these modalities provide regional lung volume measures, they are limited by a low temporal or spatial resolution or may require a large radiation dose for dynamic studies. We have previously developed a technique to measure regional changes in lung air volume between a pair of two-dimensional (2D) images recorded using propagation-based phase contrast x-ray imaging (PBI).[5] PBI (explained in more detail in Sec. I.B) produces phase-induced intensity variations between the boundary of materials exhibiting different refractive indices. The lung is ideal for PBI as it consists of conducting

airways and tiny air-filled alveoli that are surrounded by thin regions of tissue. The changes in refractive indices, between air and tissue, experienced by the x-ray as it traverses the lung either highlights single airways in projection or produces a speckle pattern when the x-ray passes through multiple airways[6] (see Sec. III). Combined with our phase retrieval analysis technique,[5] these images can simultaneously provide both higher order structural (i.e., alveolar regions seen as lung speckle) and regional volumetric information in real-time from 2D images. This approach avoids the use of a contrast agent, which is required in other volumetric techniques, to quantify lung volume.[2,4,7]

The presence and differential movement of the thoracic cage in relation to the lung during breathing limits the accuracy of the regional lung air volumes measured using our phase retrieval analysis.[5] As a result, our aim was to develop an algorithm to segment the ribs from PBI images of the chest before applying our analysis to measure changes in regional lung air volume. Segmentation of bones from chest images is a common radiography processing tool for isolating the lung to improve the detection of diseases. Techniques that are commonly employed include artificial neural networks (ANN), dual-energy subtraction (DES), and temporal subtraction (TS). DES involves imaging at two different x-ray energies to separate two materials by exploiting the difference in their energy-dependent attenuation coefficients and performing a weighted logarithmic subtraction.[8] This technique can be highly accurate in removing bone when the images are simultaneously recorded at two different x-ray energies.[9,10] TS facilitates visualization of pathological changes by subtracting an image from one previously captured, following alignment of the images. This has commonly been used to improve the visibility of lung lesions within chest radiographs, which has helped improve the sensitivity and specificity of lung tumor detection and monitoring.[11] Unlike DES, alignment of the images is required to correct for differential movement of the thoracic cage, which will likely introducing bone artifacts into the subtracted image. ANN can be trained to remove bone and once optimized can be easily utilized clinically, but the initial training of the network can be arduous. DES images have been used to train the network, but the ANN can, therefore, only at most be equally and not more accurate than DES.[12]

Carnibella, Fouras, and Kitchen[10] recently developed a single exposure DES technique using synchrotron radiation. Despite the images being recorded at finite distances between object and detector, the algorithm formulated assumes they are purely absorption-based images. If this technique was applied to measuring regional lung air volume, the prevalent phase-induced intensity variation in the lungs could lead to large errors. TS and ANN have yet not been developed for removal of bone from PBI images. Hence, in this paper we describe a novel TS-based algorithm to remove the bones from PBI chest images by first aligning the bones, then applying our phase retrieval analysis to remove the phase-induced intensity variations followed by subtraction of the images. This enabled us to measure changes in regional lung air volumes with much greater spatial resolution than previously possible. In Sec. I.A, we introduce our approach to phase contrast TS and briefly describe our lung volume analysis technique in Sec. I.C. A description of the algorithm and its implementation follows in Sec. II. In Sec. III, we evaluate the accuracy and robustness of the TS algorithm by examining the subtracted images and calculated lung air volumes. Some directions for future work are provided in Sec. IV and we conclude with Sec. V.

I.A. Temporal subtraction

Temporal subtraction of chest images require careful image alignment, or registration, to correct for movement of the thoracic cage during breathing and shifting of subject pose. Medical image registration is a well-established field with an exhaustive range of techniques, each with their own proponents, but they essentially follow a common framework. The process of aligning two images involves: (i) selecting and matching salient (control) points between the images and (ii) applying a transformation function to establish a point-by-point correspondence between them. Early work on TS by Kano *et al.*[13] developed a nonrigid area-based registration algorithm and showed it improved the discernibility of metastatic lung nodules in radiographs. This prompted the development of other registration techniques that have improved upon the accuracy and robustness against more elaborate chest movements. An excellent review on similarity measures and interpolation functions applied in medical image registration is provided by Zitová and Flusser.[14]

Here, we employ the standard approach of Kano *et al.*[13] for the purposes of measuring regional lung air volume using 2D PBI images by adapting the cross correlation (CC) similarity measure to locally match regions-of-interest (ROIs) between two images, denoted A and B. The CC can be computed efficiently using fast Fourier transforms via the relation

$$CC = \mathbf{F}^{-1}[\mathbf{F}\{\bar{a}\} \times \mathbf{F}^{*}\{\bar{b}\}], \tag{1}$$

where $\bar{a}$ and $\bar{b}$ are the mean subtracted ROI from image A (kernel) and the ROI from image B (search area), respectively, while $\mathbf{F}$ and $\mathbf{F}^{-1}$ are the Fourier and inverse Fourier transform pairs, respectively. $\mathbf{F}^{*}\{\bar{b}\}$ is the complex conjugate of $\mathbf{F}\{\bar{b}\}$.

Ideally, the peak in each CC matrix describes the representative translation vector for each ROI pair. In x-ray imaging of the chest however, multiple peaks often appear due to the repetitive structure of the ribs in the chest. Consequently, the kernel and search area are selected in close vicinity of one another and their sizes are carefully chosen. The endpoints of each representative translation vector are defined as a pair of control points (i), $(x_{A,i}, y_{A,i}) \subseteq A$ and $(x_{B,i}, y_{B,i}) \subseteq B$. CC has been employed in a wide variety of medical imaging research including the study of lung motion and blood flow, which can potentially be used for early diseases detection and with greater precision.[15,16]

To apply a transformation matrix on image A to align with image B we employ Delaunay triangulation. It returns a highly accurate interpolation as the total distance between control points from which coordinates are interpolated is minimized.[17]

The main problem with image registration is that radiographs are 2D projections of three-dimensional (3D) objects. This complicates the alignment as structures moving independently of one another in 3D may be overlaid in the projected image, thereby limiting the accuracy of the registration. A chest encompasses several independently moving parts including the ribs, heart, and lungs. Thus, most registration techniques are restricted to correcting for small movements in the projected plane.

Evaluating the registration accuracy is not straightforward as there is often no gold standard that exemplifies perfect alignment. Most registration evaluation is done by visually inspecting for artifacts present in the subtracted image and/or by computing multiple metrics such as the squared intensity error and reverse consistency error.[18]

I.B. Phase contrast x-ray imaging

Conventional x-ray imaging struggles to differentiate between soft biological tissues without the use of contrast agents.[19] Phase contrast x-ray imaging (PCXI) is able to enhance the boundaries of soft tissue by exploiting the differences in their refractive indices.[20] Many PCXI techniques have been developed that are suitable for biomedical studies, namely, PBI, analyzer-based phase contrast x-ray imaging and grating interferometry.[21] The improved contrast can be traded against a reduction in x-ray dose. Also, since the real part of the complex refractive index decreases with increasing x-ray energy at a much slower rate than the imaginary (absorptive) part, the dose can be decreased by employing higher x-ray energy.[21] Currently, PCXI is predominantly done using synchrotron radiation as it requires sufficient spatial coherence to induce edge enhancements. Despite this, there has been much success in performing PCXI imaging using laboratory-based x-ray sources.[22,23] PBI allows a simple setup as it does not require any postobject optics. Essentially, a spatially coherent source and a sufficient object-to-detector propagation distance are all that is required. The nonzero object-to-detector propagation distance enables refracted rays to produce interference/diffraction fringes.

I.C. Lung air volume analysis

Our work builds on that of Kitchen *et al.*[5] to determine the change in regional lung air volume between a pair of 2D PBI images for studying rapid changes in lung aeration. There the subject's thorax was immersed in a container of water and positioned between a partially coherent x-ray synchrotron source and detector. The change in the volume of air inside the lungs was equal to that of the water displaced from the main (sealed) chamber into the attached reservoir (water column; see Fig. 1). Determining the displaced water volume can be achieved by calculating the difference in the total volume enclosed between two images

$$\Delta V = \left\{ \sum_i^M \sum_j^N t(x_i, y_i)(\Delta x)^2 \right\}_A - \left\{ \sum_i^M \sum_j^N t(x_i, y_i)(\Delta x)^2 \right\}_B , \quad (2)$$

where t is the projected thickness of water, i and j are discrete indices of the $M \times N$ pixels in a Cartesian grid, and Δx is the pixel size.[5]

For absorption-contrast radiographs, t can easily be determined by rearranging the Beer–Lambert law as $t = -1/\mu_w \log(I_E)$, where I_E is the normalized intensity at the exit surface and μ_w is the attenuation coefficient of water for a monochromatic source. However, when using PBI to visualize the airways, the effects of propagation-based phase contrast must first be removed for volumetric analysis. Paganin *et al.*[24] showed that the projected thickness of a single-material object can be determined from a single PBI image using

$$T(x, y) = -\frac{1}{\mu_\omega} \log\left(\mathbf{F}^{-1} \left\{ \frac{\mathbf{F}[I_R(x, y, z = \Delta)]}{1 + (\delta_\omega \Delta/\mu_\omega)\,|\mathbf{k}_\perp|^2} \right\} \right), \quad (3)$$

where I_R is the normalized intensity at the detector, Δ is the object-to-detector propagation distance, δ_w is the refractive index decrement of water, and $\mathbf{k}_\perp$ represents the spatial frequency components corresponding to (x,y).

The total volume in chest images includes contributions from all materials, including bone, soft tissue, and water. Kitchen *et al.*[5] were able to accurately calculate the total change in lung air volume by ensuring the ROI chosen enclosed the entire thoracic cage such that the volume of materials other than water cancelled out when applying Eq. (2) (a proof is provided in the Appendix). They also performed a quadrant analysis whereby the chest was partitioned into four regions and the lung air volume enclosed in each was measured. This method has been utilized in several research

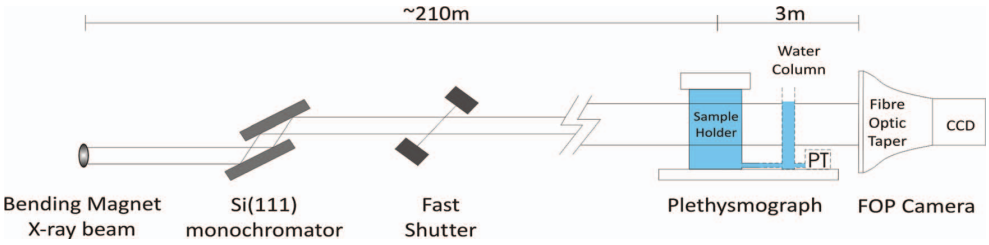

FIG. 1. A schematic of the PBI system used to acquire chest images of rabbit pups. Note that the water column is not within the path of the x-ray beam and PT = pressure transducer.

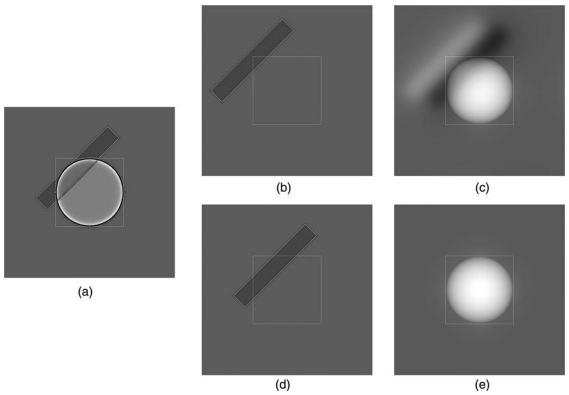

FIG. 2. Simulated images to demonstrate the necessity of aligning bone for measuring regional lung air volume. (a) A PBI image enclosing two objects, namely, a sphere (simulating an air bubble) and a cuboid (simulating bone tissue), projected onto one another and immersed in water. In (b) and (d), the PBI image of only the bone (i.e., with no air bubble) is, respectively, misaligned and aligned with that in (a). Each image underwent phase retrieval and subtraction was performed between (a) and (b) and (a) and (d) to yield the change in projected thickness at each pixel. The results are shown in (c) and (d), respectively. The change in air volume due to the sphere was calculated from these subtracted images using the entire field-of-view and using just the small ROI within the white border to demonstrate the need for image registration for regional volume measurements.

studies investigating different mechanical ventilation strategies for preterm infants, using a rabbit pup model, providing insight into the homogeneity of lung aeration at birth.[25,26] Although the bone attenuation will vary in each of the four regions, only small bone fragments will move in or out of the regions between frames, hence their movement will have little effect on the calculated lung air volumes. However, for more localized regions of the lungs, movement induced variation in the projected volume of bone can lead to large errors in lung air volumes. Our TS method corrects for this by first segmenting out the thoracic cage from the images.

To illustrate the benefit of segmenting out the thoracic cage, consider the PBI image consisting of two objects shown in Fig. 2(a). The spherical object can be considered as a pocket of air within lung tissue and the rectangular object as a bone. The PBI image was produced by generating a 1000×1000 pixel projected thickness map of the objects and using the angular spectrum formulation of scalar diffraction integrals to propagate the absorption-based image forward by 3 m with the pixel size set at 4.05 μm.[24] The δ and μ assigned for bone were 7.145×10^{-7} and 461.1 m^{-1}, respectively. For tissue, δ and μ were equal to 3.991×10^{-7} and 13.983 m^{-1}, respectively. These values were calculated from the NIST database[27] corresponding to a 24 keV source. Using the nonaerated PBI image shown in Fig. 2(b), the volume of the lung was determined using Eqs. (2) and (3). The change in projected thicknesses between the two images is shown in Fig. 2(c) and although the bones are not aligned, as long as they are both entirely within the field-of-view of the images, they will cancel each other out when the total change in volume is calculated, thus accurately yielding the air volume. The volume of the sphere was calculated as 2.218 μl in comparison to the known volume of 2.226 μl. This demonstrates that the technique developed by Kitchen *et al.*[5] is accurate in measuring the total lung air volume without needing to align the bones. However, when the field-of-view was restricted to a smaller region, as shown by the white border in Figs. 2(a)–2(e), the volume of bone within the smaller region in Figs. 2(a) and 2(b) is different. The change in volume calculated between these two subimages gave an air volume of just 1.688 μl—approximately a 32% error. By aligning the bones prior to subtraction [Fig. 2(d)], their effect can be eliminated when the images are subtracted, as shown in Fig. 2(e). The calculated lung air volume then was 2.186 μl—approximately only a 2% error.

II. MATERIALS AND METHODS

II.A. Image acquisition

Imaging experiments were performed in Hutch 3 of beamline 20B2 at the SPring-8 synchrotron radiation source, Japan.[28] A Si (111) double-bounce monochromator was tuned to 24 keV, which has been shown to provide optimum signal-to-noise ratio and bone/soft-tissue contrast for imaging rabbit pups on this beamline.[5] The PBI setup was adapted with the subject placed approximately 210 m downstream of the source with the detector positioned a further 3 m downstream (Fig. 1). Newborn rabbit pups were imaged as part of two experiments. The first group were imaged live at a frame rate of 3 Hz, with a respiratory cycle of 2.5 s, to study the efficacy of different ventilation strategies. Images were recorded with an exposure time of 40 ms using a high resolution detector composed of a tapered fiber optic bonded between the 4000×2672 pixel Hamamatsu CCD camera (C4742-95HR) and a 20 μm thick gadolinium oxysulfide ($Gd_2O_2S:Tb^+$; P43) phosphor. The effective pixel size was 16.2 μm based on the taper ratio of 1.8:1. Pups in the second group were humanely killed via anesthetic overdose prior to imaging for studying the pressure–volume characteristics of newborn lungs. These pups were imaged at a frame rate of 1 Hz, with a respiratory cycle of ~10 min, using a 25 μm thick gadolinium oxysulfide phosphor-coupled CCD camera (Hamamatsu, C4742-95HR). A tandem lens system provided an effective pixel size of 22.47 μm (2×2 pixel binning).

II.B. Sample preparation

All animal experiments were originally performed for studying lung aeration at birth.[26] Here, we have utilized the images recorded from those experiments for our study. All procedures involving animals were approved by the Monash University Animal Ethics Committee and the SPring-8 Animal Care and Use Committee. Pregnant New Zealand white rabbits at 31 days of gestation were anesthetized by an intravenous injection of propofol (Rapinovet; 12 mg kg^{-1} bolus, 40 mg h^{-1} infusion). Rabbit pups were delivered by caesarean section, sedated and surgically intubated. The umbilical cord was then cut and the pups were placed in

a water-filled cylindrical poly-methyl methacrylate (PMMA) container, with their heads out of the container and sealed by a rubber diaphragm surrounding their necks. A custom-made remotely controlled mechanical ventilator was connected to the endotracheal tube.[29] Ventilation began after several images were recorded of the lungs in their fluid-filled state. Rabbits and rabbit pups were humanely killed at the end of each experiment via anesthetic overdose.

II.C. Image processing

For quantitative volumetric analysis, the dark current arising from the detector was subtracted from the images, which were subsequently normalized against the incident beam intensity. This was achieved by first averaging 20 dark field images with the shutter closed and 20 flat field images with the shutter reopened and the object absent, at the end of each sequence. Nonlinear spatial distortions arising from the fiber optic camera, as a result of imperfect alignment of the fiber bundles at each end of the taper, were corrected by the use of Delaunay triangulation with bilinear interpolation.[17] Low-frequency trends were then removed to aid the cross correlation process since it is highly sensitive to large transverse gradients in the background intensity and their removal reduced the occurrence of misregistrations. These trends included: (i) the parabolic profile produced by the cylindrical container; (ii) the high energy (harmonic) x-rays reflected by the crystal monochromators creating a narrow horizontal band across the image; and (iii) the low frequency components of the air-filled lungs (which was added back when performing the lung volume analysis). To correct for the polynomial trend, a horizontal rectangular ROI below the lungs was selected along the container, averaged vertically, smoothed, then least-squares fitted with a 6th order polynomial. The polynomial curve was extruded vertically and subtracted from the images. The higher harmonic contaminants were corrected in the same manner but without polynomial fitting. The low frequency components of the aerated lungs were removed by subtracting a 200×200 pixel boxcar smoothed image of the lungs.

During the sequence acquisition the beam intensity was prone to fluctuation due, for example, to the loss and top-up of electrons in the synchrotron storage ring and thermal drifting of the monochromator crystals. This was corrected by rescaling each image to the reference frame using the average intensity in a region away from the moving pup. The Interactive Data Language (IDL 7.1) was used to run all custom-developed image processing algorithms on a PC using an Intel®Core™2 Duo, 3.32 GHZ CPU with 4 GB of RAM.

II.D. Image registration

A suitable fetal image with no lung aeration was selected as the reference image, which was then registered to each aerated image. This was achieved in two steps, where images were corrected first for global then local distortions. Each image pair was initially globally aligned to correct for the movement relating to the pup floating in the container. Kitchen *et al.*[5] achieved this by tracking the movement of a single vertebras using Eq. (1). Here, we have extended this approach to tracking multiple vertebras as it was found that each moved slightly independently to one another. The sizes and coordinates of the kernels enclosing each vertebras in the fetal (non-aerated) image were specified by the user. The corresponding search areas were automatically centerd at the same coordinates and enlarged by 10%. Each pair of control points were determined using Eq. (1), which were then replicated horizontally to both edges of the image, allowing the images to be interpolated in their entirety. This aligned the vertebral column of the two images and transformed the chest accordingly. This enabled the coordinates of regions where the ribs articulated with the vertebra (VR points) to be fixed between images for application of the localized distortion correction algorithm (described next).

The thoracic cavity was then partitioned into three regions: left/right lungs and the vertebral column. A series of 64×64 pixel kernels were selected at a sample rate of 32 pixels for the left and right lungs and correlated with their corresponding 128×128 pixel search areas. This corrected for localized movements associated with the expansion of the thoracic cage. This particular kernel size was chosen as it was sufficiently large to enclose a small segment of at most a single rib as each moves independently. The search area size was chosen to account for the largest likely rib displacements. These sizes can easily be modified if the parameters of the imaging system, such as magnification and pixel size, are changed.

The control points determined using Eq. (1) underwent a filtration process to remove unrealistic vectors. Control points were kept if all three of the following criteria were met: (i) the CC value was above a given threshold value;[30] (ii) the absolute difference between the angle of the shift vector and average angle of the adjacent shift vectors was less than 20°; and (iii) the absolute difference between the magnitude of the shift vector and average magnitude of the adjacent shift vectors was less than 81 μm (5 pixels). Image noise causes noise to also be present in the CC. A threshold value was applied to ensure matched regions with CC values significantly greater than that returned by a purely noisy region was accepted only. This threshold value was chosen to equal the average CC value returned when a pair of water-only 64×64 pixel ROIs chosen outside the rabbit, but within the container, were correlated. The angle 20° and magnitude 81 μm were selected based on a trial and error approach. These values were found to optimize the ratio of realistic to unrealistic shift vectors for chest images with various degrees of movement, yielding comparatively smooth transformations. The left and right lungs were transformed using the filtered control points and recombined together with the vertebral column to construct the registered image. To minimize the computation time required to perform temporal subtraction and phase retrieval, the region outside the chest, which includes the forelimbs, were masked out.

II.E. Image analysis

For the lung volume calculations, only the attenuation coefficient (μ_w) and refractive index decrement (δ_w) of

water were required. The latter was calculated from the NIST database[27] to be 3.99 × 10^{-7} (24 keV), while the former was calibrated by isolating a large section of 20 PBI images that contained water only. The lack of phase-induced intensity variations within these sections makes phase retrieval unnecessary, which allows them to be approximated as absorption-based images. The inner and outer diameter of the tube was measured to be 32.0 ± 0.1 and 39.0 ± 0.1 mm, respectively. Using the Beer–Lambert attenuation law, the attenuation coefficient of PMMA ($\mu_{\mathrm{PMMA}} = 48.91\ \mathrm{m}^{-1}$) obtained from the NIST database[27] and its thickness (7 mm), the attenuation signal of the tube was removed. μ_w was then measured to be 54.64 ± 0.01 m^{-1} using the Beer–Lambert law. The absolute uncertainty of the net water volume was then determined by measuring the standard deviation (σ) of the volume difference in a water-only ROI between the reference and set of 2252 aerated images against the ROI size (N × M pixels). The points were fitted with a rational exponent function ($3.543 \times 10^{-7} \times [\mathrm{N} \times \mathrm{M}]^{3/4} + 3.654 \times 10^{-6}$) from which we can calculate σ for any sized ROI.

III. RESULTS AND ANALYSIS

III.A. Chest segmentation

We successfully tested our TS algorithm on several sets of PBI images of rabbit pup chests during mechanical ventilation. A fetal image with fluid-filled lungs and no lung aeration (reference image) was chosen and temporally subtracted from each image recorded during ventilation. Figure 3(a) shows the fluid-filled lungs of the reference image from one such dataset. The remaining sequence of images, Figs. 3(b)–3(e), shows the chest in motion during one respiratory cycle. The speckle pattern seen in the aerated chest images is created by x-rays converging as a consequence of the alveoli mimicking aberrated compound refractive lenses.[6] As a consequence of utilizing a nonaerated image, the calculated volume difference is approximately equal to the total lung air volume in the aerated image; thus, we can measure absolute rather than relative lung air volumes. Furthermore, the lack of speckles in the nonaerated image means the kernel can treat the speckles in the search area as high frequency noise, against which CC is robust, hence only the bone is tracked.

Figure 4(a) shows the direct subtraction of Figs. 3(a) and 3(c). Due to the expansion of the thoracic cage as the lung fills with air and movement of the pup, the bones do not exactly overlap and therefore bone artifacts appear in the subtracted image. The images were then registered to correct for global movement. Here ends the similarity between our technique and that of Kitchen *et al.*[5] While in both cases the vertebral column is aligned, our technique proceeds to align the ribs, thus forming a fully registered image. Images whose vertebral column is only aligned are denoted as unregistered images. Figure 4(b) displays the images subtracted after global correction. This shows the vertebral column aligned accurately, while each rib appears to rotate about the side of the connected vertebra. This highlights our assumption made earlier on the VR points being fixed to be a good approximation when aligning the ribs.

Local translation vectors were next derived for each lung to correct for the rib movement, and screened for unrealistic vectors. Approximately one tenth of the resultant translation vectors are displayed in Fig. 4(c) for clarity. The zero magnitude translation vectors at the VR points are not visible. A histogram showing the distribution of the magnitude of the resultant translation vectors is presented in Fig. 4(d). This shows a majority of the magnitudes are realistic since they are approximately consistent with the extent of displacement of the ribs. A small minority of unrealistic translational vectors remain. Although we could alter our selection

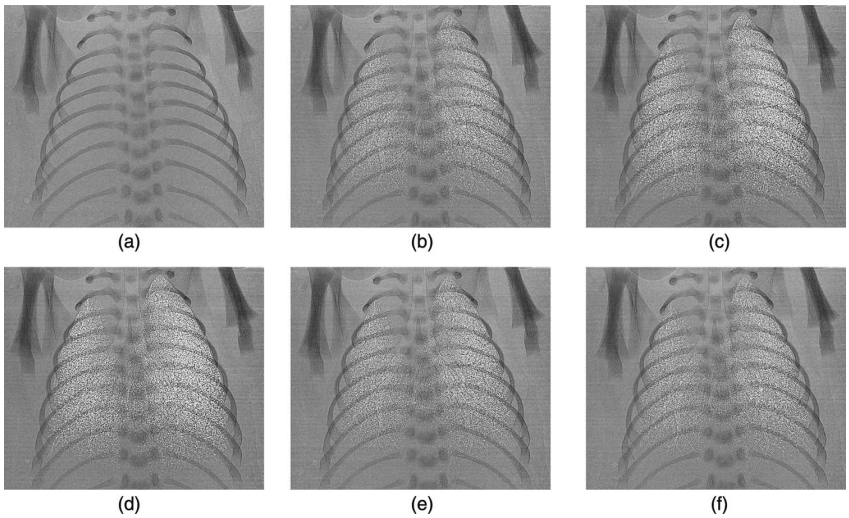

FIG. 3. A series of 24 ×21 mm^2 PBI chest images of a newborn rabbit pup recorded at 3 Hz in a (a) fluid-filled fetal state and (b)–(f) over one respiratory cycle, beginning midinspiration.

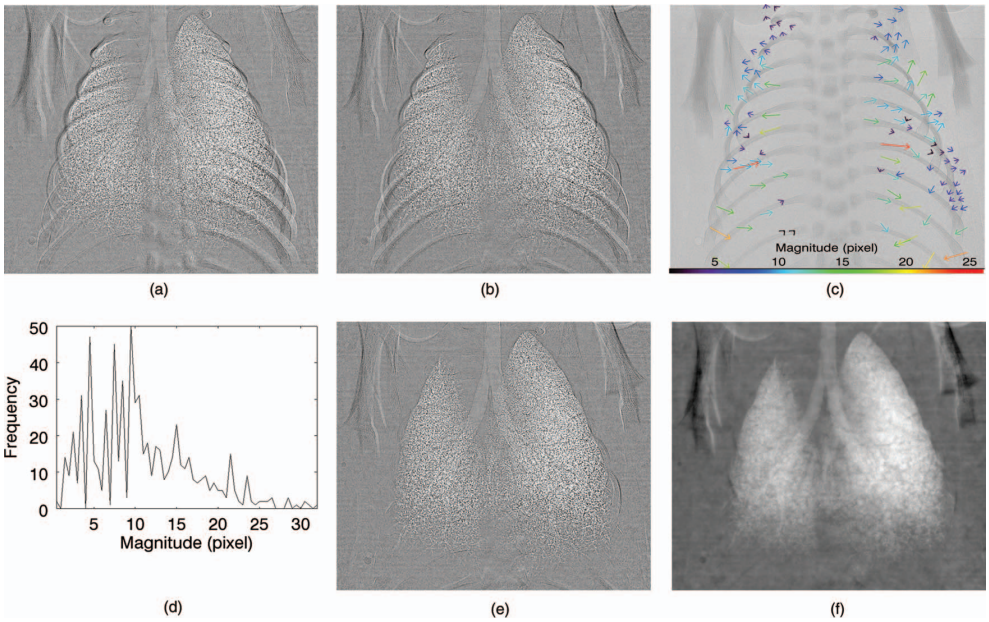

FIG. 4. Temporal subtraction. (a) The direct subtraction of the nonaerated [Fig. 3(a)] and an aerated [Fig. 3(c)] image shows the relative movement of the bony structures during image acquisition. (b) Subtraction after alignment of the vertebras in the nonaerated image with that of the aerated. (c) After correlating the entire thoracic cage, the control point pairs are represented by translational vectors (~one tenth of the vectors are shown), which enabled the nonaerated image to be transformed using bilinear interpolation. (d) A histogram showing the distribution of the magnitude of the translational vectors (the zero magnitude translation vectors have been suppressed). (e) Subtraction of the transformed image from that of the aerated image leaving only the signal due to the air (plus artifacts). (f) To perform lung volume analysis, the registered images underwent phase retrieval before subtraction, yielding the change in projected thickness at each pixel. Image size: 24×21 mm^2.

criteria to become more stringent, too many realistic translational vectors would also be filtered out, thereby adversely affecting accuracy of the alignment.

Using the control points, the reference image was transformed and subtracted from the aerated image, as shown in Fig. 4(e). Only small misalignment errors can be seen as faint artifacts predominantly along the outer borders of the chest. Since alignment was restricted to within the chest, strong artifacts are visible outside the chest. The total time taken to perform the TS was approximately 7 s on the aforementioned PC (see Sec. II.C). Figure 4(f) reveals the subtracted phase-retrieved images yielding the projected thickness of air. Note that these images underwent phase retrieval before subtraction due to the nonlinear dependence between the intensity and projected material thickness. A ROI of any size or shape could then be chosen from Fig. 4(f) to calculate the lung air volume enclosed within it.

III.B. Lung volume calculations

Figure 5(a) shows total lung air volumes calculated using the registered and unregistered reference images during mechanical ventilation of the pup. That is, we compared our technique to that of Kitchen *et al.*[5] Both techniques return almost identical total lung air volumes with the small discrepancies attributed to the rescaling of the fluid-filled nonaerated image when it was registered. The small discrepancies are well within the uncertainties of both techniques, demonstrating there is negligible detrimental effect of image registration on altering the total volume of the nonaerated image.

We proceeded to compare the ability of the two techniques to measure lung air volume on a pixel-by-pixel basis. For 1000 sequential PBI images of the same pup in Fig. 4, the lung air volume was computed at each pixel using the two techniques. The percentage difference in the calculated lung air volume between the two techniques was calculated at each pixel for the 1000 images. A histogram was computed, as shown in Fig. 5(b), which shows the distribution of the percentage difference in the calculated lung air volume averaged over all of the images. The shaded region in Fig. 5(b) shows that on average 16% of pixels within the lungs have a volume difference greater than 20%, and given that the fractional uncertainty of the measured change in lung air volume in each pixel is only ~1%, these differences are significant. The majority of these differences occurred around where the bones were not aligned, as evidenced in Figs. 5(c)–5(d) . These numbers show that the bones have a detrimental effect when performing regional lung air volume analysis and our technique is able to effectively remove the bones to accurately measure the lung air volume on a pixel-by-pixel basis.

A set of PBI chest images attained from the second group (slow inflation rates; ~10 min) was used to determine the percentage of regional lung aeration over time. Each aerated image was aligned to the first (nonaerated) image of the

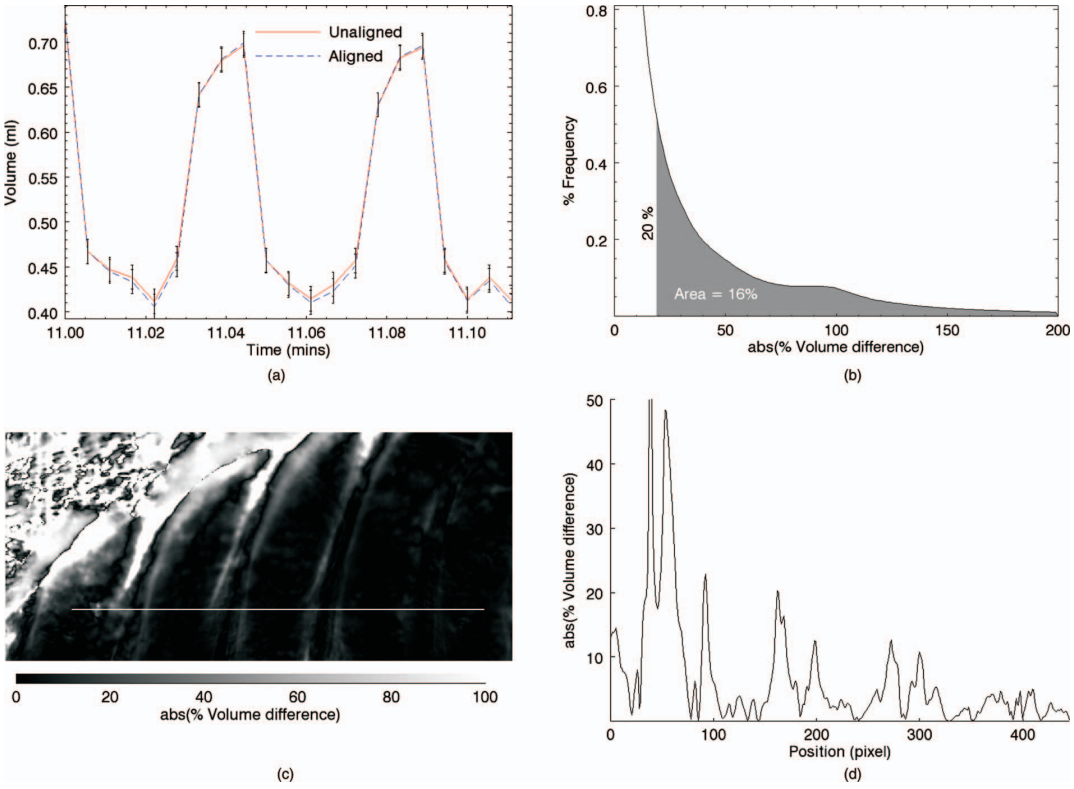

FIG. 5. Lung air volume analysis. (a) The total lung air volume was determined over several respiratory cycles beginning at $t = 11$ min, after initiation of mechanical ventilation, using the misaligned (unregistered) and aligned (registered) nonaerated images. (b) A histogram, averaged over 1000 aerated images, representing the absolute % volume difference in the calculated pixel-by-pixel lung air volume using misaligned and aligned nonaerated images. The shaded area under the plot shows the percentage of pixels with a volume difference greater than 20%. (c) An image of half a lung whose values represent the percentage difference of the lung air volume calculated between the two techniques. (d) A plot of the line profile indicated by the thick white horizontal line in (c).

sequence and underwent phase retrieval. The phase retrieved images were stacked to determine the time when each pixel within the lungs reached its maximum air volume. Figure 6 shows maps of the time taken for each region of the lungs to reach 10%, 50%, and 80% of its maximum air volume, on a pixel-by-pixel basis. We see that the major airways aerated first, as expected, followed by an otherwise relatively uniform aeration up to 10% of maximum volume [Fig. 6(a)]. However, the left lung (left side of image) then aerated more quickly in comparison to the right lung [Fig. 6(b)]. The peripheral regions of the lungs are also seen to more slowly ventilate during the latter stages of the inspiratory period. At the end of inspiration, the lungs asymptoted toward their maximum air volume more uniformly as the applied airway pressure also

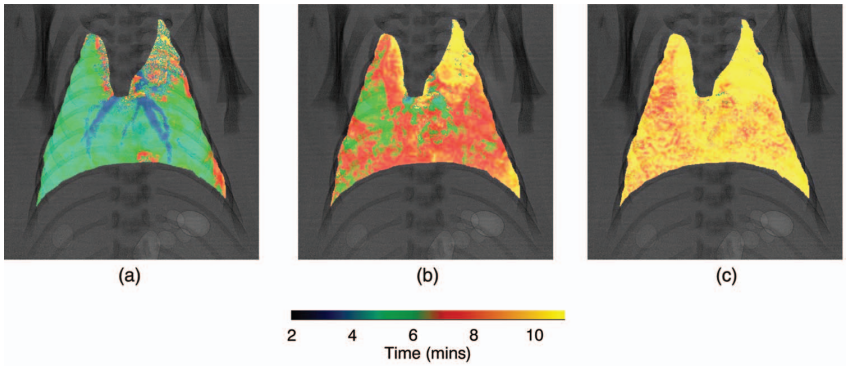

FIG. 6. Nonuniform lung aeration. A series of maps were produced showing the time taken for each pixel of the lung to reach (a) 10%, (b) 50%, and (c) 80% of their maximum air volume. Image size: 24×21 mm^2.

reached its plateau [Fig. 6(c)]. The combined panels in Fig. 6 show that the time constant of aeration is highly localized.

IV. DISCUSSION

This study demonstrates that the technique for measuring lung air volume, developed by Kitchen *et al.*,[5] can be extended to more accurately measure regional lung air volumes using TS. The image registration method adapted here has been able to accurately align PBI chest images with minimal computational cost, primarily by exploiting the use of fast Fourier transform-based CC. Other similarity measures were investigated, namely, mutual information and sums of absolute differences,[14] and the resultant subtracted images at best showed a marginal improvement, based on the visual inspection of artifacts, coinciding with a large increase in computation time. Polynomial interpolation was also considered as an alternative to bilinear interpolation since it has the ability to produce a smooth transformation; however, the complexity in the motion of the chest requires a higher order polynomial that can introduce large and unwanted oscillations around the edges of the image by the Runge phenomenon.[31]

Figure 6 shows the distribution of gas is often inhomogeneous across the lung. Hence, a regional mapping of lung aeration can reveal abnormally ventilated regions of the lung that would otherwise be undetected in global pulmonary tests. The ability to study the homogeneity of lung aeration can be beneficial in animal research studies. For example, greater understanding can be gained into lung related diseases and studying which mechanical ventilation strategies are most likely to reduce ventilator-induced lung injury (for example, for preterm infant resuscitation[26]). Our technique can also gain insight into the crucial but transient period of achieving lung aeration from birth. High-powered laboratory-based x-ray sources are being developed that enable PBI, and therefore our technique, to be performed in clinics. This presents various potential medical applications such as diagnosing respiratory related diseases earlier and with greater precision than conventional x-ray imaging and global pulmonary tests.

Compared to absorption-based x-ray imaging, PBI of the chest can provide additional structural information regarding the morphology of the conducting zone that contains the trachea, bronchi, and bronchioles, and the respiratory zone which includes the alveoli.[32] However, the signal intensity from the bone is weakened by that of the alveolar speckles. Consequently, during image registration the kernels selected in those parts of the lungs either weakly correlated, or misregistered, to regions enclosing strongly speckled intensity. This resulted in a moderate portion of translation vectors rejected in the central areas of the lungs, as shown in Fig. 4(c) by the lack of translation vectors. Despite this, the movement of the medial segment of the ribs during breathing is closely restricted to a rigid type transformation. This can be adequately accounted for by the piecewise linear interpolation between the zero magnitude VR points and their laterally closest translation vector.

The accuracy of the assumption that the medial segment of the ribs undergoes a rigid type transformation, and therefore that of alignment, depended on the amount of differential movement of the chest. A measurable indicator of the degree of motion was the volume change (the difference in volume between an aerated and nonaerated lung). It was found on average at a volume change of 0.60 ml the alignment was quite accurate but gradually deteriorated beyond this volume as the movement of the thoracic cage became overly complex (see the supplementary material for online movie).[37] Given that the average weight of a rabbit pup is 30 g, the maximum volume change per unit mass of 20 ml/kg is considered to be a large volume change.[33] Therefore, this technique could be applied to measure a range of lung air volumes in patients.

A nonaerated reference image may not always be available or possible to obtain in some studies. Alternatively, an aerated PBI chest image could be used as a reference image. While this will instead provide relative volumetric measurements, which still carries much important respiratory information, a more problematic issue is that cross-correlating ROIs that have speckles present in both is likely to increase the prevalence of misregistrations as the speckles weaken the signal intensity of the bone. Moreover, the speckles may correlate more strongly with each other than the bones themselves. Consequently, measuring relative changes in lung air volume by using an aerated chest image as a reference image decreases the maximum volume change per unit mass that our technique can measure.

Regardless of whether the reference image is an aerated or nonaerated chest image, the maximum measurable volume change could be increased either through modifying the algorithm or image acquisition process. More translation vectors could be retained by correcting rather than rejecting them. These corrections could be made based on preserving the continuity and smoothness of the transformation (see, e.g., Ref. 34). We also attempted using a smaller sized kernel to better handle the localized lung movement. This increased the number of degrees of freedom, but the structural information it enclosed was less unique and became more prone to misregistrations. Shortening the propagation distance to reduce or remove the phase contrast could improve the bone contrast relative to the speckle contrast to reduce the occurrence of misregistrations. If the reference image was an aerated PBI chest image, then it could be chosen to be the image with the least lung aeration. We have also discovered that the degree of chest wall movement is dependent on the angle between the vertebral column and the horizontal axis along the sagittal plane. We are currently attempting to optimize this orientation to enable accurate alignment at volume changes up to 40 ml/kg.

The total lung air volume was expected to remain unchanged before and after temporal subtraction considering that all the anatomical structure remained within the detector field-of-view. Due to the nonconservation of the total intensity when performing a nonrigid type transformation, there would inevitably be a small deviation. To ascertain the extent at which the nonconserving volume contributes regionally, the calculated lung air volume using temporal subtraction could be compared with that using other bone removal techniques. One example is the technique developed by Kitchen *et al.*[35]

that utilizes a Laue crystal to split the x-ray beam to create two unique images. These have been used to segment chest images to enable isolation of bony anatomy and soft tissue and regional lung volume measurement. Although that technique does not require anatomical registration, it is experimentally more challenging, the image reconstruction is also more time consuming and somewhat susceptible to low frequency noise. Nonetheless, it presents as an ideal technique with which to compare our calculated regional lung air volumes.

Throughout, we have employed a fixed sized ROI to measure lung aeration. To correctly assess regional volumes, the expansion and deflation of the lungs should be taken into account. Christensen *et al.*[36] showed that lungs do not expand or relax uniformly but in a local manner. Fouras *et al.*[15] developed a particle image velocimetry-based algorithm that is able to measure regional expansion of the lungs by tracking the motion of the lung-induced speckles. Thus, we will look to adapt the work of Fouras *et al.*[15] into our method to measure regional air volume of the entire lung by deforming the ROI in accordance with the movement of the speckles.

V. CONCLUSIONS

Accurately measuring the heterogeneity of lung aeration is likely to be highly beneficial to studying and treating child and adult lung disease and for optimizing mechanical ventilation strategies for preterm infants. Herein, a temporal subtraction algorithm was developed to remove the bony anatomy from two-dimensional propagation-based phase contrast x-ray images of the chest to isolate the lungs. Using a single image phase retrieval algorithm the change in air volumes between localized regions of the lung, down to the micron scale pixel size, could be measured. By comparing the total lung air volume measured using a registered and unregistered nonaerated image, we found that the variability in the total intensity introduced in the nonaerated chest image of preterm rabbit pups after image registration is small compared to the uncertainty in our measured change in lung air volume. In analyzing the lung air volume regionally, we showed a significant improvement, compared to images that were not registered, primarily in areas where the bones were poorly aligned. Therefore, we have demonstrated that our technique can isolate the lungs and provide high spatiotemporal resolution measures of lung aeration, without the requirement of contrast agents.

ACKNOWLEDGMENTS

The authors would like to thank Dr. David Paganin, Dr. Karen Siu, and Dr. Imants Svalbe for insightful discussions, and to Kentaro Uesugi for assistance with the experiments. A.F.T.L. acknowledges the support of an Australian Postgraduate Award. A.F., S.B.H., and M.J.K. acknowledge funding from the Australian Research Council (ARC; Grant Nos. DP110101941 and DP110101498). M.J.K. is an ARC Australian Research Fellow. S.B.H. is a NHMRC Principal Research Fellow. This research was partially funded by the Victorian Government's Operational Infrastructure Support Program. The authors acknowledge travel funding provided by the International Synchrotron Access Program managed by the Australian Synchrotron and funded by the Australian Government.

APPENDIX: MEASURING THE CHANGE IN VOLUME OF A SINGLE MATERIAL FROM A HETEROGENEOUS OBJECT

Consider a multimaterial object where the volume of only one of the materials is changing over time. If a sequence of absorption-based images were recorded of that object, the change in volume of that material can be measured between the recorded images. Here, we will demonstrate this by first considering two $M \times N$ pixel absorption-based images (I_1, I_2) at the exit surface plane of the object at time points 1 and 2. The intensity can be related to the projected thickness of the materials given by Beer–Lambert's law,

$$I(x, y) = \exp[-\textstyle\sum_{\mathrm{m}} \mu_{\mathrm{m}}(x_i, y_j) t_m(x_i, y_j)], \tag{A1}$$

where μ_m and t_m are the attenuation coefficient and projected thickness of material m, respectively. i and j are discrete indices of the $M \times N$ pixels in a Cartesian grid.

The projected thickness (t_w) corresponding to the material with a changing volume can be isolated from Eq. (A1) by assuming the other materials are also made entirely of that material to give

$$t_w(x_i, y_i) + \sum_m t'_m(x_i, y_i) = -\frac{1}{\mu_w} \log_e[I(x_i, y_i)], \tag{A2}$$

where $t'_m = \mu_w / \mu_m t_m$, which shows the projected thickness of each material rescaled to separate μ from t. t_w can be isolated by taking the difference in the projected thicknesses of I_1 and I_2, and summing over (x_i, y_j) to give

$$\begin{aligned} \triangle t_w &= \sum_i^M \sum_j^N [t_{w,1}(x_i, y_i) - t_{w,2}(x_i, y_i)] \\ &= \sum_i^M \sum_j^N \left\{ \frac{1}{\mu_w} [log_e[I_2(x_i, y_i)] - log_e[I_1(x_i, y_i)]] \right\}. \end{aligned} \tag{A3}$$

Since the total projected thickness of the other materials remain constant, the second term on the left-hand side of Eq. (A2) cancel out, thus correctly giving the change in the total projected thickness of material w. By multiplying Eq. (A3) with the pixel area, we arrive at Eq. (2). For our work, the changing volume we are measuring is air, although it cannot be directly measured due to its low attenuating strength. Instead, the lungs are immersed in a tube of water where the volume of water displaced during breathing is equivalent to that of air.

In our work, we recorded PBI images, thus the single-image phase retrieval algorithm is applied before using the steps above. This algorithm convolves the PBI image with a radially dependant low-pass filter function to obtain the absorption-based image, effectively smoothing out the phase induced intensity variations. As a consequence of using

Eq. (3) on an inhomogeneous object such as the chest, materials with a ratio μ/δ different to that of the material of interest will be over/undersmoothed. The degree of over/undersmoothing varies with lung aeration. Despite this, the work done by Kitchen *et al.*[5] shows that the change in lung air volume calculated using their technique correlates well with that measured from a plethysmograph for numerous preterm rabbit pups over a large range of lung air volumes. This demonstrates the error introduced, from over/undersmoothed materials, into the measured change in lung air volume is small relative to its uncertainty.

[a]Electronic mail: andrew.leong@monash.edu.

[1]A. Fouras, M. J. Kitchen, S. Dubsky, R. A. Lewis, S. B. Hooper, and K. Hourigan, "The past, present, and future of x-ray technology for in vivo imaging of function and form," J. Appl. Phys. **105**, 102009 (2009).

[2]S. D. Qanadli, E. Orvoen-Frija, P. Lacombe, R. Di Paola, J. Bittoun, and G. Frija, "Estimation of gas and tissue lung volumes by MRI: Functional approach of lung imaging," J. Comput. Assist. Tomogr. **23**, 743–748 (1999).

[3]S. Monfraix, S. Bayat, L. Porra, G. Berruyer, C. Nemoz, W. Thomlinson, P. Suortti, and A. R. A. Sovijärvi, "Quantitative measurement of regional lung gas volume by synchrotron radiation computed tomography," Phys. Med. Biol. **50**, 1–11 (2005).

[4]T. J. Wellman, T. Winkler, E. L. Costa, G. Musch, R. S. Harris, J. G. Venegas, and M. F. V. Melo, "Measurement of regional specific lung volume change using respiratory-gated pet of inhaled ^{13}N-nitrogen," J. Nucl. Med. **51**, 646–653 (2010).

[5]M. J. Kitchen, R. A. Lewis, M. J. Morgan, M. J. Wallace, M. L. Siew, K. K. W. Siu, A. Habib, A. Fouras, N. Yagi, K. Uesugi, and S. B. Hooper, "Dynamic measures of regional lung air volume using phase contrast x-ray imaging," Phys. Med. Biol. **53**, 6065–6077 (2008).

[6]M. J. Kitchen, D. Paganin, R. A. Lewis, N. Yagi, K. Uesugi, and S. T. Mudie, "On the origin of speckle in x-ray phase contrast images of lung tissue," Phys. Med. Biol. **49**, 4335–4348 (2004).

[7]J. F. Adam, S. Bayat, L. Porra, H. Elleaume, F. Estve, and P. Suortti, "Quantative functional imaging and kinetic studies with high-Z contrast agents using synchrotron radiation computed tomography," Clin. Exp. Pharmacol. Physiol. **36**, 95–106 (2009).

[8]P. Vock and Z. Szucs-Farkas, "Dual energy subtraction: Principles and clinical applications," Eur. J. Radiol. **72**, 231–237 (2009).

[9]T. Ishigaki, S. Sakuma, Y. Horikawa, M. Ikeda, and H. Yamaguchi, "One-shot dual-energy subtraction imaging" Radiology **161**, 271–273 (1986).

[10]R. P. Carnibella, A. Fouras, and M. J. Kitchen, "Single-exposure dual-energy-subtraction x-ray imaging using a synchrotron source," J. Synchrotron Radiat. **19**, 954–959 (2012).

[11]S. Kakeda, K. Kamada, Y. Hatakeyama, T. Aoki, Y. Korogi, S. Katsuragawa, and K. Doi, "Effect of temporal subtraction technique on interpretation time and diagnostic accuracy of chest radiography," Am. J. Roentgenol. **187**, 1253–1259 (2006).

[12]K. Suzuki, H. Abe, H. MacMahon, and K. Doi, "Image-processing technique for suppressing ribs in chest radiographs by means of massive training artificial neural network (MTANN)," IEEE Trans. Med. Imaging **25**, 406–416 (2006).

[13]A. Kano, K. Doi, H. MacMahon, D. D. Hassell, and M. L. Giger, "Digital image subtraction of temporally sequential chest images for detection of interval change," Med. Phys. **21**, 453–461 (1994).

[14]B. Zitová and J. Flusser, "Image registration methods: A survey," Image Vision Comput. **21**, 977–1000 (2003).

[15]A. Fouras, B. J. Allison, M. J. Kitchen, S. Dubsky, J. Nguyen, K. Hourigan, K. K. W. Siu, R. A. Lewis, M. J. Wallace, and S. B. Hooper, "Altered lung motion is a sensitive indicator of regional lung disease," Ann. Biomed. Eng. **40**, 1160–1169 (2012).

[16]R. A. Jamison, A. Fouras, and R. J. Bryson-Richardson, "Cardiac-phase filtering in intracardiac particle image velocimetry," J. Biomed. Opt. **17**, 036007 (2012).

[17]M. S. Islam, R. A. Lewis, K. Uesugi, and M. J. Kitchen, "A high precision recipe for correcting images distorted by a tapered fiber optic," J. Instrum. **5**, P09008 (2010).

[18]G. E. Christensen, X. Geng, J. G. Kuhl, J. Bruss, T. J. Grabowski, I. A. Pirwani, M. W. Vannier, J. S. Allen, and H. Damasio, "Introduction to the non-rigid image registration evaluation project (NIREP)," in *Biomedical Image Registration*, Lecture Notes in Computer Science Vol. 4057, edited by J. Pluim *et al*. (Springer, Berlin Heidelberg, 2006), pp. 128–135.

[19]A. Momose, T. Takeda, Y. Itai, and K. Hirano, "Phase-contrast x-ray computed tomography for observing biological soft tissues," Nat. Med. **2**, 473–475 (1996).

[20]T. E. Gureyev, S. C. Mayo, D. E. Myers, Y. Nesterets, D. M. Paganin, A. Pogany, A. W. Stevenson, and S. W. Wilkins, "Refracting Röntgen's rays: Propagation-based x-ray phase contrast for biomedical imaging," J. Appl. Phys. **105**, 102005 (2009).

[21]S. A. Zhou and A. Brahme, "Development of phase-contrast x-ray imaging techniques and potential medical applications," Phys. Medica **24**, 129–148 (2008).

[22]S. W. Wilkins, T. E. Gureyev, D. Gao, A. Pogany, and A. W. Stevenson, "Phase-contrast imaging using polychromatic hard x-rays," Nature (London) **384**, 335–338 (1996).

[23]D. J. Vine, D. M. Paganin, K. M. Pavlov, J. Kráußlich, O. Wehrhan, I. Uschmann, and E. Förster, "Analyzer-based phase contrast imaging and phase retrieval using a rotating anode x-ray source," J. Appl. Phys. **91**, 254110 (2007).

[24]D. Paganin, S. C. Mayo, T. E. Gureyev, P. R. Miller, and S. W. Wilkins, "Simultaneous phase and amplitude extraction from a single defocused image of a homogeneous object," J. Microsc. **206**, 33–40 (2002).

[25]M. L. Siew, A. B. te Pas, M. J. Wallace, M. J. Kitchen, M. S. Islam, R. A. Lewis, A. Fouras, C. J. Morley, P. G. Davis, N. Yagi, K. Uesugi, and S. B. Hooper, "Surfactant increases the uniformity of lung aeration at birth in ventilated preterm rabbits," Pediatr. Res. **70**, 50–55 (2011).

[26]S. B. Hooper, M. J. Kitchen, M. L. L. Siew, R. A. Lewis, A. Fouras, A. B. te Pas, K. K. W. Siu, N. Yagi, K. Uesugi, and M. J. Wallace, "Imaging lung aeration and lung liquid clearance at birth using phase contrast x-ray imaging," Clin. Exp. Pharmacol. Physiol. **36**, 117–125 (2009).

[27]M. J. Berger, J. H. Hubbell, S. M. Seltzer, J. Chang, J. S. Coursey, R. Sukumar, D. S. Zucker, and K. Olsen, "XCOM: Photon cross sections database," 2010 (available URL: http://www.nist.gov/pml/data/xcom/index.cfm).

[28]S. Goto, K. Takeshita, Y. Suzuki, H. Ohashi, Y. Asano, H. Kimura, T. Matsushita, N. Yagi, M. Isshiki, H. Yamazaki, Y. Yoneda, K. Umetani, and T. Ishikawa, "Construction and commissioning of a 215-m-long beamline at SPring-8," Nucl. Instrum. Meth. A **467–468**, 682–685 (2001).

[29]M. J. Kitchen, A. Habib, A. Fouras, S. Dubsky, R. A. Lewis, M. J. Wallace, and S. B. Hooper, "A new design for high stability pressure-controlled ventilation for small animal lung imaging," J. Instrum. **5**, T02002 (2010).

[30]R. D. Keane and R. J. Adrian, "Optimization of particle image velocimeters. I. Double pulsed systems," Meas. Sci. Technol. **1**, 1202–1215 (1990).

[31]E. Süli and D. F. Mayers, *An Introduction to Numerical Analysis* (Cambridge University Press, Cambridge, 2003).

[32]M. J. Kitchen, R. A. Lewis, N. Yagi, K. Uesugi, D. Paganin, S. B. Hooper, G. Adams, S. Jureczek, J. Singh, C. R. Christensen, A. P. Hufton, C. J. Hall, K. C. Cheung, and K. M. Pavlov, "Phase contrast x-ray imaging of mice and rabbit lungs: A comparative study," Br. J. Radiol. **78**, 1018–1027 (2005).

[33]M. R. Wilson, B. V. Patel, and M. Takata, "Ventilation with clinically relevant high tidal volumes does not promote stretch-induced injury in the lungs of healthy mice," Crit. Care Med. **40**, 2850–2857 (2012).

[34]Q. Li, S. Katsuragawa, and K. Doi, "Improved contralateral subtraction images by use of elastic matching technique," Med. Phys. **27**, 1934–1942 (2000).

[35]M. J. Kitchen, D. M. Paganin, K. Uesugi, B. J. Allison, R. A. Lewis, S. B. Hooper, and K. M. Pavlov, "Phase contrast image segmentation using a laue analyser crystal," Phys. Med. Biol. **56**, 515–534 (2011).

[36]G. E. Christensen, J. H. Song, W. Lu, I. E. Naqa, and D. A. Low, "Tracking lung tissue motion and expansion/compression with inverse consistent image registration and spirometry," Med. Phys. **34**, 2155–2163 (2007).

[37]See supplementary material at http://dx.doi.org/10.1118/1.4794926 for online movie.

Appendix B

Measurement of absolute regional lung air volumes from near-field x-ray speckles

by A. F. T. Leong, D. M. Paganin, S. B. Hooper, M. L. Siew, M. J. Kitchen.

Published in Optics Express **21**, pp. 777-786, 2013.

Measurement of absolute regional lung air volumes from near-field x-ray speckles

Andrew F. T. Leong,[1,*] David M. Paganin,[1] Stuart B. Hooper,[2] Melissa L. Siew,[2] and Marcus J. Kitchen[1]

[1]*School of Physics, Monash University, Vic 3800, Australia*
[2]*The Ritchie Centre and Department of Obstetrics and Gynaecology, Monash Institute of Medical Research, Monash University, Vic 3168, Australia*

Abstract: Propagation-based phase contrast x-ray (PBX) imaging yields high contrast images of the lung where airways that overlap in projection coherently scatter the x-rays, giving rise to a speckled intensity due to interference effects. Our previous works have shown that total and regional changes in lung air volumes can be accurately measured from two-dimensional (2D) absorption or phase contrast images when the subject is immersed in a water-filled container. In this paper we demonstrate how the phase contrast speckle patterns can be used to directly measure absolute regional lung air volumes from 2D PBX images without the need for a water-filled container. We justify this technique analytically and via simulation using the transport-of-intensity equation and calibrate the technique using our existing methods for measuring lung air volume. Finally, we show the full capabilities of this technique for measuring regional differences in lung aeration.

OCIS codes: (340.7440) X-ray imaging; (110.6150) Speckle imaging; (100.5070) Phase retrieval; (170.3660) Light propagation in tissues; (170.3880) Medical and biological imaging; (290.5850) Scattering, particles.

References and links

1. H. Kauczor and A. Bankier, *Functional Imaging of the Chest* (Springer, 2004).
2. A. Fouras, B. J. Allison, M. J. Kitchen, S. Dubsky, J. Nguyen, K. Hourigan, K. K. W Siu, R. A. Lewis, M. J. Wallace, and S. B. Hooper, "Altered lung motion is a sensitive indicator of regional lung disease," Ann. Biomed. Eng. **40**, 1160–1169 (2012).
3. M. J. Tobin, G. Jenouri, B. Lind, H. Watson, A. Schneider, and M. A. Sackner, "Validation of respiratory inductive plethysmography in patients with pulmonary disease," Chest **83**, 615–620 (1983).
4. M. L. Levy, M. Fletcher, D. B. Price, T. Hausen, R. J. Halbert, and B. P. Yawn, "International primary care respiratory group (IPCRG) guidelines: Diagnosis of respiratory diseases in primary care," Prim. Care Respir. J. **15**, 20–34 (2006).
5. E. Oostveen D. MacLeod H. Lorino, R. Farr, Z. Hantos, K. Desager, F. Marchal, and on behalf of the ERS Task Force on Respiratory Impedance Measurements, "The forced oscillation technique in clinical practice: methodology, recommendations and future developments," Eur. Respir. J. **22**, 1026–1041 (2003).
6. A. Kyriazis, I. Rodriguez, N. Nin, J. Izquierdo-Garcia, J. Lorente, J. Perez-Sanchez, J. Pesic, L. Olsson, and J. Ruiz-Cabello, "Dynamic ventilation 3He MRI for the quantification of disease in the rat lung," IEEE Trans. Biomed. Eng. **59**, 777–786 (2012).
7. K. S. Mueller, F. R. Long, R. L. Flucke, and R. G. Castile, "Volume-monitored chest CT: a simplified method for obtaining motion-free images near full inspiratory and end expiratory lung volumes," Pediatr. Radiol. **40**, 1663–1669 (2010).

#196046 - $15.00 USD Received 28 Aug 2013; revised 21 Oct 2013; accepted 21 Oct 2013; published 6 Nov 2013

8. T. J. Wellman, T. Winkler, E. L. Costa, G. Musch, R. S. Harris, J. G. Venegas, and M. F. V. Melo, "Measurement of regional specific lung volume change using respiratory-gated PET of inhaled 13N-nitrogen," J. Nucl. Med. **51**, 646–653 (2010).
9. S. Bayat, G. Le Duc, L. Porra, G. Berruyer, C. Nemoz, S. Monfraix, S. Fiedler, W. Thomlinson, P. Suortti, C. G. Standertskjld-Nordenstam, and A. R. A. Sovijrvi, "Quantitative functional lung imaging with synchrotron radiation using inhaled xenon as contrast agent," Phys. Med. Biol. **46**, 3287–3299 (2001).
10. L. Porra, S. Monfraix, G. Berruyer, G. Le Duc, C. Nemoz, W. Thomlinson, P. Suortti, A. R. A. Sovijrvi, and S. Bayat, "Effect of tidal volume on distribution of ventilation assessed by synchrotron radiation CT in rabbit," J. Appl. Physiol. **96**, 1899–1908 (2004).
11. E. M. Law, A. F. Little, and J. C. Salanitri, "Non-vascular intervention with real-time CT fluoroscopy," Australas. Radiol. **45**, 109–112 (2001).
12. M. Uecker, S. Zhang, D. Voit, A. Karaus, K.-D. Merboldt, and J. Frahm, "Real-time MRI at a resolution of 20 ms," NMR Biomed. **23**, 986–994 (2010).
13. M. J. Kitchen, R. A. Lewis, M. J. Morgan, M. J. Wallace, M. L. Siew, K. K. W. Siu, A. Habib, A. Fouras, N. Yagi, K. Uesugi, and S. B. Hooper, "Dynamic measures of regional lung air volume using phase contrast x-ray imaging," Phys. Med. Biol. **53**, 6065–6077 (2008).
14. M. J. Kitchen, D. M. Paganin, K. Uesugi, B. J. Allison, R. A. Lewis, S. B. Hooper, and K. M. Pavlov, "Phase contrast image segmentation using a Laue analyser crystal," Phys. Med. Biol. **56**, 515–534 (2011).
15. A. F. T. Leong, A. Fouras, M. S. Islam, M. J. Wallace, S. B. Hooper, and M. J. Kitchen, "High spatiotemporal resolution measurement of regional lung air volumes from 2D phase contrast x-ray images," Med. Phys. **40**, 041909 (2013).
16. M. L. Siew, A. B. te Pas, M. J. Wallace, M. J. Kitchen, M. S. Islam, R. A. Lewis, A. Fouras, C. J. Morley, P. G. Davis, N. Yagi, K. Uesugi, and S. B. Hooper, "Surfactant increases the uniformity of lung aeration at birth in ventilated preterm rabbits," Pediatr. Res. **70**, 50–55 (2011).
17. M. L. Siew, M. J. Wallace, B. J. Allison, M. J. Kitchen, A. B. te Pas, M. S. Islam, R. A. Lewis, A. Fouras, N. Yagi, K. Uesugi, and S. B. Hooper, "The role of lung inflation and sodium transport in airway liquid clearance during lung aeration in newborn rabbits," Pediatr. Res. **73**, 443–449 (2013).
18. K. Wheeler, M. Wallace, M. Kitchen, A. te Pas, A. Fouras, M. Islam, M. Siew, R. Lewis, C. Morley, P. Davis, and S. Hooper, "Establishing lung gas volumes at birth: interaction between positive end-expiratory pressures and tidal volumes in preterm rabbits," Pediatr. Res. **73**, 734–741 (2013).
19. D. Paganin, S. C. Mayo, T. E. Gureyev, P. R. Miller, and S. W. Wilkins, "Simultaneous phase and amplitude extraction from a single defocused image of a homogeneous object," J. Microscopy **206**, 33–40 (2002).
20. S. W. Wilkins, T. E. Gureyev, D. Gao, A. Pogany, and A. W. Stevenson, "Phase-contrast imaging using polychromatic hard x-rays," Nature **384**, 335–338 (1996).
21. R. P. Carnibella, M. J. Kitchen, and A. Fouras, "Determining particle size distributions from a single projection image," Opt. Express **20**, 15962–15968 (2012).
22. J. Goodman, *Speckle Phenomena in Optics: Theory and Applications* (Roberts & Co., 2007).
23. M. Giglio, M. Carpineti, A. Vailati, and D. Brogioli, "Near-field intensity correlations of scattered light," Appl. Opt. **40**, 4036–4040 (2001).
24. M. I. Mishchenko, "Multiple scattering by particles embedded in an absorbing medium. 1. foldy–lax equations, order-of-scattering expansion, and coherent field," Opt. Express **16**, 2288–2301 (2008).
25. T. Fricke-Begemann and K. D. Hinsch, "Measurement of random processes at rough surfaces with digital speckle correlation," J. Opt. Soc. Am. A **21**, 252–262 (2004).
26. S. J. Kirkpatrick, D. D. Duncan, R. K. Wang, and M. T. Hinds, "Quantitative temporal speckle contrast imaging for tissue mechanics," J. Opt. Soc. Am. A **24**, 3728–3734 (2007).
27. N. Yagi, Y. Suzuki, K. Umetani, Y. Kohmura, and K. Yamasaki, "Refraction-enhanced x-ray imaging of mouse lung using synchrotron radiation source," Med. Phys. **26**, 2190–2193 (1999).
28. M. J. Kitchen, D. Paganin, R. A. Lewis, N. Yagi, K. Uesugi, and S. T. Mudie, "On the origin of speckle in x-ray phase contrast images of lung tissue," Phys. Med. Biol. **49**, 4335–4348 (2004).
29. J. García, Z. Zalevsky, P. García-Martínez, C. Ferreira, M. Teicher, and Y. Beiderman, "Three-dimensional mapping and range measurement by means of projected speckle patterns," Appl. Opt. **47**, 3032–3040 (2008).
30. E. R. Weibel, *Morphometry of the Human Lung* (Academic, 1963).
31. NIST, "National institute of standards and technology, physical reference data," (2010)
32. R. W. James, *The Crystalline State: The Optical Principles of the Diffraction of X-Rays* (Cornell University, 1965).
33. J. Moosmann, R. Hofmann, and T. Baumbach, "Single-distance phase retrieval at large phase shifts," Opt. Express **19**, 12066–12073 (2011).
34. S. Sýkora, "K-space images of n-dimensional spheres and generalized sinc functions," 2008, http://www.ebyte.it/library/docs/math07/SincN.html.
35. L. Brancazio, G. Franz, E. Petsonk, and D. Frazer, "Lung area-volume models in relation to the recruitment-derecruitment of individual lung units," Ann. Biomed. Eng. **29**, 252–262 (2001).
36. D. S. Wilks, *Statistical Methods in the Atmospheric Sciences* (Elsevier Science, 2011).

#196046 - $15.00 USD Received 28 Aug 2013; revised 21 Oct 2013; accepted 21 Oct 2013; published 6 Nov 2013

37. S. Goto, K. Takeshita, Y. Suzuki, H. Ohashi, Y. Asano, H. Kimura, T. Matsushita, N. Yagi, M. Isshiki, H. Yamazaki, Y. Yoneda, K. Umetani, and T. Ishikawa, "Construction and commissioning of a 215-m-long beamline at SPring-8," Nucl. Instrum. Methods Phys. Res., Sect. A **467–468**, 682–685 (2001).
38. M. J. Kitchen, A. Habib, A. Fouras, S. Dubsky, R. A. Lewis, M. J. Wallace, and S. B. Hooper, "A new design for high stability pressure-controlled ventilation for small animal lung imaging," J. Instrum. **5**, T02002 (2010).
39. S. B. Hooper, M. J. Kitchen, M. J. Wallace, N. Yagi, K. Uesugi, M. J. Morgan, C. Hall, K. K. W. Siu, I. M. Williams, M. Siew, S. C. Irvine, K. Pavlov, and R. A. Lewis, "Imaging lung aeration and lung liquid clearance at birth," FASEB J. **21**, 3329–3337 (2007).
40. M. S. Islam, R. A. Lewis, K. Uesugi, and M. J. Kitchen, "A high precision recipe for correcting images distorted by a tapered fiber optic," J. Instrum. **5**, P09008 (2010).
41. A. Pogany, D. Gao, and S. W. Wilkins, "Contrast and resolution in imaging with a microfocus x-ray source," Rev. Sci. Instrum. **68**, 2774–2782 (1997).
42. J. Wang, G. Wang, and M. Jiang, "Blind deblurring of spiral CT images based on ENR and wiener filter," J. x-ray sci. technol. **13**, 49–60 (2005).
43. J. Ewald and T. Wilhein, "Source size characterization of a microfocus x-ray tube used for in-line phase-contrast imaging," AIP Conf. Proc. **1365**, 81–83 (2011).
44. T. Tuohimaa, M. Otendal, and H. M. Hertz, "Phase-contrast x-ray imaging with a liquid-metal-jet-anode microfocus source," Appl. Phys. Lett. **91**, 074104 (2007).
45. A. B. Garson III, E. W. Izaguirre, S. G. Price, and M. A. Anastasio, "Characterization of speckle in lung images acquired with a benchtop in-line x-ray phase-contrast system," Phys. Med. Biol. **58**, 4237 (2013).
46. M. R. Teague, "Deterministic phase retrieval: a green's function solution," J. Opt. Soc. Am. **73**, 1434–1441 (1983).
47. L. Turner, B. Dhal, J. Hayes, A. Mancuso, K. Nugent, D. Paterson, R. Scholten, C. Tran, and A. Peele, "X-ray phase imaging: Demonstration of extended conditions for homogeneous objects," Opt. Express **12**, 2960–2965 (2004).
48. J. H. Talbot, "Fraunhofer diffraction pattern of a random distribution of identical apertures in a plane screen," Proc. Phys. Soc. **89**, 1043–1053 (1966).
49. D. Paganin, *Coherent X-ray Optics* (Oxford University, 2006).

1. Introduction

X-ray imaging is commonly used to reveal the internal structure of the chest, differentiating materials such as soft tissue and bone by their densities. Lung diseases in their early stages, such as emphysema, cystic fibrosis and cancer are difficult to detect in a conventional x-ray image [1]. Since early diagnosis of lung disease is a critical factor for patient prognosis, improved diagnostic methods during the early stages underpins advances in the treatment of these diseases [1]. Lung functional x-ray imaging is more sensitive for detecting lung diseases than anatomical imaging, making it a prospective complementary diagnostic tool to x-ray imaging [2].

Pulmonary functional tests, such as the forced oscillation and spirometry techniques, are performed in clinical diagnostics of respiratory diseases together with x-ray imaging [3–5]. However, these tests give limited information on the location and extent of the abnormality. The need to detect regional lung pathology has produced many different tomographic-based volumetric techniques [6–8]. Some of these techniques have been combined with k-edge subtraction to help resolve small airways [9, 10]. However, they require inhalation of a contrast agent to assess regional lung ventilation except when using computed tomography (CT). Yet, CT imparts a relatively large dose of radiation particularly when several three-dimensional (3D) images need to be reconstructed from many projections in order to measure regional lung air volume (V_L) over time. The length of time involved in recording the projected images to reconstruct a three-dimensional (3D) image of the chest reduces temporal resolution significantly and so, to minimize motion blurring, breath holds or gated imaging is required. Although CT and magnetic resonance imaging (MRI) techniques can acquire and reconstruct images in real-time on the order of milliseconds, the spatial resolution achievable is only of the order of millimeters, which is insufficient to resolve the minor airway structures [11, 12].

Regional volumetric analysis techniques using two-dimensional (2D) phase contrast x-ray (PCX) imaging from a synchrotron x-ray source have emerged to offer superior temporal res-

#196046 - $15.00 USD Received 28 Aug 2013; revised 21 Oct 2013; accepted 21 Oct 2013; published 6 Nov 2013

olution over those that use tomography [13–15]. PCX is a class of imaging modalities that produce phase-induced intensity variations between the boundary of materials exhibiting different complex refractive indices. With a sufficiently spatially coherent x-ray source they provide high contrast images of soft tissues. When employed to image the chest, the boundaries of the conducting airways and alveoli are rendered highly visible (see Fig. 6). Thus, performing volumetric analysis on 2D PCX images simultaneously provides a detailed image of the chest and information on regional lung aeration with high spatial and temporal resolution. One major benefit of this is allowing mechanical ventilators to be adjusted in real time and on a breath-by-breath basis to avoid lung injury [16–18].

Kitchen *et al.* [13] developed a technique to measure changes in V_L from 2D propagation-based phase contrast x-ray (PBX) images using a single image phase retrieval algorithm (SIPRA) [19]. PBX imaging is the simplest of the PCX modalities as only a partially coherent source and a sufficiently large object-to-detector propagation distance (ODD) is required [20]. In that technique the animal is immersed upright in water and it is assumed that only the volume of air/water changes within the field of view of the detector. This is an accurate assumption for measuring the total change in V_L as the volume of all other materials, namely bone, can be made to remain constant by choosing a sufficiently large region of interest (ROI) to encompass the entire chest. Reducing the size of the ROI to measure regional changes in V_L can result in bone moving inside and outside the ROI leading to incorrect measures of V_L. Thus, that technique was shown to accurately measure changes in V_L over areas as small as one quarter of the lung, where the change in volume of air was not significantly affected by relative displacement of bones. Leong *et al.* [15] improved on this by removing the bone using a temporal subtraction-based algorithm to measure V_L on a pixel-by-pixel basis of micron-scale spatial resolution. That technique, however, is prone to misregistrations when the differential motion of the chest becomes overly complex at large V_L. Regional V_L has also been measured from analyzer-based phase contrast x-ray images [14]. A Laue crystal was used to split the x-ray beam to produce two complementary images that were used to create separate images of bone and soft tissue, thus enabling regional V_L measurement. That technique does not require anatomical registration, but it is experimentally more challenging and also requires the chest to be immersed in water for V_L extraction [14].

The planar imaging-type volumetric techniques described above work only when the chest is upright and enclosed in water. Moreover, these techniques are limited to measuring changes in V_L unless an image of a non-aerated lung is available, which is not always easily attainable. This restricts the type of studies that can be performed, for example, it would not be possible to analyze V_L if the animal was ventilated in a supine/prone position or determining its functional residual capacity (FRC; the volume of air at end-expiration). The attenuating medium also reduces the signal-to-noise ratio (SNR). Whilst SNR can be improved by increasing the intensity of the x-ray source, a concomitant increase in radiation dose ensues. In this study, we developed a novel approach for measuring regional V_L of PBX chest images without needing to immerse the object in a water bath. This technique relates the power spectra of lung speckle patterns directly to V_L.

1.1. Lung speckle

Spatially random samples such as particles suspended in liquid and optically rough surfaces of textured materials produce rapid complex refractive index fluctuations [21–26]. The phase of an incident wavefield is randomly altered as it traverses through or reflects off such an object [22]. Downstream of the exit surface of the object, the intensity of the randomized wavefield exhibits bright and dark spots, known as speckles, formed by constructive and destructive interferences, respectively. This is the most likely explanation, for the origin of lung speckle observed using

#196046 - $15.00 USD Received 28 Aug 2013; revised 21 Oct 2013; accepted 21 Oct 2013; published 6 Nov 2013

PBX imaging, as the lung contains many air-filled alveoli that are pseudo-randomly distributed and enclosed by thin regions of tissue.

Yagi *et al.* [27] were one of the first to encounter lung speckle, which was observed using PBX imaging, in a mouse model. They hypothesized that speckles formed as a consequence of alveoli present in the lungs. Kitchen *et al.* [28] investigated the origin of these speckles by simulating projected PBX images of lung tissue. Here they modeled the alveoli as spheres and generated synthetic PBX images of a lung by numerically propagating the wavefield at the contact plane to the detector surface using the angular spectrum formalism of scalar wave optics. Speckles similar to those seen in PBX chest images of a rabbit pup were observed, and it was shown that this was because the alveoli acted locally as aberrated compound refractive lenses.

Speckle possesses statistical properties that depend on that of the scattering object. The space intensity correlation function, or in Fourier space the power spectrum, is a second order statistical measure that has been used in studying spatially random objects from their speckle pattern; for our study it is the alveoli [22, 23, 29]. Approximately 90% of the total V_L can be accounted for in the alveoli [30]; the remainder is the volume of the airways of the lungs (this includes the trachea, bronchi and bronchioles). Thus, measuring the volume of air in the alveoli is a good approximation of V_L. Herein, we develop a mathematical model to show how lung speckle is related to V_L. In our study, lung speckle is quantified by the integral of its power spectrum between certain radial spatial frequencies, as explained in section 1.2.

1.2. Theory

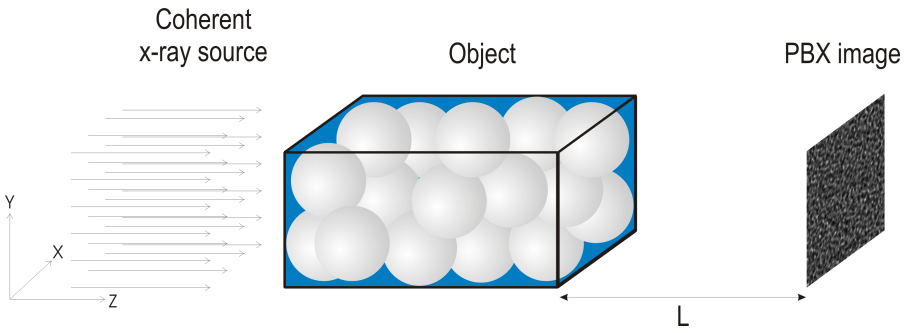

Fig. 1. Alveoli in lung tissue, modeled by voids randomly embedded within an absorbing medium, is illuminated by a coherent x-ray source and a PBX image is recorded a distance L from the exit surface of the object.

Consider a lung being made of non-overlapping air-filled voids, where the projected thickness of each void with radius R is described by the object function $G(x,y) = 2\sqrt{R-x^2-y^2}$, embedded randomly in soft tissue (or equivalently in water), as shown in Fig. 1. We assume that the x-rays follow a straight path from the x-ray source to the exit surface of the object. This is known as the projection approximation and it is used to fully describe the phase and intensity changes of the x-ray wave traversing the lung at the exit surface [19]. Using Monte Carlo simulations, Kitchen *et al.* [28] showed that for the lungs of a mouse the projection approximation was valid at diagnostic x-ray energies (i.e. $>$6 keV). In the near-field regime, the altered x-ray wave produces a speckled PBX image ($I(x,y,z=L)$) whose power spectrum can be described as (see Appendix A):

#196046 - $15.00 USD Received 28 Aug 2013; revised 21 Oct 2013; accepted 21 Oct 2013; published 6 Nov 2013

$$\left|\mathbf{F}\left\{\frac{I(x,y,z=L)}{I(x,y,z=0)}-1\right\}\right|^2 = L^2\delta_T^2 k_\perp^4 N\left|\mathbf{F}\left\{G(x,y)\right\}\right|^2, \tag{1}$$

where $I(x,y,z=0)$ is the absorption contrast image, $T(x,y)$ is the projected thickness of the object function, δ_T is the refractive index decrement of lung tissue, L is the ODD, $k_\perp = \sqrt{k_x^2+k_y^2}$ is the transverse wavenumber in the (x,y) plane, N is the number of voids, and $\mathbf{F}$ is the Fourier transform with respect to x and y. $I(x,y,z=0)$ was recovered using SIPRA [19]:

$$I(x,y,z=0) = \mathbf{F}^{-1}\left\{\frac{\mathbf{F}\left[I(x,y,z=L)\right]}{1+(\frac{\delta_T L}{\mu_T})k_\perp^2}\right\}, \tag{2}$$

where $\mathbf{F}^{-1}$ is the inverse Fourier transform with respect to x and y, and μ_T is the absorption coefficient of lung tissue. μ_T and δ_T were set to 54.7 m^{-1} and 3.99×10^{-7}(24 keV), respectively. The former was calculated using the National Institute of Standards and Technology database (NIST) [31] and the latter was calculated using [32]:

$$\delta = \frac{r_e\lambda^2}{2\pi}\sum_i n_i(f_1)_i, \tag{3}$$

where r_e is the classical electron radius, n_i is the concentration of type i atoms per unit volume and f_1 is the real part of the atomic scattering factor in the forward direction provided by NIST [31].

The definition of what is considered near-field depends on multiple factors. These can be succinctly summarized by the Fresnel number (N_F) [33]:

$$N_F = \frac{a}{L\lambda\left|\nabla_\perp\varphi\right|_{max}}, \tag{4}$$

where a is a characteristic length scale of the object over which the intensity changes appreciably and $|\nabla_\perp\varphi|_{max}$ is the maximum phase gradient transverse to the direction of propagation. The near-field regime is defined to be at $L_{max} < \frac{a}{\lambda|\nabla_\perp\varphi|_{max}}$.

The alveoli were modeled as spheres with radius R. To determine the 2D power spectrum of its PBX image, the following integral was solved:

$$\left|\mathbf{F}\left\{\tilde{G}(x,y,z)\right\}\right|^2 = \left|\int \tilde{G}(x,y,z)\exp(2\pi i\mathbf{k}\cdot\mathbf{r})d\mathbf{r}\right|^2, \tag{5}$$

where $\mathbf{k}=(k_x,k_y,k_z)$ and $\mathbf{r}=(x,y,z)$ are 3D vectors in Fourier and real space, respectively. The shape function $\tilde{G}(x,y,z)=1$ for $R\leq 1$ and $\tilde{G}(x,y,z)=0$ elsewhere. The evaluation of Eq. (5) is simplified by the radial symmetry of $\tilde{G}(x,y,z)$, which effectively reduces it to a one-dimensional problem. The integral in Eq. (5) can then be expressed analytically by first expanding then evaluating the exponential term as a Taylor series to give an exact solution [34]:

$$\left|\mathbf{F}\left\{G(x,y,z)\right\}\right|^2 = \left|V\frac{3}{(kR)^2}\left[\frac{\sin(kR)}{kR}-\cos(kR)\right]\right|^2, \tag{6}$$

where $k=|\mathbf{k}|=\sqrt{k_x^2+k_y^2+k_z^2}$ and $V=\frac{4\pi R^3}{3}$ is the volume of a sphere.

According to the Fourier slice theorem, the 2D power spectrum of a projected sphere is a slice of its 3D power spectrum through the origin. Since the 3D power spectrum is radially

#196046 - $15.00 USD Received 28 Aug 2013; revised 21 Oct 2013; accepted 21 Oct 2013; published 6 Nov 2013

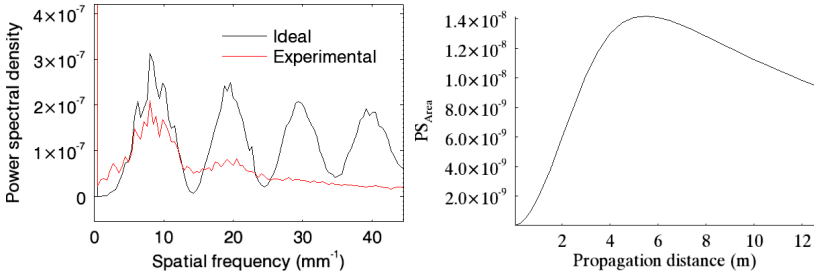

(a) (b)

Fig. 2. Lung speckle simulations. (a) Azimuthally averaged power spectra of a random distribution of 45 µm air-filled voids simulated within a 10 mm thick water-filled container with a volume packing density of 54%. Under ideal conditions (black), the power spectrum is a damped oscillatory function. To mimic our experimental conditions, ODD was increased from 0.1 m to 2 m, the PBX image was convolved with a Gaussian function, with FWHM=20 um, to simulate the PSF of a detector, and white noise was added, with a standard deviation (σ_{noise}) of 0.1 intensity. This yielded an image with $SNR \approx 10$, which was determined from taking the ratio of the mean intensity of the image and σ_{noise}. This results in only one prominent peak in the power spectrum (red). (b) A plot displaying the PS_{Area} of the same sample, but with mean void size of 130 µm, against ODD. (for details on the simulation of lung speckles, see section 2.1)

symmetric, the equation of the 2D power spectrum is identical to Eq. (6) but the z-coordinate is dropped and k is redefined as $k_\perp = \sqrt{k_x^2 + k_y^2}$.

The 2D version of Eq. (6) is combined with Eq. (1) to give:

$$\left| \mathbf{F}\left\{ \frac{I(x,y,z=L)}{I(x,y,z=0)} - 1 \right\} \right|^2 = L^2 \delta_w^2 k_\perp^4 N \left| \frac{4\pi R^3}{(k_\perp R)^2} \left[\frac{\sin(k_\perp R)}{k_\perp R} - \cos(k_\perp R) \right] \right|^2 . \tag{7}$$

Equation (7) assumes there is only one alveolus size whereas a realistic lung model would have a distribution of sizes typically with a coefficient of variation as large as 0.6; however, the error introduced in assuming an average alveolus size is small ($< 5\%$) [35]. To determine the area under the power spectrum (PS_{Area}), Eq. (7) is integrated over a select domain of radial frequencies, $k_{\perp 0} \leq |k_\perp| \leq k_{\perp N}$, then $\xi = k_\perp R$ is substituted to give:

$$PS_{Area} = 16\pi^2 L^2 \delta_w^2 NR \int_{\xi_0/R}^{\xi_N/R} \left| \left[\frac{\sin(\xi)}{\xi} - \cos(\xi) \right] \right|^2 d\xi . \tag{8}$$

The limits of the integral in Eq. (8) are dependent on R. However, under experimental conditions, the higher order peaks of the oscillatory function in the integral are suppressed by the detector point spread function (PSF) and penumbral blurring. Consequently, PS_{Area} is dominated by the lowest order peak (see Fig. 2(a)). This means the limits can be fixed, and be independent of R, so long as it includes the first peak. The area under the first peak bounded by the minimas $\xi = 0$ and $\xi = 4.493$ (these are the first two solutions to $(\frac{\sin(\xi)}{\xi} - \cos(\xi) = 0)$ is 2.141. Hence, the integral is approximately 2.141, and Eq. (8) can be simplified to:

$$PS_{Area} = 34\pi^2 L^2 \delta_w^2 NR. \tag{9}$$

There are additional factors that we have not entirely accounted for in deriving Eq. (9): penumbral blurring, detector PSF and asymmetrically shaped alveoli. If the imaging setup re-

#196046 - $15.00 USD Received 28 Aug 2013; revised 21 Oct 2013; accepted 21 Oct 2013; published 6 Nov 2013

mains unchanged between recordings over time then the power spectra are equally affected by penumbral blurring and the detector PSF. While alveoli are not perfectly spherical, but resemble more like polyhedra, they are randomly positioned and oriented. Consequently, the derivations above is still valid and the only aspect altered is the solution for Eq. (8). The alveoli were modelled as spheres because a simple analytic solution for Eq. (8) exists. Unless these factors are accounted for, Eq. (9) cannot be directly used to measure V_L. Instead, PS_{Area} can be calibrated against known V_L values as described in section 2.3. As well as accounting for the factors listed above, the calibration curve would also account for the alveoli changing shape during respiration.

The relationship between V_L and PS_{Area} will depend on how N and R vary over time (t). That is, if N and R were parameterized to $N \propto t^n$ and $R \propto t^r$, respectively, where n and r are constants, then,

$$V_L \propto PS_{Area}^{\frac{n+3r}{n+r}} \tag{10}$$

Having presented the theoretical background of near-field lung speckle and how it relates to V_L in this section, we test this model by simulating lung tissue in section 2 and present the results and analysis in section 3. Also in section 3, we evaluate how accurately our model can measure changes in V_L in a rabbit pup model. Some directions for future work are provided in section 4 and we conclude with section 5.

2. Methodology

2.1. Simulated lung tissue

To directly validate our theory, simulations were performed with conditions set similarly to that of imaging real lung tissue. The conditions for our simulations are summarized in Table 1. 11.8 mm $\times$ 11.8 mm projected lung thickness images, with pixel size 0.59 μm, were simulated for two different sets of samples. The pixel size was chosen to adequately sample the phase map of the exit surface and propagated wavefield (that is, the maximum wavefield phase gradient is less than $\frac{\pi}{2}$ radians per pixel). In the first set of samples, spherical voids of mean radius 65 μm were randomly suspended in a rectangular water-filled volume of thickness 1 mm. Several non-identical 1 mm thick samples were generated and stacked to achieve different sample thicknesses. This was to simulate lung tissue with varying N while R was fixed. In the second set of samples, for each of the different mean sized voids, 5900 voids were suspended in a rectangular water-filled volume of thickness 10 mm. In contrast to the first set, this was to simulate lung tissue with varying R while N was fixed. A maximum volume packing fraction of 75% was achieved from the largest mean size void (70 μm).

In both sample sets, the position of each void was created using the Box-Muller method to generate random coordinates [36]. If the void's volume space intersected with that of a void already in the volume then a new coordinate would be generated until an unoccupied location was found. The samples were summed along the axis of propagation to produce the projected thickness images. Despite choosing a small pixel size, $|\nabla_\perp \varphi|_{max}$ was greater than $\frac{\pi}{2}$ radians per pixel in some parts of the images. The images were therefore filtered with a Gaussian kernel, which at a Full-Width Half-Maximum (FWHM) of 16 μm, was sufficient to reduce $|\nabla_\perp \varphi|_{max}$ to less than $\frac{\pi}{2}$ radians per pixel. Using the projection approximation, the wavefunction at the exit surface of the sample was calculated from the projected thickness image, and forward propagated using the angular spectrum method [19]. Penumbral blurring was effected by convolving the PBX sample images with a Gaussian PSF of FWHM = DR_2/R_1 (where D is the x-ray source size). D was set to 150 μm $\times$10 μm, which was the x-ray source size of the beamline used. The detector PSF was accounted for by increasing the FWHM of the Gaussian PSF by 20 μm. PS_{Area}

#196046 - $15.00 USD Received 28 Aug 2013; revised 21 Oct 2013; accepted 21 Oct 2013; published 6 Nov 2013

was calculated by integrating their power spectrums from $k_o = 0.85$ (since the zero frequency is a Dirac delta function this value is the next closest to the zero frequency) to k_N =Nyquist frequency.

Table 1. Parameters used for simulating PBX images of lung tissue.

Pixel size (μm)	0.59
Mean alveolar radius (μm)	30, 35, 40, 45, 50, 55, 60, 65, 70
Alveolar radius standard deviation (μm)	$\frac{3}{4}\times$alveolar diameter
Source-to-detector distance (m; R_1)	∞
Sample-to-detector distances (m; R_2)	3
Attenuation coefficient (μ_w [31])	54.735 m^{-1} (at 24 keV)
Refractive index decrement (δ_w [31])	3.99 (at 24 keV)
Maximum volume packing fraction	75%
Lung thickness (mm)	10

2.2. Rabbit pup lungs

All imaging experiments took place in Hutch 3 of beamline 20B2 at the SPring-8 synchrotron in Japan [37] with a Si (111) double-bounce monochromator tuned to 24 keV. The x-ray source-to-sample distance was set at 210 m. All animal procedures were conducted in accordance with the protocol approved by the Monash University Animal Ethics Committee and the SPring-8 Animal Care and Use Committee. At 31 days of gestation, pregnant New Zealand white rabbits were anesthetized initially by an intravenous injection (Rapinovet [Schering-Plough Animal Health, USA]; 12 mg kg^{-1} bolus, 40 mg h^{-1} infusion) and anesthesia was maintained via isoflurane inhalation (1.5– 4%; Isoflurane, Delvet Pty. Ltd., Australia). Pups were delivered by caesarean section, sedated and surgically intubated. Pups in the first group (Group-Water, n = 15) were immersed in a water-filled cylindrical poly-methyl methacrylate container (plethysmograph) with their head out and the chamber sealed with a rubber diaphragm enclosing their necks. The plethysmograph is routinely used for V_L measurement. At birth, the lungs of the newborn are completely liquid-filled and so imaging the lungs in their fluid-filled state was performed as soon as possible after the pup's delivery. Two different detectors were used to acquire PBX images: (i) a large format (4000×2672 pixels) Hamamatsu CCD camera (C9300-124F21) with a tapered fiber optic (FOP) coupling the sensor to a 20 μm thick gadolinium oxysulfide ($Gd_2O_2S:Tb^+;P43$) phosphor, and (ii) a tandem lens-coupled scientific-CMOS imaging sensor coupled to a 50 μm thick gadolinium oxysulfide ($Gd_2O_2S:Tb^+;P43$) phosphor (pco.edge; 2560×2160 pixels). The effective pixel sizes were for these two detectors 16.2 μm, based on the taper ratio of 1.8:1, and 15.23 μm, respectively. Imaging sequences were respiratory gated, with timing controlled by a custom-designed pressure-controlled ventilator [38] at a frame rate of 3 Hz, with a respiratory cycle of 2.5 s and exposure time of 40 ms. All animals were humanely killed at the end of each experiment via anesthetic overdose of Nembutal (Abbott Laboratories, USA, 100 mg/kg).

Pups in the second group (Group-Air, n=3) were initially used for studying the effect of different mechanical ventilation strategies on lung aeration and humanely killed via anesthetic overdose at the end of experiment. The deceased pups were supported in an upright position and connected to a pneumotach (flowmeter) to measure differential airflow at the mouth opening throughout each respiratory cycle. The pups were imaged in air under identical conditions to the first group imaged in water but at a frame rate of 10 Hz, using only the sCMOS camera.

The optimal ODD to image the pups was determined by modeling a 10 mm thick container packed with 130 μm sized voids. The size of the void and container thickness corresponds

#196046 - $15.00 USD Received 28 Aug 2013; revised 21 Oct 2013; accepted 21 Oct 2013; published 6 Nov 2013

closely to that of an alveolus [39] and a rabbit pup's lung, measured from a lateral PBX image of the chest, respectively. Using the steps and conditions as described in section 2.1, several PBX images were simulated from the model at different ODD. Figure 2(b) shows, based on Eq. (9), the near-field regime extends up to $\sim$3 m but not beyond 5 m. L_{max} was computed to be 2.7 m. This is consistent with Fig. 2(b). PBX images of pups were therefore recorded at a propagation distance 3 m. While choosing propagation distances much less than 2.7 m would ensure the TIE approximation was well satisfied, the contrast-to-noise ratio of lung speckles would be small and weaken the correlation between V_L and PS_{Area}.

2.3. Image processing and analysis

Immediately before imaging each pup, multiple dark field (no x-rays) and flat field (x-rays; no sample) images were recorded then averaged to correct for the detector dark current and to normalize against the incident beam intensity, respectively. Nonlinear spatial distortions arising from the FOP camera, as a result of imperfect alignment of the fiber bundles at each end of the taper, were corrected by the use of Delaunay triangulation with bilinear interpolation [40].

Pups from Group-Water were used to generate a $PS_{Area} - V_L$ calibration curve. Each PBX chest image was divided into quadrants. Quadrants were created by partitioning the chest along the spinal column to separate the left and right lungs and the seventh rib down from the neck to separate the apical and basal lobes. This increased the number of points and also helped determine whether variability in the lung thickness between quadrants affected the calibration curve. PS_{Area} was calculated using the LHS of Eq. (1) and integrated from $k_o = 2\,\mathrm{mm}^{-1}$ to k_N =Nyquist frequency. Given our experimental conditions we found this k_o value optimized the correlation strength of the $PS_{Area} - V_L$ curves between pups and quadrants. This is supported by Figs. 6(c) and 6(d), which shows low frequency components at up to $2\,\mathrm{mm}^{-1}$ are notably contaminated by remnant low frequency trends arising predominately from the bones. The technique developed by Kitchen *et al.* [13] was used to calculate V_L for pups from Group-Water. For those from Group-Air a flowmeter (pneumotach), measuring the rate of air flowing in and out of the lungs, was employed to validate our technique. Both PS_{Area} and V_L were normalized against the number of pixels so that PS_{Area} measured from a ROI of any size can be directly converted to V_L.

3. Results & analysis

3.1. Validation of theory using simulated lung tissue

Before validating our theory, simulated lung speckles were qualitatively compared with real lung speckles in real and reciprocal space. The intensity contrast of real speckles in Fig. 3(a) is lower than that of simulated speckles in Fig. 3(b). This is reflected in their azimuthally averaged power spectra, where for real lungs (see Fig. 3(c)) the peak is broader and weaker than that of simulated lungs (see Fig. 3(d)). We believe this could be due to incoherent scattering from the alveoli and in air between the object and detector, and that in real lungs, the alveoli are closely packed rather than randomly positioned as in our simulated lung tissue.

To verify the linear relationship between N and PS_{Area}, PS_{Area} was plotted against the sample thickness of simulated lung tissue from the first sample set at 1 m and 3 m ODD (see Fig. 4(a)). The sample thickness is essentially proportional to N as the total volume fraction was made approximately constant throughout the sample. At 3 m ODD, Fig. 4(a) shows N at first varies linearly with PS_{Area} but begins to breakdown at $N = 3000$ as $|\nabla_\perp \varphi|_{max}$ increases, resulting in N_F approaching and then being less than unity. Pogany *et al.* [41] showed that phase contrast decreases beyond the near-field region, which is reflected in reduction of the rate of increase of PS_{Area} in Fig. 4(a) with respect to N. At 1 m ODD, N_F remained >1 for all sample thickness, thus PS_{Area} was proportional to N throughout. The dependance between R and PS_{Area} was

#196046 - $15.00 USD Received 28 Aug 2013; revised 21 Oct 2013; accepted 21 Oct 2013; published 6 Nov 2013

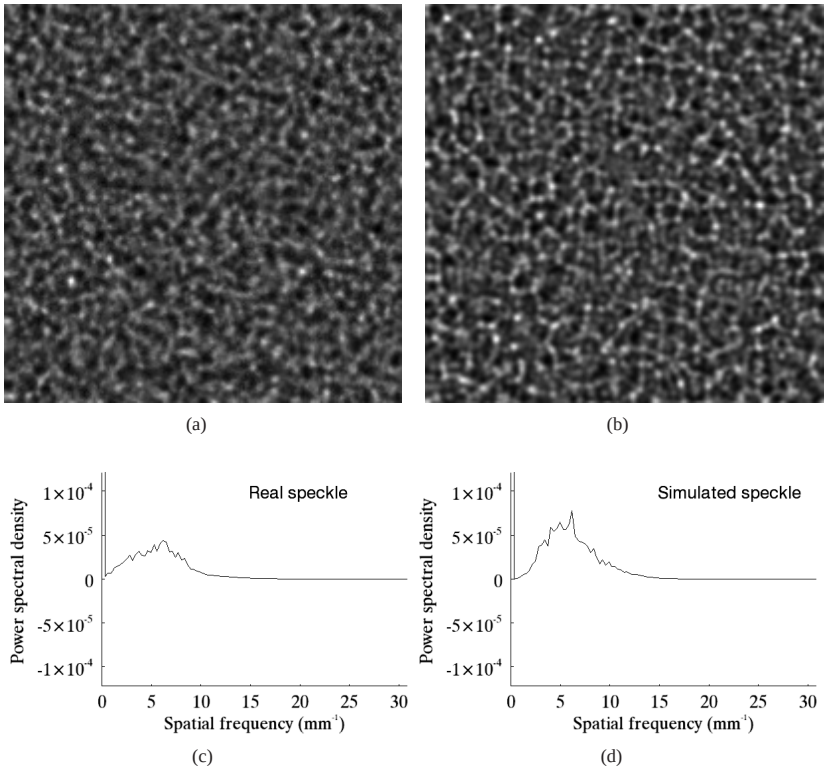

Fig. 3. 3.24 mm × 3.24 mm PBX images of a ∼10 mm thick sample (a) of real and (b) simulated (mean diameter of 130 μm) lung tissue normalized against their phase retrieved absorption image. Their corresponding power spectra are shown in (c) and (d), respectively.

investigated by plotting PS_{Area} against R of simulated lung tissue from the second sample set packed in a 10 mm thick container at 3 m ODD, as shown in Fig. 4(b). As predicted by Eq. (9), PS_{Area} varies linearly with R even at this large ODD.

3.2. Regional lung air volume measurements

A $PS_{Area} - V_L$ calibration curve was generated from the 15 newborn rabbit pups in Group-Water. Since for each pup a PBX image of its lung in a fluid-filled state was recorded, PS_{Area} was calibrated against absolute V_L. Two cameras were used that had slightly dissimilar spatial frequency responses, or modulation transfer functions (MTFs). The MTF represents the camera's ability to accurately preserve the amplitudes of each of the spatial frequencies in an image and this depends on the design of the camera. This resulted in two distinct calibration curves originating from the two cameras, which differed by a multiplicative factor of 3.35. This is likely due to the different phosphor thicknesses coupled to the two detectors. Thus, PS_{Area} calculated from using the sCMOS camera was multiplied by 3.35 to align with the calibration curve attained from the FOP camera. While this highlights the need to produce a calibration curve for each of the detectors, a calibration curve would also be needed for other different

#196046 - $15.00 USD Received 28 Aug 2013; revised 21 Oct 2013; accepted 21 Oct 2013; published 6 Nov 2013

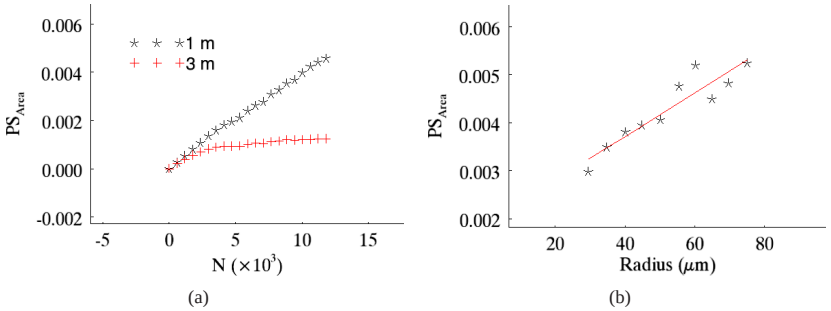

Fig. 4. Plots of PS_{Area} of simulated lung tissue versus (a) number of voids, of size 130 μm (at 1 m and 3 m ODD), and (b) radius of voids with a maximum volume packing density of 75% (at 3 m), all at energy 24 keV.

experimental configurations. This includes different types of animals due to variability in lung morphology and imaging setups since the power spectrum of the speckle produced would be affected by factors such as beam characteristics. A direct plot of V_L against PS_{Area} showed a non-linear relationship. It was found that raising V_L to the power $\frac{3}{4}$ best linearized the curve based on the chi-square goodness-of-fit test.

Figure 5(a) shows the linearized $PS_{Area} - V_L$ calibration curve. A weighted linear trend ($V_L^{3/4} = a \times PS_{Area} + b$) was fitted with coefficients $a = (1.345 \pm 0.001) \times 10^{-4}$ and $b = (-6.84 \pm 0.02) \times 10^{-7}$. The uncertainty in $V_L^{3/4}$ was determined by measuring the standard deviation (σ) of the volume change over time of a water-only ROI against the ROI size ($N \times M$ pixel). A rational exponent function was fitted to give $\sigma = 3.5 \times 10^{-7} \times [N \times M]^{3/4} + 3.7 \times 10^{-6}$ (see [15, section IIE]). The same ROIs were used to measure σ of PS_{Area} to determine its uncertainty. A $PS_{Area} - V_L$ curve from the quadrants from one of the pups used for Fig. 5(a) is plotted in Fig. 5(b). This shows the $PS_{Area} - V_L$ curve from the quadrants diverge from each other at large V_L. This divergence was observed in other pups at different V_L that depended on their total lung capacity. However, this degree of divergence is comparable to that of the points in Fig. 5(a).

The phase gradient across the interface between water and tissue is considerably smaller than between air and tissue. When the PBX chest images of rabbit pups were divided by their absorption images to remove the absorption-induced intensity trends, the boundary of the skin was enhanced for pups imaged in air (see Fig. 6(a)) compared to those imaged in water (see Fig. 6(b)). Consequently, the azimuthally averaged power spectra of pups imaged in air showed a larger amplitude between frequencies 0 mm^{-1} and 2 mm^{-1} compared to that of pups imaged in water (see Fig. 6(c)). Beyond the frequency 2 mm^{-1}, the shape of the power spectra were of similar magnitude, which was the range PS_{Area} is calculated in. Thus, the calibration curve in Fig. 5(a) generated from pups imaged in water was used to measure the total change in V_L of 3 pups imaged in air and then compared with the volume measured using a flowmeter (see Fig. 7(a)). A straight line was fitted to Fig. 7(a) with a gradient of 1.06 ±0.06 (R^2= 0.978). This shows the calibration curve to be a highly accurate tool for determining the total change in V_L without needing to immerse the animal in water. This gives us confidence for retrieving accurate regional volumetric information.

A quadrant-based analysis of a single pup imaged in air (see Fig. 7(b)) reveals non-uniform lung aeration. Figure 6(a) shows how the quadrants were delineated. As expected, the volumetric curves of each quadrant oscillates in phase with the mechanical ventilator. However, there

#196046 - $15.00 USD Received 28 Aug 2013; revised 21 Oct 2013; accepted 21 Oct 2013; published 6 Nov 2013

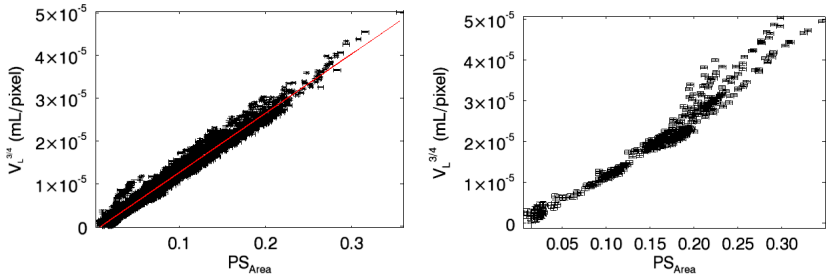

Fig. 5. (a) A calibration curve between V_L and the PS_{area} from PBX chest images divided into quadrants consisting of (a) a subset of points ($\sim$ 10%) from multiple pups and (b) a single pup. A weighted linear fit was performed on (a) and is shown as a red line.

are subtle but important physiological differences between quadrants. The upper left quadrant shows a lack of increase in tidal volume (i.e. volume of air entering the lungs) despite the increasing volume of air supplied by the ventilator, while the upper right quadrant is the only quadrant showing a significant increase in FRC. This quantification of non-uniform aeration using regional analysis is critical for assessing the efficacy of resuscitation strategies for newborn infants.

Next we demonstrate the ability of our technique to build a pixel-by-pixel map of V_L using 128 x 128 pixel sized ROIs to measure the volume from the speckle pattern. The calibration curve was used to convert PS_{Area} measured from the speckle pattern into V_L in each ROI. This was performed on pairs of images where each pair was a PBX chest image of a pup recorded at end-inspiration and at end-expiration. A volumetric map was constructed for each image of each pair and the difference was taken between them to give the tidal volume at each pixel. At a low tidal volume, Fig. 8(a) shows lung aeration to be highly localized where the greatest change in V_L is at the bifurcation of the left/right main bronchi into tertiary bronchi. As the tidal volume increased (see Figs. 8(b) and 8(c)), the flow of air became more apparent at the peripheral regions where lung expansion occurred. Summation of the pixels in Fig. 8 gave the total V_L (Fig. 8(a): 0.15 ml, Fig. 8(b): 0.27 ml, Fig. 8(c): 0.37 ml), which agreed closely with that from calculating PS_{Area} of the total lung (Fig. 8(a): 0.12 ml, Fig. 8(b): 0.24 ml, Fig. 8(c): 0.36 ml). These values respectively correspond to a percentage difference of 4.6%, 2.7% and 1.3%. This was predominantly attributed to having a discrete frequency domain. Since different sized ROI sample the frequency domain differently, a small error is introduced into V_L. Accuracy can be improved by interpolating the discrete spatial frequencies.

4. Discussion

The technique outlined here presents a novel approach to measuring absolute lung air volume (V_L) regionally from PBX chest images without requiring the use of a contrast agent. Imaging modalities such as positron emission tomography or MRI require a medium to be injected inside the lungs with which to measure V_L while water acts as a contrast agent for techniques that use PCX modalities. Here, no such contrast agent was required as speckle is an inherent feature of PBX images of the lung that was related to the properties of the airway morphology to measure V_L.

There are three limitations that we foresee in our technique: (i) motion blur, (ii) the multi-valued relationship between PS_{Area} and V_L, and (iii) the minimum size of the region from which

#196046 - $15.00 USD Received 28 Aug 2013; revised 21 Oct 2013; accepted 21 Oct 2013; published 6 Nov 2013

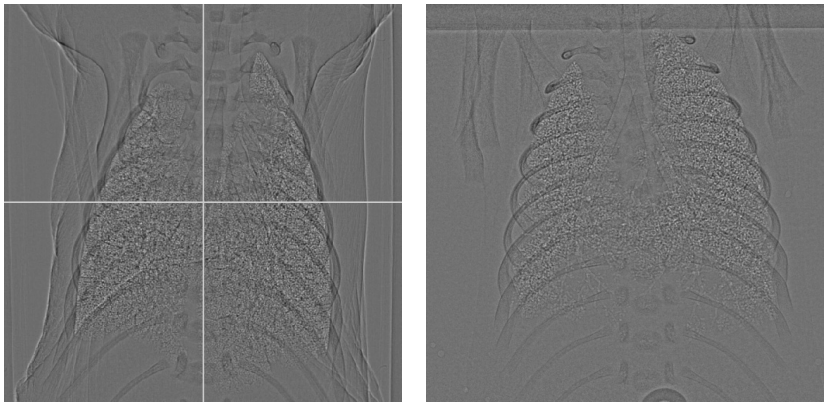

(a) (b)

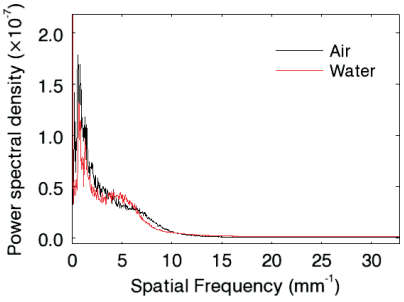

(c)

Fig. 6. A pair of 24 mm × 21 mm PCX chest images of a newborn rabbit pup in (a) a water-filled tube and in (b) air. (c) shows their respective power spectra after dividing by their absorption image reconstructed using phase retrieval.

V_L can be measured. The motion of the chest wall causes blurring in images; which results in a reduction in PS_{Area} [22]. The zero spatial frequency is however largely unchanged, which is why those techniques previously discussed that measure V_L from the intensity of pixels/voxels are unaffected by motion blur. Reducing the exposure time can reduce the degree of motion blur but this coincides with a decrease in SNR. There are techniques that could measure and correct the degree of motion blur [42]. However, respiratory-induced motion blur is non-linear and difficult to correct. Motion blur can also be avoided through patient breath holds or taking measurements towards the end of inspiration/expiration when there is minimal chest motion.

The difference in the dependance of R and N with V_L and PS_{Area} means a dynamic relationship exists between V_L and PS_{Area}. The calibration curve in Fig. 5(a) showed PS_{Area} was approximately proportional to $V_L^{3/4}$. From Eq. (10), the exponent ($\frac{4}{3}$) is close to 1, which indicates the lungs accommodated the flow of air by changing the number of alveoli. This is expected since we are imaging the lungs from an non-aerated state, hence new alveoli are being recruited as the lungs fill with air, thereby increasing N It was found, however, a $PS_{Area} - V_L$ curve of a single breath showed subtle changes in the exponent (other than $\frac{4}{3}$). This was masked in the calibration curve as it was made up of multiple single breath curves from pups mechan-

#196046 - $15.00 USD Received 28 Aug 2013; revised 21 Oct 2013; accepted 21 Oct 2013; published 6 Nov 2013

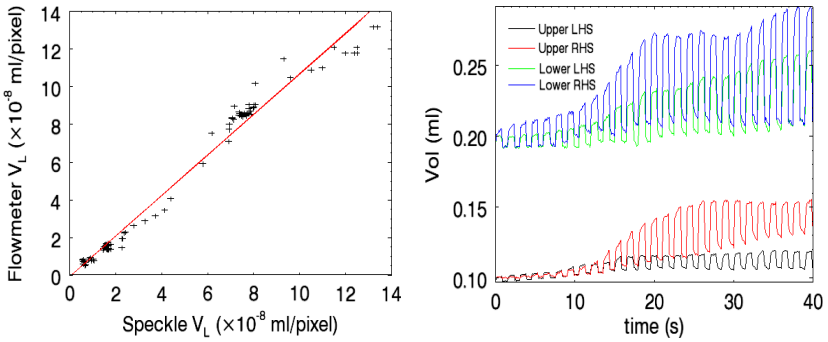

(a) (b)

Fig. 7. (a) A representation of the accuracy of using the calibration curve to measure the change in total V_L of pups imaged in air in comparison to using a flowmeter. The red line is the line of best fit. (b) Regional lung volume measurements from a lung image sequence after partitioning the images into quadrants. Note that the lower quadrant curves have been offset by 0.1 ml to better distinguish them from the upper quadrant curves.

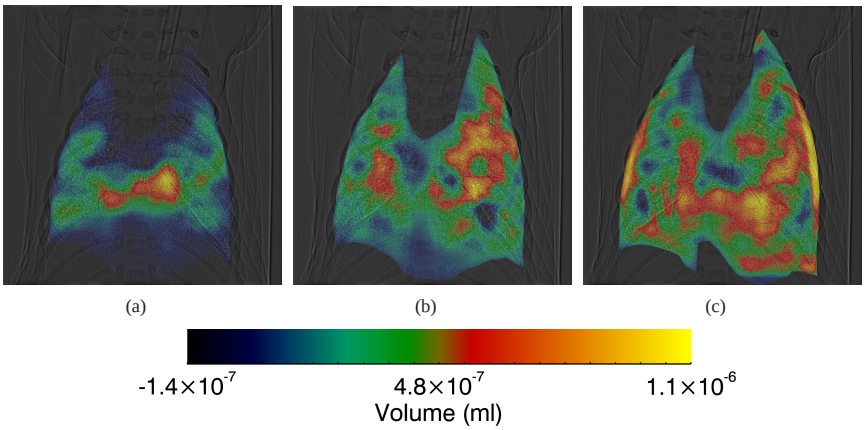

(a) (b) (c)

Fig. 8. 14.6 mm $\times$14.6 mm regional volumetric maps from a mechanically ventilated rabbit pup in air ventilated using three different tidal volumes: (a) 0.12 ml, (b) 0.24 ml and (c) 0.35 ml. Map demonstrate the distribution of air when it enters the lung.

#196046 - $15.00 USD Received 28 Aug 2013; revised 21 Oct 2013; accepted 21 Oct 2013; published 6 Nov 2013

ically ventilated with different positive inspiratory and positive end-expiratory pressures. This allowed a single calibration curve to approximate V_L. At large volumes ($\geq$10 ml/kg) however, a slight divergence in the calibration curve between quadrants appears (see Fig. 5(b)). This may either be the variable relationship between V_L and PS_{Area} or the breakdown of the TIE approximation. The average projected thickness between quadrants is different in that the apical region the lungs is thinner than that adjacent to the diaphragm. Thus, the TIE approximation may breakdown sooner for the lower quadrants at large volumes as the lungs increase in thickness.

When performing regional V_L analysis, the region must be large enough to sufficiently sample the spatial frequencies of a power spectrum. As detector technology continues to improve, we expect that detectors with larger numbers of pixels producing lower noise levels coupled with better detector spatial resolution to be available. Hence we anticipate being able to measure V_L in smaller ROIs in the future. Another major benefit of having lower noise level detectors is a reduced ODD. In our study, the ODD was set at 3 m to produce a sufficiently strong speckle contrast-to-noise ratio (CNR), but this distance was found to be at the edge of the near-field regime. To that end, PBX chest images were also recorded at 1.5 m ODD but were not included in this manuscript because V_L weakly correlated with PS_{Area} due to the weak CNR of the speckle. Thus, a lower noise level will allow PBX images to be recorded at shorter ODD while still having a short exposure time to minimize chest-induced motion blur.

Since our technique does not require the subject to be immersed in water, the much improved SNR allows significant reduction in the exposure time. The SNR of an image of a pup imaged in air was measured to be $\sim 1.4\times$ larger than a pup imaged in water. The region chosen in calculating SNR was at the thickest (central) portion of the body below the lungs. This improvement in SNR will be important for translating this research for use with lower power laboratory-based x-ray machines [43–45].

5. Conclusions

Propagation-based phase contrast x-ray (PBX) images, of lungs modeled as a random distribution of hollow spheres, were simulated. The speckle pattern observed from the PBX image was quantified by the area under its power spectrum (PS_{Area}), and was found to be dependent on the absolute lung air volume (V_L). Herein we developed a simple method for measuring V_L regionally from the speckle patterns commonly seen in PBX images of the chest. This can be a useful measure of lung disease and injury. Unlike our previous techniques of measuring V_L from two-dimensional images, the subject does not need to be immersed in water, which significantly boosts the signal-to-noise ratio of the image. This has a two-fold advantage; the exposure time can be reduced to minimize both motion blur and radiation dose. Importantly, our technique is able to perform absolute measurements of V_L in select ROI; this was previously only possible if we were able to image the lungs starting from a fluid-filled state. We successfully tested this method in measuring both the total and regional changes in V_L of several newborn rabbit pups, and validated it against other proven techniques.

Appendix A: Power spectrum of a near-field 2D intensity map of a 3D random distribution of identical voids

Consider N voids randomly embedded in an absorbing medium, as shown in Fig. 1. We assume the path of the rays within the object is unperturbed, this is known as the projection approximation, and it allows the absorption ($I(x,y,z=0)$) and phase shift ($\varphi(x,y,z=0)$) induced by the object up to its exit surface to be considered projections through, respectively, the absorption index (β) and refractive index decrement (δ) with:

#196046 - $15.00 USD Received 28 Aug 2013; revised 21 Oct 2013; accepted 21 Oct 2013; published 6 Nov 2013

$$I_A(x,y,z=0) = \exp[-2k\int \beta(x,y,z)dz] \tag{11}$$

and

$$\varphi(x,y,z=0) = -k\int \delta(x,y,z)dz. \tag{12}$$

Here, $k = 2\pi/\lambda$ is the wavenumber and λ is the wavelength of the source illuminating the object along the z direction. We assume the medium is composed of a single material of projected thickness *T(x,y)* along the *z* direction, and since any voids are non-absorbing (i.e. $\beta_{void} = \delta_{void} = 0$), Eqs. (11) and (12) reduce to:

$$I(x,y,z=0) = \exp[-2k\beta T(x,y)] \tag{13}$$

and

$$\varphi(x,y,z=0) = -k\delta T(x,y), \tag{14}$$

where $\mu = 2k\beta$ is the linear attenuation coefficient of the medium. At short distances (L) along the z direction from the exit surface of the object, the free space evolution of the intensity distribution can be described by the transport-of-intensity equation (TIE) [46]:

$$-k\frac{\partial I(x,y,z)}{\partial z} = \nabla_\perp \cdot [I(x,y,z=0)\nabla_\perp \varphi(x,y,z=0)], \tag{15}$$

where $\nabla_\perp = \hat{\mathbf{x}}\frac{\partial}{\partial x} + \hat{\mathbf{y}}\frac{\partial}{\partial y}$.

The TIE assumes paraxial wave propagation (i.e. $k \gg \sqrt{k_x^2 + k_y^2}$ where (k_x, k_y, k_z) is the x, y, z components of the wavevector k). The validity of the TIE is given by the Fresnel number when, $N_F = \frac{a}{L\lambda|\nabla_\perp\varphi|_{max}} \geq 1$ [33]. Here, a is the characteristic length scale over which the object changes appreciably and $|\nabla_\perp\varphi|_{max}$ is the maximum absolute transverse phase gradient. This form of N_F is very similar to another commonly used condition $\frac{a^2}{L\lambda} \geq 1$, but this condition does not consider $|\nabla_\perp\varphi|_{max}$. From the ray optics perspective, the degree of deflection of the rays depends on both a and $|\nabla_\perp\varphi|_{max}$. The importance of this in the context of lung imaging is that N_F can be overestimated if $|\nabla_\perp\varphi|_{max} > 1$ radians per unit length was not considered, thus unknowingly imaging outside the near-field region.

To remove any dependency on absorption in Eq. (15), we begin with a finite difference approximation on the left hand side, $\frac{dI(x,y)}{dz} \approx \frac{I(x,y,z=L)-I(x,y,z=0)}{L}$, while the the right hand side (RHS) is expanded, with Eqs. (13) and (14) substituted into Eq. (15), to give:

$$\frac{I(x,y,z=L)}{I(x,y,z=0)} - 1 = L\delta[\nabla_\perp^2 T(x,y) - \mu\,|\nabla_\perp T(x,y)|^2], \tag{16}$$

where $\nabla_\perp^2 = \frac{\partial^2}{\partial x^2} + \frac{\partial^2}{\partial y^2}$ denotes the Laplacian, respectively, in the xy plane. The second, and only, term on the RHS of Eq. (16) is dependent on μ but can be neglected if $\mu\,|\nabla_\perp T(x,y)|^2 \ll \left|\nabla_\perp^2 T(x,y)\right|$. To explicitly show when this is true, we make the substitutions $|\nabla_\perp T| \leq |\Delta T|/a$ where $|\Delta T|$ is the maximum magnitude of the difference in projected thickness across the length a, and $\left|\nabla_\perp^2 T\right| \leq |\Delta T|/a^2$. This simplifies the inequality to $\mu\Delta T(x,y) \ll 1$, that is, the object is weakly absorbing [47]. The lung tissue thickness in rabbit pups is typically on average 6 mm and at 24 keV, $\mu = 54.7\ \mathrm{m}^{-1}$ for lung tissue, thus $\mu|\Delta T(x,y)| \leq 0.328$. Consequently, the second term on the RHS of Eq. (16) can be ignored, hence the absolute square of the Fourier transform of Eq. (16) gives the power spectrum:

#196046 - $15.00 USD Received 28 Aug 2013; revised 21 Oct 2013; accepted 21 Oct 2013; published 6 Nov 2013

$$\left|\mathbf{F}\left\{\frac{I(x,y,z=L)}{I(x,y,z=0)}-1\right\}\right|^2 = L^2\delta^2 k_\perp^4 \left|\mathbf{F}\left\{T(x,y)\right\}\right|^2. \tag{17}$$

Here we have made use of the Fourier derivative theorem to replace $\nabla_\perp^2$ with $k_\perp^2 = (k_x)^2 + (k_y)^2$. Returning to our object of interest, for a random distribution of N air-filled voids, described by the object function $\tilde{G}(x,y,z)$ where $\tilde{G}(x,y,z) = 1$ for $\sqrt{x^2+y^2+z^2} \leq R$ and $\tilde{G}(x,y,z) = 0$ elsewhere, embedded in an absorbing medium ($V(x,y,z) = 1$ everywhere), the object can be expressed as a sum of convolutions:

$$\tilde{T}(x,y,z) = V(x,y,z) - \sum_{n=0}^{N} \delta(x-x_n)\delta(y-y_n)\delta(z-z_n) \otimes \tilde{G}(x,y,z), \tag{18}$$

where δ's are the unit impulse functions and (x_n,y_n,z_n) represents the random position of the nth void within the dimensions of the medium. For simplicity, the first term on the RHS of Eq. (18) will be dropped as it affects only the zero frequency in its corresponding power spectrum, which is unimportant for our analysis. Generally the random positions of the voids are unknown but the expectation value of the power spectrum of $\tilde{T}(x,y,z)$ can be evaluated without this information [48]. With equal probability of finding a void within the medium, we have for the expectation value of the power spectrum of $\tilde{T}(x,y,z)$:

$$\left\langle \left|\mathbf{F}\left\{\tilde{T}(x,y,z)\right\}\right|^2 \right\rangle = \left[N^2\hat{\delta}(0,0,0) + N\right] \left|\mathbf{F}\left\{\tilde{G}(x,y,z)\right\}\right|^2, \tag{19}$$

where $\hat{\delta}(0,0,0)$ has a value of unity at (0,0,0) and zero elsewhere (Kronecker delta). The expected value operator will be dropped for notational simplicity and the first term inside the square brackets of Eq. (19) will also be dropped as it only affects the zero frequency. It can then be seen that the power spectrum of the random distribution of voids is N times the power spectrum of a single void for $k_\perp \neq 0$. This remains valid if the voids are randomly positioned and do not overlap with neighboring voids [48].

To determine $T(x,y) = \int_z \tilde{T}(x,y,z)dz$, we make use of the Fourier slice theorem [49],

$$\left|\mathbf{F}\left\{\tilde{T}(x,y,z)\right\}\right|^2 (k_x,k_y,0) = \left|\mathbf{F}\left\{\int_z \tilde{T}(x,y,z)dz\right\}\right|^2 (k_x,k_y) = \left|\mathbf{F}\left\{T(x,y)\right\}\right|^2 (k_x,k_y), \tag{20}$$

with a similar conclusion made for $|\mathbf{F}\{G(x,y)\}|^2$. If $\tilde{G}(x,y,z)$ is azimuthally symmetric (i.e. spherical) then $G(x,y)$ is independent of the orientation of $\tilde{G}(x,y,z)$. However, if $\tilde{G}(x,y,z)$ is not azimuthally symmetric, but randomly orientated, like the alveoli, then $\left\langle \left|\mathbf{F}\left\{\tilde{T}(x,y,z)\right\}\right|^2 \right\rangle$ is approximately azimuthally symmetric with $\left|\mathbf{F}\left\{\tilde{G}(x,y,z)\right\}\right|^2$ being the azimuthal average of the power spectrum of a single void replicated azimuthally. Thus, Eq. (19) can be reduced to 2D,

$$\left|\mathbf{F}\left\{T(x,y)\right\}\right|^2 = N\left|\mathbf{F}\left\{G(x,y)\right\}\right|^2. \tag{21}$$

This shows that even though increasing the number of voids results in an increase in the amount of overlap between them seen in the projected thickness image, the power spectrum only changes by a factor. This may seem counter-intuitive as the more voids there are the shorter the characteristic length scale of the image, which would shift the peaks in the power spectra to higher frequencies. But this is untrue as long as there is no physical overlap between neighboring voids and the positions of the voids are sufficiently random.

#196046 - $15.00 USD Received 28 Aug 2013; revised 21 Oct 2013; accepted 21 Oct 2013; published 6 Nov 2013

Finally, substituting Eq. (21) into Eq. (17) we arrive at the power spectrum of the near-field intensity map of a 3-dimensional random distribution of identical voids normalized against its absorption image:

$$\left|\mathbf{F}\left\{\frac{I(x,y,z=L)}{I(x,y,z=0)}-1\right\}\right|^2 = L^2\delta^2k_\perp^4 N\left|\mathbf{F}\left\{G(x,y)\right\}\right|^2. \tag{22}$$

Acknowledgments

The authors would like to thank Kentaro Uesugi and Naoto Yagi for assistance with the experiments. AFTL acknowledges the support of an Australian Postgraduate Award. SBH and MJK acknowledge funding from the Australian Research Council (ARC; Grant Nos. DP110101941 and DP130104913). MJK is an ARC Australian Research Fellow. SBH is a NHMRC Principal Research Fellow. This research was partially funded by the Victorian Government's Operational Infrastructure Support Program. We acknowledge travel funding provided by the International Synchrotron Access Program managed by the Australian Synchrotron and funded by the Australian Government.

#196046 - $15.00 USD Received 28 Aug 2013; revised 21 Oct 2013; accepted 21 Oct 2013; published 6 Nov 2013

Appendix C

Real-time measurement of alveolar size and population using phase contrast x-ray imaging

by A. F. T. Leong, G. A. Buckley, D. M. Paganin, S. B. Hooper, M. J.Wallace, M. J. Kitchen.

Published in Biomedical Optics Express **5**, pp. 4024-4038, 2013.

Biomedical Optics EXPRESS

Real-time measurement of alveolar size and population using phase contrast x-ray imaging

Andrew F.T. Leong,[1,*] Genevieve A. Buckley,[1] David M. Paganin,[1] Stuart B. Hooper,[2] Megan J. Wallace,[2] and Marcus J. Kitchen[1]

[1] *School of Physics, Monash University, Vic 3800, Australia*
[2] *The Ritchie Centre MIMR-PHI Institute of Medical Research and the Department of Obstetrics and Gynaecology, Monash University, Vic 3168, Australia*

Abstract: Herein a propagation-based phase contrast x-ray imaging technique for measuring particle size and number is presented. This is achieved with an algorithm that utilizes the Fourier space signature of the speckle pattern associated with the images of particles. We validate this algorithm using soda-lime glass particles, demonstrating its effectiveness on random and non-randomly packed particles. This technique is then applied to characterise lung alveoli, which are difficult to measure dynamically *in vivo* with current imaging modalities due to inadequate temporal resolution and/or depth of penetration and field-of-view. We obtain an important result in that our algorithm is able to measure changes in alveolar size on the micron scale during ventilation and shows the presence of alveolar recruitment/de-recruitment in newborn rabbit kittens. This technique will be useful for ventilation management and lung diagnostic procedures.

OCIS codes: (340.7440) X-ray imaging; (110.6150) Speckle imaging; (100.5070) Phase retrieval; (170.3660) Light propagation in tissues; (170.3880) Medical and biological imaging; (290.5850) Scattering, particles.

References and links

1. M. J. Kitchen, D. Paganin, R. A. Lewis, N. Yagi, K. Uesugi, and S. T. Mudie, "On the origin of speckle in x-ray phase contrast images of lung tissue," Phys. Med. Biol. **49**(18), 4335–4348 (2004).
2. S. P. Albert, J. DiRocco, G. B. Allen, J. H. T. Bates, R. Lafollette, B. D. Kubiak, J. Fischer, S. Maroney, and G. F. Nieman, "The role of time and pressure on alveolar recruitment," J. Appl. Physiol. **106**(3), 757–765 (2009).
3. S. Meissner, L. Knels, M. Mertens, M. Wendel, A. Tabuchi, W. M. Kuebler, T. Koch, and E. Koch,J. Sloten, P. Verdonck, M. Nyssen, and J. Haueisen, eds., "Three-dimensional Imaging of subpleural Alveoli by Fourier Domain Optical Coherence Tomography," in *4th European Conference of the International Federation for Medical and Biological Engineering,* J. Sloten, P. Verdonck, M. Nyssen, and J. Haueisen, eds. (Springer Berlin Heidelberg, 2009), pp. 2035–2039.
4. E. Namati, J. Thiesse, J. de Ryk, and G. McLennan, "Alveolar dynamics during respiration: are the pores of Kohn a pathway to recruitment?" Am. J. Respir. Cell Mol. Biol. **38**(5), 572–578 (2008).
5. D. Schwenninger, H. Runck, S. Schumann, J. Haberstroh, S. Meissner, E. Koch, and J. Guttmann, "Intravital microscopy of subpleural alveoli via transthoracic endoscopy," J. Biomed. Opt. **16**(4), 046002 (2011).
6. H. Liu, H. Runck, M. Schneider, X. Tong, and C. A. Stahl, "Morphometry of subpleural alveoli may be greatly biased by local pressure changes induced by the microscopic device," Respir. Physiol. Neurobiol. **178**(2), 283–289 (2011).
7. F. Ossant, M. Lebertre, L. Pourcelot, and F. Patat, "Ultrasonic characterization of maturation of fetal lung microstructure: an animal study," Ultrasound Med. Biol. **27**(2), 157–169 (2001).
8. S. Chang, N. Kwon, B. M. Weon, J. Kim, C. K. Rhee, H. S. Choi, Y. Kohmura, M. Yamamoto, T. Ishikawa, and J. H. Je, "Tracking x-ray microscopy for alveolar dynamics in live intact mice," Sci. Rep. **3**, 1304 (2013).
9. J. Tsao, "Ultrafast imaging: principles, pitfalls, solutions, and applications," J. Magn. Reson. Imaging **32**(2), 252–266 (2010).
10. S. Dubsky, S. B. Hooper, K. K. W. Siu, and A. Fouras, "Synchrotron-based dynamic computed tomography of tissue motion for regional lung function measurement," J. R. Soc. Interface **9**(74), 2213–2224 (2012).
11. S. Fichele, N. Woodhouse, A. J. Swift, Z. Said, M. N. J. Paley, L. Kasuboski, G. H. Mills, E. J. R. van Beek, and J. M. Wild, "MRI of helium-3 gas in healthy lungs: posture related variations of alveolar size," J. Magn. Reson. Imaging **20**(2), 331–335 (2004).

#222268 - $15.00 USD Received 2 Sep 2014; revised 16 Oct 2014; accepted 18 Oct 2014; published 24 Oct 2014

12. T. J. Wellman, T. Winkler, E. L. V. Costa, G. Musch, R. S. Harris, J. G. Venegas, and M. F. V. Melo, "Measurement of regional specific lung volume change using respiratory-gated PET of inhaled 13N-nitrogen," J. Nucl. Med. **51**(4), 646–653 (2010).
13. J. T. Bushberg, J. A. Seibert, E. M. Leidholdt, and J. M. Boone, *The Essential Physics of Medical Imaging* (Wolters Kluwer Health, 2011).
14. T. E. Gureyev, S. C. Mayo, D. E. Myers, Y. Nesterets, D. M. Paganin, A. Pogany, A. W. Stevenson, and S. W. Wilkins, "Refracting Röntgen's rays: propagation-based x-ray phase contrast for biomedical imaging," J. Appl. Phys. **105**(10), 102005 (2009).
15. R. P. Carnibella, M. J. Kitchen, and A. Fouras, "Determining particle size distributions from a single projection image," Opt. Express **20**(14), 15962–15968 (2012).
16. R. P. Carnibella, M. J. Kitchen, and A. Fouras, "Decoding the structure of granular and porous materials from speckled phase contrast x-ray images," Opt. Express **21**(16), 19153–19162 (2013).
17. R. Cerbino, L. Peverini, M. A. C. Potenza, A. Robert, P. Bösecke, and M. Giglio, "X-ray-scattering information obtained from near-field speckle," Nat. Phys. **4**(3), 238–243 (2008).
18. J. D. Escolar and A. Escolar, "Lung hysteresis: a morphological view," Histol. Histopathol. **19**(1), 159–166 (2004).
19. L. Brancazio, G. N. Franz, E. L. Petsonk, and D. G. Frazer, "Lung area--volume models in relation to the recruitment--derecruitment of individual lung units," Ann. Biomed. Eng. **29**(3), 252–262 (2001).
20. S. B. Hooper, M. J. Kitchen, M. J. Wallace, N. Yagi, K. Uesugi, M. J. Morgan, C. Hall, K. K. W. Siu, I. M. Williams, M. Siew, S. C. Irvine, K. Pavlov, and R. A. Lewis, "Imaging lung aeration and lung liquid clearance at birth," FASEB J. **21**(12), 3329–3337 (2007).
21. A. F. T. Leong, D. M. Paganin, S. B. Hooper, M. L. Siew, and M. J. Kitchen, "Measurement of absolute regional lung air volumes from near-field x-ray speckles," Opt. Express **21**(23), 27905–27923 (2013).
22. T. E. Gureyev, Y. I. Nesterets, A. W. Stevenson, P. R. Miller, A. Pogany, and S. W. Wilkins, "Some simple rules for contrast, signal-to-noise and resolution in in-line x-ray phase-contrast imaging," Opt. Express **16**(5), 3223–3241 (2008).
23. H. Itoh, M. Nishino, and H. Hatabu, "Architecture of the lung: morphology and function," J. Thorac. Imaging **19**(4), 221–227 (2004).
24. P. Debye, "Zerstreuung von Röntgenstrahlen," Annalen der Physik **351**(6), 809–823 (1915).
25. S. Sykora, "K-space images of n-dimensional spheres and generalized sinc functions" (February 19, 2008, 2/19/2008), retrieved May 1, 2014, *http://www.ebyte.it/library/docs/math07/SincN.html*.
26. M. J. Kitchen, R. A. Lewis, M. J. Morgan, M. J. Wallace, M. L. Siew, K. K. W. Siu, A. Habib, A. Fouras, N. Yagi, K. Uesugi, and S. B. Hooper, "Dynamic measures of regional lung air volume using phase contrast x-ray imaging," Phys. Med. Biol. **53**(21), 6065–6077 (2008).
27. M. J. Kitchen, D. M. Paganin, K. Uesugi, B. J. Allison, R. A. Lewis, S. B. Hooper, and K. M. Pavlov, "Phase contrast image segmentation using a Laue analyser crystal," Phys. Med. Biol. **56**(3), 515–534 (2011).
28. A. F. T. Leong, A. Fouras, M. S. Islam, M. J. Wallace, S. B. Hooper, and M. J. Kitchen, "High spatiotemporal resolution measurement of regional lung air volumes from 2D phase contrast x-ray images," Med. Phys. **40**(4), 041909 (2013).
29. D. Paganin, S. C. Mayo, T. E. Gureyev, P. R. Miller, and S. W. Wilkins, "Simultaneous phase and amplitude extraction from a single defocused image of a homogeneous object," J. Microsc. **206**(1), 33–40 (2002).
30. M. J. Kitchen, A. Habib, A. Fouras, S. Dubsky, R. A. Lewis, M. J. Wallace, and S. B. Hooper, "A new design for high stability pressure-controlled ventilation for small animal lung imaging," J. Instrum. **5**(02), T02002 (2010).
31. M. M. Hall, Jnr., V. G. Veeraraghavan, H. Rubin, and P. G. Winchell, "The approximation of symmetric x-ray peaks by Pearson type VII distributions," J. Appl. Cryst. **10**(1), 66–68 (1977).
32. M. Stewart, "Signal processing," in *Handbook of Linear Algebra*, L. Hogben, ed. (CRC Press, Boca Raton, FL, 2006), pp. 10–12.
33. NIST Physical Reference Data" (US Department of Commerce, 1st May, 2014), retrieved *http://www.nist.gov/pml/data/*.
34. J. Serra, *Image Analysis and Mathematical Morphology* (Academic Press, Inc., Orlando, FL, 1983).
35. S. Goto, K. Takeshita, Y. Suzuki, H. Ohashi, Y. Asano, H. Kimura, T. Matsushita, N. Yagi, M. Isshiki, H. Yamazaki, Y. Yoneda, K. Umetani, and T. Ishikawa, "Construction and commissioning of a 215-m-long beamline at SPring-8," Nucl. Instrum. Methods Phys. Res. A **467–468**(Part 1), 682–685 (2001).
36. K. Nugent, C. Tran, and A. Roberts, "Coherence transport through imperfect x-ray optical systems," Opt. Express **11**(19), 2323–2328 (2003).
37. K. Miyomoto, "Particle number and sizes estimated from sections," in *Research of Pattern Formation*, R. Takaki, ed. (KTK Scientific Publishers, 1994), pp. 507–516.
38. L. Vincent and P. Soille, "Watersheds in digital spaces: an efficient algorithm based on immersion simulations," IEEE Trans. Pattern Anal. Mach. Intell. **13**(6), 583–598 (1991).
39. A. B. Garson 3rd, E. W. Izaguirre, S. G. Price, and M. A. Anastasio, "Characterization of speckle in lung images acquired with a benchtop in-line x-ray phase-contrast system," Phys. Med. Biol. **58**(12), 4237–4253 (2013).
40. T. E. Gureyev and S. W. Wilkins, "On x-ray phase retrieval from polychromatic images," Opt. Commun. **147**(4-6), 229–232 (1998).

#222268 - $15.00 USD Received 2 Sep 2014; revised 16 Oct 2014; accepted 18 Oct 2014; published 24 Oct 2014

1. Introduction

The lung is comprised of bifurcating hollow branches that carry air to the terminal airways (alveoli) where gas exchange takes place. Lung injury and diseases, such as ventilation-induced lung injury and emphysema, compromise the structure of the alveoli and consequently their function. Here we present a non-invasive phase contrast x-ray (PCX) imaging technique to measure the size and population of alveoli *in situ*. To do this we exploit the image texture associated with the speckle pattern that results from propagation-based phase contrast x-ray (PB-PCX) imaging of the lungs [1]. Repeating this measure over several time points during breathing provides functional information regarding the changing morphology of lung tissue. This has potential benefit for the diagnosis and treatment of lung diseases and the development of safer ventilation strategies to reduce the incidence of ventilation-induced lung injury [2].

Previous investigation of lung structure at the alveolar scale have been done using imaging techniques that include; optical coherence tomography (OPCT), confocal laser scanning microscopy (CLSM) and endoscopy microscopy [3–5]. These techniques provide highly spatially-resolved images of individual alveoli that are used to assess alveolar structure during respiration. However, they have short penetrative depth even after invasive manoeuvres to bypass the skin. Endoscopy microscopy is relatively non-invasive as it places an endoscope in the pleura visceralis. However, that was shown to alter the intrapleural pressure, which artificially changes the alveolar morphology [6]. Ultrasound measures scatterer sizes in the lungs from backscattered sound waves, but has yet to be proven to be that of alveolar sacs [7]. The deep penetrative power of synchrotron x-rays has previously enabled non-invasive imaging of the alveoli but was still restricted to less concentrated regions of alveoli that undergo minimal movement to accurately track them individually [8].

Tomographic-based imaging modalities provide insight into alveolar mechanics of the entire lung. However, the acquisition time for these modalities are long compared to the length of a single spontaneous breathing cycle, which makes dynamic imaging of the alveoli in real-time unfeasible because of motion artefacts. Although there has been progress towards improving the imaging acquisition frame rate, there is always a trade-off against poor spatial resolution and signal-to-noise ratio (SNR) to resolve the alveoli [9]. Alternatively, post-hoc respiratory gating, where projections from similar time points in the respiratory cycle are grouped together during post-processing, allows multiple reconstructions per respiratory cycle with comparable temporal resolution to x-ray imaging, but requires stable ventilation [10]. Another drawback to these modalities is the high exposure to ionizing radiation, either in the form of a radionuclide contrast agent in positron emission tomography [11, 12], or an x-ray source in x-ray computed tomography (CT) [13].

PCX imaging converts changes in the phase of an x-ray wavefield into visible intensity modulations [14]. The air-tissue interfaces of the lung are ideal for PCX imaging as they yield significant phase shifts [1]. This markedly increases the contrast of tissue compared to that seen in absorption-based x-ray images. PB-PCX imaging has the simplest PCX experimental setup. It requires only a sufficiently spatially coherent x-ray source and a detector placed some distance behind the sample. The boundary between materials with different refractive index decrements becomes enhanced by Fresnel interference fringes upon free space propagation. The Fresnel fringes arising from many alveoli are projected onto the imaging plane to form a speckled pattern (Figs. 1(a) and 1(b)) [1]. Roughly textured materials and spatially random samples, such as colloidal glass particles, also produce speckled images. The parameters of speckle patterns (for example, size, intensity and contrast) have been shown to depend on the structural properties of the illuminated object [15–17]. Here, we devise a way to extract structural properties of the alveoli, specifically their size and population from PB-PCX lung speckle images, which is quantified via analysis in the Fourier domain.

#222268 - $15.00 USD Received 2 Sep 2014; revised 16 Oct 2014; accepted 18 Oct 2014; published 24 Oct 2014

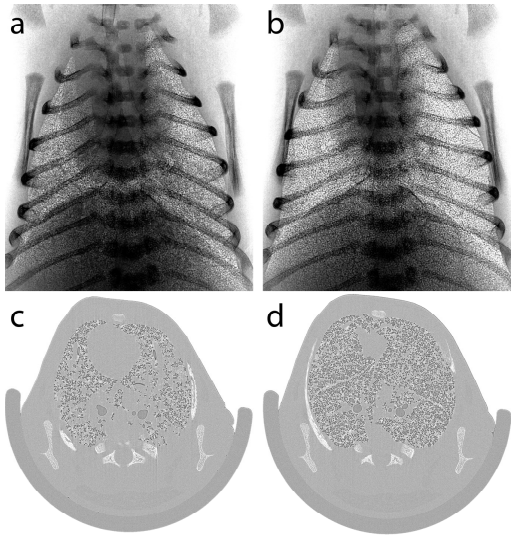

Fig. 1. 19.8× 22.8 mm^2 2D propagation-based phase contrast x-ray (PB-PCX) image of the chest at (a) low and (b) high lung air volumes of the same rabbit kitten. These PB-PCX images were one of 1800 projections used to reconstruct 27.6× 26.4 mm^2 CT slices as shown in (c) and (d), respectively. ODD = 1 m. Energy = 24 keV. Exposure time per projection = 50 ms. (See section 3 for further experimental details).

Previous evidence on how human alveoli behave during respiration has been inconclusive, partly due to the inherently complicated interconnecting nature of alveoli, but also because previous studies used different experimental techniques, animal subjects and morphemetrics techniques [18]. While it was initially believed alveolar size varied monotonically with lung volume, there has been some evidence of alveoli opening and closing during respiration [19]. This is often termed alveolar recruitment/de-recruitment although, in the neonatal lung, aeration and reflooding may be more accurate terminology [20].

The theoretical basis of our work is presented in section 2. This is validated using colloidal soda-lime glass (SLG) microspheres, which closely resemble alveoli in size and shape, then applied to newborn rabbit kittens to measure alveolar size and compared with a gold standard using high-resolution CT images (see section 3 for details). The results and analysis from both microspheres and rabbit lungs is presented in section 4. The prospect of applying our work to human patients forms part of our discussion in section 5. We conclude with section 6.

2. Background theory

Here we show how the alveolar size and population can be determined from lung speckled PB-PCX chest images if the lung air volume is known. This derivation follows closely to that developed in Leong *et al.* [21], but in that derivation alveoli were assumed to be randomly distributed. In Figs. 1(c) and 1(d) we see that the alveoli become relatively closely packed and therefore less randomly ordered at increasing volume. Herein, we take into account potential short-range ordering associated with close packing.

Consider an object comprised of a single material with complex refractive index, $n = 1-\delta + i\beta$, where δ and β are the refractive index decrement and attenuation index, respectively. The imaginary number is denoted by i. The power spectrum of its PB-PCX image ($I(\vec{r}_\perp, z = L)$) in the plane $\vec{r}_\perp = (x, y)$ that is normalized against its contact image ($I(\vec{r}_\perp, z = 0)$), at

#222268 - $15.00 USD Received 2 Sep 2014; revised 16 Oct 2014; accepted 18 Oct 2014; published 24 Oct 2014

object-to-detector propagation distance (ODD) L, along the optic axis z can be expressed as [21]:

$$\left|\mathbf{F}\left\{\frac{I(\vec{r}_\perp, z=L)}{I(\vec{r}_\perp, z=0)}-1\right\}\right|^2 = L^2\delta^2 k_\perp^4 \left|\mathbf{F}\left\{T\left(\vec{r}_\perp\right)\right\}\right|^2. \quad (1)$$

Here, $T\left(\vec{r}_\perp\right)$ is the projected thickness of the object, $\mathbf{F}$ is the Fourier transform with respect to spatial variables x and y, $k_\perp = \sqrt{k_x^2 + k_y^2}$ is the transverse wavenumber in $\vec{r}_\perp$ where (k_x, k_y) are vectors in two-dimensional (2D) Fourier space. The technique employed to determine $I(\vec{r}_\perp, z=0)$ is detailed in section 3.4.

In deriving Eq. (1), two assumptions were made regarding the object: (1) lateral displacement of the x-ray beam at the exit surface due to scattering within the object must be less than the detector spatial resolution, and (2) it weakly absorbs (i.e., $\mu T<1$ where μ is the attenuation coefficient of the object). These assumptions have been shown to be valid when imaging the thorax of a newborn rabbit kitten using 24 keV x-rays [21]. Equation (1) is restricted to the near-field regime, which is where the Fresnel number, N_F, defined by,

$$N_F = \frac{a^2}{L\lambda}, \quad (2)$$

to be such that $N_F \geq \max\{1, |\varphi|_{max}\}$ [22]. Here, a is the characteristic length scale of the object over which $I(\vec{r}_\perp, z=0)$ varies appreciably, λ is the incident wavelength, and the maximum magnitude of the phase gradient in $\vec{r}_\perp$ is defined by $|\varphi|_{max}$. Note that the reciprocal of 'a' in the near-field condition quantifies the area of the 2D Fourier support.

To determine the form of Eq. (1) for lungs, the lung is modeled as N air-filled spherical cavities of radius R (representing alveoli) that are randomly distributed in lung tissue volume with refractive index decrement δ. This model provides a simple analytic solution to Eq. (1) for the lungs. Highly magnified images of the alveoli show they resemble pseudo-randomly orientated dodecahedrons, which for our purpose are sufficiently close to being spherical [23]. To that end, the object function of the modeled lung can be expressed as a sum of convolutions:

$$\tilde{T}(\vec{r}) = V(\vec{r}) - \sum_{n=0}^{N} \int_{\vec{r}} \delta(\vec{r} - \vec{r}_n) G(\vec{r}) d\vec{r}, \quad (3)$$

where $\delta(\vec{r})$ is the unit impulse function and $\vec{r}_n = (x_n, y_n, z_n)$ is a vector in 3D Cartesian space representing the random position of the n^{th} alveoli in the volume $V(\vec{r})$, where $V(\vec{r})$ is the object function of lung tissue and is equal to unity everywhere in the volume and zero everywhere else. The integral of the modeled lung $\tilde{T}(\vec{r})$ along the optic axis z gives the projected thickness $T(\vec{r}_\perp)$. The object function of a sphere is represented by $G(\vec{r})$ where $G = 1$ for $|\vec{r}| \leq R$ and $G = 0$ everywhere else. The power spectrum of Eq. (3) is written as:

$$\left|\mathbf{F}\left\{\tilde{T}(\vec{r})\right\}^2\right| = \left|\int_V \tilde{T}(\vec{r}) e^{-i2\pi\vec{k}\cdot\vec{r}} d\vec{r}\right|^2, \quad (4)$$

where $\vec{k} = \left(k_x, k_y, k_z\right)$ are vectors in 3D Fourier space.

The first term of Eq. (3) is a constant function and so contributes only to the zero (DC) frequency. The DC frequency, however, is not relevant to our analysis and will be ignored hereafter. To derive an analytic solution of the integral in Eq. (4), and hence obtain explicit

#222268 - $15.00 USD Received 2 Sep 2014; revised 16 Oct 2014; accepted 18 Oct 2014; published 24 Oct 2014

dependence on *N* and *R*, Eq. (3) (minus $V(\vec{r})$) is substituted into Eq. (4), and making use of the convolution theorem and the sifting property of the unit impulse, we arrive at,

$$\left|\mathbf{F}\left\{\tilde{T}(\vec{r})\right\}\right|^2 = \left|\mathbf{F}\left\{G(\vec{r})\right\}\right|^2 \left[N + \sum_{n=1}^{n\neq m}\sum_{m=1}\cos\left(2\pi\vec{k}\cdot\vec{D}_{nm}\right)\right], \tag{5}$$

where $\left|\mathbf{F}\left\{G(\vec{r})\right\}\right|^2$ is the power spectrum of a sphere and $\vec{D}_{nm}$ is the vector from sphere *n* to *m*. The arrangement of alveoli is macroscopically isotropic making their power spectrum rotationally symmetric. Thus, the sum in Eq. (5) is averaged over the polar angle defined between $\left|\vec{k}\right|$ and $\left|\vec{D}_{nm}\right|$, and the azimuthal angle formed by the plane containing $\vec{k}$ and $\vec{D}_{nm}$ with an arbitrary plane. Furthermore, the power spectrum of a sphere is also rotationally symmetric. Thus, Eq. (5) can be simplified into one-dimensional form with independent variable $\left|\vec{k}\right|$, to give a result equivalent to the Debye scattering formula, which was derived for predicting the diffraction patterns of gases and liquids [24]:

$$\overline{\left|\mathbf{F}\left\{\tilde{T}(\vec{r})\right\}\right|^2} = \left|\mathbf{F}\left\{G(\vec{r})\right\}\right|^2 \left[N + \sum_{n=1}^{n\neq m}\sum_{m=1}\frac{\sin\left(\left|\vec{k}\right|\left|\vec{D}_{nm}\right|\right)}{\left|\vec{k}\right|\left|\vec{D}_{nm}\right|}\right]. \tag{6}$$

The overbar represents the rotational average of $\left|\mathbf{F}\left\{\tilde{T}(\vec{r})\right\}\right|^2$, hereafter the overbar will be dropped for notational simplicity. According to the Fourier slice theorem, $\left|\mathbf{F}\left\{\int_z \tilde{T}(\vec{r})\,dz\right\}\right|^2(k_x,k_y) = \left|\mathbf{F}\left\{\tilde{T}(\vec{r})\right\}\right|^2(k_x,k_y,0)$. This is also true for $\left|\mathbf{F}\left\{G(\vec{r})\right\}\right|^2$ and therefore allows $\left|\vec{k}\right|$ to be replaced with $k_\perp = \left|\vec{k}_\perp\right|$ in Eq. (6) to give an expression for the power spectrum of $T(\vec{r}_\perp)$. Substituting this 2D form of Eq. (6) into Eq. (1), and given that the power spectrum of a sphere is $\left|\mathbf{F}\left\{G(\vec{r})\right\}\right|^2 = \left|\frac{4\pi R^3}{(k_\perp R)^2}\left[\frac{\sin(k_\perp R)}{k_\perp R} - \cos(k_\perp R)\right]\right|^2$ [25], we arrive at the main equation of this study, the PB-PCX speckle image power spectrum,

$$\left|\mathbf{F}\left\{\frac{I(x,y,z=L)}{I(x,y,z=0)} - 1\right\}\right|^2 = L^2\delta^2 k_\perp^4 N \left|\frac{4\pi R^3}{(k_\perp R)^2}\left[\frac{\sin(k_\perp R)}{k_\perp R} - \cos(k_\perp R)\right]\right|^2 \times\left[1 + \int_V \rho(D)\frac{\sin(k_\perp D)}{k_\perp D}\,dV\right]. \tag{7}$$

Here, the summation term in Eq. (6) has been rewritten as an integral, over the volume $V(\vec{r})$, weighted by the function *ρ(D)* that is defined as the frequency of occurrence of alveoli separated by distance $D = \left|\vec{D}\right|$. For randomly distributed alveoli, *ρ(D)*≈constant. Consequently, the integral in Eq. (7) becomes the Fourier transform of $V(\vec{r})$ (remember that the sinc term is the polar and azimuthal average of the exponential term in Fourier space). If the ratio of the sphere size $G(\vec{r})$ to the dimension of $V(\vec{r})$ is much less than unity then the integral tends to zero everywhere except at $k_\perp = 0$, and given the DC frequency is irrelevant for our analysis, this reduces Eq. (7) to the expression first derived by Leong *et al.* [21]:

#222268 - $15.00 USD Received 2 Sep 2014; revised 16 Oct 2014; accepted 18 Oct 2014; published 24 Oct 2014

$$\left|\mathbf{F}\left\{\frac{I(x,y,z=L)}{I(x,y,z=0)}-1\right\}\right|^2 = L^2\delta^2 k_\perp^4 N\left|\frac{4\pi R^3}{(k_\perp R)^2}\left[\frac{\sin(k_\perp R)}{k_\perp R}-\cos(k_\perp R)\right]\right|^2. \quad (8)$$

Leong *et al.* [21] showed that the area under the first peak in the spectrum, which is bounded by adjacent minima $k_\perp R = 0$ and $k_\perp R = 4.493$, is given by,

$$PS_{Area} = 34\pi^2 L^2\delta^2 NR. \quad (9)$$

This is approximately equivalent to integrating over all $k_\perp$, except at $k_\perp = 0$, of experimentally measured power spectra as the higher order peaks are suppressed by the detector point spread function (d-PSF) and penumbral blurring. If the total lung air volume (V_L) within the alveoli is known, which is approximated under the assumption of N isolated spheres of radius R,

$$V_L = \frac{4}{3}NR^3, \quad (10)$$

then N and R can be solved, given if δ is known, which can be readily calculated for a given material at a given x-ray energy using the National Institute of Standards and Technology (NIST) database, as described in section 3.4. An alternative method to calculating R from PS_{Area} is using the position of the maximum value of the first order peak (PS_{Peak}) defined by $PS_{Peak}R$ = 2.74 (see Eq. (8)). N could then be calculated from either the known V_L or PS_{Area}, but in this study, V_L was used. However, as is apparent from Figs. 1(c) and 1(d), at increasing V_L, alveoli exhibit short-range order as the alveoli become more closely packed. Equation (7) accounts for this reduction in randomness. Comparing Eqs. (7) and (8), it can be shown that both are oscillatory functions in Fourier space. As the packing fraction increases, their first order peaks differ in position as do the area under their curves. Calculating R from the position of the first order peak using Eq. (8) would become less accurate for increasing alveolar density. A more accurate expression for PS_{Peak} and PS_{Area} can be derived from Eq. (7); however, $\rho(D)$ will likely vary during breathing and is difficult to determine exactly. To test the effect of short-range ordering, SLG microspheres, randomly arranged and closely packed, were imaged. Equations (9) and (10) were then used to measure N and R and compared with their known values (see section 4). This would indicate if Eq. (9) provides sufficiently accurate measures of N and R for closely packed alveoli.

Our team has devised several methods to calculate V_L from 2D images [21, 26–28]. Here we employ the algorithm of Kitchen *et al.* [26], that is simple, accurate and robust for this type of imaging. It measures the change in regional lung air volumes between pairs of PB-PCX images by using a single image phase retrieval algorithm (SIPR) [29]. Having an image of non-aerated lungs enables us to calculate absolute regional lung air volumes [26]. V_L represents the lung air volume within the alveoli while the volumetric technique employed measures the previously mentioned volume plus the volume of air in the airway branches. Nevertheless, given that approximately 90% of the total lung air volume resides in the alveoli, the algorithm by Kitchen *et al.* [26] can be used to adequately approximate V_L.

3. Methodology

3.1 Image acquisition

The Medical and Imaging centre of beamline 20B2 (Hutch 3) at the SPring-8 synchrotron radiation source in Japan was used for all imaging experiments. A Si (111) non-dispersive monochromator was tuned to different energies for imaging glass particles and rabbit kittens with relative energy width of $\Delta E/E \sim 10^{-4}$ and photon flux density ~2×10^8 photons/s/mm^2. Images were flat field corrected using flat and dark field images recorded at the beginning of each image sequence to normalize against the incident intensity of the x-ray beam and to offset

#222268 - $15.00 USD Received 2 Sep 2014; revised 16 Oct 2014; accepted 18 Oct 2014; published 24 Oct 2014

the intrinsic detector noise, respectively. For long image sequences (>2 mins), the intensity of each frame was rescaled to the first frame. This corrected for synchrotron beam fluctuations caused by periodic injections of electrons into the storage ring, and heating/cooling of optical elements.

Two detectors were used in this study: a 2560 × 2160 pixel tandem lens-coupled scientific-CMOS (sCMOS) imaging sensor (pco.edge; PCO AG, Germany) coupled to a 25 μm thick gadolinium oxysulfide ($Gd_2O_2S:Tb^+$;P43) powdered phosphor, and a 2048 × 2048 pixel sCMOS imaging sensor (ORCA-Flash4.0; Hamamatsu, Japan) with a direct fiber optic coupling the sensor to a 150 μm thick columnar CsI scintillator. Their effective pixel sizes were 15.23 μm and 6.38 μm, respectively.

3.2 Glass particles

SLG microspheres (Whitehouse Scientific Ltd.) were used to test and validate our theory. They are a good model for alveoli and their average size and population are accurately known. Both detectors were used for imaging microspheres to test the robustness of our technique against detector types. Microspheres were imaged at 30 keV and with an exposure time of 1.2 s. 150-180 μm sized microspheres were sprinkled onto a cover slip to produce a sparse random distribution and then sealed with another cover slip placed on top. A hollow step-wedge made of polymethylmethacrylate was designed with the height (i.e. thickness) of the steps at 1 mm, 2 mm, 5 mm, 10 mm and 20 mm. The hollow step-wedge was separately filled with closely packed microspheres of sizes 43-55 μm, 63-75 μm, 75-90 μm, 90-106 μm, 106-125 μm, 150-180 μm, 180-212 μm and 250-300 μm.

3.3 Rabbit kittens

All animal experiments performed were approved by the Monash University Animal Ethics Committee and the SPring-8 Animal Care and Use Committee. Pregnant New Zealand white rabbits (27-30 days of gestation, term = 31-32 days; n = 4) were anaesthetized initially using propofol (i.v; 12 mg/kg bolus, 150-500 mg/h infusion), then via inhalation following intubation (Isoflurane 1.5-4%). Rabbit kittens (n = 10) were delivered by caesarean section, then humanely killed using an overdose of sodium pentabarbitone (>100 mg/kg i.p.). Immediately after euthanasia, they were surgically intubated before being placed upright in a water-filled cylinder with their head out and supported by a rubber diaphragm around their necks. A custom-built mechanical ventilator was connected to the endotracheal tubes, which were inserted into the trachea of the rabbit kittens, and sent out trigger signals for gated imaging [30]. Before ventilation several non-aerated images of the chest were recorded. Thereafter ventilation was initiated with an initial airway pressure (AP) of 16 cmH_2O. AP was then gradually increased to 27 cmH_2O and decreased back to 16 cmH_2O via 1 cmH_2O increments, each of which was held for 5 s. The images were recorded at 24 keV with a frame rate of 20 Hz, 40 ms exposure time, and 1 m ODD. This amounts to an absorbed radiation dose per PB-PCX image of ~1 mGy. While this is more than the standard chest x-ray image, the spatial resolution is significantly higher and the dose is still much lower than a standard chest CT [13]. Furthermore, the SNR was measured to be ~10 from several regions that were away from the rabbit kitten but within the water-filled cylinder.

The ventilator was disconnected with AP last set at 2 cmH_2O. High resolution CT images (1800 projections from 0 to 180° with 50 ms exposures and 1 m ODD) were then acquired for a gold standard comparison. Additional CT images were recorded after the kitten's lungs were filled with 100% N_2 (to prevent absorption of gas into the pulmonary capillaries) at 29 cmH_2O AP with the intubation tube then tied off to prevent lung collapse. Each rabbit kitten was fixed in a test tube filled with agar to reduce motion blur. PB-PCX images of the same animal were also recorded at different ODDs to measure the degree of validity of Eq. (1) at large ODD. The pco.edge detector was used because only it had a sufficiently large field of view to image the entire chest of a rabbit kitten in a single exposure.

#222268 - $15.00 USD Received 2 Sep 2014; revised 16 Oct 2014; accepted 18 Oct 2014; published 24 Oct 2014

3.4 Image analysis

Equation (8) does not account for the d-PSF and penumbral blurring. Given that the synchrotron source size of the beamline used for this study was 150 μm × 10 μm, the source-to-object distance was 210 m, and the maximum ODD set was 2 m, the degree of penumbral blurring is less than a pixel width for both detectors [14]. However, the d-PSF alters the power spectrum significantly, and was therefore measured and corrected for each PB-PCX image before subsequent image analysis. The edge spread function was measured both vertically and horizontally using a 5.25 mm thick lead block. The transverse spatial derivatives of the resulting images were averaged over many pixels, extruded azimuthally to construct the d-PSF, and fitted with a 2D Pearson type VII distribution function (PVII) [31]. The Wiener deconvolution algorithm was used to deconvolve the PB-PCX images with the fitted d-PSF [32]. This algorithm is stable against the input parameter, the SNR of the deconvolved image, particularly at low spatial frequencies where the first order peak of the power spectrum of lung speckle presides, thus it need not be known exactly. An optimal SNR value of 500 was found to provide consistent values of N and R for microspheres and alveoli. Wiener deconvolution amplifies high frequency noise but the degree of noise amplification is similar between frames of the same animal. To suppress this effect, the power spectra of images without speckle (e.g. the non-aerated lung images) were subtracted from that of the speckled image (e.g. aerated lung images).

The contact (absorption) image ($I\left(\vec{r}_{\perp}, z=0\right)$) is required to calculate PS_{Area}. This was estimated using SIPR [29]. It requires both μ and δ as inputs for the filter, which were calculated from the NIST database [33]. For SLG microspheres (30 keV), $\mu_{SLG} = 197$ m^{-1} and $\delta_{SLG} = 5.09 \times 10^{-7}$, and for lung tissue (24 keV), $\mu_{LT} = 54.74$ m^{-1} and $\delta_{LT} = 3.99 \times 10^{-7}$. SIPR assumes a single-material object, but the chest comprises of bone and soft tissue. Setting the parameters of SIPR for lung tissue will accurately reverse the lung tissue-induced phase contrast but over-smooth that of the bone [28]. To that end, dividing PB-PCX chest images by their contact image (using SIPR) will accurately remove the absorption contrast of lung tissue but not entirely that of the bone, particularly along the edges of the bone. Nevertheless, its contribution to the power spectra is small compared to the lung speckle signal.

To summarize, PS_{Area} was calculated using the following sequence of steps applied to the PB-PCX lung speckle image: (i) deconvolving the d-PSF, (ii) dividing by its contact image, (iii) computing its azimuthally averaged power spectrum, (iv) subtracting from that of its non-aerated PB-PCX image, and (v) integrating between 2 mm^{-1} and the Nyquist frequency. The lower limit was chosen to exclude the peak at the origin of Fourier space but still included the first order peak.

Grayscale 3D granulometry [34] was considered the 'gold standard' for our technique for measuring alveolar dimensions. Spheres of various sizes were created as structural elements to survey the lung for alveoli of similar size using the morphological opening operator on 7.5 mm^3 CT volumes of rabbit kitten lungs. The CT volumes were magnified by a factor of 4 and bilinearly interpolated beforehand to increase the spatial sampling rate. Alveolar dimensions were measured from our technique by calculating PS_{Area} from one of the CT projection images. For this data set V_L was calculated by intensity thresholding the CT images to segment the airways before counting the total voxels within them.

4. Results

Three types of 150-180 μm microsphere samples were investigated: single and multiple particles randomly dispersed between cover slips, and a hollow step-wedge filled with particles. These samples were recorded at 15 cm ODD using the pco.edge detector and are shown in Figs. 2(a-c). Both N and R were calculated using Eqs. (9) and (10). N and R were also determined from the position of the first order peak in the speckle power spectrum, that is, PS_{Peak}. The calculated values of N and R along with their expected values are presented in Table 1.

#222268 - $15.00 USD Received 2 Sep 2014; revised 16 Oct 2014; accepted 18 Oct 2014; published 24 Oct 2014

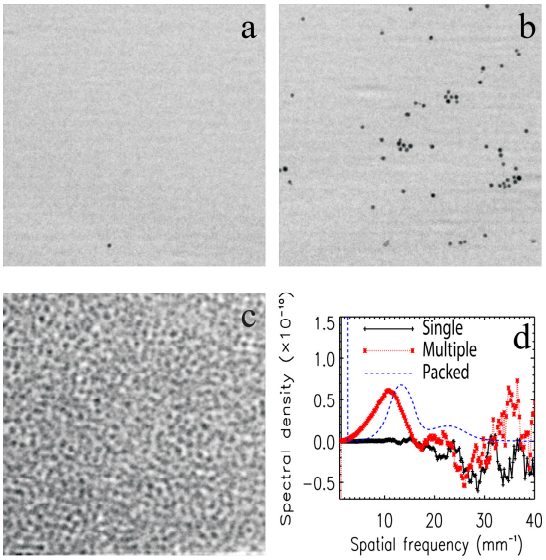

Fig. 2. 3.83 × 3.83 mm^2 propagation-based phase contrast x-ray images of 150-180 μm sized (a) single glass particle, (b) multiple glass particles and (c) a 1 mm thick container of glass particles with volume packing density ≈ 55%. (d) shows the corresponding power spectra of (a)-(c), after deconvolving to remove the detector point spread function, dividing by their contact image, normalizing against the total pixels in the image and the number of microspheres. ODD = 15 cm. Energy = 30 keV. Exposure time = 1 s.

For single and multiple particles placed between cover slips, V_L was calculated using Eq. (10) with N and an average value for R measured directly from their images for comparison with our technique. The calculated and expected values of N and R for a single microsphere agree poorly because the image noise masked its signal (Fig. 2(d)). However, as the number of microspheres increased, a clear peak in the power spectrum becomes evident above the noise in Fig. 2(d). This resulted in excellent agreement between the calculated and expected values of N and R using both the PS_{Area} and PS_{Peak} (Table 1). The uncertainties in N and R were propagated from the uncertainty in V_L, which was the difference in using the average rather than the distribution of R, except for R calculated from PS_{Peak} which was determined from weighted fitting a PVII function to the centroid. Comparing the uncertainties in N and R, at low packing fraction, they are more precisely measured from PS_{Peak} than from PS_{Area} as PS_{Peak} does not depend on how precisely V_L is measured.

Table 1. The number and mean radius of glass particles calculated from the propagation-based phase contrast x-ray images in Figs. 2(a)-2(c) compared with the expected values shown in brackets.

	Number		Radius (μm)	
Microspheres	PS_{Area}	PS_{Peak}	PS_{Area}	PS_{Peak}
Single (Fig. 2(a))	0.67±0.03(1)	2.7 ± 0.1	96 ± 4(83 ± 8)	59.55 ± 0.01
Multiple (Fig. 2(b))	52 ± 3(59)	59.63 ± 0.08	87 ± 4(83 ± 8)	83.47 ± 0.08
Packed (Fig. 2(c))	3730 ± 460(3600 ± 800)	7500 ± 1600	82 ± 9(83 ± 8)	64.90±0.01

Microspheres poured into a container inevitably stack on top of one another to produce some short-range order. V_L was determined using SIPR to calculate the projected thickness of

#222268 - $15.00 USD Received 2 Sep 2014; revised 16 Oct 2014; accepted 18 Oct 2014; published 24 Oct 2014

glass at each pixel then summed and multiplied by the pixel area [29]. Surprisingly, the presence of short-range order did not adversely affect the calculation of N and R using PS_{Area}. The uncertainty was propagated from that of V_L, which was determined using a calibration curve that plots the uncertainty in V_L against the image size, developed by Leong *et al.* [28]. Conversely, PS_{Peak} shifted to higher frequencies (Fig. 2(d)), thereby underestimating R and overestimating N. Again, the uncertainty of the former was determined from weighted fitting a PVII function to the centroid while that of the latter was determined in a similar manner to N that was calculated from PS_{Area}. Two important and consequential points arise from these findings: (1) there is short-range order in closely packed particles, as indicated by the shift in PS_{Peak}, and (2) despite this, Eqs. (9) and (10) can still accurately calculate N and R. Figure 2(d) provides a clue to why Eqs. (9) and (10) remain valid. There we see that the shape and position of the first order peak is altered by short-range order, but the area under the curve remains virtually unchanged. This presents a favourable outcome, since the packing density of alveoli will vary during respiration.

PB-PCX images of the 1 mm thick region of the step-wedge, each containing different sized microspheres, were recorded using the ORCA detector to better resolve the smaller sized microspheres. N and R were calculated from PS_{Area} for each and are plotted in Fig. 3(a) and are in close agreement with the expected values. However, at increasing sample thickness (that is, at increasing $|\varphi|_{max}$) and ODD, large errors accumulated in the calculation of R as N_F reduces below $\max\{1,|\varphi|_{max}\}$. This is shown in Fig. 3(b). A similar trend (not shown) was found when plotting N as a function of ODD. The accuracy of calculating R of a single layer of microspheres also decreases despite $N_F \geq \max\{1,|\varphi|_{max}\}$ of up to 2 m ODD ($R \approx 165$ µm, $|\varphi|_{max} = |-k\delta_{SLG}2R| = 13.5$, $L = 2$ m, $a = 2R$, $N_F = 61.6$). The consistent overestimation of PS_{Area} with respect to that obtained experimentally, which we denote as large distance error, could be due to a number of possible effects. While partial coherence (penumbral blurring) was deemed negligible based on the source size given by Goto *et al.* [35], the effects on speckle contrast may be larger than expected. Our group has also found discrepancies between simulated lung speckle contrast using the projection approximation and the more rigorous multi-slice diffraction method, which may also account for the differences. Finally, Nugent *et al.* [36] showed a loss of contrast from imaging random phase screens (akin to the lungs) can be caused by limited spatial resolution. A complete study of these competing effects is warranted, but is beyond the scope of this paper.

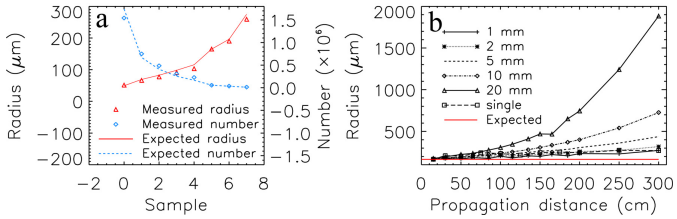

Fig. 3. Evaluating the accuracy of calculating the number and mean radius of microspheres from propagation-based phase contrast x-ray images of (a) 1 mm thick container filled separately with different sized microspheres at 15 cm object-to-detector distance (ODD) and (b) containers with variable thickness filled with 150-180 µm sized microspheres, and a single layer of 150-180 um microspheres, at various ODDs.

Considering that the typical alveolar radius and projected thickness of a fully aerated lung of a rabbit kitten are 75 µm and 10 mm, respectively, and given that the ODD used in our experiments was 1 m, $N_F = 435$ and $|\varphi|_{max} = |-k\delta_{SLG}2R| = 363$. Since $N_F \geq \max\{1,|\varphi|_{max}\}$, this shows the PB-PCX lung images recorded in this study satisfy the near-field condition. To account for the large distance error for the lungs, images of sets of lungs aerated to various degrees of the same rabbit kitten were acquired at multiple ODDs. The PS_{Area} was calculated at

#222268 - $15.00 USD Received 2 Sep 2014; revised 16 Oct 2014; accepted 18 Oct 2014; published 24 Oct 2014

each ODD and compared with the expected PS_{Area}, which was determined by assuming the calculated PS_{Area} at the lowest ODD of 15 cm was accurate and subsequent PS_{Area} were extrapolated to larger ODD using Eq. (1). This was done for several rabbit kittens at 1 m ODD, and on average their calculated PS_{Area} differed by a factor of 2.3 ± 0.6 from the expected value. This factor was accounted for in all PB-PCX rabbit kitten images recorded at 1 m to give a more reliable measure of the alveolar dimensions and number.

3D granulometry was utilized to test the accuracy of measuring alveolar dimensions from PS_{Area} and PS_{Peak}, although it does not yield their number, N. Figure 4(a) shows typical granulometry curves that correspond to a 7.5 mm^3 cube region-of-interest (ROI) in Figs. 1(c) and 1(d). The maximum value represents the dominant alveolar dimension. 3D granulometry was performed on several more rabbit kittens and compared with PS_{Area} and PS_{Peak} (Fig. 4(b)). The uncertainty in R measured from 3D granulometry was determined by the width of the flat top of the peak while that measured from PS_{Area} was propagated from the uncertainty in the factor, 2.3 ± 0.6, used to correct for the large distance error. The uncertainty in PS_{Peak}, determined from weighted fitting to the PVII function, was negligible (<1 μm). The gradients for PS_{Area} and PS_{Peak} against 3D granulometry were 0.9 ± 0.3 (Pearson product-moment correlation coefficient ρ = 0.6) and 0.2 ± 0.1 (ρ = 0.3), respectively. The gradient of the latter indicates the insensitivity of PS_{Peak} with R, which is likely caused by short-range ordering of alveoli affecting the measured size (see section 2), while the former shows a strong positive correlation. From the results of the SLG microspheres, this further demonstrates our technique is immune to short-range ordering effects.

To demonstrate the presence of alveolar recruitment and de-recruitment, the number of alveoli was manually counted from a transaxial slice for each CT recorded of a rabbit kitten at different stages of respiration, which in stereology shows that it is approximately proportional to the alveolar number in 3D (see section 5 for automated methods trialled as gold standards for validating N) [37]. The transaxial slices were chosen to be approximately at the same axial position in the lung. Figure 4(c) shows alveolar number correlated with the total lung volume of the entire CT.

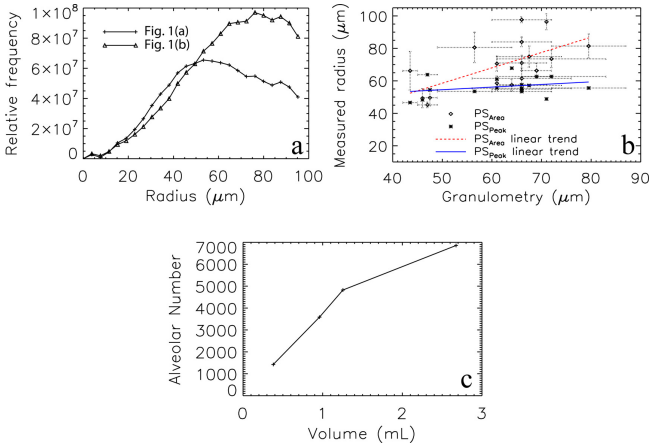

Fig. 4. (a) Distribution of alveolar dimensions determined from 7.5 mm^3 regions centred about the two CT slices in Figs. 1(c) and 1(d), respectively, using 3D granulometry. (b) The average alveoli size was measured both from PS_{Area} and PS_{Peak} and was compared with that measured from 3D granulometry for several rabbit kittens. (c) The alveolar number was approximated by manually counting the number of alveoli surface profiles from one transaxial slice per CT of a ventilating kitten and plotted against the total lung air volume determined by intensity thresholding the entire CT.

#222268 - $15.00 USD Received 2 Sep 2014; revised 16 Oct 2014; accepted 18 Oct 2014; published 24 Oct 2014

The ability of our technique to dynamically measure N and R during ventilation is demonstrated in Fig. 5; from the first breath and several respiratory cycles later. From the first breath (Fig. 5(a)), Fig. 5(b) shows that N (calculated from PS_{Area}) first increases then plateaus after t = 5 s. This increase in N coincides with the clearing of fetal lung liquid and consequent recruitment of alveoli [20]. An increase in R, computed from PS_{Area}, follows the same trend as V_L. Conversely, R that was derived from PS_{Peak}, remains largely unchanged, which may be caused by alveoli becoming more closely packed. At $t \geq 27$ s, a sudden drop in V_L sees R decreasing (calculated from PS_{Area}), but interestingly N concomitantly increased. The increase in N may be caused by the trapping of air as the airways collapse to produce the appearance of additional alveoli in the form of air bubbles. During a second respiratory cycle of the partially aerated lung (Fig. 5(c)), the independent calculations of R shown in Fig. 5(d) closely agree, but after $t \geq 8$ s they diverge. This is likely due to effects of short-range order affecting peak position. N (calculated from PS_{Area}) remains approximately constant throughout except at the beginning and end of the respiratory cycle. This shows evidence of alveolar opening/recruitment followed by flooding/de-recruitment.

5. Discussion

The structural and functional complexity of the lung makes it both intriguing to understand yet difficult to study. Many lung imaging techniques are limited to studying only small regions of the lungs accessible to invasive instruments, or lungs that are effectively stable which therefore precludes the extraction of dynamic information. Here, the method developed by Leong *et al.* [21] was applied, after accounting for the large distance error and d-PSF, to measure the N and R of alveoli from the speckle patterns of PB-PCX ventilated chest images. Highly spatially resolved PB-PCX images can be recorded in real-time during a respiratory cycle by using intense and coherent synchrotron light coupled with detectors with high spatial resolution and quantum efficiency. Our technique can therefore provide valuable insight into the structural lung changes during respiration, which could prove useful for developing safe ventilation strategies or studying lung diseases.

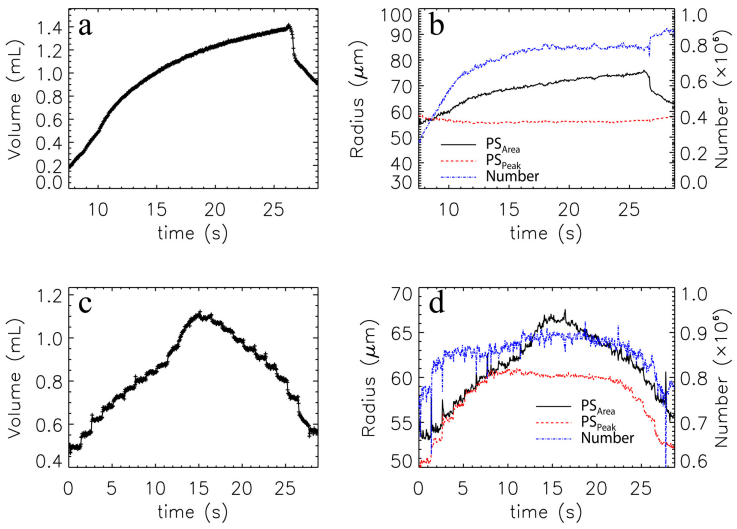

Fig. 5. Lung air volumes from PB-PCX chest images of a kitten mechanically ventilated (a) from its first breath, and (c) over a single respiratory cycle several breaths after its first. The corresponding calculation of number and mean radius of alveoli are shown in (b) and (d).

#222268 - $15.00 USD Received 2 Sep 2014; revised 16 Oct 2014; accepted 18 Oct 2014; published 24 Oct 2014

In this study, N and R were measured for the whole lungs. However, a key benefit of this technique is its ability to also measure N and R locally, if PS_{Area} and V_L are regionally measured. The minimum size of the ROI from which that V_L can be measured, using the technique adapted in this study, is limited by the differential movement of the bone. Previously, Leong *et al.* [28] developed a cross correlation-based technique that aligned the bones between two PB-PCX chest images, which effectively removes the bone, before applying the volumetric analysis of Kitchen *et al.* [26] to calculate V_L on a pixel-by-pixel basis. For calculating PS_{Area}, the ROI must be large enough to adequately sample the power spectrum. Given the detector pixel size of 15.23 μm and typical alveolar size of 150 μm, N and R can be calculated from a ROI as small as ~0.5 mm^2 compared to that of the entire lung being 230 mm^2. This would be important in optimizing ventilation strategies to ensure all parts of the lung are adequately aerated without over-distending the alveoli leading to conditions such as ventilation-induced lung injury and bronchopulmonary dysplasia. Diagnosis and treatment of respiratory diseases including emphysema could also benefit by better localizing and targeting the diseased region.

Non-aerated PB-PCX images of the lungs are required for our technique but are not always accessible, particularly for studying subjects that are not newborn. One alternative is intensity thresholding a low dose chest CT image reconstructed from phase retrieved PB-PCX images (using SIPR) to remove the aerated alveoli, with the resulting image being Radon-transformed then propagated using Eq. (1) to obtain the non-aerated PB-PCX chest image. While CT can provide information on N and R, our technique can achieve this using single projections. Consequently, the temporal resolution of our technique is far superior in allowing dynamic measures at a significantly lower radiation dose than CT. Similarity in anatomical structure of the chest within a species should also make it possible to use a non-aerated PB-PCX image for different subjects of the same species. This would avoid doing CT and imparting unnecessary radiation dose to every subject.

Grayscale 3D granulometry cannot be used to measure the number of alveoli from CT images. To that end, an automated algorithm, watershedding [38], was tried in this study on the CT images. This image processing technique can measure both N from the number of local minima and R from the size of the valleys centring those minima. However, watershedding was found to be unstable against image noise as the dominant spatial frequency of the noise was comparable to that of the alveoli.

The success of translating our technique for clinical use will depend on achieving adequate SNR at short exposure times. This would be important for *in vivo* imaging of the rapid rate of spontaneous breathing as opposed to controlled ventilation that was performed in our study. Moreover, human lungs are significantly larger than those of the rabbit kittens used in this study. While this lowers the image signal from an increase in attenuation, the x-ray energy can be increased without significant loss in phase contrast [14]. There is potential for synchrotron imaging of human patients, but the cost and limited availability of synchrotrons makes this unfeasible. Lower powered laboratory-based x-ray sources have been shown to produce well defined lung speckle in mice [39]. The challenge here will be optimizing the x-ray source spot size and ODD first for imaging animals and then human patients to produce speckles minimally affected by penumbral or motion blur. Also, while laboratory x-rays sources are polychromatic and the technique presented herein has only been developed for quasi-monochromatic sources, it has been shown that the transport-of-intensity equation, from which Eq. (1) was derived, can be generalized for a polychromatic source given the projection approximation is valid across the x-ray energy spectra [40]. For larger lungs, higher x-ray energies may be required to ensure the projection approximation holds.

6. Conclusions

We have demonstrated a novel non-invasive *in situ* imaging-based technique that is able to quantify the number and average size of densely packed particles and cavities. We have applied this technology to measure the same parameters of alveoli in the lungs. This information is

#222268 - $15.00 USD Received 2 Sep 2014; revised 16 Oct 2014; accepted 18 Oct 2014; published 24 Oct 2014

encoded in the speckle pattern seen in propagation-based phase contrast x-ray images in which multiple particles and cavities overlap in projection. The morphological parameters were extracted by calculating the area under the image power spectrum of the speckled images and by simultaneously measuring the particulate volume from the image. Our technique revealed recruitment and de-recruitment of alveoli in mechanically ventilating newborn rabbit kittens. 3D grayscale granulometry was employed as a gold standard for alveolar dimensions and agreed well with our technique. As well as furthering our conceptual understanding of the structural behaviour of the lung, our technique has potential to be performed with a laboratory-based x-ray source and consequently applied to clinical diagnosis of respiratory diseases, evaluating the effect of therapeutic treatments, and monitoring of assisted ventilation.

Acknowledgment

The authors would like to thank Kentaro Uesugi and Naoto Yagi for assistance with the experiments, and SPring-8 for providing access to their facility and equipment. AFTL acknowledges the support of an Australian Postgraduate Award. SBH and MJK acknowledge funding from the Australian Research Council (ARC; Grant Nos. DP110101941 and DP130104913) and National Health & Medical Research Council (NHMRC; APP1064973). MJK is an ARC Australian Research Fellow. SBH is a NHMRC Principal Research Fellow. This research was partially funded by the Victorian Government's Operational Infrastructure Support Program. We acknowledge travel funding provided by the International Synchrotron Access Program managed by the Australian Synchrotron and funded by the Australian Government.

#222268 - $15.00 USD Received 2 Sep 2014; revised 16 Oct 2014; accepted 18 Oct 2014; published 24 Oct 2014